

**UNIVERSIDAD COMPLUTENSE DE MADRID**  
**FACULTAD DE FARMACIA**



**TESIS DOCTORAL**

**Stimuli-responsive mesoporous nanomatrices for drug  
delivery**

**Nanomatrices mesoporosas estímulo-respuesta para la  
liberación de fármacos**

MEMORIA PARA OPTAR AL GRADO DE DOCTOR

PRESENTADA POR

**Miguel Gisbert Garzarán**

Director

**Miguel Manzano García**

Madrid

© Miguel Gisbert Garzarán, 2019

# Stimuli-Responsive Mesoporous Nanomatrices for Drug Delivery

*Nanomatrices Mesoporosas Estímulo-Respuesta para la Liberación de Fármacos*



Miguel Gisbert Garzarán

Memoria para Optar al Grado de Doctor por la  
Universidad Complutense de Madrid

Departamento de Química en Ciencias Farmacéuticas  
Facultad de Farmacia, UCM  
Madrid 2019

Director: Miguel Manzano García





UNIVERSIDAD  
COMPLUTENSE  
MADRID

**DECLARACIÓN DE AUTORÍA Y ORIGINALIDAD DE LA TESIS  
PRESENTADA PARA OBTENER EL TÍTULO DE DOCTOR**

D./Dña. MIGUEL GISBERT GARZARÁN,  
estudiante en el Programa de Doctorado FARMACIA,  
de la Facultad de Farmacia de la Universidad Complutense de  
Madrid, como autor/a de la tesis presentada para la obtención del título de Doctor y  
titulada:

STIMULI-RESPONSIVE MESOPOROUS NANOMATRICES FOR DRUG DELIVERY  
NANOMATRICES MESOPOROSAS ESTÍMULO-RESPUESTA PARA LA LIBERACIÓN DE FÁRMACOS

y dirigida por: MIGUEL MANZANO GARCÍA

**DECLARO QUE:**

La tesis es una obra original que no infringe los derechos de propiedad intelectual ni los derechos de propiedad industrial u otros, de acuerdo con el ordenamiento jurídico vigente, en particular, la Ley de Propiedad Intelectual (R.D. legislativo 1/1996, de 12 de abril, por el que se aprueba el texto refundido de la Ley de Propiedad Intelectual, modificado por la Ley 2/2019, de 1 de marzo, regularizando, aclarando y armonizando las disposiciones legales vigentes sobre la materia), en particular, las disposiciones referidas al derecho de cita.

Del mismo modo, asumo frente a la Universidad cualquier responsabilidad que pudiera derivarse de la autoría o falta de originalidad del contenido de la tesis presentada de conformidad con el ordenamiento jurídico vigente.

En Madrid, a 6 de septiembre de 2019

Fdo.: MIGUEL GISBERT GARZARÁN

Esta DECLARACIÓN DE AUTORÍA Y ORIGINALIDAD debe ser insertada en  
la primera página de la tesis presentada para la obtención del título de Doctor.





UNIVERSIDAD  
**COMPLUTENSE**  
MADRID

**AUTORIZACIÓN DEL DIRECTOR DE TESIS  
PARA SU PRESENTACIÓN**

Dr. Miguel Manzano García con DNI 33519758H como Director de la Tesis Doctoral


**Stimuli-Responsive Mesoporous Nanomatrices for Drug  
Delivery**

**Nanomatrices Mesoporosas Estímulo-Respuesta para la  
Liberación de Fármacos**

Realizada en el **Departamento de Química en Ciencias Farmacéuticas, Unidad de Química Inorgánica y Bioinorgánica** por el doctorando **Miguel Gisbert Garzarán**, autorizo la presentación de la citada Tesis Doctoral, dado que reúne las condiciones necesarias para su defensa.

En Madrid, a 6 de septiembre de 2019

EL DIRECTOR DE TESIS

  
Fdo.: **Miguel Manzano García**



Siempre he pensado que los agradecimientos son la parte más humana de una tesis doctoral, la que refleja a la persona, sus vivencias y su evolución. Por ello, de igual forma que siempre decís que cuando doy charlas soy “muy yo”, me he esforzado en escribir estas palabras de forma que al leerlas seáis capaces de verme reflejado en ellas. Además, me siento especialmente contento a la hora de escribir esto al ver que me ha ocupado tantas páginas, pues me hace ver lo afortunado que soy. Llevo tiempo pensando que el punto en el que me encuentro ahora mismo es consecuencia de todas las (afortunadas) malas decisiones que he ido tomando a lo largo mi vida, por eso hoy en *Érase una vez...El Maño* os voy a contar la historia de cómo hemos llegado hasta aquí.

Recuerdo que la primera vez que estudié física en el colegio no me gustó. Aun así, acabé estudiando física en la universidad y oh, sorpresa, tampoco me gustó. Pero como soy bastante terco, como buen aragonés, acabé siendo físico. El caso es que allá por tercero de carrera, como consecuencia de lo poco motivado que estaba, empecé a interesarme de nuevo por el deporte, en particular por la fisiología del deporte y eso hizo que me entrara el gusanillo por las ciencias de la salud. Por aquel entonces yo pensaba que ojalá pudiera estudiar algo que pudiera ayudar a mejorar la salud de la gente, así que me decidí por estudiar un máster sobre física de la radioterapia y el radiodiagnóstico gracias a una asignatura que había cursado. Por casualidades de la vida, en quinto de carrera cursé una asignatura de magnetismo y me tocó hacer un trabajo sobre superparamagnetismo en el que vi que había nanopartículas superparamagnéticas que podían usarse con aplicaciones biológicas. Como cabría esperar el máster tampoco me gustó, pero tuve la grandísima suerte de ver que se ofertaba un TFM en este departamento sobre nanopartículas y cáncer. Así que me pareció la oportunidad perfecta para poder hacer algo de aquello que había leído para mi trabajo sobre magnetismo... y gracias a ello descubrí un campo que me fascina, que me hace feliz cada vez pienso en él. Y al final tuve suerte, pues tras realizar el TFM se me ofreció la posibilidad de continuar aquí realizando la tesis y así empezó todo.

Por suerte o por desgracia me tocó empezar con la química desde cero, lo cual sin duda fue (es y será) un gran reto. En estos 4 años me he vuelto a encontrar a mí mismo, y es por ello que salgo plenamente satisfecho en lo personal de esta etapa. He recuperado esa ilusión por aprender que siempre tuve de niño y que perdí durante la carrera. He vuelto a disfrutar estudiando, pocos días recuerdo que no haya leído al menos un artículo. Para mí esto no ha sido un trabajo, ha sido ir cada día a hacer lo que me gusta y a lo que me quiero seguir dedicando. Sin embargo, salgo frustrado en cierto modo, con la sensación de que se podría haber conseguido mucho más. Pero al final somos el producto de nuestras circunstancias y no cambiaría nada, pues seguramente con otra secuencia de acontecimientos no hubiera tenido la oportunidad de aprender ni la mitad de lo que lo he hecho.

En cualquier caso, durante estos años han sucedido multitud de cosas que seguro recordaré con cariño en unos años. He montado por primera vez en avión (tras haber perdido por primera vez un avión, ¿quién iba a pensar que hacía falta un pasaporte o un DNI en vigor para volar?). He tenido la oportunidad de viajar a Alemania, Italia, Grecia y Japón, así como descubrir parte de la geografía española. He descubierto el amor por la cocina y, para qué engañarnos, también por el vino blanco (sobre todo por el vino blanco). Incluso me he vuelto un poco laísta. También me ha tocado pasar fines de semana en el laboratorio, pero aun así siempre he podido organizar todo para poder hacer lo que, junto con la ciencia, seguramente más feliz me hace en esta vida: ver al Zaragoza. Recuerdo salir un sábado corriendo, literalmente, del laboratorio bajo un diluvio para coger un autobús a Majadahonda para ver al Zaragoza (2-2, por cierto) o levantarme de madrugada en Japón para poder ver los partidos. ¡Incluso me entrevistaron en Aragón Radio en la sección de zaragocistas por el mundo! Y sobre todo he tenido la oportunidad de disfrutar a diario de personas maravillosas, que son las que al final han hecho que tantas horas en el laboratorio hayan merecido la pena no solo en lo intelectual sino también en lo personal. Así que a continuación, y sin más dilación, procedo a agradecer a quienes han estado ahí durante esta tesis doctoral.

A la Profesora María Vallet-Regí, Marita, por darme la oportunidad de haber podido realizar la tesis doctoral en tu grupo de investigación. Un grupo lleno de medios y conocimiento que sin duda me ha dotado de una serie de recursos que seguro me ayudarán en el futuro a ser un buen científico.



A Miguel Manzano, por ser mi director de tesis y por permitirme la libertad creativa que ha hecho que pueda desarrollarme como científico a lo largo de estos años. Gracias también por todas las aportaciones y correcciones que han hecho de esta tesis doctoral algo que dentro de unos años leeré con satisfacción.

A la Unión Europea, por la financiación proporcionada a través del proyecto MOZART dentro del programa Horizon 2020, que me ha permitido interactuar con multitud de grupos de investigación y empresas de toda Europa, y en definitiva poder llevar a cabo esta tesis doctoral. Al Centro de Investigación Biomédica en Red (CIBER-BBN), por la financiación que me permitió realizar una estancia predoctoral en Japón.

A Juan Carlos Doadrio, director del departamento, por haber estado siempre dispuesto a ayudarme con cualquier problema que pueda haber tenido, por tus palabras amables diarias y por esos ratos de conversación sobre la Bolsa y sobre Teruel.

He tenido la suerte de cruzarme con multitud de personas que, en mayor o menor medida, han estado en mi día a día en el laboratorio o la facultad. Gracias a África, María Teresa, Antonio, Montse, Marina, Fer, Sandra e Isabel, por haberme dedicado siempre buenas palabras y ayudarme cuando ha hecho falta. A Pili, Jose, Lidia y Yolanda, por estar siempre dispuestos a ayudarme con cualquier problema que pudiera surgir tanto en el día a día como con el MOZART. A Alejandro, por las interesantes conversaciones científicas. A Dani Arcos, por todas las risas, momentos de desconexión y consejos que me has dado en estos 4 años de compañeros de despacho, estoy seguro que podré sacar partido de ellos. Gracias también al personal de la cafetería (Jose, Perla, Javi...) por ser siempre tan amables y hacerme pasar tan buenos ratos de desconexión, así como al de limpieza, por mantener el orden en esta jungla llamada laboratorio.

Esta tesis no hubiera sido lo mismo sin todos esos compañeros al pie del cañón. Compañeros que me han enseñado, o que incluso han confiado en que yo les enseñara algo. Gracias a todos ellos. Empezando por el principio, gracias a todas mis compañeras del TG, porque ahí empezó todo. Gracias en especial a Valentina Nairi (ho trattore e terre, ti piazza?) y a Silvia la canaria por todas las turras que os comisteis y sobre todo por las innumerables risas. A Edu Guisasola, por transmitirme siempre la confianza de que acabarían saliéndome las cosas, que podría llegar a desenvolverme como científico. A Sergio, por todos esos ratos hablando sobre mil y unas cosas y porque contigo tuve la oportunidad de trabajar por primera vez en un proyecto diferente. A Sandra titi, Irene y Anna, por aportar siempre dosis de alegría. A la Rebe, por las infinitas risas que nos echamos y todas las turras que aguantaste, volaste pronto del laboratorio, pero estoy seguro de que el cambio compensó. A Víctor, por estar siempre dispuesto a discutir sobre cosas orgánicas. A Javi, por todas las risas que me has proporcionado (a veces a base de pilladotes). A Claudia, Manuel y Álvaro, por aportar esa savia nueva que me ayudó a tomar con más optimismo los últimos momentos de escritura de la tesis. A Carla, última incorporación, por tu salero y alegría. A Naiara, por esa alegría que me llevas siempre en el cuerpo y esas ganas de aprender que tienes, envidio tu actitud guerrera. A Noemí, por estar siempre dispuesta a ayudarme, hablar sobre ciencia e informarme sin cesar sobre cómo seguir en esta selva llamada investigación. A Dani Lozano, por estar siempre dispuesto a ayudarme y por el apoyo cuando ha sido necesario, a pesar de no haber ido finalmente al Mondo.

A Ana Fontecha y Blanca. Siempre he pensado que estáis llenas de conocimiento y me ha encantado haber podido escucharos cada vez que he tenido ocasión. Gracias a Ana por tratar de llevar siempre el optimismo por bandera y por todos los truquis que me has enseñado, podrá haber muchas Anas pero tú siempre serás la mejor. Gracias a Blanca, mi compañera habitual de cierre de departamento, por estar siempre dispuesta a explicarme cosas cuando te las he preguntado y por aquel cursazo del Escorial.

A Vicky, Juan y Jesús, por acogerme casi a diario en vuestra mesa como a uno más. Gracias a Vicky por toda la ayuda burocrática, y no burocrática, prestada prácticamente a diario. Gracias a Juan por convertirte en un teenager más, por participar de nuestras bromas y por ser un big machine. Gracias a Jesús por tener siempre un tema de conversación interesante a mano y por ese sentido del humor que tanta gracia me hace. A diario deseo que el día de mañana, sea donde sea que trabaje, pueda formar un grupo tan fiel como el vuestro.

A mis amigos de orgánica (Marta, José, Olmo, Jorge, Marco, Cristina...), por todos esos ratos de risas en el cuarto del RMN y fuera de él, que me sacaban todos los días una sonrisa cuando quizás menos ganas tenía.

A Clara, por tratar de mantener siempre una actitud positiva y tratar de inculcármela cuando más falta hacía. Mi día a día no será lo mismo sin tus términos modernos, los cuales nos han dado grandes momentos de cringe pero también continuos ghostings por Instagram. Algún día acabaremos yendo al cine.

A Patricia. Después de que el primer día que nos conocimos me dijeras que el Zaragoza no era un equipo de verdad te odie un poco, pero con los años aprendí a lidiar con tu vitalidad y entusiasmo. Gracias por estos años, primero en el TG y luego ya en nuestro despacho. Hemos comido chocolate, nos hemos reído, hemos jugado a las palabras encadenadas, hemos hecho memes, hemos ensayado teatro... En definitiva, nos lo hemos pasado muy bien. Pdta.: Si fumara, lo dejaría por ti Patricia, porque te quiero

A Juan Luis. Me siento afortunado por haber podido compartir prácticamente la totalidad del tiempo de mi tesis contigo. Eres una persona brillante, con una capaz de aprendizaje increíble y por encima de todo comprometida y trabajadora. Ha sido un placer poder aprender prácticamente cada día algo nuevo gracias a ti. Gracias también por esos ratos en el Glacé que sin duda ayudaron a acabar días buenos, y no tan buenos, con unas buenas risas. Estoy seguro de que llegarás muy lejos en esto y ojalá esté ahí para poder verlo.

A Elena. Listen to me, understand it, it is impossible our love. Gracias por todas las incontables risas que nos hemos echado, por repetir una y otra vez las mismas estupideces y seguir riéndonos, por aguantar mis problemas cuando ha hecho falta, por la semana del Escorial. Hemos compartido un vaso rellenable del BK entre 3 e incluso nos hemos ido a Milán. No decaigas porque esto es una carrera de fondo, aunque estoy seguro de que aprobarás el First y serás feliz cada día del resto de tu vida.

A Rocío. Hemos tenido nuestros más y nuestros menos, creo que eso es indudable, pero ante todo creo que hemos pasado grandes momentos y fuiste, eres y serás una persona muy importante para mí. Gracias también por todo el tiempo compartido en el laboratorio, los paseos hasta plaza España o incluso hasta Manuel Becerra, por todas las veces que hemos ido a cenar después del trabajo (no habremos salido veces borrachos de comida del buffet del Domino's o de los family days...!). En definitiva, gracias, porque toda esta experiencia seguramente no hubiera sido lo mismo sin ti.

A Gonzalo. Gracias por creer en mí, por ayudarme, por decirme las cosas claras cuando había que decirlas. Eres honrado, íntegro y, para mí, un ejemplo a seguir. De mayor quiero ser como tú y trabajo a diario para poder llegar a serlo. Gracias no sólo por lo científico, sino también por lo personal, son incontables las veces que he acudido a ti para contarte mis problemas y, a pesar de tú tener los tuyos, siempre me has escuchado y dado los mejores consejos. No cambies nunca porque el mundo merece una persona como tú.

A Nati (MaríaNatividadGómez-Cerezo). Gracias por todo. Por las idas en metro, las vueltas andando, los planes de fin de semana, los cafés en tu casa, los cafés en la mía, por explicarme cualquier duda que haya podido tener, por “prestarte” para mis típicos primeros planos con zoom x8 sin avisar a la policía y sobre todo por haberte preocupado por mí todos y cada uno de los días desde que nos conocimos.

To the MOZART researchers from Demokritos and Charité, for all your experimental efforts and the rewarding contributions to the manuscript. In particular, I'd like to thank Julia for always believing in the SIP-coated carbons and Dimitra for her willingness to continuously improve every single detail of the work. Besides, thank you for being so kind with me every time we've met.

To Professor Fuyuhiko Tamanoi and his research group (Imai San, Matsumoto San, Albane San, Grace San, Komatsu San...), for being so kind with me during my stay in Kyoto, where I had the opportunity to learn from you and enjoy such a different culture.

A Raquel y Carolina, chino y zapato, por esos breves pero geniales ratos que hemos pasado desde que vinisteis a Madrid como continuación a aquellos grandes años en el Cerbuna.

A Dani, compañero de piso sin igual, por todos esos ratos de risas durante las cenas que me ayudaban a desconectar y por ser, sin duda, el mejor compañero de piso que he tenido y tendré. Confío en que nuestra convivencia sirviera para que dejaras de ver tanto a equipos minoritarios como el Barça y te aficionaras al Zaragoza.

A Diana, Isa y Joaquín. Gracias por ser mi triángulo, que no cuadrado, de amistad. Gracias por haberme aguantado todos estos años, desde que mis padres os pagaban por ello hasta que dejaron de hacerlo (porque dejaron de hacerlo, ¿verdad?). Gracias por venir a visitarme a Japón (previo paso por cárcel rusa), la ilusión por vuestra llegada hizo que los peores momentos pasaran realmente rápido y sin duda la semana de vuestra visita fue maravillosa.

A Pawnee, por los infinitos paseos hablando sobre la familia (primas, primas y más primas) y por todos aquellos viajes en los que nos conocimos los alrededores de la geografía madrileña o incluso Teruel. Recuerdo con cariño aquel finde de fútbol que nos llevó del Bernabeu a la Romareda en 24 horas. Siempre nos quedará la duda de saber cómo es más probable morir, si aplastado por 1000 kilos de plátanos o debido a la radiación producida por 1000 kilos de plátanos. Pane...ttone. A Isain Bolt, por todos los interesantes debates que hemos tenido. Por haberme obligado a aprender a comer con palillos en aquel restaurante en Shibuya. Por ese afán tuyo por lo cretino y decadente. Y, sobre todo, gracias por no salir huyendo tras aquellas 48 horas en las que hablé ininterrumpidamente en Tokio hasta que llegaron los demás. Al King, por los buenos momentos que hemos pasado cada vez que te has podido subir de Cádiz. Siempre recordaré morirme de la risa cuando fuimos a comprarte esa tienda de campaña que seguramente nunca uses y lo mal que lo pasé cuando casi pierdo a Trufa por mitad de la Castellana en el poquísimosmo rato que me dejaste a su cargo.

A Marina Sazatornil, por todas las interminables conversaciones y la complicidad a lo largo de estos años a pesar de la distancia. Recuerdo buenos momentos, pero sin duda lo que siempre recuerdo y cuento de ti es cuando te pregunté “si fueras un árbol, qué rama de la física serías” y tú me dijiste que a ti te gustaba la fotosíntesis.

A mis amigos de Teruel (Alba, Edu, Fran, Javi, Raquel...) por hacer agradables mis breves estancias en Teruel, ayudándome a coger fuerzas para volver de nuevo a la batalla.

A Isaac. Gracias por todo. Gracias por estar siempre dispuesto a resolver mis dudas, por todas las conversaciones de ciencia que hemos tenido y sobre todo por ser como un hermano para mí desde que tengo consciencia. Recuerdo aquel último septiembre en tu casa de Zaragoza, tú preparando la presentación de tu TAD y yo estudiando los dos últimos exámenes de la carrera. Recuerdo estar realmente perdido, sin saber qué hacer con mi futuro y dudando que yo sirviese para *ser físico* (daría para un buen debate saber qué es ser físico). Tú, mientras nos tomábamos aquel caldo en tu terraza de madrugada, me dijiste algo así como (de forma resumida) que simplemente uno tiene que encontrar su lugar, que seguro que acababa encontrando algo en lo que me sintiera útil. Cinco años después, puedo decirte que tenías razón. No sé si soy bueno, malo o regular en esto, pero sé que la investigación es lo mío, que me siento útil y feliz, y que algún día montaremos nuestro grupo de investigación, como tantas veces hemos hablado.

Y por último a mi familia, por esencialmente todo. Por inculcarme la cultura del esfuerzo que tan útil me ha sido en este periodo. Por facilitarme la vida de forma que únicamente me he tenido que preocupar de estudiar y aprender. Y, sobre todo, por proporcionarme los valores necesarios para tratar de ser una buena persona, ayudando en la medida de mis posibilidades al que lo ha necesitado y tratando de llevar la honradez como bandera.

*A mi abuela por, sin pretenderlo, hacerme mejor persona.*



<a href="#"><u>Summary/Resumen</u></a> .....	9/24
<b>1. <a href="#"><u>CHAPTER 1: General Introduction to Nanomedicine</u></a></b> .....	25/52
<b>1.1. Introduction</b> .....	27
<b>1.2. Types of Particles</b> .....	27
1.2.1. <a href="#"><u>Organic Nanoparticles</u></a> .....	28
1.2.2. <a href="#"><u>Inorganic Nanoparticles</u></a> .....	29
<b>1.3. Stimuli-Responsive Mesoporous Nanoparticles</b> .....	33
1.3.1. <a href="#"><u>External Stimuli-Responsive Nanoparticles</u></a> .....	34
1.3.2. <a href="#"><u>Internal Stimuli-Responsive Nanoparticles</u></a> .....	35
<b>1.4. Nanotechnology and Cancer</b> .....	36
<b>2. <a href="#"><u>CHAPTER 2: Stimuli-Responsive Drug Delivery</u></a></b> .....	53/216
<b>2.1. Introduction</b> .....	55
2.1.1. <a href="#"><u>Aims</u></a> .....	55
2.1.2. <a href="#"><u>pH-Responsive Mesoporous Nanoparticles</u></a> .....	58
2.1.3. <a href="#"><u>Redox-Responsive Mesoporous Nanoparticles</u></a> .....	69
2.1.4. <a href="#"><u>Self-Immolative Chemistry in Nanomedicine</u></a> .....	73
<b>2.2. Self-Immolative Polymers as Novel pH-Responsive Gatekeepers for Drug Delivery</b> .....	98
2.2.1. <a href="#"><u>Introduction</u></a> .....	98
2.2.2. <a href="#"><u>Materials and Methods</u></a> .....	100
2.2.3. <a href="#"><u>Results and Discussion</u></a> .....	104
2.2.4. <a href="#"><u>Conclusions</u></a> .....	121
<b>2.3. Engineered pH-Responsive Mesoporous Carbon Nanoparticles for Drug Delivery</b> .....	125
2.3.1. <a href="#"><u>Introduction</u></a> .....	125
2.3.2. <a href="#"><u>Materials and Methods</u></a> .....	127
2.3.3. <a href="#"><u>Results and Discussion</u></a> .....	132
2.3.4. <a href="#"><u>Conclusions</u></a> .....	149

<b>2.4. Design of pH-Responsive Mesoporous Silica and Mesoporous Bioactive Glasses.....</b>	<b>154</b>
2.4.1. <u>Introduction</u> .....	154
2.4.2. <u>Materials and Methods</u> .....	156
2.4.3. <u>Results and Discussion</u> .....	158
2.4.4. <u>Conclusions</u> .....	168
<b>2.5. Design of Self-Immolative Polymers Responsive to Alternative pH Values.....</b>	<b>171</b>
2.5.1. <u>Introduction</u> .....	171
2.5.2. <u>Materials and Methods</u> .....	173
2.5.3. <u>Results and Discussion</u> .....	177
2.5.4. <u>Conclusions</u> .....	190
<b>2.6. Redox-Responsive Mesoporous Silica Nanoparticles.....</b>	<b>195</b>
2.6.1. <u>Introduction</u> .....	195
2.6.2. <u>Materials and Methods</u> .....	197
2.6.3. <u>Results and Discussion</u> .....	199
2.6.4. <u>Conclusions</u> .....	213
<b><u>3. CHAPTER 3: Overcoming Biological Barriers</u>.....</b>	<b>217/270</b>
<b>3.1. Introduction.....</b>	<b>219</b>
3.1.1. <u>Aims</u> .....	219
3.1.2. <u>Passive and Active Targeting of Solid Tumor Tissues</u> .....	221
3.1.3. <u>Journey Inside the Cells</u> .....	223
3.1.4. <u>Towards Efficient Cytosolic Delivery: Endosomal Escape</u> .....	228
<b>3.2. Targeted Mesoporous Silica Nanoparticles with Enhanced Endosomal Escape Capabilities.....</b>	<b>237</b>
3.2.1. <u>Introduction</u> .....	237
3.2.2. <u>Materials and Methods</u> .....	241
3.2.3. <u>Results and Discussion</u> .....	245
3.2.4. <u>Conclusions</u> .....	264

<b>4. <u>CHAPTER 4: Conclusions/Conclusiones</u></b> .....	273/282
Appendix I: Characterization techniques.....	284
Appendix II: Publications.....	290





## Glossary of terms

<sup>1</sup>H-NMR: <sup>1</sup>H-Nuclear magnetic resonance

ABA: 4-Aminobenzyl alcohol

AcN: Acetonitrile

APTES: 3-(Aminopropyl)triethoxysilane

Ava: Fmoc-5-Ava-OH

BOC: *tert*-Butoxycarbonyl protecting group

BOC<sub>2</sub>O: Di-*tert*-butyl dicarbonate

C1Sph: CMK-1-like mesoporous carbon nanospheres

C3: CMK-3-like mesoporous carbon nanoparticles

CDI: 1,1'-Carbonyldiimidazole

CTAB: Cetyltrimethylammonium bromide

DBTL: Dibutyltin dilaurate

DCC: *N,N'*-Dicyclohexylcarbodiimide

DCM: Dichloromethane

DIPEA: *N,N*-Diisopropylethylamine

DLS: Dynamic light scattering

DMAP: 4-Dimethylaminopyridine

DMEM: Dulbecco's modified eagle's medium

DMF: *N,N*-Dimethylformamide

DMSO: Dimethyl sulfoxide

DOX: Doxorubicin

DTT: Dithiothreitol

EPR effect: Enhanced permeability and retention effect

FBS: Fetal bovine serum

FITC: Fluorescein isothiocyanate isomer I

FTIR spectroscopy: Fourier transformed infrared spectroscopy

GSH: Glutathione ( $\gamma$ -glutamyl-cysteinyl-glycine)

H&E: Hematoxylin and eosin staining

HAVAB: Peptide-like molecule bearing biotin as binding motif and histidine as endosomal escape agent

HBA: 4-Hydroxybenzyl alcohol

HBDA: 4-Hydroxybenzaldehyde

HBTU: *N,N,N',N'*-Tetramethyl-*O*-(1*H*-benzotriazol-1-yl)uronium hexafluorophosphate

His: Fmoc-His(Trt)-OH

HOBt: 1-Hydroxybenzotriazole hydrate

MOZART: Mesoporous matrices for localized pH-triggered release of therapeutic ions and drugs

MSNs: Mesoporous silica nanoparticles

PBS: Phosphate buffered saline

PDI: Polydispersity index

PEG: Poly(ethylene glycol)

ROS: Reactive oxygen species

RPMI: Roswell park memorial institute

rt: Room temperature

Ru: Tris(2,2'-bipyridyl)dichlororuthenium(II) hexahydrate

SEM: Scanning electron microscopy

SIPs: Self-immolative polymers

TBAF: Tetra-*n*-butylammonium fluoride

TBDMS: *tert*-Butyldimethylsilyl ether protecting group

TBDMS-Cl: *tert*-Butyldimethylsilyl chloride

*t*BuOH: *tert*-butanol

TEM: Transmission electron microscopy

TEOS: Tetraethyl orthosilicate

TFA: Trifluoroacetic acid

TGA analysis: Thermogravimetric analysis

THF: Tetrahydrofuran

THP: tetrahydropyranyl protecting group

TOP: Topotecan

TsOH: *p*-Toluenesulfonic acid

XPS: X-ray photoelectron spectroscopy

XRD: X-ray diffraction





# Summary / Resumen

*La ciencia no sabe de países, porque el conocimiento le pertenece a la humanidad y es la antorcha que ilumina al mundo. La ciencia es el alma de la prosperidad de las naciones y la fuente de todo progreso.*

*Louis Pasteur*



## Summary

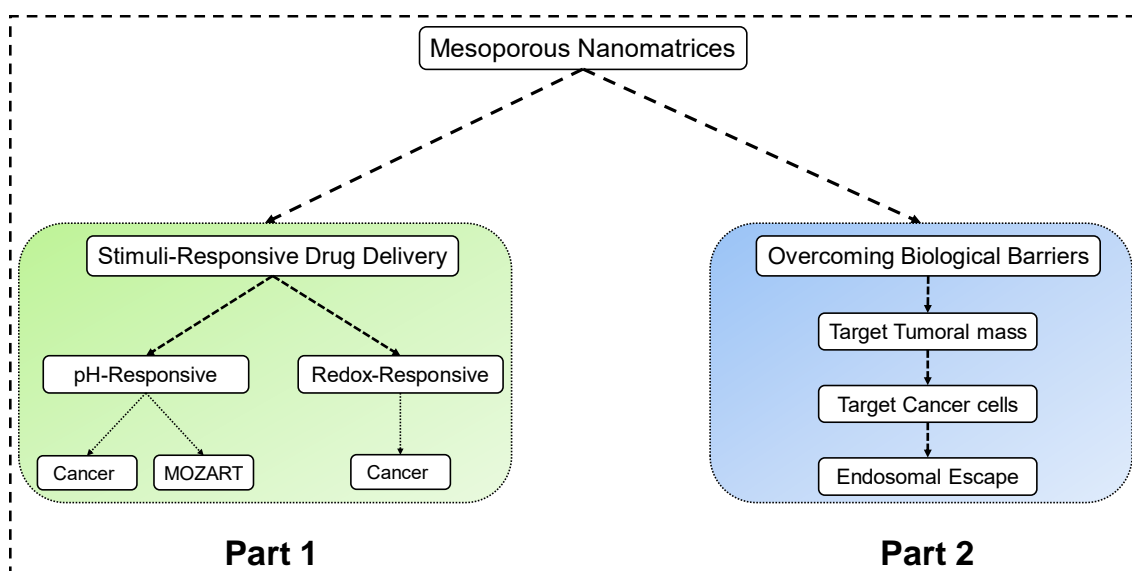
The overall objective of this PhD thesis has been the design and production of engineered mesoporous nanoparticles for biomedical applications. In this sense, the efforts during this doctoral thesis have been headed towards the development of nanomatrices with potential applicability in the treatment of complex diseases, such as bone and wound healing and cancer.

The initial context of this doctoral thesis was the European project “MOZART” (“*Mesoporous matrices for localized pH-triggered release of therapeutic ions and drugs*”), which included many different European partners (11) from both academic and industrial environments. The proposal involved the use of mesoporous materials to treat delayed bone healing and chronic wound healing. The objective was to load therapeutic agents and ions within the mesoporous framework that would be released in the affected areas, boosting the healing and improving the health of the patients. The use of a stimuli-responsive gatekeeper for the pore entrances to minimize potential premature release was considered. In this sense, the acid pH that was expected to be found in those pathological scenarios was selected as stimulus to trigger the payload release.

In addition to MOZART, much work during this PhD has been focused on developing smart approximations based on stimuli-responsive nanomatrices to improve current chemotherapeutic treatments. The administration of free drugs leads to non-selective distribution throughout the organism. In this sense, the encapsulation of cytotoxic compounds in mesoporous nanomatrices allows the preferential accumulation of the particles in the tumoral mass, owing to the Enhanced Permeability and Retention (EPR) effect. This effect has fueled the development of commercialized nanomedicines such as Doxil®, and it is consequence of the defective vasculature of tumoral blood vessels, which allows the extravasation and retention of molecules in the tumors.

This doctoral thesis is divided in 2 general parts. The **first part** comprises the development of stimuli-responsive mesoporous nanomatrices able to achieve on-demand drug release under specific conditions. These smart particles find application in the treatment of bone and wound healing (MOZART) and cancer. The **second part** is focused on the potential treatment of cancer. In particular, this part involves the design and evaluation of smart approximations to overcome relevant biological barriers that nanocarriers may have to face when administered *in vivo*.





Graphical summary of this PhD thesis.

As shown in the Graphical summary of the thesis, the work has focused on the use of mesoporous nanomatrices owing to their attractive properties, such as excellent textural properties or the ease of their surface functionalization with smart moieties. The use of Mesoporous Silica Nanoparticles (MSNs) as nanocarriers was initially devised. In addition, several types of nanomatrices were provided by the MOZART consortium, including Mesoporous Carbon Nanoparticles (MCNs) (National Center of Scientific Research “Demokritos”, Greece), Mesoporous Bioactive Glasses (MBGs) (Friedrich-Alexander-Universität of Erlangen, Germany, and Politecnico di Torino, Italy) and alternative MSNs (*Nanolith*, a Swedish company).

The **first part** covers the design of stimuli-responsive drug delivery systems based on the above-mentioned mesoporous nanomatrices. The origin of these stimuli can be external (applied by the clinician from outside the body) or internal (based on alterations of relevant biomarkers). In particular, this doctoral thesis has focused on the use of internal stimuli, namely **pH** and **redox** agents, to trigger the drug release.

One of the most relevant objectives during this PhD has been the design of stimuli-responsive moieties with smart behavior to functionalize the surface of the different nanomatrices here employed and prevent as much premature release as possible. In this sense, a type of chemistry, referred to as self-immolative chemistry, has been extensively employed to engineer such smart structures.

Much of the work carried out in the **first part** has comprised the use of **pH** as trigger. This part devoted to pH can be divided into two more subparts: (1) nanoparticles for

cancer treatment and (2) nanoparticles for bone and wound healing (MOZART). The overall approximation here has been the design of a pH-responsive self-immolative polyurethane, whose grafting and pH-responsivity have been evaluated in many different nanomatrices.

The application of nanoparticles to cancer treatment has comprised the use of the above-mentioned pH-responsive polyurethane in combination with (a) Mesoporous Silica Nanoparticles (Section 2.2) and (b) various types of Mesoporous Carbon Nanoparticles (Section 2.3). The rationale behind the use of acid pH to trigger the release is the acid environment found in certain subcellular organelles (pH *ca.* 5). In this way, the drugs would remain within the mesopores until the particles were internalized. Then, that acid pH would trigger the self-immolation, opening the pores and leading to the drug release.

The initial studies were carried out using MSNs, which were functionalized with the pH-responsive self-immolative polymer (SIP). The functionalized nanoparticles were fully characterized and their pH-responsiveness was confirmed *in vial*. In addition, a preliminary *in vitro* experiment with normal and tumoral cells was conducted, where it was shown that the SIP-coated MSNs were biocompatible.

Once the SIP coating was shown to be functional, the next step was to translate the technology to the different matrices provided by the MOZART consortium. In this sense, the preliminary results obtained with MCNs were very satisfactory. In addition, it was observed that these particles showed outstanding loading capacity and, consequently, they were proposed as candidates for the design of an anticancer nanoplatform, instead of just being applied for the initial purposes considered in the proposal. This work is the result of an intense collaboration between our university (UCM), Demokritos (Athens, Greece), which provided the carbon matrices and Charité-Universitätmedizin (Berlin, Germany), where the *in vivo* experiments were carried out, producing outstanding results in terms of biocompatibility and performance in the animal models. The SIP-coated carbons were fully characterized and their pH-responsive behavior was validated *in vial*, *in vitro* and *in vivo*. In addition, the SIP-coated carbons were shown to be biocompatible *in vivo* and their ability to inhibit cell viability when loaded with a cytotoxic compound was evaluated *in vitro*, showing excellent results.

The second subpart of the **first part** consisted in the application of the pH-responsive self-immolative technology to the different mesoporous silica-based nanomatrices

provided by the MOZART consortium to address bone and wound healing (Section 2.4). In this way, the acid environment expected in delayed bone healing and chronic wound healing (pH *ca.* 5) would trigger the release of the therapeutic agents and ions. In this sense, the particles were functionalized with the pH-responsive self-immolative polyurethane and the correct grafting was evaluated using different characterization techniques. Their ability to close the pore entrances was evaluated *via* release experiments.

Further experiments carried out by members of the consortium demonstrated that the initial assumption of an acidic environment in delayed bone healing and chronic wound healing was inaccurate. In consequence, the self-immolative polyurethane previously employed with the MOZART nanomatrices had to be modified to be responsive to newly relevant pH values. In particular, it was found that pH 6.8 and 8 were the values that had to be addressed. In this regard, the efforts were headed towards the development of self-immolative polyurethanes bearing alternative triggers sensitive to those pH values (Section 2.5). Many different approximations were attempted for the effective synthesis of both triggers but not fully satisfactory results could be obtained, even though a contingency plan considered in the proposal was activated.

The second approach considered in the **first part** was the use of redox stimulus to trigger the drug release (Section 2.6). The rationale behind the use of this stimulus was the overexpression of redox species, namely glutathione, in the cytoplasm of cells compared to the extracellular fluids. In this way, premature release would be hampered until the particles were internalized, where the reductive environment would trigger the release. In this case, MSNs were used as nanocarrier and the innovative self-immolative technology was considered again as basis for the design of a redox-responsive self-immolative molecule. This molecule could act as a diffusion barrier and provided reactive points for additional functionalizations. In particular, the redox-responsive particles were further functionalized with poly(ethylene glycol), a polymer that is known to be biocompatible, improve the colloidal stability and endow particles with stealth properties. The functionalized particles were fully characterized and the redox-responsiveness was validated. In addition, the ability of the self-immolative molecule to delay premature release was verified *in vial*, paving the way for future biological experiments.

The **second part** involved the design of a nanocarrier able to overcome relevant biological barriers present in cancer scenarios. When nanoparticles are administered in

the bloodstream they may have to face several biological barriers. Overcoming these barriers is of vital importance as, otherwise, the efficacy of the treatment could be too low and no significant improvements could be observed despite the application of nanotechnology. This **second part** deals with 3 relevant biological barriers: (1) the lack of preferential particles accumulation in tumor tissues so the particles might be distributed throughout the organism, (2) the lack of selectivity towards cancer cells so normal cells could also internalize the drug-loaded particles and (3) nanoparticle sequestration in the endo-lysosomal pathway (pathway normally employed for the internalization of nanoparticles) so the payload may be degraded or multidrug resistance may be developed.

The PEGylated MSNs functionalized with the self-immolative linker were selected as starting material, since delivering the redox-responsive particle to the cytoplasm to interact with the overexpressed glutathione is of major importance. In this sense, a polyvalent peptidic compound was developed and grafted to the redox-responsive nanoparticles (Section 3.2). This peptide-like compound combines in a single structure a motif able to specifically recognize tumoral cells over normal cells and a fragment able to induce endosomal escape. The biological performance of the carrier was evaluated in 2D and 3D cell cultures, showing excellent results in terms of internalization and achievement of endosomal escape. In addition, the ability of the system to preferentially accumulate in the tumoral mass was validated in a pseudo-*in vivo* model, using tumor-bearing chicken embryos. In addition, a preliminary experiment of tumor elimination in this model was also carried out. Most of the biological studies carried out for this material were performed in the *Institute for Integrated Cell-Material Sciences (iCeMS)* at Kyoto University, Japan, as a result of a research stay that took place during this doctoral thesis.

In summary, all the results obtained in this PhD thesis highlight the convenience of using mesoporous nanomaterials to design smart drug delivery systems thanks to their biocompatibility and multifunctionality. In addition, it has been shown the suitability of using stimuli-responsive self-immolative structures to control the drug release. Finally, a simple but smart approximation to overcome some relevant biological barriers has been developed and could constitute a breakthrough to achieve more efficient drug delivery in complex diseases such as cancer.



## Resumen

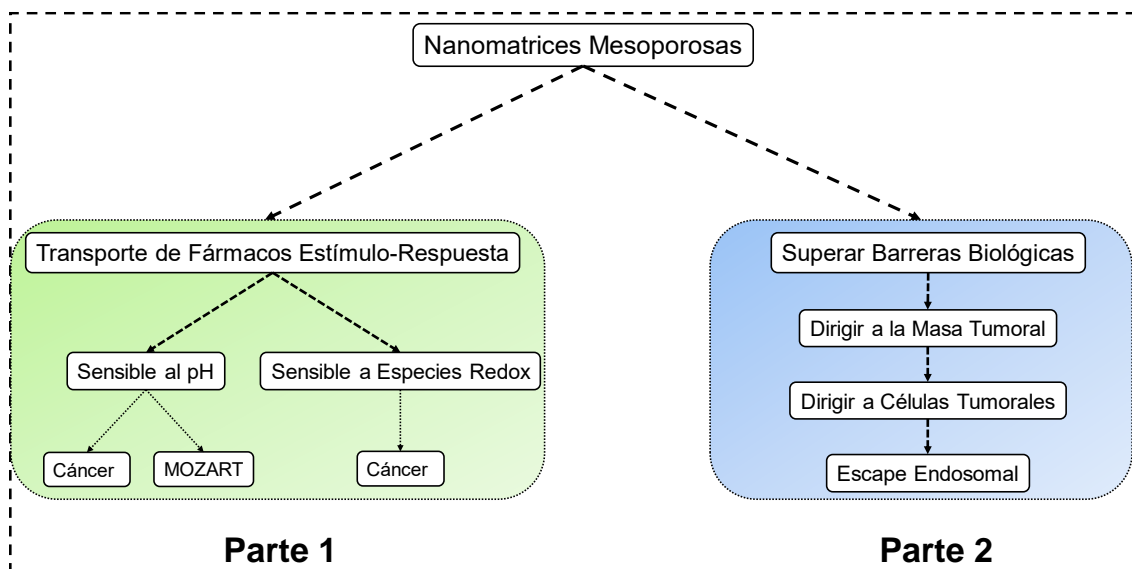
El objetivo principal de esta tesis ha sido el diseño y la producción de nanopartículas mesoporosas para aplicaciones biomédicas. En este sentido, los esfuerzos durante esta tesis doctoral han estado dirigidos hacia el desarrollo de nanomatrices con potencial aplicabilidad en el tratamiento de enfermedades complejas, como pueden ser la reparación de fracturas crónicas graves de hueso y de heridas piel o el cáncer.

El contexto inicial de esta tesis doctoral fue el proyecto europeo “MOZART” (“*Mesoporous matrices for localized pH-triggered release of the therapeutic ions and drugs*”), que incluía diferentes miembros europeos (11) del ámbito académico e industrial. La proposición implicaba el uso de materiales mesoporosos para tratar enfermedades de hueso y piel. El objetivo era cargar agentes e iones terapéuticos en la matriz mesoporosa, los cuales serían liberados en las zonas de interés, fomentando la curación y mejorando la vida de los pacientes. El uso de compuertas estímulo-respuesta para cerrar los mesoporos fue considerada. En ese sentido, el pH ácido que se esperaba encontrar en estas patologías fue considerado como estímulo para iniciar la liberación de la carga.

Al margen del trabajo realizado para MOZART, se ha llevado a cabo el desarrollo de diferentes aproximaciones estímulo-respuesta para mejorar los actuales tratamientos quimioterapéuticos. La administración de fármacos libres da lugar a una distribución no selectiva a largo de todo el organismo. En este sentido, la encapsulación de citotóxicos en nanomatrices mesoporosas permite la acumulación preferencial de las partículas en la masa tumoral, debido al efecto de Retención y Permeabilidad Aumentada (efecto EPR, por sus siglas en inglés, *Enhanced Permeability and Retention Effect*). Este efecto ha potenciado el desarrollo de nanofármacos que ya están comercializados como el Doxil®, y es consecuencia de la deficiente estructura de los vasos sanguíneos tumorales, lo cual permite la extravasación y retención de las moléculas en los tumores.

Esta tesis doctoral consta de 2 partes principales. La **primera parte** comprende el desarrollo de nanomatrices mesoporosas estímulo-respuesta capaces de lograr la liberación del fármaco bajo condiciones concretas. Estas partículas encuentran aplicación en el tratamiento de enfermedades de hueso y piel (MOZART) y en cáncer. La **segunda parte** está centrada en el potencial tratamiento del cáncer. En particular, esta parte comprende el diseño y evaluación de aproximaciones inteligentes para superar barreras

biológicas relevantes a las que puede que tengan que enfrentarse los nanotransportadores cuando son administrados *in vivo*.



Resumen gráfico de esta tesis doctoral.

Como se muestra en el resumen gráfico de la tesis, el trabajo se ha centrado en el uso de nanomatrices mesoporosas debido a sus excelentes propiedades texturales o la facilidad para funcionalizarlas con estructuras inteligentes. El uso de Nanopartículas Mesoporosas de Sílice (MSNs) como nanotransportadores fue inicialmente considerada. Además, varios tipos de nanomatrices fueron proporcionadas por el consorcio MOZART, incluyendo Nanopartículas Mesoporosas de Carbono (MCNs) (National Center of Scientific Research “Demokritos”, Grecia), Vidrios Mesoporosos Bioactivos (MBGs) (Friedrich-Alexander-Universität of Erlangen, Alemania, y Politecnico di Torino, Italia) y MSNs alternativas (*Nanolith*, una compañía sueca).

La **primera parte** comprende el diseño de sistema de estímulo-respuesta de transporte de fármacos basados en las mencionadas nanomatrices mesoporosas. El origen de estos estímulos puede ser externo (aplicado por el sanitario) o interno (basado en alteraciones de biomarcadores relevantes). En particular, esta tesis doctoral se ha centrado en el uso de estímulos internos, pH y agentes redox, para iniciar la liberación de fármacos.

Uno de los objetivos más relevantes durante esta tesis ha sido el diseño de estructuras estímulo-respuesta con comportamiento inteligente para funcionalizar la superficie de las distintas nanomatrices empleadas y así prevenir la liberación prematura del fármaco tanto como sea posible. En este sentido, la denominada química autoinmolativa ha sido ampliamente empleada para diseñar dichas estructuras inteligentes.

Gran parte del trabajo desarrollado en la **primera parte** ha comprendido el uso del **pH** como estímulo. Esta parte relativa al pH puede ser a su vez dividida en dos subpartes: (1) nanopartículas para el tratamiento del cáncer y (2) nanopartículas para curación de fracturas crónicas de hueso y heridas de piel (MOZART). La aproximación general aquí ha sido el diseño de un poliuretano autoinmolutivo sensible al pH, cuyo anclaje y respuesta al pH han sido evaluados en diferentes nanomatrices.

La aplicación de nanopartículas para tratamiento del cáncer ha comprendido el uso del mencionado poliuretano sensible al pH en combinación con (a) Nanopartículas Mesoporosas de Sílice (Sección 2.2) y (b) varios tipos de Nanopartículas Mesoporosas de Carbono (Sección 2.3). El motivo por el cual se ha utilizado pH para iniciar la liberación es el ambiente ácido encontrado en ciertos orgánulos subcelulares (pH *ca.* 5). De esta forma, los fármacos permanecerían en los mesoporos hasta que las partículas fueran internalizadas. Tras ello, ese pH ácido iniciaría la autoinmolación, abriendo los poros y dando lugar a la liberación del fármaco.

Los estudios iniciales fueron realizados usando MSNs, las cuales fueron funcionalizadas con el polímero autoinmolutivo sensible al pH (SIP). Las partículas funcionalizadas fueron completamente caracterizadas y su respuesta al pH fue confirmada *in vial*. Además, un experimento *in vitro* preliminar con células normales y tumorales fue llevado a cabo, donde se demostró que las MSNs funcionalizadas con el SIP eran biocompatibles.

Una vez que se demostró que el recubrimiento autoinmolutivo era funcional, el siguiente paso fue trasladar esta tecnología a las diferentes matrices proporcionadas por el consorcio MOZART. En este sentido, los resultados preliminares obtenidos con los MCNs fueron muy satisfactorios. Además, se observó que estas partículas poseían una extraordinaria capacidad de carga y, como consecuencia, estas matrices fueron propuestas como candidatas para el diseño de un nanotransportador con propósitos antitumorales, en lugar de ser sólo aplicadas para los propósitos iniciales considerados en el proyecto. Este trabajo es el resultado de una profunda colaboración entre nuestra universidad (UCM), Demokritos (Atenas, Grecia), que proporcionó las matrices de carbono y Charité-Universitätmedizin (Berlín, Alemania), donde se llevaron a cabo los experimentos *in vivo*, dando lugar a excelentes resultados en términos de biocompatibilidad y actuación en los modelos animales. Las MCNs funcionalizadas con SIPs fueron completamente caracterizadas y su respuesta al pH fue evaluada *in vial*, *in vitro* e *in vivo*. Además, se



demonstró que eran biocompatibles *in vivo* y su habilidad para inhibir la viabilidad celular *in vitro* fue evaluada cargando un antitumoral, mostrando resultados excelentes.

La segunda subparte de la **primera parte** consistió en la aplicación de la tecnología autoinmolutiva sensible al pH a las diferentes nanomatrices mesoporosas basadas en sílice proporcionadas por el consorcio MOZART para tratar enfermedades de hueso y piel (Sección 2.4). De esta forma, el ambiente ácido esperado en estos escenarios (pH *ca.* 5) iniciaría la liberación de los agentes e iones terapéuticos. En este sentido, las partículas fueron funcionalizadas con el poliuretano autoinmolutivo sensible al pH y su correcto anclaje se validó a través de diferentes técnicas de caracterización. Su habilidad para cerrar los poros se c a través de experimentos de liberación.

Algunos miembros del consorcio realizaron experimentos para determinar la magnitud del pH encontrado en estos escenarios, y se observó que la suposición de un pH ácido en fracturas crónicas de hueso y heridas de piel era inexacta. En consecuencia, el poliuretano usado previamente con las matrices mesoporosas proporcionadas por MOZART tuvo que ser modificado para responder a los nuevos valores de pH relevantes. En particular, se observó que pH 6.8 y 8 eran los pHs objetivo, respectivamente. En este sentido, los esfuerzos se centraron en desarrollar poliuretanos autoinmolutivos sensibles a esos valores de pH (Sección 2.5). Se desarrollaron diferentes estrategias para la síntesis de ambas moléculas iniciadoras de la autoinmolación, pero no se obtuvieron resultados del todo satisfactorios, a pesar incluso de que el plan de contingencia considerado en el proyecto fue activado.

La segunda aproximación considerada en la **segunda parte** fue el uso de estímulos **redox** para iniciar la liberación del fármaco (Sección 2.6). La razón de ser del uso de este estímulo fue la sobreexpresión de especies redox, glutatión, en el citoplasma de las células comparado con los fluidos extracelulares. De esta forma, la liberación prematura sería ralentizada hasta que las partículas fueran internalizadas, donde el ambiente reductor iniciaría la liberación. En este caso, las MSNs fueron utilizadas como nanotransportador y la innovadora tecnología autoinmolutiva fue considerada de nuevo como base para el diseño de una molécula autoinmolutiva sensible a estímulos redox. Esta molécula podría actuar como barrera de difusión y proporcionar puntos reactivos por funcionalizaciones adicionales. En particular, las partículas sensibles a especies redox fueron funcionalizadas con polietilenglicol, un polímero que se sabe que es biocompatible, que mejora la estabilidad coloidal y que proporciona propiedades furtivas a las partículas. Las partículas

funcionalizadas fueron completamente caracterizadas y la respuesta a las especies redox fue validada. Además, la habilidad de la molécula autoinmolativa para retrasar la liberación prematura fue verificada *in vial*, sentando las bases para futuros experimentos biológicos.

La **segunda parte** comprende el diseño de un nanotransportador capaz de superar barreras biológicas relevantes presentes en escenarios tumorales. Cuando las partículas son administradas en el torrente sanguíneo puede que tengan que enfrentarse a varias barreras biológicas. Superarlas es muy importante pues, de otro modo, la eficacia del tratamiento podría ser demasiado baja y no se verían mejoras en el paciente a pesar de usar nanotecnología. Esta **segunda parte** afronta 3 barreras biológicas: (1) la falta de acumulación preferencial de las partículas en el tumor, de modo que las partículas podrían ser distribuidas a lo largo de todo el organismo, (2) la falta de selectividad hacia células cancerosas de modo que las normales también podrían internalizar las partículas y (3) el atrapamiento de las partículas en la ruta endo-lisosomal (ruta empleada normalmente para la internalización de nanopartículas) de modo que la carga podría ser degradada o podría desarrollarse resistencia a los fármacos.


Las nanopartículas PEGiladas a través del *linker* autoinmolativo fueron seleccionadas como material de partida, pues transportar la partícula sensible a estímulos redox hasta el citoplasma para que interactúe con el glutatión allí sobreexpresado es de vital importancia. En este sentido, un compuesto peptídico polivalente fue desarrollado y anclado a las nanopartículas sensibles a redox (Sección 3.2). Este compuesto combina en una única estructura un fragmento capaz de reconocer específicamente células tumorales frente a normales y otro fragmento capaz de inducir escape endosomal. El desempeño biológico del sistema fue evaluado en cultivos celulares 2D y 3D, mostrando resultados excelentes en términos de internalización e inducción de escape endosomal. Además, la habilidad del sistema para acumularse preferencialmente en el tumor fue validado en un modelo pseudo-*in vivo*, usando embriones de pollo en los cuales se había crecido un tumor. Además, se llevó a cabo un experimento preliminar de eliminación tumoral en este modelo. La mayoría de los experimentos de esta parte fueron realizados en el *Institute for Integrated Cell-Material Sciences (iCeMS)*, Kyoto University, Japón, como resultado de una estancia predoctoral de tres meses realizada durante esta tesis.

En resumen, los resultados obtenidos en esta tesis doctoral resaltan la conveniencia de usar nanomatrices mesoporosas para diseñar sistemas de transporte de fármacos

inteligentes gracias a su biocompatibilidad y multifuncionalidad. Además, se ha demostrado la idoneidad de usar estructuras autoinmolativas para controlar la liberación del fármaco. Finalmente, se desarrolló una aproximación simple pero útil para superar algunas barreras biológicas relevantes que podría constituir un avance significativo para conseguir un transporte de fármacos más efectivo en enfermedades complejas como puede ser el cáncer.







# Chapter 1

## General Introduction to Nanomedicine

*El placer en la tarea pone la perfección en el trabajo.*

*Aristóteles*



## 1.1. Introduction

As stated in 2000 by the US National Nanotechnology Initiative, “*Nanotechnology is concerned with materials and systems whose structures and components exhibit novel and significantly improved physical, chemical and biological properties, phenomena and processes due to their nanoscale size*”.<sup>1</sup> In other words, reducing the size of some materials may lead to novel properties that might generate a wide variety of new potential applications. From a general point of view, a material can be considered as a nanomaterial if at least one of its dimensions belongs to the nanometric scale ( $1\text{ nm}=1\cdot 10^{-9}\text{ m}$ ).<sup>2</sup>

In the last decades, nanotechnology has been applied to a wide variety of fields, ranging from the development of electronic devices to the study of biological processes.<sup>3</sup> In particular, the application of nanotechnology to medicine, the so-called nanomedicine, has attracted the attention of many researchers. The first examples of the application of nanotechnology to medicine were reported in the early 60’s when liposomes were first described as carriers.<sup>4,5</sup> Since then, a wide number of nanomaterials have been engineered to achieve effective delivery of therapeutics, including organic, inorganic and hybrid combinations.<sup>6</sup>

## 1.2. Types of Particles

Many different nanocarriers have been applied as nanomedicines in the last decades. These carriers can be classified as either organic (*e.g.*, micelles polymeric nanoparticles) or inorganic (*e.g.*, metallic nanoparticles, silica nanoparticles), although several hybrid organic-inorganic nanocarriers have also been reported (Figure 1.1).

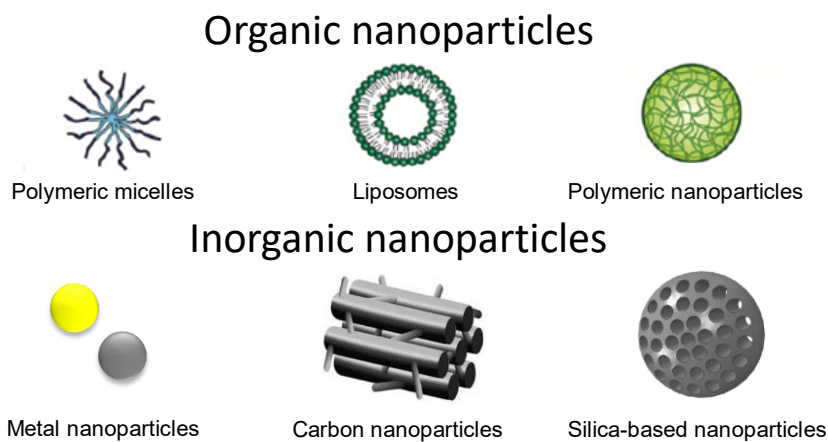


**Figure 1.1.** Some representative examples of nanoparticles employed in nanomedicine. Top: Organic nanoparticles (polymeric micelles, liposomes and polymeric nanoparticles). Bottom: Inorganic nanoparticles (metal, carbon and silica-based nanoparticles).



## 1.2.1. Organic Nanoparticles

### 1.2.1.1. Polymeric micelles

Polymeric micelles are colloidal nanoparticles of *ca.* 5-100 nm composed by amphiphilic block copolymers capable of self-assembling when placed in aqueous medium. The copolymer is produced with a hydrophobic chain and a hydrophilic part, usually being the latter the well-known poly(ethylene glycol). Their hydrophobic section allows the loading of hydrophobic compounds to enhance their bioavailability and the hydrophilic content enhances the stability and biocompatibility. In addition, they can be loaded with gamma emitters or paramagnetic metals to carry out nuclear imaging or magnetic resonance imaging, respectively.<sup>7</sup>

### 1.2.1.2. Liposomes

Liposomes consist of amphiphilic lipids (natural or synthetic) that rearrange in aqueous environment to yield vesicles containing an aqueous compartment surrounded by a variable number of lipid bilayers. Thanks to that architecture, they can load both hydrophilic and hydrophobic drugs in the core and in the lipid bilayer, respectively.<sup>8</sup> Furthermore, due to their biocompatibility and biodegradability, liposomes were the first drug delivery nanosystems to be successfully translated into the clinic (Doxil®). Since then, other liposomal formulations have been approved (DaunoXome®, Ambisome®, DepoDur®, etc),<sup>9</sup> paving the way for the future translation of other nanomaterials.

### 1.2.1.3. Polymeric nanoparticles

Polymeric nanoparticles can be synthesized from a wide variety of polymers which can be composed of monomers with many different chemical functionalities. This allows the design of a variety of versatile and multifunctional nanocarriers. The most common methods to obtain such nanoparticles are nanoprecipitation, emulsification-diffusion, solvent emulsion-evaporation and interfacial deposition. As polymeric source, either non-biodegradable or biodegradable polymers can be employed, being the latter particularly interesting thanks to their elimination from the body (as long as the degradation by-products are biocompatible).<sup>10</sup> The co-polymer poly(lactic-co-glycolic acid) has already been approved by the Food and Drug Administration (FDA) for its use in drug delivery and diagnostic.<sup>11</sup>

## 1.2.2. Inorganic Nanoparticles

### 1.2.2.1. Metal-based nanoparticles

The synthesis of novel metal nanoparticles, specially gold and silver nanoparticles, and their application to nanomedicine have increased in the last few years.

Gold nanoparticles are metal nanoparticles prepared from the reduction of a gold salt in the presence of stabilizing agents that prevent agglomeration.<sup>12</sup> Although they have been applied to drug delivery technologies,<sup>13</sup> their nonporous structure leads to poor storage capacity and lacks of a protective shell for the drugs. Accordingly, gold nanoparticles find major application as contrast agents for imaging<sup>14</sup> or as photothermal therapy agents due to the surface plasmon resonance.<sup>15</sup> Gold nanoparticles are usually thought to be highly biocompatible due to their inertness, although their size and low clearance rate might affect their biocompatibility.<sup>16</sup>

Silver nanoparticles are metal nanoparticles that can be produced by means of physical or chemical methods.<sup>17</sup> They are attractive in nanomedicine due to their bactericidal properties.<sup>18–20</sup> In addition, their plasmon surface resonance has been applied to the design of sensors<sup>17</sup> and their anticancer activity has been validated.<sup>21,22</sup>

### 1.2.2.2. Carbon nanoparticles

Within the large family of carbon-based materials, those showing  $sp^2$  hybridation have attracted much attention owing to their interesting physical-chemical properties. Examples are fullerene or carbon nanotubes. However, their cytotoxicity is still controversial because factors such as the degree of surface functionalization or the shape seem to influence their biocompatibility.<sup>23–28</sup> On the contrary, mesoporous carbon materials have received growing attention. Their unique characteristics include (1) excellent biocompatibility; (2) outstanding textural properties; (3) controlled drug release of hydrophobic and hydrophilic compounds; (4) easy surface modification; (5) photothermal conversion capability and (6) supramolecular  $\pi$ - $\pi$  stacking possibilities, which are interesting for loading aromatic drugs.<sup>29–32</sup> Their synthesis can be accomplished by either hard or soft templating approaches, being the former based on the use of pre-synthesized organic or inorganic templates and the latter on the use of organic molecules that self-assemble to generate nanostructures.<sup>33</sup> Some of their recent applications are drug delivery, chemo-photothermal therapy, *in vivo* real-time imaging or gene transfection, among others.<sup>34</sup>

### 1.2.2.3. Mesoporous silica nanoparticles

Ordered mesoporous silica-based materials were first reported in the early 90's by Mobil Oil Corporation researchers<sup>35</sup> and researchers from Waseda university.<sup>36</sup> These materials are characterized by (1) tunable and narrow pore size distributions (2-30 nm); (2) adjustable pore structures; (3) high specific surface areas (up to 1500 cm<sup>2</sup>/g); (4) high pores volumes (*ca.* 1 cm<sup>3</sup>) and (5) high silanol density on the surface that allows further modifications.<sup>37-41</sup> Owing to their exquisite physical-chemical properties, mesoporous silica materials have been broadly applied in a number fields, including heavy metal adsorption<sup>42-44</sup> or separation,<sup>45-47</sup> catalysis,<sup>48-53</sup> food<sup>54</sup> or energy storage,<sup>55,56</sup> among others.

In addition, these materials find broad application within the field of biomaterials, and have been widely studied since Prof. Vallet-Regí and coworkers first reported their suitability as drug delivery systems.<sup>57</sup> Since then, several porous silica-based nanocarriers have been engineered and applied to controlled drug delivery,<sup>58-62</sup> efficient gene transfection,<sup>63-66</sup> bone tissue regeneration<sup>67-72</sup> or antibacterial treatment,<sup>73-78</sup> among others applications.

Since their discovery, several families of mesoporous silica materials have been developed. In particular, the MCM-n (*Mobil Composition of Matter*) and SBA-n (*Santa Barbara Amorphous*) series have attracted much of the attention.<sup>79</sup> In general, the synthesis of mesoporous silica materials is based on the *sol-gel* process in the presence of surfactant molecules acting as template. Depending on the particular conditions of the synthesis, it is possible to obtain several pore structures. Examples of the MCM-n family are MCM-41, MCM-48 and MCM-50 materials, which present hexagonal *p6mm*, cubic *Ia3d* and laminar *p2* arrangement of the mesopores, respectively (Figure 1.2).

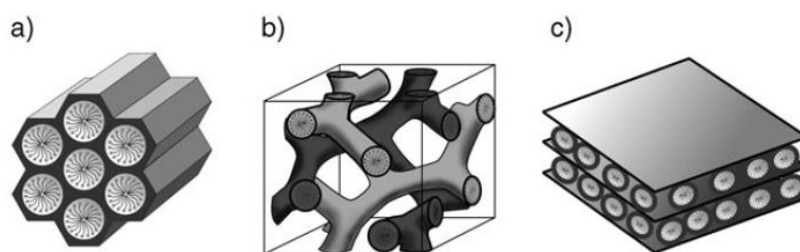


**Figure 1.2.** Spatial arrangement of the pores in a) MCM-41 (hexagonal). b) MCM-48 (cubic). c) MCM-50 (laminar) mesoporous materials. Reproduced from Ref 79 with permission of Wiley.

### ❖ Synthesis of Mesoporous Silica Nanoparticles

The synthesis of MCM-41-like Mesoporous Silica Nanoparticles (MSNs) is based on a modification of the method reported by Stöber to obtain micron-sized monodispersed silica spheres in 1968.<sup>80</sup> With this method the solid particles were formed by means of the hydrolysis and subsequent condensation of alkyl silicates catalyzed by ammonia in an alcoholic solution.

Mesoporous silica materials were initially produced as bulk materials, but it did not take very long to develop nanoparticles with the same textural properties. To obtain such materials, the above-mentioned Stöber method was modified and the addition of surfactants as structure-directing agents yielded silica nanoparticles showing mesoporosity rather than nonporous spheres. The morphology and dimensions of these surfactant-templated mesoporous silicas can be tailored by controlling the reaction conditions (*e.g.*, temperature, pH, surfactant concentration or type of silica precursor, among others).<sup>81</sup> The mechanism proposed for the formation of MSNs (*Cooperative Liquid Cristal* template) is depicted in Figure 1.3.

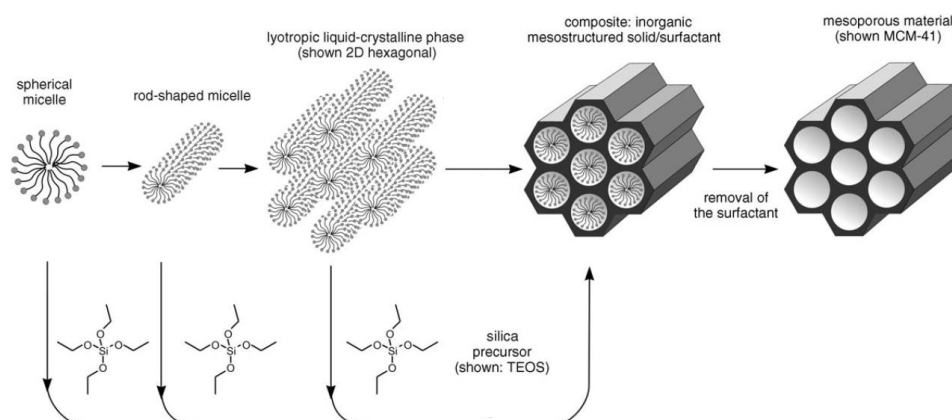


**Figure 1.3.** Mechanism proposed for the formation of MCM-41 mesoporous materials. The surfactant molecules self-assembly and the silica precursors polymerize around them from the beginning, leading to the formation of a silica backbone with hexagonally ordered pores. Adapted from Ref 79 with permission of Wiley.

The hydrolysis, condensation and polymerization of the silica precursors occur from the very beginning. They are deposited around individual surfactant micelles prior to their arrangement in a hexagonal fashion and further silica network formation.<sup>79</sup> According to Hou *et al.*,<sup>82,83</sup> the formation of MSNs depends on the interactions among the inorganic precursor, the polar head of the surfactant and the ions present in the solution as a function of the pH of the synthesis. Depending on the pH, anionic, cationic and neutral surfactants

can be employed to yield mesoporous materials. The inorganic precursor is negatively charged and the polar head positively charged for MCM-41 mesoporous silica.

The next step consists in removing the surfactant to obtain accessible mesopores with large surface areas and pore volumes. In general, the template can be removed by either calcination or solvent extraction, although a mixed method involving the use of solvents with high boiling points has also been reported.<sup>84</sup> The solvent extraction method is usually preferred over calcination, since the latter may cause irreversible aggregation of the MSNs and limit their potential bioapplication.<sup>84–86</sup> In addition, it preserves the functional organic moieties in the nanoparticles that otherwise would be thermally destroyed during calcination.<sup>86</sup> However, the solvent extraction method may induce higher cytotoxicity if surfactant molecules are not completely removed, so several extraction steps are usually needed.<sup>86,87</sup>

#### ❖ Functionalization of Mesoporous Silica Nanoparticles

One of the most attractive features of MSNs is their surface with a high density of silanol groups. That surface chemistry allows to anchor other chemical groups on the surface (*i.e.*, functionalize the surface), which are usually introduced using organosilanes. The interactions between the silica matrix and the payload can be tuned depending on the organosilane employed.<sup>38,88</sup> There are two approximations for an effective functionalization of MSNs, the so-called post-synthesis and co-condensation methods (Figure 1.4).<sup>79</sup>

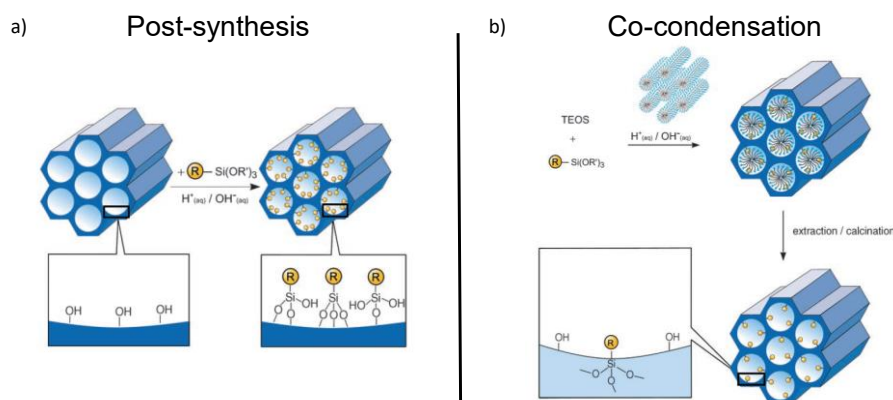


**Figure 1.4.** Functionalization of MSNs. a) Post-synthesis method. The functionalities are introduced after synthesizing the MSNs. b) Co-condensation method. The functionalities are introduced during the synthesis of the MSNs. Adapted from Ref 79 with permission of Wiley.

The post-synthesis method (Figure 1.4a) consists in the modification of the surface after the synthesis. If this process is done before removing the surfactant template, this method leads to MSNs bearing different groups inside (silanol) and outside the pores. If the

functionalization is carried out after removing the template the new functional groups can also be found in the mesopores. An advantage of this approach is the possibility to introduce different functional groups at the same time (*e.g.* amine and thiol, amine and carboxylic acid, etc). The main disadvantage is that if a bulky organosilane is used, its anchoring might lead to the complete closure of the pores and the molecules might not be loaded inside.<sup>79</sup>

The co-condensation method (Figure 1.4b) consists in the simultaneous addition of the silica precursor and the functional organosilane during the formation of the particle. This yields MSNs with functional groups homogeneously distributed throughout the silica backbone. Its main advantage is that it is a one step process, which might be interesting for industrial purposes. However, if too much functional organosilane is added the mesostructure may be compromised.<sup>79,89</sup> In addition, it is also possible to co-condensate periodic, labile chemical groups during the synthesis, leading to biodegradable periodic mesoporous nanoparticles.<sup>90</sup>

### 1.3. Stimuli-Responsive Mesoporous Nanoparticles

Mesoporous nanoparticles have attracted great attention in nanomedicine due to their capacity to entrap molecules within their pores. Thanks to the open porous structure, it is very easy for the drugs to locate inside the pores but, for the same reason, they can easily diffuse out. When using a cytotoxic drug this phenomenon may lead to undesired side effects and a reduction of the efficacy of the treatment.

A smart approximation to minimize that premature drug release would be the use of pore blocker structures, the so-called gatekeepers, to close the pore entrances. In addition, it would be desirable to open them and allow the release only under very specific conditions. The concept of stimuli-responsive nanocarriers arose to achieve that on-demand drug delivery. It is based on the use of very specific stimulus, that can be characteristic of a particular disease or externally administered, to open the pores and trigger the release only in the area of interest. In the last years, several examples of gatekeepers controlled by either internal or external stimuli have been reported (Figure 1.5).

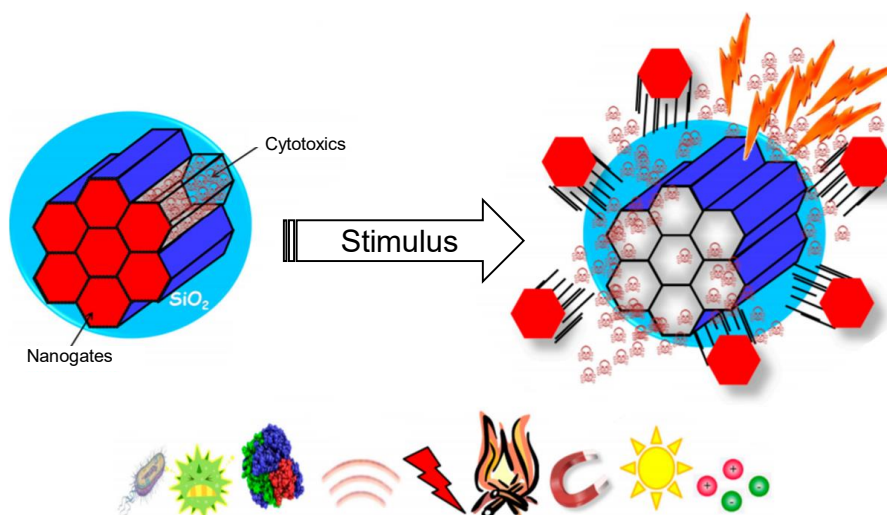


**Figure 1.5.** Schematic representation of a stimuli-responsive mesoporous silica nanocarrier and the types of stimuli that can be applied for the on-demand delivery of drugs, including pH, redox species, magnetic fields or light, among others.

### 1.3.1. External Stimuli-Responsive Mesoporous Nanoparticles

In the case of externally triggered gatekeepers the stimulus comes from outside of the body. The main advantage of these nanocarriers is that the stimulus is provided by an external apparatus, and then, it might be applied on-demand by the clinician. The most common external stimuli employed with mesoporous nanoparticles are alternating magnetic fields, light and ultrasounds.

#### 1.3.1.1. Thermo-responsive mesoporous nanoparticles

Heat generation can be used for two main purposes, (1) induction of hyperthermia-mediated cell death and (2) triggering the opening of the mesopores. Researchers have been mainly focused on superparamagnetic iron oxide nanoparticles, which are known to generate heat upon application of an alternating magnetic field.<sup>91</sup> These particles can be used as seeds for the growth of mesoporous silica shells to yield nanocarriers with high loading capacity and ability to generate heat. Several thermosensitive gatekeepers have been described to close the pore entrances of mesoporous nanocarriers, including  $\beta$ -cyclodextrin-based diels-alder nanovalves,<sup>92</sup> thermosensitive nucleic acid strands<sup>93</sup> or thermosensitive polymers,<sup>94,95</sup> among others.

#### 1.3.1.2. Light-responsive mesoporous nanoparticles

Researchers using light as stimulus have focused on the use of ultraviolet (UV), near-infrared and visible light. This stimulus is interesting because of the ease of its application, since only a lamp or laser adjusted to the target wavelength are needed.

UV light has the lowest penetration in tissue<sup>96</sup> yet the highest energy which leads to (1) radiation-induced cell damage and (2) high ability to break bonds. Examples of these bonds include the cleavage of the *o*-nitrobenzyl<sup>97,98</sup> or the isomerization from *trans*-to-*cis* of the azo-benzene group, that open the pore entrances upon UV light irradiation and allow the drug release.<sup>99,100</sup>

Near-infrared light has lower energy and therefore lower scattering in the tissues than UV light, reaching deeper lengths while being harmless. It is useful to irradiate upconversion nanoparticles (transition metal-based nanoparticles that generate UV light in the vicinity of the carrier upon near-infrared irradiation) to break the above-mentioned bonds without affecting healthy tissues.<sup>101,102</sup> In addition, it can be used to generate heat through many inorganic materials, such as gold nanorods<sup>103</sup> or CuS crystals,<sup>104</sup> among others.

Visible light penetrates deeper than UV does. Despite having low energy it is still able to break some types of bonds without inducing cellular damage. Examples are double bonds<sup>105</sup> or coordination bonds.<sup>106</sup> In addition, visible light can mediate the formation of reactive oxygen species (ROS) that can be used to induce bond cleavage and subsequent drug release.<sup>107</sup>

#### 1.3.1.3. Ultrasound-responsive mesoporous nanoparticles

The use of ultrasounds in drug delivery is attractive due to their non-invasiveness, the absence of ionizing radiations and their high tissue penetration depth.<sup>108</sup> Additionally, the ultrasound generator is inexpensive and can easily be transported and used by the clinician, which might favor the translation to the clinic. Despite this stimulus has not been as explored as the others, it has been successfully employed to trigger the release from MSNs bearing ultrasound-responsive polymeric coatings<sup>109,110</sup> or supramolecular nanovalves.<sup>111</sup> In addition, ultrasounds can macroscopically increase the temperature and have been used to promote the cellular internalization of MSNs through the cleavage of thermo-responsive bonds.<sup>112</sup>

### 1.3.2. Internal Stimuli-Responsive Mesoporous Nanoparticles

Internal stimuli-responsive nanocarriers take advantage of the variations of some biomarkers in some diseases. Examples include variations in the concentration of enzymes, the value of pH or the concentration of redox species.



#### 1.3.2.1. Enzyme-responsive mesoporous nanoparticles

The overexpression of particular enzymes is a well-established phenomenon in diseases such as cancer,<sup>113</sup> osteoporosis<sup>114</sup> or inflammation scenarios.<sup>115</sup> They are interesting due to their ability to break certain bonds. Based on that, several enzyme-responsive gatekeepers have been used to block the mesopores and allow the release under very specific conditions.<sup>116–120</sup> In addition, they can also be used to engineer strategies to reduce the off-target through the uncaging of targeting groups as a consequence of the enzymatic activity.<sup>121,122</sup>

#### 1.3.2.2. pH-responsive mesoporous nanoparticles

The use of pH as trigger relies on its variations throughout the organism (bloodstream, stomach, lysosomes, etc) and during some specific diseases (cancer, osteoporosis).<sup>123,124</sup> In this sense, several pH-responsive gatekeepers have been successfully applied to close the pore entrances, including polymers,<sup>125–127</sup> small particles<sup>128–130</sup> or pH-labile bonds,<sup>131–133</sup> among others.

#### 1.3.2.3. Redox-responsive mesoporous nanoparticles

Redox-responsive nanoparticles take advantage of the differences in the concentration of glutathione (GSH) found inside and outside the cells. Moreover, the levels of GSH are even higher in cancer cells, as a consequence of an enhanced production of ROS.<sup>134,135</sup> The main strategy consists in the use of disulfide bonds to engineer gatekeepers because they are easily cleaved in the presence of redox species. Examples are polymers conjugated *via* disulfide bonds<sup>136</sup> or redox-responsive cross-linkers.<sup>137</sup>

## 1.4. Nanotechnology and Cancer

In the last few years, the efforts of many nanotechnologists have been headed towards the design of nanomaterials capable of diagnosing or treating the challenging area of cancer. In addition, nanotechnology has also been applied for the treatment of other diseases such as diabetes<sup>138</sup> or those related to kidney<sup>139</sup> or lung,<sup>140</sup> among others.

According to the World Health Organization, cancer is one of the leading causes of death worldwide.<sup>141</sup> Most of the current cancer treatments rely on the use radiotherapy or chemotherapy. Additionally, patients may undergo surgery to remove certain tumors, although they still might have to be irradiated or go through chemotherapy, depending on the particularities of each patient.<sup>142</sup>

Radiation therapy consists in the use of ionizing radiation able to induce DNA damage in the cells. It is based on the fact that normal cells show faster repair of radiation damage than cancer cells. Depending on the particularity of the tumor the radiation can be administered from inside (radioactive sources introduced in the body) or outside the body (high energy rays: photons, protons or particle radiation). Current research efforts are headed towards the development of more precise equipment and the optimization of the algorithms applied for the planning of the treatments.<sup>143</sup>

Chemotherapy consists in the administration of drugs able to induce cell death. However, these compounds do not show preferential accumulation in the tumor tissues and distribute throughout the entire body, leading to severe side effects.<sup>144</sup> In this sense, it would be desirable to specifically deliver the chemotherapeutics only to cancer cells. A smart approximation would be the use of nanoparticles since they (1) can retain drugs until reaching the tumor; (2) allow the delivery of hydrophobic drugs that otherwise would not be soluble in the bloodstream; (3) provide a protective shell for the drugs so their degradation can be delayed and their cellular uptake enhanced; (4) allow the co-loading of several drugs to improve the efficacy of the treatment and (5) can be modified with targeting moieties to specifically recognize tumoral cells over normal cells and improve the selectivity of the treatment.<sup>58,65,145,146</sup>

The main rationale behind the use of nanocarriers is their passive and preferential accumulation into the tumors as a consequence of the Enhanced Permeability and Retention effect, the so-called EPR effect. The EPR effect was first reported in 1986 when Maeda and coworkers observed that proteins above a certain molecular weight spontaneously accumulated in tumoral tissues and remained there for a long time.<sup>147</sup> Their research showed that solid tumors present blood vessels with abnormal architecture and poor lymphatic drainage as a consequence of their rapid growth. As a result, macromolecules larger than 40 kDa tend to leak out from the tumor vessels and accumulate in the tumor. This effect has not been observed in healthy tissues.<sup>148</sup>

Unfortunately, the magnitude of the EPR effect and its ability to accumulate macromolecules in the tumor highly depend on the particularities of the patient and the tumor.<sup>149</sup> For such reason, even when existing a significant EPR effect, nanocarriers have to face consecutive physical and biochemical biological barriers (Figure 1.6), including (1) opsonization and subsequent nanocarrier removal from the bloodstream by the

mononuclear phagocyte system; (2) nonspecific distribution throughout the body; (3) premature release of the antitumoral drugs; (4) high intratumoral pressure and dense collagen matrix that prevent nanoparticles from reaching deeper regions of the tumor; (5) low selectivity towards cancer cells or (6) entrapment of nanoparticles in the lysosomes so effective payload may be compromised, among others.<sup>150</sup>

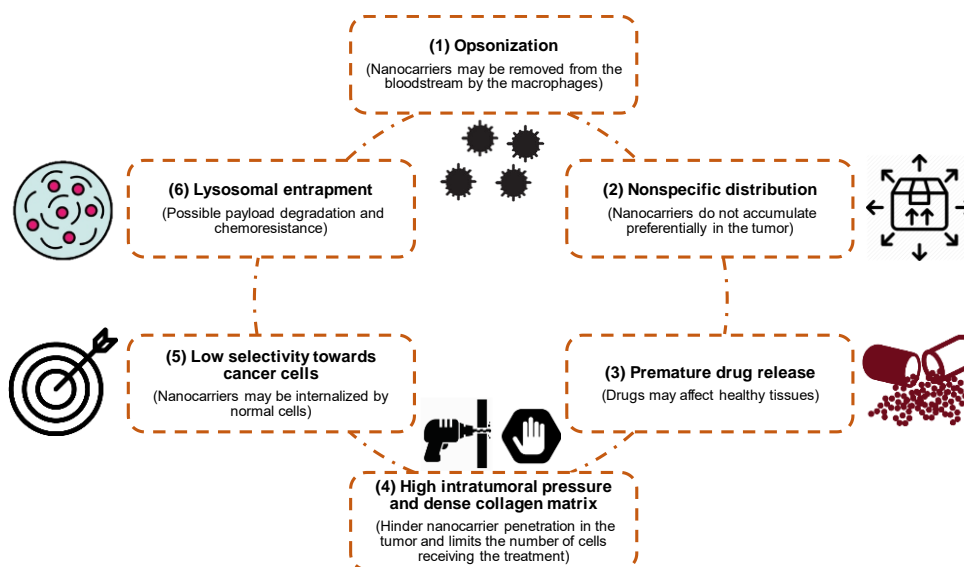


**Figure 1.6.** Sequential biological barriers that nanocarriers may have to face when administered to the patient, ordered from their administration in the bloodstream (1) to an eventual internalization in the cells (6).

In the last few years, several approximations have been reported in order to overcome some of these limitations, including (1) chemical species that avoid or reduce opsonization of the carriers;<sup>151–153</sup> (2) tumor-homing peptides<sup>154</sup> or mesenchymal stem cells<sup>155</sup> that spontaneously migrate to tumoral areas; (3) stimuli-responsive gatekeepers that hamper premature drug release until some specific event happens;<sup>156</sup> (4) proteolytic enzymes that digest the collagen matrix<sup>157</sup> or ultrasound-induced cavitation that enhance extravasation into the tumor;<sup>158</sup> (5) biomolecules that specifically bind receptors only overexpressed on the tumoral cell membranes;<sup>146</sup> or (6) agents able to induce endosomal escape,<sup>159</sup> among others.

However, the implementation of all these strategies in a single carrier remains elusive due to the complexity of the interactions between these nanomaterials and the living organisms. In consequence, the translation from the bench to the bed still constitutes the bottleneck of this field.<sup>160</sup>

## References

- (1) National Nanotechnology Initiative. The Initiative and its Implementation Plan. [https://www.nano.gov/sites/default/files/pub\\_resource/nni\\_implementation\\_plan\\_2000.pdf](https://www.nano.gov/sites/default/files/pub_resource/nni_implementation_plan_2000.pdf).
- (2) Riehemann, K.; Schneider, S. W.; Luger, T. A.; Godin, B.; Ferrari, M.; Fuchs, H. Nanomedicine — Challenge and Perspectives. *Angew. Chemie Int. Ed.* **2009**, *48*, 872–897.
- (3) Mobasser, S.; Firoozi, A. A. Review of Nanotechnology Applications in Science and Engineering. *J. Civ. Eng. Urban.* **2016**, *6*, 84–93.
- (4) Bangham, A. D.; Standish, M. M.; Weissmann, G. The Action of Steroids and Streptolysin S on the Permeability of Phospholipid Structures to Cations. *J. Mol. Biol.* **1965**, *13*, 253–259.
- (5) Bangham, A. D.; Horne, R. W. Negative Staining of Phospholipids and Their Structural Modification by Surface-Active Agents as Observed in the Electron Microscope. *J. Mol. Biol.* **1964**, *8*, 660–668.
- (6) Wicki, A.; Witzigmann, D.; Balasubramanian, V.; Huwyler, J. Nanomedicine in Cancer Therapy: Challenges, Opportunities, and Clinical Applications. *J. Control. Release* **2015**, *200*, 138–157.
- (7) Oerlemans, C.; Bult, W.; Bos, M.; Storm, G.; Nijssen, J. F. W.; Hennink, W. E. Polymeric Micelles in Anticancer Therapy: Targeting, Imaging and Triggered Release. *Pharm. Res.* **2010**, *27*, 2569–2589.
- (8) Bozzuto, G.; Molinari, A. Liposomes as Nanomedical Devices. *Int. J. Nanomedicine* **2015**, *10*, 975–999.
- (9) Bulbake, U.; Doppalapudi, S.; Kommineni, N.; Khan, W. Liposomal Formulations in Clinical Use: An Updated Review Development. *Pharmaceutics* **2017**, *9*, 1–33.
- (10) Kumari, A.; Yadav, S. K.; Yadav, S. C. Biodegradable Polymeric Nanoparticles Based Drug Delivery Systems. *Colloids Surfaces B Biointerfaces* **2010**, *75*, 1–18.
- (11) Lü, J.-M.; Wang, X.; Marin-Muller, C.; Wang, H.; Lin, P. H.; Yao, Q.; Chen, C. Current Advances in Research and Clinical Applications of PLGA-Based Nanotechnology. *Expert Rev. Mol. Diagn.* **2010**, *9*, 325–341.
- (12) Ghosh, P.; Han, G.; De, M.; Kim, C.; Rotello, V. Gold Nanoparticles in Delivery Applications. *Adv. Drug Deliv. Rev.* **2008**, *60*, 1307–1315.
- (13) Du, Y. O.; Yang, X. X.; Li, W. L.; Wang, J.; Huang, C. Z. A Cancer-Targeted Drug Delivery System Developed with Gold Nanoparticles Mediated DNA-Doxorubicin Conjugates. *RSC Adv.* **2014**, *4*, 34830–34835.
- (14) Cole, L. E.; Ross, R. D.; Tilley, J. M.; Vargo-Gogola, T.; Roeder, R. K. Gold Nanoparticles as Contrast Agents in X-Ray Imaging and Computed Tomography. *Nanomedicine* **2015**, *10*, 321–341.
- (15) Jaque, D.; Maestro, L. M.; Rosal, B. del; Haro-González, P.; Benayas, A.; Plaza, J. L.; Rodríguez, E. M.; Solé, J. G. Nanoparticles for Photothermal Therapies. *Nanoscale* **2014**, *6*, 9494–9530.

- (16) Ventola, C. L. Progress in Nanomedicine: Approved and Investigational Nanodrugs. *P&T* **2017**, *42*, 742–755.
- (17) Lee, S. H.; Jun, B. Silver Nanoparticles: Synthesis and Application for Nanomedicine. *Int. J. Mol. Sci.* **2019**, *20*, 865.
- (18) Tang, S.; Zheng, J. Antibacterial Activity of Silver Nanoparticles: Structural Effects. *Adv. Healthc. Mater.* **2018**, *7*, 1701503.
- (19) Salomoni, R.; Léo, P.; Montemor, A. F.; Rinaldi, B.; Rodrigues, M. Antibacterial Effect of Silver Nanoparticles in *Pseudomonas Aeruginosa*. *Nanotechnol. Sci. Appl.* **2017**, *10*, 115–121.
- (20) Gherasim, O.; Fikai, A.; Andronescu, E. Biomedical Applications of Silver Nanoparticles: An Up-to-Date Overview. *Nanomaterials* **2018**, *8*, 861.
- (21) Yuan, Y.; Zhang, S.; Hwang, J.; Kong, I. Silver Nanoparticles Potentiates Cytotoxicity and Apoptotic Potential of Camptothecin in Human Cervical Cancer Cells. *Oxid. Med. Cell. Longev.* **2018**, *2018*, 1–21.
- (22) Huang, Z.; Jiang, X.; Guo, D.; Gu, N. Controllable Synthesis and Biomedical Applications of Silver Nanomaterials. *J. Nanosci. Nanotechnol.* **2011**, *11*, 9395–9408.
- (23) Usenko, C. Y.; Harper, S. L.; Tanguay, R. L. *In vivo* Evaluation of Carbon Fullerene Toxicity Using Embryonic Zebrafish. *Carbon.* **2008**, *45*, 1891–1898.
- (24) Yamawaki, H.; Iwai, N. Cytotoxicity of Water-Soluble Fullerene in Vascular Endothelial Cells. *Am. J. Physiol. Physiol.* **2006**, *290*, 1495–1502.
- (25) Sayes, C. M.; Fortner, J. D.; Guo, W.; Lyon, D.; Boyd, A. M.; Ausman, K. D.; Tao, Y. J.; Sitharaman, B.; Wilson, L. J.; Hughes, J. B.; *et al.* The Differential Cytotoxicity of Water-Soluble Fullerenes. *Nano Lett.* **2004**, *4*, 1881–1887.
- (26) Patlolla, A.; Knighten, B.; Tchounwou, P. Multi-Walled Carbon Nanotubes Induce Cytotoxicity, Genotoxicity and Apoptosis in Normal Human Dermal Fibroblast Cells. *Ethn. Dis.* **2010**, *20*, 65–72.
- (27) Tian, F.; Cui, D.; Schwarz, H.; Estrada, G. G.; Kobayashi, H. Cytotoxicity of Single-Wall Carbon Nanotubes on Human Fibroblasts. *Toxicol. Vitro.* **2006**, *20*, 1202–1212.
- (28) Fiorito, S.; Serafino, A.; Andreola, F.; Togna, A.; Togna, G. Toxicity and Biocompatibility of Carbon Nanoparticles. *J. Nanosci. Nanotechnol.* **2006**, *6*, 591–599.
- (29) Yan, A.; Lau, B. W.; Weissman, B. S.; Külaots, I.; Yang, N. Y. C.; Kane, A. B.; Hurt, R. H. Biocompatible, Hydrophilic, Supramolecular Carbon Nanoparticles for Cell Delivery. *Adv. Mater.* **2006**, *18*, 2373–2378.
- (30) Kim, T.; Chung, P.; Slowing, I. I.; Tsunoda, M.; Yeung, E. S.; Lin, V. S. Structurally Ordered Mesoporous Carbon Nanoparticles as Transmembrane Delivery Vehicle in Human Cancer Cells. *Nano Lett.* **2008**, *8*, 3724–3727.
- (31) Gu, J.; Su, S.; Li, Y.; He, Q.; Shi, J. Hydrophilic Mesoporous Carbon Nanoparticles as Carriers for Sustained Release of Hydrophobic Anti-Cancer Drugs. *Chem. Commun.* **2011**, *47*, 2101–2103.

- (32) Saha, D.; Warren, K. E.; Naskar, A. K. Soft-Templated Mesoporous Carbons as Potential Materials for Oral Drug Delivery. *Carbon*. **2014**, *71*, 47–57.
- (33) Liang, C.; Li, Z.; Dai, S. Mesoporous Carbon Materials: Synthesis and Modification. *Angew. Chemie Int. Ed.* **2008**, *47*, 3696–3717.
- (34) Zhao, Q.; Lin, Y.; Han, N.; Li, X.; Geng, H.; Wang, X.; Cui, Y.; Wang, S. Mesoporous Carbon Nanomaterials in Drug Delivery and Biomedical Application. *Drug Deliv.* **2017**, *24*, 94–107.
- (35) Kresge, C. T.; Leonowicz, M. E.; Roth, W. J.; Vartuli, J. C.; Beck, J. S. Ordered Mesoporous Molecular Sieves Synthesized by a Liquid-Crystal Template Mechanism. *Nature* **1992**, *359*, 710–712.
- (36) Yanagisawa, T.; Shimizu, T.; Kuroda, K.; Kato, C. The Preparation of Alkyltrimethylammonium-Kanemite Complexes and Their Conversion to Microporous Materials. *Bull. Chem. Soc. Jpn.* **1990**, *63*, 988–992.
- (37) Colilla, M.; Balas, F.; Manzano, M.; Vallet-Regí, M. Novel Method to Synthesize Ordered Mesoporous Silica with High Surface Areas. *Solid State Sci.* **2008**, *10*, 408–415.
- (38) Nieto, A.; Balas, F.; Manzano, M.; Vallet-Regí, M. Functionalization Degree of SBA-15 as Key Factor to Modulate Sodium Alendronate Dosage. *Microporous Mesoporous Mater.* **2008**, *116*, 4–13.
- (39) Horcajada, P.; Rámila, A.; Férey, G.; Vallet-Regí, M. Influence of Superficial Organic Modification of MCM-41 Matrices on Drug Delivery Rate. *Solid State Sci.* **2006**, *8*, 1243–1249.
- (40) Colilla, M.; Manzano, M.; Izquierdo-Barba, I.; Vallet-Regí, M.; Boissière, C.; Sanchez, C. Advanced Drug Delivery Vectors with Tailored Surface Properties Made of Mesoporous Binary Oxides Submicronic Spheres. *Chem. Mater.* **2010**, *5*, 1821–1830.
- (41) Colilla, M.; Balas, F.; Manzano, M.; Vallet-Regí, M. Novel Method To Enlarge the Surface Area of SBA-15. *Chem. Mater.* **2007**, *19*, 3099–3101.
- (42) Walcarius, A.; Mercier, L. Mesoporous Organosilica Adsorbents: Nanoengineered Materials for Removal of Organic and Inorganic Pollutants. *J. Mater. Chem.* **2010**, *20*, 4478–4511.
- (43) Sangvanich, T.; Morry, J.; Fox, C.; Ngamcherdtrakul, W.; Goodyear, S.; Castro, D.; Fryxell, G. E.; Addleman, R. S.; Summers, A. O.; Yantasee, W. Novel Oral Detoxification of Mercury, Cadmium, And Lead with Thiol-Modified Nanoporous Silica. *ACS Appl. Mater. Interfaces* **2014**, *6*, 5483–5493.
- (44) Yantasee, W.; Rutledge, R. D.; Chouyyok, W.; Sukwarotwat, V.; Orr, G.; Warner, C. L.; Warner, M. G.; Fryxell, G. E.; Wiacek, R. J.; Timchalk, C.; *et al.* Functionalized Nanoporous Silica for the Removal of Heavy Metals from Biological Systems: Adsorption and Application. *ACS Appl. Mater. Interfaces* **2010**, *2*, 2749–2758.
- (45) Li, X.; Ri, Y.; Kyung, L.; Row, H. Synthesis of Mesoporous Siliceous Materials in Choline Chloride Deep Eutectic Solvents and the Application of These Materials to High-Performance Size Exclusion Chromatography. *Chromatographia* **2016**,

79, 375–382.

- (46) Tian, R.; Sun, J.; Ye, M.; Xie, C.; Dong, J.; Hu, J.; Ma, D.; Bao, X.; Zou, H. Large-Pore Mesoporous SBA-15 Silica Particles with Submicrometer Size as Stationary Phases for High-Speed CEC Separation. *Electrophoresis* **2006**, *27*, 742–748.
- (47) Taylor, P.; Tang, B.; Bi, W.; Row, K. H. Exploration of Mesoporous Siliceous Particle-Based High-Performance Size Exclusion Chromatography for the Quantitation of Biomacromolecular Polysaccharides. *J. Liq. Chromatogr. Relat. Technol.* **2015**, *38*, 774–780.
- (48) Yan, Z.; Meng, H.; Shi, L.; Li, Z.; Kang, P. Synthesis of Mesoporous Hollow Carbon Hemispheres as Highly Efficient Pd Electrocatalyst Support for Ethanol Oxidation. *Electrochem. commun.* **2010**, *12*, 689–692.
- (49) Serrano, E.; Linares, N.; García-Martínez, J.; Berenguer, J. R. Sol–Gel Coordination Chemistry: Building Catalysts from the Bottom-Up. *ChemCatChem* **2013**, *5*, 844–860.
- (50) Sun, J.; Bao, X. Textural Manipulation of Mesoporous Materials for Hosting of Metallic Nanocatalysts. *Chem. Eur. J.* **2008**, *14*, 7478–7488.
- (51) Zhang, H.; Li, X. Novel Mesoporous Silica Materials with Hierarchically Ordered Nanochannel: Synthesis with the Assistance of Straight-Chain Alkanes and Application. *J. Chem.* **2016**, *2016*, 16.
- (52) Villaverde, G.; Corma, A.; Iglesias, M.; Sánchez, F. Heterogenized Gold Complexes: Recoverable Catalysts for Multicomponent Reactions of Aldehydes, Terminal Alkynes, and Amines. *ACS Catal.* **2012**, *2*, 399–406.
- (53) Villaverde, G.; Corma, A.; Iglesias, M.; Sánchez, F. Chiral NHC-Complexes with Dioxolane Backbone Heterogenized on MCM-41. Catalytic Activity. *ChemCatChem* **2011**, *3*, 1320–1328.
- (54) Bernardos, A.; Kouřimská, L. Applications of Mesoporous Silica Materials in Food—a Review. *Czech J. Food Sci.* **2013**, *31*, 99–107.
- (55) Zhang, Y.; Zheng, S.; Zhu, S.; Ma, J.; Sun, Z.; Farid, M. Evaluation of Paraffin Infiltrated in Various Porous Silica Matrices as Shape-Stabilized Phase Change Materials for Thermal Energy Storage. *Energy Convers. Manag.* **2018**, *171*, 361–370.
- (56) Mitran, R. A.; Berger, D.; Munteanu, C.; Matei, C. Evaluation of Different Mesoporous Silica Supports for Energy Storage in Shape-Stabilized Phase Change Materials with Dual Thermal Responses. *J. Org. Chem. C* **2015**, *119*, 15177–15184.
- (57) Vallet-Regí, M.; Rámila, A.; Real, R. P. del; Pérez-Pariante, J. A New Property of MCM-41: Drug Delivery System. *Chem. Mater.* **2001**, *13*, 308–311.
- (58) Wang, Y.; Zhao, Q.; Han, N.; Bai, L.; Li, J.; Liu, J.; Che, E.; Hu, L.; Zhang, Q.; Jiang, T.; *et al.* Mesoporous Silica Nanoparticles in Drug Delivery and Biomedical Applications. *Nanomedicine Nanotechnology, Biol. Med.* **2015**, *11*, 313–327.
- (59) Giret, S.; Wong Chi Man, M.; Carcel, C. Mesoporous-Silica-Functionalized Nanoparticles for Drug Delivery. *Chem. Eur. J.* **2015**, *21*, 13850–13865.

- (60) Karimi, M.; Ghasemi, A.; Zangabad, P. S.; Rahighi, R.; Basri, S. M. M.; Mirshekari, H.; Amiri, M.; Pishabad, Z. S.; Aslani, A.; Bozorgomid, M.; *et al.* Smart Micro/Nanoparticles in Stimulus-Responsive Drug/Gene Delivery Systems. *Chem. Soc. Rev.* **2016**, *45*, 1457–1501.
- (61) Lozano, D.; Trejo, C. G.; Gómez-Barrena, E.; Manzano, M.; Doadrio, J. C.; Salinas, A. J.; Vallet-Regí, M.; García-Honduvilla, N.; Esbrit, P.; Buján, J. Osteostatin-Loaded onto Mesoporous Ceramics Improves the Early Phase of Bone Regeneration in a Rabbit Osteopenia Model. *Acta Biomater.* **2012**, *8*, 2317–2323.
- (62) Izquierdo-Barba, I.; Sousa, E.; Doadrio, J. C.; Doadrio, A. L.; Pérez-Pariente, J.; Martínez, A.; Babonneau, F.; Vallet-Regí, M. Influence of Mesoporous Structure Type on the Controlled Delivery of Drugs: Release of Ibuprofen from MCM-48, SBA-15 and Functionalized SBA-15. *J. Sol-Gel Sci. Technol.* **2009**, *50*, 421–429.
- (63) Trewyn, B. G.; Nieweg, J. A.; Zhao, Y.; Lin, V. S. Biocompatible Mesoporous Silica Nanoparticles with Different Morphologies for Animal Cell Membrane Penetration. *Chem. Eng. J.* **2008**, *137*, 23–29.
- (64) Radu, D. R.; Lai, C.; Jeftinija, K.; Rowe, E. W.; Jeftinija, S.; Lin, V. S. A Polyamidoamine Dendrimer-Capped Mesoporous Silica Nanosphere-Based Gene Transfection Reagent. *J. Am. Chem. Soc.* **2004**, *126*, 13216–13217.
- (65) Slowing, I. I.; Vivero-Escoto, J. L.; Wu, C.-W.; Lin, V. S. Mesoporous Silica Nanoparticles as Controlled Release Drug Delivery and Gene Transfection Carriers. *Adv. Drug Deliv. Rev.* **2008**, *60*, 1278–1288.
- (66) Paris, J. L.; De la Torre, P.; Cabañas, M. V.; Manzano, M.; Flores, A. I.; Vallet-Regí, M. Suicide-Gene Transfection of Tumor-Tropic Placental Stem Cells Employing Ultrasound-Responsive Nanoparticles. *Acta Biomater.* **2019**, *83*, 372–378.
- (67) Vallet-Regí, M.; Doadrio, J. C.; Doadrio, A. L.; Izquierdo-Barba, I.; Pérez-Pariente, J. Hexagonal Ordered Mesoporous Material as a Matrix for the Controlled Release of Amoxicillin. *Solid State Ionics* **2004**, *172*, 435–439.
- (68) Izquierdo-Barba, I.; Sánchez-Salcedo, S.; Colilla, M.; Feito, M. J.; Ramírez-Santillán, C.; Portolés, M. T.; Vallet-Regí, M. Inhibition of Bacterial Adhesion on Biocompatible Zwitterionic SBA-15 Mesoporous Materials. *Acta Biomater.* **2011**, *7*, 2977–2985.
- (69) Arcos, D.; Vallet-Regí, M. Sol–Gel Silica-Based Biomaterials and Bone Tissue Regeneration. *Acta Biomater.* **2010**, *6*, 2874–2888.
- (70) Alcaide, M.; Portolés, P.; López-Noriega, A.; Arcos, D.; Vallet-Regí, M.; Portolés, M. T. Interaction of an Ordered Mesoporous Bioactive Glass with Osteoblasts, Fibroblasts and Lymphocytes, Demonstrating Its Biocompatibility as a Potential Bone Graft Material. *Acta Biomater.* **2010**, *6*, 892–899.
- (71) Izquierdo-Barba, I.; Santos-Ruiz, L.; Becerra, J.; Feito, M. J.; Fernández-Villa, D.; Serrano, M. C.; Díaz-Güemes, I.; Arcos, D.; Vallet-Regí, M. Synergistic Effect of Si-Hydroxyapatite Coating and VEGF Adsorption on Ti6Al4V-ELI Scaffolds for Bone Regeneration in an Osteoporotic Bone Environment. *Acta Biomater.* **2019**, *83*, 456–466.



- (72) Gómez-Cerezo, N.; Sánchez-Salcedo, S.; Izquierdo-Barba, I.; Arcos, D.; Vallet-Regí, M. *In vitro* Colonization of Stratified Bioactive Scaffolds by Pre-Osteoblast Cells. *Acta Biomater.* **2016**, *44*, 73–84.
- (73) Vallet-Regí, M.; Colilla, M.; Izquierdo-Barba, I. Bioactive Mesoporous Silicas as Controlled Delivery Systems: Application in Bone Tissue Regeneration. *J. Biomed. Nanotechnol.* **2008**, *4*, 1–13.
- (74) Polo, L.; Gómez-Cerezo, N.; Aznar, E.; Vivancos, J.-L.; Sancenón, F.; Arcos, D.; Vallet-Regí, M.; Martínez-mañez, R. Molecular Gates in Mesoporous Bioactive Glasses for the Treatment of Bone Tumors and Infection. *Acta Biomater.* **2017**, *50*, 114–126.
- (75) Polo, L.; Gómez-Cerezo, N.; García-Fernández, A.; Aznar, E.; Vivancos, J. L.; Arcos, D.; Vallet-Regí, M.; Martínez-Mañez, R. Mesoporous Bioactive Glasses Equipped with Stimuli-Responsive Molecular Gates for the Controlled Delivery of Levofloxacin against Bacteria. *Chem. Eur. J.* **2018**, *24*, 18944–18951.
- (76) Cicuéndez, M.; Doadrio, J. C.; Hernández, A.; Portolés, M. T.; Izquierdo-Barba, I.; Vallet-Regí, M. Multifunctional pH Sensitive 3D Scaffolds for Treatment and Prevention of Bone Infection. *Acta Biomater.* **2018**, *65*, 450–461.
- (77) González, B.; Díez, J.; Pedraza, D.; Guembe, M.; Izquierdo-Barba, I.; Vallet-Regí, M. Mesoporous Silica Nanoparticles Decorated with Polycationic Dendrimers for Infection Treatment. *Acta Biomater.* **2018**, *68*, 261–271.
- (78) Paris, J. L.; Lafuente-Gómez, N.; Cabañas, M. V.; Román, J.; Peña, J.; Vallet-Regí, M. Fabrication of a Nanoparticle-Containing 3D Porous Bone Scaffold with Proangiogenic and Antibacterial Properties. *Acta Biomater.* **2019**, *86*, 441–449.
- (79) Hoffmann, F.; Cornelius, M.; Morell, J.; Fröba, M. Silica-Based Mesoporous Organic–Inorganic Hybrid Materials. *Angew. Chemie Int. Ed.* **2006**, *45*, 3216–3251.
- (80) Stöber, W.; Fink, A.; Bohn, E. Controlled Growth of Monodisperse Silica Spheres in the Micron Size Range. *J. Colloid Interface Sci.* **1968**, *26*, 62–69.
- (81) Wu, S. H.; Lin, H. P. Synthesis of Mesoporous Silica Nanoparticles. *Chem. Soc. Rev.* **2013**, *42*, 3862–3875.
- (82) Huo, Q.; Margolese, D. I.; Ciesla, U.; Feng, P.; Gier, T. E.; Sieger, P.; Leon, R.; Petroff, P. M.; Schüth, F.; Stucky, G. D. Generalized Synthesis of Periodic Surfactant/Inorganic Composite Materials. *Nature* **1994**, *368*, 317–321.
- (83) Huo, Q.; Margolese, D. I.; Ciesla, U.; Demuth, D. G.; Feng, P.; Gier, T. E.; Fiouzi, A.; Chmelka, B. F.; Schüth, F.; Stucky, G. D. Organization of Organic Molecules with Inorganic Molecular Species into Nanocomposite Biphasic Arrays. *Chem. Mater.* **1994**, *6*, 1176–1191.
- (84) Cauda, V.; Argyo, C.; Piercey, D. G.; Bein, T. “Liquid-Phase Calcination” of Colloidal Mesoporous Silica Nanoparticles in High-Boiling Solvents. *J. Am. Chem. Soc.* **2011**, *133*, 6484–6486.
- (85) Kecht, J.; Bein, T. Oxidative Removal of Template Molecules and Organic Functionalities in Mesoporous Silica Nanoparticles by H<sub>2</sub>O<sub>2</sub> Treatment. *Microporous Mesoporous Mater.* **2008**, *116*, 123–130.

- (86) Möller, K.; Bein, T. Talented Mesoporous Silica Nanoparticles. *Chem. Mater.* **2017**, *29*, 371–388.
- (87) Al Samri, M. T.; Biradar, A. V.; Alsuwaidi, A. R.; Balhaj, G.; Al-Hammadi, S.; Shehab, S.; Al-Salam, S.; Tariq, S.; Pramathan, T.; Benedict, S.; *et al.* *In vitro* Biocompatibility of Calcined Mesoporous Silica Particles and Fetal Blood Cells. *Int. J. Nanomedicine* **2012**, *7*, 3111–3121.
- (88) Wang, G.; Otuonye, A. N.; Blair, E. A.; Denton, K.; Tao, Z.; Asefa, T. Functionalized Mesoporous Materials for Adsorption and Release of Different Drug Molecules: A Comparative Study. *J. Solid State Chem.* **2009**, *182*, 1649–1660.
- (89) Shylesh, S.; Samuel, P. P.; Parischa, R.; Singh, A. P. Ethane Bridged Hybrid Mesoporous Silsesquioxanes with Sulfonic Acid Functionalities: Synthesis, Characterization and Catalytic Applications. In *From Zeolites to Porous MOF Materials - The 40th Anniversary of International Zeolite Conference*; Elsevier, 2007; pp 1899–1904.
- (90) Croissant, J.; Cattoën, X.; Wong Chi Man, M.; Gallud, A.; Raehm, L.; Trens, P.; Maynadier, M.; Durand, J.-O. Biodegradable Ethylene-Bis(Propyl)Disulfide-Based Periodic Mesoporous Organosilica Nanorods and Nanospheres for Efficient *in vitro* Drug Delivery. *Adv. Mater.* **2014**, *26*, 6174–6180.
- (91) Gamarra, L.; Silva, A. C.; Oliveira, T. R.; J. B. Mamani; Malheiros, S. M. F.; Malavolta, L.; Pavon, L. F.; Sibov, T. T.; Amaro Jr, E.; Gamarra, L. Application of Hyperthermia Induced by Superparamagnetic Iron Oxide Nanoparticles in Glioma Treatment. *Int. J. Nanomedicine* **2011**, *6*, 591–603.
- (92) B. Rühle; Datz, S.; Argyo, C.; Bein, T.; Zink, J. I. A Molecular Nanocap Activated by Superparamagnetic Heating for Externally Stimulated Cargo Release. *Chem. Commun.* **2016**, *9*, 1843–1846.
- (93) Ruiz-Hernández, E.; Baeza, A.; Vallet-Regí, M. Smart Drug Delivery through DNA/Magnetic Nanoparticle Gates. *ACS Nano* **2011**, *5*, 1259–1266.
- (94) Guisasola, E.; Asín, L.; Beola, L.; De La Fuente, J. M.; Baeza, A.; Vallet-Regí, M. Beyond Traditional Hyperthermia: *In vivo* Cancer Treatment with Magnetic-Responsive Mesoporous Silica Nanocarriers. *ACS Appl. Mater. Interfaces* **2018**, *10*, 12518–12525.
- (95) Guisasola, E.; Baeza, A.; Talelli, M.; Arcos, D.; Moros, M.; De La Fuente, J. M.; Vallet-Regí, M. Magnetic-Responsive Release Controlled by Hot Spot Effect. *Langmuir* **2015**, *31*, 12777–12782.
- (96) Gupta, A.; Avci, P.; Dai, T.; Huang, Y.-Y.; Hamblin, M. R. Ultraviolet Radiation in Wound Care: Sterilization and Stimulation. *Adv. Wound Care* **2013**, *2*, 422–437.
- (97) Martínez-Carmona, M.; Baeza, A.; Rodríguez-Milla, M. A.; García-Castro, J.; Vallet-Regí, M. Mesoporous Silica Nanoparticles Grafted with a Light-Responsive Protein Shell for Highly Cytotoxic Antitumoral Therapy. *J. Mater. Chem. B* **2015**, *3*, 5746–5752.
- (98) Zhang, Y.; Ang, C. Y.; Li, M.; Tan, S. Y.; Qu, Q.; Luo, Z.; Zhao, Y. Polymer-Coated Hollow Mesoporous Silica Nanoparticles for Triple-Responsive Drug

- Delivery. *ACS Appl. Mater. Interfaces* **2015**, *7*, 18179–18187.
- (99) Ferris, D. P.; Zhao, Y.; Khashab, N. M.; Khatib, H. A.; Stoddart, J. F.; Zink, J. I. Light-Operated Mechanized Nanoparticles. *J. Am. Chem. Soc.* **2009**, *131*, 1686–1688.
- (100) Moorthy, M. S.; Kim, H.; Bae, J.; Kim, S.; Ha, C. Design of Core-Shell Magnetic Mesoporous Silica Hybrids for pH and UV Light Stimuli-Responsive Cargo Release. *RSC Adv.* **2016**, *6*, 29106–29115.
- (101) Zhao, L.; Peng, J.; Huang, Q.; Li, C.; Chen, M.; Sun, Y.; Lin, Q. Near-Infrared Photoregulated Drug Release in Living Tumor Tissue via Yolk-Shell Upconversion Nanocages. *Adv. Funct. Mater.* **2014**, *24*, 363–371.
- (102) Yang, Y.; Velmurugan, B.; Liu, X.; Xing, B. NIR Photoresponsive Crosslinked Upconverting Nanocarriers Toward Selective Intracellular Drug Release. *Small* **2013**, *9*, 2937–2944.
- (103) Villaverde, G.; Gómez-Graña, S.; Guisasaola, E.; García, I.; Hanske, C.; Liz-Marzán, L. M.; Baeza, A.; Vallet-Regí, M. Targeted Chemo-Photothermal Therapy: A Nanomedicine Approximation to Selective Melanoma Treatment. *Part. Part. Syst. Charact.* **2018**, *35*, 1800148–1800158.
- (104) Wei, Q.; Chen, Y.; Ma, X.; Ji, J.; Qiao, Y.; Zhou, B.; Ma, F.; Ling, D.; Zhang, H.; Tian, M.; *et al.* High-Efficient Clearable Nanoparticles for Multi-Modal Imaging and Image-Guided Cancer Therapy. *Adv. Funct. Mater.* **2018**, *28*, 1704634–1704646.
- (105) Jiang, M. Y.; Dolphin, D. Site-Specific Prodrug Release Using Visible Light. *J. Am. Chem. Soc.* **2008**, *130*, 4236–4237.
- (106) Knežević, N. Ž.; Trewyn, B. G.; Lin, V. S.-Y. Functionalized Mesoporous Silica Nanoparticle-Based Visible Light Responsive Controlled Release Delivery System. *Chem. Commun.* **2011**, *47*, 2817–2819.
- (107) Martínez-Carmona, M.; Lozano, D.; Baeza, A.; Colilla, M.; Vallet-Regí, M. A Novel Visible Light Responsive Nanosystem for Cancer Treatment. *Nanoscale* **2017**, *9*, 15967–15973.
- (108) Mura, S.; Nicolas, J.; Couvreur, P. Stimuli-Responsive Nanocarriers for Drug Delivery. *Nat. Mater.* **2013**, *12*, 991–1003.
- (109) Paris, J. L.; Villaverde, G.; Cabañas, M. V.; Manzano, M.; Vallet-Regí, M. From Proof-of-Concept Material to PEGylated and Modularly Targeted Ultrasound-Responsive Mesoporous Silica Nanoparticles. *J. Mater. Chem. B* **2018**, *6*, 2785–2794.
- (110) Paris, J. L.; Cabanas, M. V.; Manzano, M.; Vallet-Regí, M. Polymer-Grafted Mesoporous Silica Nanoparticles as Ultrasound-Responsive Drug Carriers. *ACS Nano* **2015**, *9*, 11023–11033.
- (111) Lee, S. F.; Zhu, X. M.; Wang, Y. X. J.; Xuan, S. H.; You, Q.; Chan, W. H.; Wong, C. H.; Wang, F.; Yu, J. C.; Cheng, C. H. K.; *et al.* Ultrasound, pH and Magnetically Responsive Crown-Ether-Coated Core/Shell Nanoparticles as Drug Encapsulation and Release Systems. *ACS Appl. Mater. Interfaces* **2013**, *5*, 1566–1574.

- (112) Paris, J. L.; Manzano, M.; Cabañas, M. V.; Vallet-Regí, M. Mesoporous Silica Nanoparticles Engineered for Ultrasound-Induced Uptake by Cancer Cells. *Nanoscale* **2018**, *10*, 6402–6408.
- (113) Mohamed, M. M.; Sloane, B. F. Cysteine Cathepsins: Multifunctional Enzymes in Cancer. *Nat. Rev. Cancer* **2006**, *6*, 764–775.
- (114) Bromme, D.; Lecaille, F. Cathepsin K for Osteoporosis and Potential Off-Target Effects. *Expert Opin. Investig. Drugs* **2011**, *18*, 585–600.
- (115) Fang, J.; Zhao, L.; Deng, J.; Chen, L.; Li, Y.; Cui, H.; Zuo, Z.; Wang, X.; Deng, H. Inflammatory Responses and Inflammation-Associated Diseases in Organs. *Oncotarget* **2017**, *9*, 7204–7218.
- (116) Sun, X.; Luo, Y.; Huang, L.; Yu, B. Y.; Tian, J. A Peptide-Decorated and Curcumin-Loaded Mesoporous Silica Nanomedicine for Effectively Overcoming Multidrug Resistance in Cancer Cells. *RSC Adv.* **2017**, *7*, 16401–16409.
- (117) de la Torre, C.; Mondragón, L.; Coll, C.; Sancenón, F.; Marcos, M. D.; Martínez-Mañez, R.; Amorós, P.; Pérez-Payá, E.; Orzáez, M. Cathepsin-B Induced Controlled Release from Peptide-Capped Mesoporous Silica Nanoparticles. *Chem. Eur. J.* **2014**, *20*, 15309–15314.
- (118) Hu, Y.; Zhou, J.; Liu, J.; Ding, X.; Li, J.; Cai, K.; Liu, Y.; Hou, C.; Luo, Z.; Dai, L. Enzyme Responsive Drug Delivery System Based on Mesoporous Silica Nanoparticles for Tumor Therapy *in vivo*. *Nanotechnology* **2015**, *26*, 145102–145116.
- (119) Liu, J.; Zhang, B.; Luo, Z.; Ding, X.; Li, J.; Dai, L.; Zhou, J.; Zhao, X.; Ye, J.; Cai, K. Enzyme Responsive Mesoporous Silica Nanoparticles for Targeted Tumor Therapy *in vitro* and *in vivo*. *Nanoscale* **2015**, *7*, 3614–3626.
- (120) Liu, Y.; Ding, X.; Li, J.; Luo, Z.; Hu, Y.; Liu, J.; Dai, L.; Zhou, J.; Hou, C.; Cai, K. Enzyme Responsive Drug Delivery System Based on Mesoporous Silica Nanoparticles for Tumor Therapy *in vivo*. *Nanotechnology* **2015**, *26*, 145102–145116.
- (121) Villaverde, G.; Nairi, V.; Baeza, A.; Vallet-Regí, M. Double Sequential Encrypted Targeting Sequence: A New Concept for Bone Cancer Treatment. *Chem. Eur. J.* **2017**, *23*, 7174–7179.
- (122) Yuan, Z.-F.; Chen, W.-H.; Zhang, X.-Z.; Zhuo, R.-X.; Zhang, J.; Wang, Y.; Cheng, S.-X.; Luo, G.-F. Multifunctional Envelope-Type Mesoporous Silica Nanoparticles for Tumor-Triggered Targeting Drug Delivery. *J. Am. Chem. Soc.* **2013**, *135*, 5068–5073.
- (123) Gisbert-Garzarán, M.; Manzano, M.; Vallet-Regí, M. pH-Responsive Mesoporous Silica and Carbon Nanoparticles for Drug Delivery. *Bioengineering* **2017**, *4*.
- (124) Yuan, F. L.; Xu, M. H.; Li, X.; Xinlong, H.; Fang, W.; Dong, J. The Roles of Acidosis in Osteoclast Biology. *Front. Physiol.* **2016**, *7*, 1–8.
- (125) Pourjavadi, A.; Mazaheri Tehrani, Z.; Jokar, S. Chitosan Based Supramolecular Polypseudorotaxane as a pH-Responsive Polymer and Their Hybridization with Mesoporous Silica-Coated Magnetic Graphene Oxide for Triggered Anticancer Drug Delivery. *Polym.* **2015**, *76*, 52–61.

- (126) Choi, S. R.; Jang, D.-J.; Kim, S.; An, S.; Lee, J.; Oh, E.; Kim, J. Polymer-Coated Spherical Mesoporous Silica for pH-Controlled Delivery of Insulin. *J. Mater. Chem. B* **2014**, *2*, 616–619.
- (127) Han, J.; Sun, J.; Bai, S.; Panezai, H.; Jin, X.; Wu, X. “Graft to” Synthesis and Ibuprofen-Loading Performance of pH-Sensitive PMAA-Silica Hybrid Nanoparticles with Controlled Bimodal Mesopores. *J. Pharm. Sci.* **2015**, *104*, 4299–4306.
- (128) Muhammad, F.; Guo, M.; Qi, W.; Sun, F.; Wang, A.; Guo, Y.; Zhu, G. pH-Triggered Controlled Drug Release from Mesoporous Silica Nanoparticles via Intracellular Dissolution of ZnO Nanolids. *J. Am. Chem. Soc.* **2011**, *133*, 8778–8781.
- (129) Wu, S.; Huang, X.; Du, X. pH- and Redox-Triggered Synergistic Controlled Release of a ZnO-Gated Hollow Mesoporous Silica Drug Delivery System. *J. Mater. Chem. B* **2015**, *3*, 1426–1432.
- (130) Zhang, J.; Wu, D.; Li, M. F.; Feng, J. Multifunctional Mesoporous Silica Nanoparticles Based on Charge-Reversal Plug-Gate Nanovalves and Acid-Decomposable ZnO Quantum Dots for Intracellular Drug Delivery. *ACS Appl. Mater. Interfaces* **2015**, *7*, 26666–26673.
- (131) Chen, T.; Yu, H.; Yang, N.; Wang, M.; Ding, C.; Fu, J. Graphene Quantum Dot-Capped Mesoporous Silica Nanoparticles through an Acid-Cleavable Acetal Bond for Intracellular Drug Delivery and Imaging. *J. Mater. Chem. B* **2014**, *2*, 4979–4982.
- (132) Dai, L.; Zhang, Q.; Shen, X.; Sun, Q.; Mu, C.; Gu, H.; Cai, K. PH-Responsive Nanocontainer Based on Hydrazone-Bearing Hollow Silica Nanoparticles for Targeting Tumor Therapy. *J. Mater. Chem. B* **2016**, *4*, 4594–4604.
- (133) Yan, Y.; Fu, J.; Liu, X.; Wang, T.; Lu, X. Acid-Responsive Intracellular Doxorubicin Release from Click Chemistry Functionalized Mesoporous Silica Nanoparticles. *RSC Adv.* **2015**, *5*, 30640–30646.
- (134) Bansal, A.; Celeste Simon, M. Glutathione Metabolism in Cancer Progression and Treatment Resistance. *J. Cell Biol.* **2018**, *217*, 2291–2298.
- (135) Balendiran, G. K.; Dabur, R.; Fraser, D. The Role of Glutathione in Cancer. *Cell Biochem. Funct.* **2004**, *22*, 343–352.
- (136) Cui, Y.; Dong, H.; Cai, X.; Wang, D.; Li, Y. Mesoporous Silica Nanoparticles Capped with Disulfide-Linked PEG Gatekeepers for Glutathione-Mediated Controlled Release. *ACS Appl. Mater. Interfaces* **2012**, *4*, 3177–3183.
- (137) Chang, B.; Chen, D.; Wang, Y.; Chen, Y.; Jiao, Y.; Sha, X.; Yang, W. Bioresponsive Controlled Drug Release Based on Mesoporous Silica Nanoparticles Coated with Reductively Sheddable Polymer Shell. *Chem. Mater.* **2013**, *25*, 574–585.
- (138) Sun, L.; Zhang, X.; Wu, Z.; Zheng, C.; Li, C. Oral Glucose- and pH-Sensitive Nanocarriers for Simulating Insulin Release *in vivo*. *Polym. Chem.* **2014**, *5*, 1999–2009.
- (139) Brede, C.; Labhasetwar, V. Applications of Nanoparticles in the Detection and

- Treatment of Kidney Diseases. *Adv. Chronic Kidney Dis.* **2013**, *20*, 454–465.
- (140) Azarmi, S.; Roa, W. H.; Löbenberg, R. Targeted Delivery of Nanoparticles for the Treatment of Lung Diseases. *Adv. Drug Deliv. Rev.* **2008**, *60*, 863–875.
- (141) World Health Organization. Cancer. <https://www.who.int/news-room/fact-sheets/detail/cancer>.
- (142) Wyld, L.; Audisio, R. A.; Poston, G. J. The Evolution of Cancer Surgery and Future Perspectives. *Nat. Rev. Clin. Oncol.* **2015**, *12*, 115–124.
- (143) Baskar, R.; Lee, K. A.; Yeo, R.; Yeoh, K.-W. Cancer and Radiation Therapy: Current Advances and Future Directions. *Int. J. Med. Sci.* **2012**, *9*, 193–199.
- (144) Chari, R. V. J. Targeted Cancer Therapy: Conferring Specificity to Cytotoxic Drugs. *Acc. Chem. Res.* **2008**, *39*, 98–107.
- (145) Manzano, M.; Vallet-Regí, M. New Developments in Ordered Mesoporous Materials for Drug Delivery. *J. Mater. Chem.* **2010**, *20*, 5593–5604.
- (146) Baeza, A.; Colilla, M.; Vallet-Regí, M. Advances in Mesoporous Silica Nanoparticles for Targeted Stimuli-Responsive Drug Delivery. *Expert Opin. Drug Deliv.* **2015**, *12*, 319–337.
- (147) Matsumura, Y.; Maeda, H. A New Concept for Macromolecular Therapeutics in Cancer Chemotherapy: Mechanism of Tumoritropic Accumulation of Proteins and the Antitumor Agent Smancs. *Cancer Res.* **1986**, *46*, 6387–6392.
- (148) Fang, J.; Nakamura, H.; Maeda, H. The EPR Effect: Unique Features of Tumor Blood Vessels for Drug Delivery, Factors Involved, and Limitations and Augmentation of the Effect. *Adv. Drug Deliv. Rev.* **2011**, *63*, 136–151.
- (149) Natfji, A. A.; Ravishankar, D.; Osborn, H. M. I.; Greco, F. Parameters Affecting the Enhanced Permeability and Retention Effect: The Need for Patient Selection. *J. Pharm. Sci.* **2017**, *106*, 3179–3187.
- (150) Blanco, E.; Shen, H.; Ferrari, M. Principles of Nanoparticle Design for Overcoming Biological Barriers to Drug Delivery. *Nat. Biotechnol.* **2015**, *33*, 941–951.
- (151) Izquierdo-Barba, I.; Colilla, M.; Vallet-Regí, M. Zwitterionic Ceramics for Biomedical Applications. *Acta Biomater.* **2016**, *40*, 201–211.
- (152) Schlapschy, M.; Binder, U.; Börger, C.; Theobald, I.; Wachinger, K.; Kisling, S.; Haller, D.; Skerra, A. PASylation: A Biological Alternative to PEGylation for Extending the Plasma Half-Life of Pharmaceutically Active Proteins. *Protein Eng. Des. Sel.* **2013**, *26*, 489–501.
- (153) Jokerst, J. V.; Lobovkina, T.; Zare, R. N.; Gambhir, S. S. Nanoparticle PEGylation for Imaging and Therapy. *Nanomedicine* **2011**, *6*, 715–728.
- (154) Liu, X.; Jiang, J.; Ji, Y.; Lu, J.; Chan, R.; Meng, H. Targeted Drug Delivery Using IRGD Peptide for Solid Cancer Treatment. *Mol. Syst. Des. Eng.* **2017**, *2*, 370–379.
- (155) Paris, J. L.; De la Torre, P.; Manzano, M.; Cabañas, M. V.; Flores, A. I.; Vallet-Regí, M. Decidua-Derived Mesenchymal Stem Cells as Carriers of Mesoporous Silica Nanoparticles. *In vitro* and *in vivo* Evaluation on Mammary Tumors. *Acta*

- Biomater.* **2016**, *33*, 275–282.
- (156) Zhou, L.; Wang, H.; Li, Y. Stimuli-Responsive Nanomedicines for Overcoming Cancer Multidrug Resistance. *Theranostics* **2018**, *8*, 1059–1074.
- (157) Villegas, M. R.; Baeza, A.; Vallet-Regí, M. Hybrid Collagenase Nanocapsules for Enhanced Nanocarrier Penetration in Tumoral Tissues. *ACS Appl. Mater. Interfaces* **2015**, *7*, 24075–24081.
- (158) Paris, J. L.; Mannaris, C.; Cabañas, M. V.; Carlisle, R.; Manzano, M.; Vallet-Regí, M.; Coussios, C. C. Ultrasound-Mediated Cavitation-Enhanced Extravasation of Mesoporous Silica Nanoparticles for Controlled-Release Drug Delivery. *Chem. Eng. J.* **2018**, *340*, 2–8.
- (159) Smith, S. A.; Selby, L. I.; Johnston, A. P. R.; Such, G. K. The Endosomal Escape of Nanoparticles: Toward More Efficient Cellular Delivery. *Bioconjug. Chem.* **2018**, *30*, 263–272.
- (160) Hassan, S.; Prakash, G.; Bal, A.; Saghazadeh, S.; Shrike, Y.; Khademhosseini, A. Evolution and Clinical Translation of Drug Delivery Nanomaterials. *Nano Today* **2017**, *15*, 91–106.







## Chapter 2

# Stimuli-Responsive Drug Delivery

*El éxito no es definitivo, el fracaso no es fatal: lo que realmente cuenta es el valor para continuar.*

*Winston Churchill*



## 2.1. Introduction

### 2.1.1. Aims

The objective of this chapter was to design and produce different stimuli-responsive nanocarriers based on mesoporous nanoparticles within the frame of the European Project “MOZART” (“*Mesoporous matrices for localized pH-triggered release of the therapeutic ions and drugs*”). According to MOZART proposal, the objective of project can be stated as follows:

*“The MOZART project involves 8 different countries and 11 partners, 5 high tech SMEs and 6 top European Universities. The concept behind MOZART is to develop a library of inorganic nanomatrices to be used as smart platforms for effective, non-invasive and highly targeted therapies to treat delayed bone healing and non-healing chronic skin wounds, which are both characterized by an inflammation and often infection. Mesoporous therapeutic glasses, doped with selected ions, will be synthesized and then loaded with the chosen payload. Ordered mesoporous carbons will also be manufactured to host a wide range of biomolecules and higher payload. As in an orchestra, where the integration among the different participants allows a harmonious symphony to be created, in MOZART the synergistic release of ions and drugs will be directed to achieve a radically improved therapeutic effect. Mozart aims to translate these new and innovative medical products into the clinic and market for the benefit of the patients and the industrial healthcare sector in Europe.”*

In particular, the overall objective of this project was to engineer a stimuli-responsive gatekeeper, graft it to different mesoporous carriers and evaluate its on-demand drug delivery capabilities. The proposal considered variations in pH characteristic of certain scenarios to trigger the release. In this way, the ions and drugs would only leave the matrix in the diseased site, avoiding nonspecific and premature release.

The use of self-immolative polymers (SIPs) as gatekeepers for those nanomatrices was explored. These polymers are interesting because they are able to disassemble into their functional units upon application of a particular stimulus, such as pH. When grafted to the nanomatrices, they would be stable at physiological pH, hampering premature release. However, after a pH drop the chain would self-immolate, opening the pores and leading to the cargo release. Then, the **first objective** was to synthesize a polymeric chain

showing this self-immolative behavior and bearing an acid-responsive trigger to start the disassembling in these scenarios.

The grafting of the self-immolative polymers to the particles was initially optimized for MSNs and tested at pH 5. In this sense, many pH-responsive systems reported as anticancer nanotechnological approximations are able to hamper the drug release at physiological pH and trigger it at acid pH, as this system did. Therefore, translating the above-mentioned self-immolative technology to the design of pH-responsive nanocarriers applied to cancer treatment seemed appropriate. In consequence, the **second objective** was to apply the self-immolative technology to MSNs to design a system with anticancer application. This study comprised the evaluation of their pH-responsive capabilities as well as their preliminary biological performance.

As a result of the collaboration among some of the MOZART partners, the possibility of using mesoporous carbon nanomatrices to engineer a pH-responsive solution for cancer treatment was explored. In this sense, the **third objective** was to apply the self-immolative technology to mesoporous carbon nanoparticles (MCNs). In particular, these materials showed outstanding textural properties and the initial task was to demonstrate that they could load significantly higher amounts of molecules than the well-studied MSNs. In this way, these nanomatrices would constitute a step ahead in the design of anticancer formulations. Then, the self-immolative technology was applied and their pH-responsiveness evaluated. In view of the promising results, the materials were subjected to further biological experiments, including the study of their performance *in vivo*, as it will be described in this chapter.

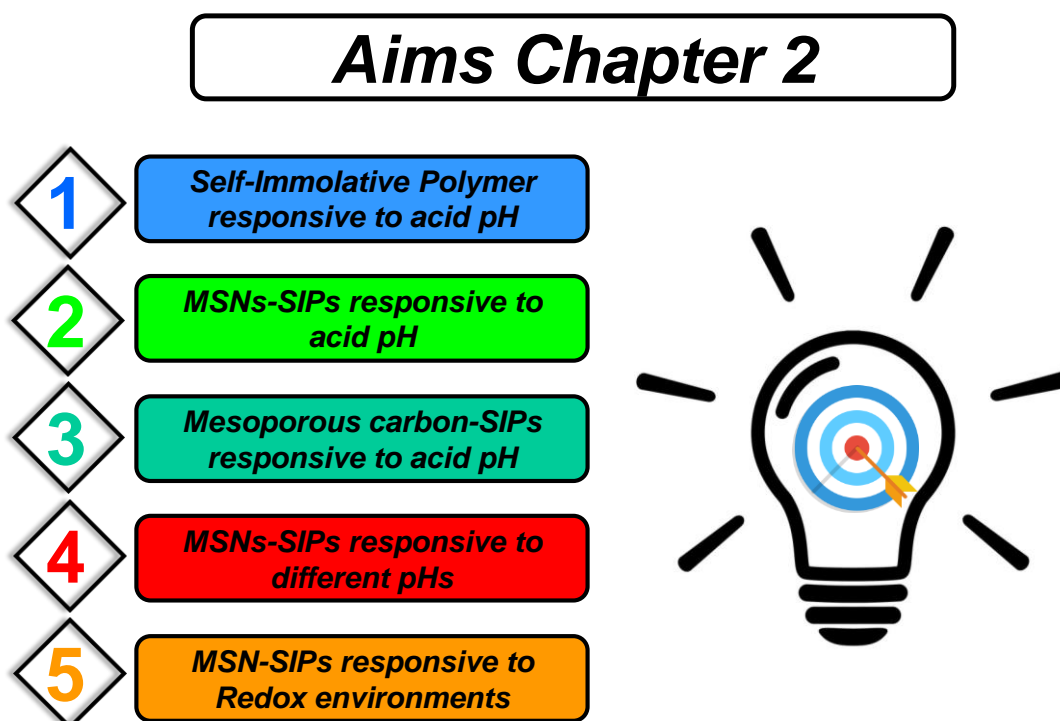
The proposal considered the use of acid-responsive self-immolative polymers to seal the pore entrances. In consequence, the **fourth objective** was to functionalize the different nanomatrices provided by the consortium with this polymeric coating and test their pH-responsive behavior at acid pH.

One of the initial tasks of the MOZART consortium was to provide an accurate pH value for the above-mentioned scenarios (delayed bone healing and non-healing chronic skin wounds) using *in vivo* animal models. Initially, the proposal considered the use of acid pH as trigger. However, the *in vivo* experiments demonstrated the existence of several pHs, spanning from acid to basic values, confronting the initial hypothesis of a discrete pH value as trigger. Nonetheless, two pH values, 6.8 and 8, seemed to recurrently

be present in the diseased models. In consequence, the polymer above-described had to be modified, so the **fifth objective** was the development of alternative triggers able to initiate the self-immolation and trigger the release at the new target pH values.

The possibility of using an alternative and relevant stimulus found in cancer scenarios to trigger the release was explored once all the requirements of MOZART were fulfilled. In this sense, the **sixth objective** was to develop a self-immolative gatekeeper sensitive to high concentrations of redox species, which are known to be found within tumoral cells. This study comprised the development of a novel redox-responsive self-immolative linker. Its grafting to the surface of MSNs was optimized and their redox-responsive behavior evaluated.

In summary, this chapter will provide a detailed introduction to the different topics above-described, *i.e.*, pH-responsive drug delivery, redox-responsive drug delivery and self-immolative technology. Then, the methodology and results derived from the application of the self-immolative technology for the design of anticancer formulations will be described. Finally, the results derived from the MOZART project will be presented and discussed.



Scheme 2.1. Schematic representation of the aims of Chapter 2.

## 2.1.2. pH-responsive mesoporous nanoparticles

The different pHs that can be found throughout the organism provide a useful tool for the design of stimuli-responsive drug delivery nanocarriers. These pH-responsive systems are able to avoid premature drug release at the bloodstream pH while promoting it once in the tumoral area or inside particular organelles within the tumoral cells.

In this section the biological rationale behind the use of the differences in pH as a relevant biomarker will be presented. Then, different approximations for the design of pH-responsive mesoporous nanoparticles will be introduced, including the use of (1) electrostatic interactions between the mesoporous matrix and the payload, (2) acid-labile bonds as linkers between the nanocarriers and the gatekeepers and (3) several supramolecular structures employed as pore capping agents.

### 2.1.2.1. The role of pH in drug delivery

The maintenance of the different physiological pHs along the body is of vital importance for the organism to keep alive. For instance, variations in pH of body fluids within 7.35 and 7.45 can be corrected, but greater alterations may lead to acidosis or alkalosis events that may even cause death. However, there are particular areas in the body or some diseases that present values that deviate from physiological pH. In particular, the pH throughout the digestive system and within some cellular compartments differ from that of the bloodstream. Moreover, the pH found in the extracellular tumor tissues is also slightly different as a consequence of the special metabolism of tumor cells.

#### ❖ *Digestive system*

Due to the various conditions needed for the digestion of the different nutrients, pH is not kept constant throughout the organs of the gastrointestinal tract. This fact has been exploited for the design of oral drug delivery carriers.<sup>1,2</sup> In particular, the pH in the stomach is between 1–2, and reaches pH 7–8 after leaving it. In the stomach the pH is lowered by the secretion of protons by the parietal cells, which can be suppressed by different hormones. As a protective mechanism, the epithelium secretes bicarbonate ions to regulate the pH. After leaving the stomach, the bile salts are responsible for increasing the pH up to 7-8.<sup>3</sup>

❖ *Extracellular tumor microenvironment*

In presence of  $O_2$ , nonproliferating healthy cells, *i.e.*, differentiated tissue, metabolize glucose to  $CO_2$  through the highly efficient oxidative phosphorylation process (Figure 2.1a, left). Under anaerobic conditions, normal cells can also produce energy through anaerobic glycolysis, leading to the production of lactate (Figure 2.1a, right). On the contrary, most cancer cells, and any proliferating cell in general, produce large amounts of lactate regardless of the oxygen supply through the aerobic glycolysis process (Figure 2.1b). The generation of lactate through this process is called *Warburg effect*, and is responsible for the slight acidification of the extracellular tumoral matrix.<sup>4</sup>

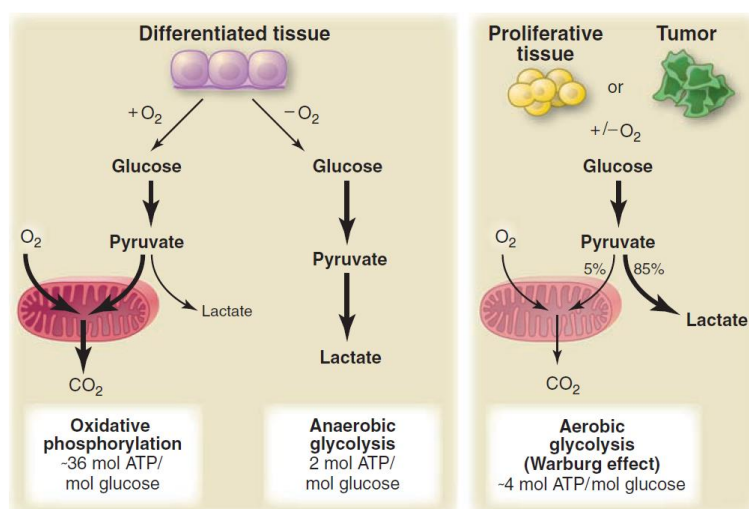


**Figure 2.1.** Schematic representation of the different mechanisms of energy production by normal nonproliferating cells (differentiated tissue) *vs* normal proliferating and cancer cells. a) Healthy nonproliferating cells efficiently produce energy from glucose in the presence of oxygen *via* oxidative phosphorylation (left) or less efficiently *via* anaerobic glycolysis when no oxygen available (right). b) Cancer and healthy proliferative cells almost always produce their energy *via* aerobic glycolysis, regardless of the presence of oxygen, leading to the acidification of the extracellular tumoral matrix. Adapted from Ref 4 with permission of AAAS.

Those large amounts of lactate are secreted outside the cells, leading to the acidification of the extracellular tumoral matrix. In addition, the excess of  $CO_2$  generated as a by-product can also contribute to the extracellular acidification thanks to the activity of the carbonic anhydrase. This acidification has a major role in cancer development: (1) it enhances tumor cell migration and radioresistance; (2) it mediates chronic inflammation in tumor microenvironments by increasing interleukin production by T-cells and macrophages and (3) it disturbs the metabolism and function of T-cells.<sup>5</sup> This decrease in the extracellular pH has been quantified to be within the range 6.5-7.<sup>6-8</sup>



### ❖ *Intracellular pH*

There are some compartments and organelles inside all cells that show slight differences with respect to the near neutral pH found in the cytoplasm. Those differences can be used to design smart pH-responsive systems.

Cells internalize substances through different mechanisms, being the endocytic pathway one of them. Briefly, the cell membrane creates a vesicle around these substances that is subsequently transported inside the cell. This vesicle matures from the early endosomes to the late endosomes and eventually to the lysosomes. The function of these organelles is the degradation of compounds that are no longer useful for the cell. For that reason, these compartments present acid pH. In particular, pH becomes more acidic as the substances go from the endocytic vesicles (pH 6.5) to the lysosomes (pH 4.5-5). The different organelles have an intrinsic capacity to buffer slight changes, which is provided by the weak acids and bases present there. However, this buffer is finite and there must be another mechanism to control the pH of each compartment. That precise regulation of pH is provided by the presence of proton-pumping ATPases. The injection of protons by these pumps together with the existence of channels capable of introducing negative ions lead to the final pH of each organelle.<sup>9</sup>

These differences in pH can be employed for the design of stimuli-responsive mesoporous materials sensitive to pH variations. In this way, the drugs would be confined within the mesopores at physiological pH and they would only be released upon a change in the pH value. The most common approximations that can be found in the literature fall into three types of strategies: electrostatic host-guest interactions, acid-labile bonds and supramolecular capping agents.

#### **2.1.2.2. Host-guest interactions**

The use of the electrostatic interactions between the functional groups present in the mesopores and those in the payload constitutes the simplest approximation to engineer pH-responsive nanocarriers. In this way, at physiological pH the molecules remain retained inside the pores, avoiding premature release. However, when pH changes the electrostatic interactions weaken, leading to the drug release.

These host-guest interactions have been employed to induce the pH-responsive release of several drugs, including ibuprofen, 5-fluoracil, mitoxantrone, methotrexate, sulfasalazine or doxorubicin.<sup>1,10-12</sup> In particular, doxorubicin (DOX), which is a cationic

drug widely used for more than 30 years to treat many types of tumors,<sup>13</sup> has been recurrently loaded as model drug in mesoporous materials.

The storage in MSNs takes place through the electrostatic interaction between DOX and the silanol groups of the nanoparticles. The silanol groups of MSNs are deprotonated at physiological pH and the amino group of DOX is positively charged, remaining electrostatically attracted. However, at acid pH the silanol groups protonate and, consequently, repulsion interactions appear, leading to the drug release (Figure 2.2).

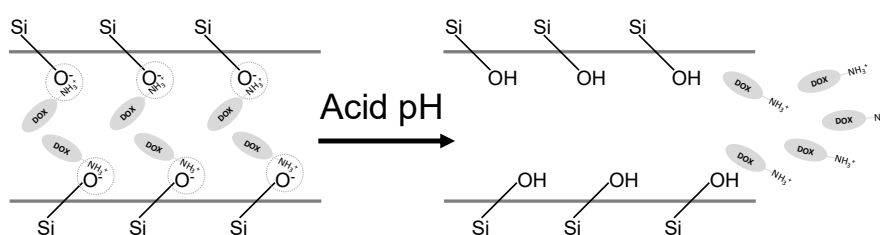


**Figure 2.2.** Example of DOX storage and release from the mesopores of MSNs through host-guest interactions. At physiological pH, DOX interacts with the deprotonated silanol groups (depicted by the dotted line). However, when the pH drops, silanol groups protonate and these interactions weaken, leading to the drug release.

When MCNs are used, DOX is retained in the mesopores through the  $\pi$ - $\pi$  stacking interactions, which are non-covalent hydrophobic interactions between aromatic structures due to the  $sp^2$  hybridization. In this way, at neutral pH the aromatic rings of DOX are attracted by the aromatic framework of the carbon nanocarriers. However, a decrease in pH leads to an increase in the hydrophilicity of DOX, thereby reducing the strength of the  $\pi$ - $\pi$  interactions with the surface. In this way, the  $\pi$ - $\pi$  interactions are disrupted, triggering the drug release.<sup>14</sup>

### 2.1.2.3. Acid-labile bonds

Labile bonds are interesting for drug delivery as they can remain stable until some specific event takes place. In particular, there are several types of acid-responsive bonds that can be used to exploit the differences in pH within the body. In this way, it is possible to synthesize mesoporous nanoparticles with smart pH-responsive behavior. Some representative examples of pH-responsive linkers are shown in Table 2.1.

**Table 2.1.** Acid-labile bonds that have been used in the design of pH-responsive mesoporous nanoparticles.

Bond	pH-Responsive Mechanism		References	
Hydrazone		$\longrightarrow$		15–22
Acetal		$\longrightarrow$		23–28
Imine		$\longrightarrow$		29–35
Ester-based		$\longrightarrow$		36–45
Citraconic		$\longrightarrow$		46,47
Coordination bonds	The host-metal-guest interaction weakens at acid pH, leading to the release of either the drug or the metal ion and the drug		48–54	

❖ *Hydrazone bond*

Hydrazone bonds have been widely explored in the design of prodrugs, which are masked forms of active drugs that remain inactive until a particular event takes place. In this way, the prodrugs would remain inactive at physiological pH, undergoing fast hydrolysis at pH 5.<sup>55,56</sup> In this sense, it is possible to decorate the surface of MSNs with hydrazine groups to then add active drugs to these groups to yield a prodrug-like nanocarrier. In this way, the drugs would remain inactive at physiological pH and they would recover their activity at the lysosomal acid pH, leading to the drug release. Examples include the conjugation of cisplatin<sup>15</sup> or doxorubicin,<sup>16,17</sup> either on the external surface or within the mesopores (Figure 2.3).

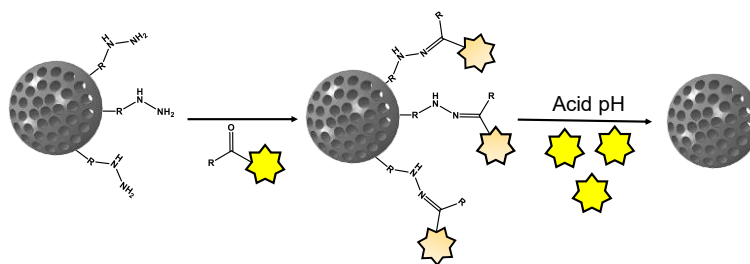


**Figure 2.3.** Example of MSNs decorated with a prodrug *via* hydrazone bond on the surface. In this case, at neutral pH the inactive drug (represented by the orange star) remains covalently attached to the silica matrix. However, the acid environment of the lysosomes hydrolyzes the bond and the active drug (represented by the yellow star) is released.

In addition, this approach can be used to engineer labile gatekeepers. In this way, the pore entrances remain closed at physiological pH. However, at acid pH the bond suffers hydrolysis and the gatekeeper leaves the pores open, leading to the drug release. Examples

are the use of gold nanoparticles<sup>19,20</sup> or hyaluronic acid<sup>22</sup> as gatekeepers *via* formation of a hydrazone bond.

❖ *Acetal bond*

The acetal bond is stable at physiological pH and hydrolyzes at acid pH. Similarly to the previous case, it is useful for the design of prodrug-functionalized mesoporous carriers.<sup>23</sup> In addition, it also finds application in the design of acid-labile gatekeepers able to be cleaved only within the cells, leading to the drug release. Examples of gatekeepers grafted *via* acetal bond are small metal<sup>24,28</sup> and carbon<sup>25</sup> nanoparticles or polymeric coatings.<sup>26,27</sup>

❖ *Imine-based bond*

Imine bonds are condensation products of primary amines with carbonyl compounds that hydrolyze at acid pH. In particular, benzoic-imine bonds have attracted much attention because they hydrolyze at pH *ca.* 6.8 (*i.e.*, extracellular tumor pH).<sup>57</sup> For such reason, imine bonds have been applied to design mesoporous nanoparticles able to overcome the so-called *PEG dilemma*. This phenomenon is consequence of two facts: (1) PEGylation of nanocarriers increases their circulation time and (2) the presence of PEG chain difficulties the cellular uptake owing to the steric hindrance and the hydration layer created by the PEG chains.<sup>58</sup> Figure 2.4 represents the behavior of these nanocarriers. The PEG layers are attached to the surface *via* benzoic imine bonds, that remain stable at physiological pH. However, at the acidic pH of the extracellular tumoral matrix the bond is cleaved and the positive charge of the nanoparticle surface is exposed, increasing the uptake.<sup>30,31</sup>

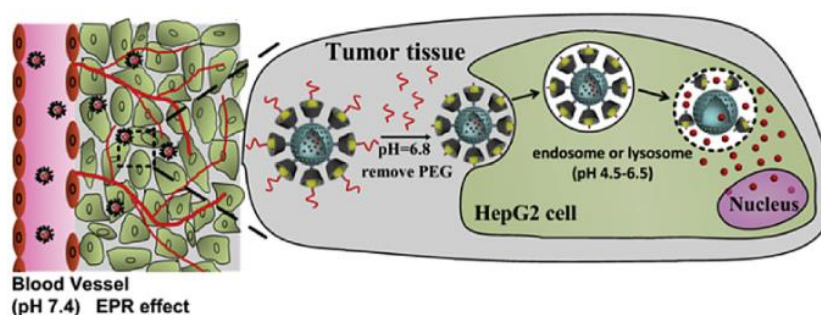


**Figure 2.4.** Cleavage of a benzoic-imine bond to overcome the PEG dilemma. At neutral pH the PEG chain remain attached to the surface, avoiding protein adsorption. However, the slightly acidic pH found in the extracellular tumoral matrix cleaves the imine bond, exposing a positive charge on the nanoparticle surface that enhances the cellular uptake. Adapted from Ref 30 with permission of Elsevier.

Imine bond-based compounds are also useful as cross-linking agents. For instance, it is possible to design pH-sensitive protective layers on the nanocarriers by reacting amine-

containing compounds with carbonyl-containing macromolecules, such as chitosan with dialdehyde starch,<sup>32</sup> dextrin with tetraethylenepentamine<sup>33</sup> or glutaraldehyde with polyethyleneimine.<sup>34</sup>

❖ *Ester-based bond*

Ester-based pH-sensitive bonds find broad application as linkers between the nanocarriers and the gatekeepers, although it is possible to use polyesters as pore blockers.<sup>36</sup> In particular, the most employed ester is the boronate ester bond, which is known to undergo reversible hydrolysis at acid pH.<sup>59</sup> This behavior allows to design pulsatile systems where gatekeepers can open and close the pores upon pH changes. Examples of such gatekeepers are small Au or Fe<sub>3</sub>O<sub>4</sub> nanoparticles,<sup>38,39</sup> lactobionic acid<sup>40</sup> and β-CD.<sup>44,45</sup>

❖ *Citraconic-based bonds*

Citraconic anhydride is usually reacted with amines to yield a pH-responsive amide. This bond is stable at physiological pH but undergoes rapid hydrolysis upon a drop in pH. In this sense, this pH-responsive bond also finds application in the design of prodrug-like nanocarriers, where the release would be triggered by the acid pH found in the tumors.<sup>46</sup> In addition, it can be employed to mask the positive charge of cell-penetrating peptides. In this way, the nonspecific interactions with healthy cells are minimized. However, the acid pH found in the tumoral matrix cleaves the bond, exposing the positive charge of the peptide again to lead to enhanced nanoparticle uptake by tumoral cells.<sup>47</sup>

❖ *Coordination bonds*

This approach is based on loading metal ions within the mesopores. The ions can form stable coordination bonds with the mesoporous matrix (host) and with loaded drugs (guests). However, when the pH decreases there are competition events and either the host-metal or the metal-guest may be cleaved. In this way, it is possible to modify the functional groups of the nanoparticles to tune the host-metal-guest interactions (Figure 2.5).<sup>60</sup>

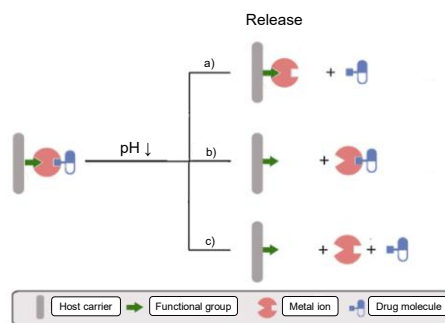


**Figure 2.5.** Schematic representation of the release of guest molecules upon cleavage of coordination bonds. Depending of strength of the interactions, the drug (a), the metal coordinated to the drug (b) or both independent elements (c) can leave the mesopores. This strategy may enhance the therapeutic effect of the drugs due to the presence of therapeutic ions. Adapted from Ref 60 with permission of Elsevier.

Nanoparticles are usually functionalized with amino-based groups that can coordinate with the metal ions, including  $\text{Zn}^{2+}$ ,  $\text{Fe}^{3+}$ ,  $\text{Co}^{+2}$ ,  $\text{In}^{3+}$  or  $\text{Cu}^{2+}$ , among others.<sup>48–54</sup> Depending on the strength of the interactions, it is possible to deliver a simple drug (Figure 2.5a) or to deliver both drugs and ions (Figure 2.5c), which are known to have therapeutic properties.<sup>61</sup>

#### 2.1.2.4. Supramolecular pore-capping agents

##### ❖ *Small degradable nanoparticles*

In the previous section, some examples of gatekeepers based on small nondegradable nanoparticles grafted to MSNs *via* different acid-cleavable bonds have been described. In addition to this approximation, it is also possible to close the pore entrances with some types of small nanoparticles that degrade in acidic environments. In this way, the gatekeepers close the pores at physiological pH, but degrade when pH decreases, opening the pores and leading to the drug release.

ZnO quantum dots are known to be stable at physiological pH, but rapidly dissolve at pH below 5. An extended strategy is using them as gatekeepers to close the mesopores. At physiological pH the quantum dots are stable and keep the pore entrances closed. However, they rapidly degrade at lysosomal pH, leading to the drug release and the generation of cytotoxic  $\text{Zn}^{2+}$  ions as a by-product of the dissolution.<sup>62–66</sup> In addition, MnO nanoparticles can also be used as gatekeepers, leading in this case to manganese ions as degradation by-products that can be used for imaging purposes.<sup>67,68</sup>

##### ❖ *Cyclodextrins*

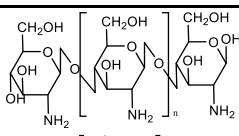
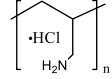
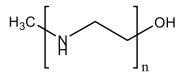
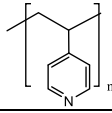
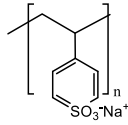
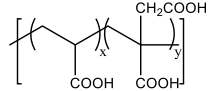
Cyclodextrins (CD) are water-soluble and biocompatible macromolecules obtained from the enzymatic degradation of starch. They have a hydrophilic outer surface and a

hydrophobic cavity that allows the complexation of various structures inside. In particular,  $\beta$ -CD are useful in drug delivery because of their convenient cavity size, which is able to block the pore entrances.<sup>69</sup>  $\beta$ -CD-based drug delivery systems usually present an amine-based stalk covalently attached to the surface of the nanoparticles that interacts electrostatically with the hydrophobic cavity of a  $\beta$ -CD. At neutral pH, the stalk and the cap interact tightly, preventing the drug release. However, at lower pH the affinity between the stalk and the cap decreases, opening the pores and allowing the cargo release.<sup>70,71</sup> In addition, it is also possible to use complementary base pairs to control the interaction of the  $\beta$ -CD gates with the surface.<sup>72</sup>

#### ❖ Polyelectrolytes

Polyelectrolytes are polymers that have ionizable groups along the polymeric chain. A smart approximation is to close the pore entrances with these polymers through electrostatic interactions with the surface of the nanoparticle. In this way, upon a change in pH electrostatic repulsion forces will appear, opening the pores and allowing the release. Cationic or anionic polymers could be used depending on the electric charge of the particle. Table 2.2 summarizes some of the most used polyelectrolytes employed in the design of pH-responsive mesoporous nanocarriers.

**Table 2.2.** Polyelectrolytes most commonly used in the design of pH-responsive mesoporous nanocarriers through electrostatic interactions.

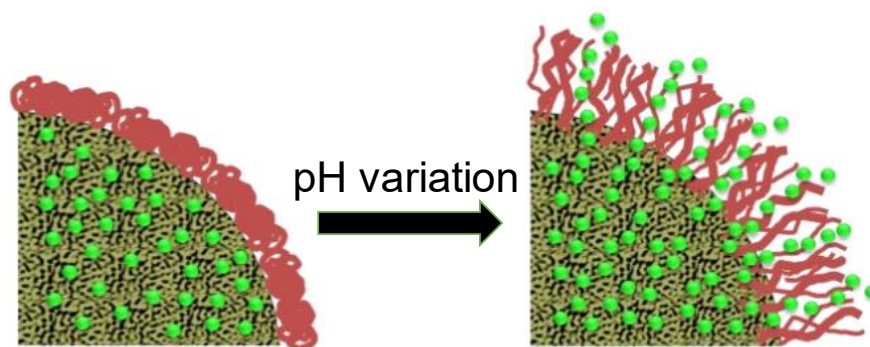
Polycation	Structure	References
Chitosan		73–76
Poly(allylamine hydrochloride)		77–79
Polyethyleneimine		80,81
Poly(vinyl pyridine)		82
Polyanion	Structure	References
Poly(styrene sulfonate)		79
Poly(acrylic acid-co-itaconic acid)		83

A common approach when using the polyelectrolytes depicted in Table 2.2 is their arrangement in multilayers. At neutral pH, the layers are close to each other, leading to a robust coating that prevents premature release. However, when the pH decreases, the interactions weaken, and the multilayer disassembles, allowing the payload release. Examples of such gatekeepers are the combination of chitosan with sodium alginate<sup>84,85</sup> or poly(allylamine hydrochloride) with poly(styrene sulfonate).<sup>77,86</sup>

It is also possible the coating of mesoporous carriers with only one type of polyelectrolyte. Depending on the charge of the nanoparticle surface, a specific polyelectrolyte can be used. In this sense, the most representative polyelectrolyte is chitosan. This polymer can be used to coat the surface because it swells reversibly at acid pH, leading to pulsatile systems.<sup>73,74,76,87</sup> Other representative polyelectrolytes used in this way are polyethyleneimine,<sup>80,81</sup> poly(vinyl pyridine),<sup>82</sup> poly(2-diethylamino ethyl methacrylate)<sup>88</sup> or the polyanionic poly(acrylic acid-co-itaconic acid).<sup>83</sup>

❖ *Polymers that undergo conformational changes*

Many polymers are able to change their conformation under pH variations. In general, the polymeric coating is collapsed on the surface at neutral pH, blocking the pore entrances. However, upon a variation in pH the polymers change their hydrophobicity and adopt an extended conformation, allowing the drug release (Figure 2.6).

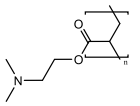
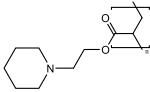
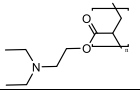
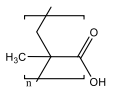
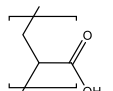


**Figure 2.6.** Collapse-to-extended phase transition of a polymer upon changes in pH that allows the drug release. At physiological pH the polymeric coating is collapsed on the surface. When the pH varies, the polymers undergo a conformational change to an extended conformation, opening the pores and allowing the release. Adapted from Ref 89 with permission of The Royal Society of Chemistry.

These polymers present ionizable groups that remain neutral at physiological pH and acquire net charge upon pH variations. This behavior leads to the appearance of repulsion forces among the chains appear, becoming hydrophilic and adopting an extended conformation that open the pores. Some of the polymers that behave in that way and have been used to engineer pH-responsive mesoporous nanocarriers are shown in Table 2.3.



**Table 2.3.** Phase-transition polymers usually employed as gatekeepers in pH-responsive mesoporous nanocarriers. PMAA: poly(methacrylic acid); PAA: poly(acrylic acid); PDMAEA: poly(2-(dimethylamino)ethyl acrylate); PPEMA: poly(2-(pentamethyleneimino)ethyl methacrylate); PDEAEMA: poly(2-(diethylamino)ethyl methacrylate).

Cationic Polymers	Structure	Refs
Polyamine-based	--	90–92
PDMAEA		93,94
PPEMA		95
PDEAEMA		96–99
Anionic Polymers	Structure	Refs
PMAA		100–106
PAA		107–112

Cationic polymers are composed of amine-containing monomers that remain neutral at physiological pH and protonate when the pH decreases below a certain value. This behavior can be exploited to design pH-responsive mesoporous nanoparticles that impede the release until the nanocarrier is internalized by the cell. Once there, the acidic organelles protonate the amine groups of the polymer chain, leading to an extended conformation that opens the pores and triggers the drug release. Examples of polymers showing this behavior are polyamine-based polymers/dendrimers,<sup>90–92</sup> amino-based acrylates and methacrylates,<sup>96,97</sup> poly(L-histidine)<sup>113</sup> and poly(n-vinyl pyridine).<sup>114–116</sup>

Anionic polymers are usually composed of monomers that contain either a carboxyl or a sulfonyl functional groups.<sup>117</sup> Poly(acrylic acid) (PAA) has pKa=3 and poly(methacrylic acid) (PMAA) has pKa=5–6. Consequently, at neutral pH these polymers are expected to show an extended conformation due to repulsion forces. For that reason, nanocarriers functionalized with these polymers would avoid the release at acid pH, being good candidates for oral drug delivery.<sup>107–109</sup>

The examples described so far involve the use of a single type of polymer. However, the copolymerization with other polymers provides polymeric coatings with an increased span of functionalities. For instance, the introduction of anionic polymers during the polymerization allows to tune the hydrophilic/hydrophobic behavior of the final

polymer.<sup>93,94</sup> In addition, it is also possible to copolymerize monomers showing different responsiveness to yield multiresponsive drug carriers.<sup>118–121</sup>

❖ *Biological macromolecules that undergo conformational changes*

Some biological macromolecules, such as small peptides, proteins or DNA, undergo reversible conformational changes when exposed to heat or changes in pH, ranging from a more compact structure to a scattered conformation. This behavior can be used to design pulsatile pH-responsive gates to close the pore entrances of mesoporous nanoparticles (Figure 2.7). In this sense, it is possible to design pH-responsive gates that open the pores when the pH decreases<sup>122–125</sup> or when the pH recovers the physiological value, being the latter case particularly useful for oral drug delivery.<sup>126,127</sup>

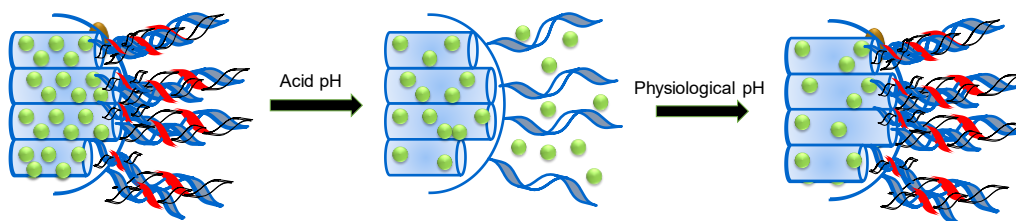


**Figure 2.7.** Reversible pH-responsive DNA strands as gatekeepers. At neutral pH the strands remain hybridized. However, these strands dehybridize when the pH drops, opening the pores and leading to the drug release. When the pH recovers the physiological value again, the strands hybridize again and close the pores, hampering the drug release.

### 2.1.3. Redox-responsive mesoporous nanoparticles

Redox species are molecules able to change the oxidation state of atoms of other molecules. In particular, the levels of this class of compounds in the cellular cytosol are significantly higher than those outside the cell membrane. In addition, the concentration of these molecules in tumoral cells is higher than that in healthy tissues. Therefore, it is possible to take advantage of these variations to design highly specific stimuli-responsive nanocarriers.

In this section the biological relevance of antioxidants will be stated. In addition, it will be described how the overexpression of those antioxidants can be employed to design organic and inorganic nanocarriers with redox stimuli-responsive behavior.

#### 2.1.3.1. The role of glutathione

Under physiological conditions, there is a balance between the production of ROS and that of antioxidants inside the cells. However, in cancer cells ROS levels are significantly increased due to some genetic mutations, an altered metabolism and mitochondrial

dysfunction. To counteract that, cancer cells present elevated levels of ROS scavengers that prevent tumor cells from suffering apoptosis.<sup>128</sup>

The most representative antioxidant molecule is the tripeptide GSH ( $\gamma$ -glutamyl-cysteinyl-glycine). It participates in the metabolism of many molecules, being a free-radical scavenger, playing a role in cell-cycle regulation or regulating protein function and gene expression, among others.<sup>129</sup> Interestingly, it also has an important role in cancer development and may contribute to increase the resistance to radio- and chemotherapy.<sup>130</sup> It is mainly located in the cytoplasm and mitochondria, although the redox-active nature of the endosomal compartment has also been reported (controlled by the gamma-interferon-inducible lysosomal thiol reductase).<sup>131</sup>

It is particularly interesting the fact that glutathione levels in cells vary from 2-10 mM in the cytosol to 2-20  $\mu$ M in the extracellular microenvironment.<sup>132</sup> Moreover, the much higher presence of its reductive state compared to the reduced one has grabbed the attention of many researchers and several examples of nanocarriers sensitive to GSH have been reported in the last years.<sup>133</sup>

While many pH-responsive moieties are based on protonation-deprotonation processes, the design of redox-responsive nanocarriers normally relies on the use of GSH-cleavable bonds. Redox-responsive systems are usually based on disulfide, diselenide or carbon-selenium bonds. Besides, some oxidation-responsive agents such as boronic esters, ferrocene or tetrathiafulvalene can also be used to design such carriers.<sup>134</sup> In particular, the low energy of diselenide and carbon-selenium bonds, compared to their disulfide counterpart, makes them more sensitive to both reducing and oxidation agents, although the disulfide bond remains the most employed.<sup>135</sup>

### **2.1.3.2. Redox-responsive organic nanocarriers**

Disulfide bonds are particularly useful to synthesize block copolymers from hydrophobic and hydrophilic blocks. Then, these polymers can be applied to the design of polymeric nanocarriers. For instance, it is possible to synthesize redox-responsive micelles that disassemble only inside the cells due to the overexpression of GSH, leading to the drug release (Figure 2.8). Examples are the combination of hydrophobic poly( $\epsilon$ -caprolactone) with PEG,<sup>136,137</sup> dextran<sup>138</sup> or poly(ethyl ethylene phosphate).<sup>139</sup> This strategy is useful to design multiresponsive micelles if one of the blocks presents stimuli-responsive behavior. For instance, the combination of poly(N-isopropylacrylamide) with

tetrahydropyran-protected 2-hydroxyethyl methacrylate through disulfide bonds yields micelles with sensitivity to heat, pH and redox species.<sup>140</sup>

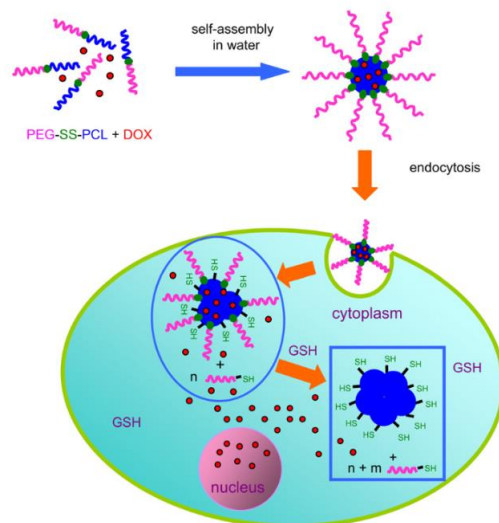


**Figure 2.8.** Schematic representation of the formation and subsequent degradation of micelles formed from disulfide bond-containing block copolymers. When the micelles reach the cytosol, the overexpressed GSH cleaves the hydrophilic PEG, leading to the disruption of the micelles and the drug release. Reproduced from Ref 136 with permission of Elsevier.

Analogously, there are several examples of redox-responsive polymersomes<sup>141–144</sup> and polymer capsules<sup>145,146</sup> synthesized from disulfide-containing polymers. In this way, the nanocarriers show negligible drug release outside the cancer cells. However, when they are internalized the overexpression of GSH induces to the disruption of the particle, leading to the drug release.

In addition, the use of redox-cleavable bonds is also interesting for the design of redox-responsive prodrugs<sup>147,148</sup> and polymer-drug conjugates.<sup>149–151</sup> In this way, the therapeutic agents would become active only inside the cytoplasm of cells and the efficacy of the treatment would increase. Gene therapies can also benefit from this stimulus. For instance, the design of thiolated polyplexes that release the nucleic acids only in the cytoplasm avoids potential degradation and increases the therapy efficacy.<sup>152,153</sup>

### 2.1.3.3. Redox-responsive inorganic nanocarriers

Many inorganic nanoparticles have been modified with redox-sensitive bonds to introduce different functionalities, including magnetic<sup>154,155</sup> and gold<sup>156,157</sup> nanoparticles, quantum dots<sup>158</sup> or mesoporous hydroxyapatite,<sup>159</sup> among others.

The main disadvantage of mesoporous nanoparticles is their potential premature release owing to their open porous structure. In this sense, the use of a stimulus that only

triggers the release inside the cells seems convenient. For such reason, the development of redox-labile gatekeepers has attracted much attention. In this way, the pore entrances remain closed in the bloodstream, avoiding undesired premature release. However, after being internalized the overexpression of GSH triggers the cleavage of the gatekeepers, leading to the drug release.

Much work has been done on MSNs. In this sense, many supramolecular structures have been employed to seal the mesopores. The use of disulfide bonds as linkers with the surface allows the conjugation of macromolecules whose sizes are big enough to close the pores, avoiding the release. Besides, these macromolecules can provide further functionalities to the nanocarrier. For instance, the use of  $\beta$ -CD,<sup>160,161</sup> collagen,<sup>162</sup> PEG,<sup>163</sup> or peptides<sup>31,164</sup> introduces targeting possibilities (Figure 2.9).

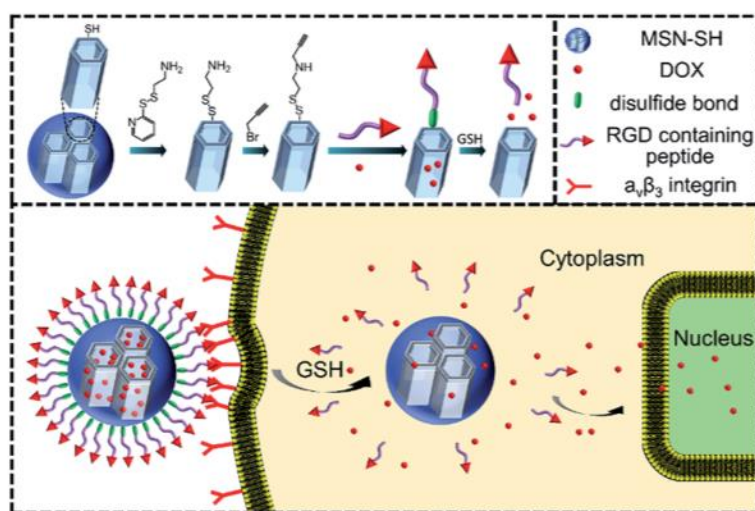


**Figure 2.9.** Example of a redox-responsive mesoporous nanocarrier where the gatekeeper is conjugated *via* disulfide bonds. In this case, a peptide acts as gatekeeper and targeting agent at the same time, allowing the release once the bond is cleaved in the cytoplasm. Reproduce from Ref 164 with permission of The Royal Society of Chemistry.

Another interesting example is the conjugation of cytochrome *c* to MSNs through disulfide bonds, since it works as gatekeeper and at the same time it generates ROS in the cells, triggering their death.<sup>165</sup>

This approximation also allows the grafting of small nanoparticles such as gold<sup>166</sup> or cerium nanoparticles<sup>167</sup> to the surface of MSNs. As with micelles, it is possible to use disulfide bonds as cross-linking agents in MSNs. Examples are the cross-linking of grafted PAA<sup>168</sup> or the design of biodegradable MSNs presenting disulfide bonds throughout their backbone.<sup>169</sup>

The field of mesoporous carbon materials is still at its early stage and less examples are available. Some polymers have been attached to their surface *via* disulfide bonds, such as PEG,<sup>170</sup> pluronic<sup>171</sup> or PAA.<sup>112</sup> Besides, small carbon dots have been connected to the surface of mesoporous carbon nanoparticles to act as gatekeepers and trackers of the release, since their fluorescence is quenched when coupled to the carbon matrix and recovered when the disulfide bond is cleaved.<sup>112</sup>

#### 2.1.4. Self-immolative chemistry in nanomedicine

The challenge when designing stimuli-responsive nanomedicines relies on the moiety employed to confer that responsiveness. An interesting approach consists of the so-called self-immolative systems, which are macromolecules programmed through their synthesis to undergo head-to-tail disassembly into their building blocks in response to certain events in a domino-like fashion (Figure 2.10).

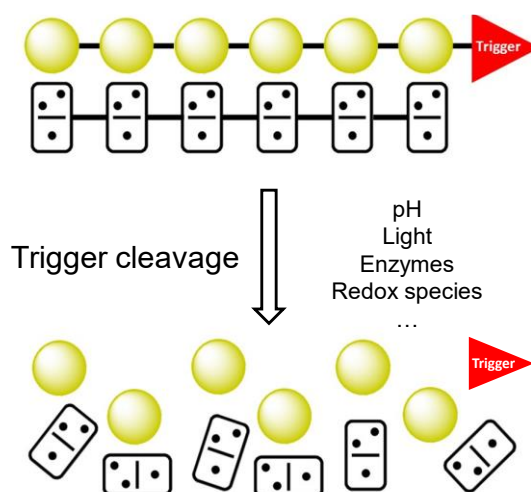


**Figure 2.10.** Schematic representation of the cleavage of a trigger on a self-immolative polymer leading to the head to tail disassembly into its building blocks. When the trigger is removed, the electron pair generated induces a cascade of electron movements that disassembles the polymer chain in a domino-like fashion.

Doron Shabat and coworkers laid the foundations of this new chemistry in 2003, when they reported for the first time smart self-immolative dendrimers undergoing self-degradation upon stimulation.<sup>172</sup> Later on, they reported an interesting design based on a linear polyurethane bearing a protecting group on the terminal amine that acted as trigger. Once the protecting group was removed, sequential 1,6-elimination and decarboxylation reactions led to the original monomer precursors.<sup>173</sup>

In general, Self-Immolative Polymers are produced through a polymerization reaction of the appropriate monomer to then cap the terminal head-group of the polymer with a specific protecting group, leading to a polymer with a trigger. Then, the selective cleavage

of the protecting group would initiate the polymer sequential fragmentation into the original building blocks from head to tail. Therefore, the appropriate selection of the trigger would allow the design of many different responsive materials.

In this section some general concepts of self-immolative chemistry will be described, including the main properties of self-immolative spacers. Then, the application of self-immolative chemistry to nanomedicine will be revised, including some examples of prodrugs and particle-like polymeric vehicles.

#### 2.1.4.1. Self-immolative spacers

The simplest self-immolative moiety is composed of a protecting group linked to a spacer, which is also linked to a reporter, that will eventually be released. The reporter can be a drug, a dye or a polymeric chain (Figure 2.11).



**Figure 2.11.** General structure of a self-immolative spacer: A protecting group connected to a spacer which is linked to a reporter. The reporter can be a drug, a dye or a polymeric chain.

The use of self-immolative spacers allows the release of a single molecule upon application of a certain stimulus. That stimulus cleaves the protecting group, leading to the generation of a free electron pair. Then, an electronic cascade starts, finally leading to the release of the reporter (Figure 2.12).

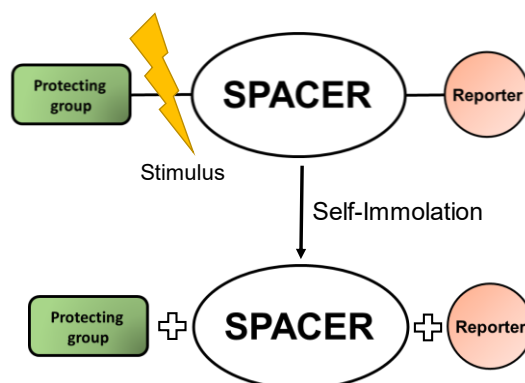


**Figure 2.12.** Schematic representation of the self-immolation of a self-immolative spacer upon application of a stimulus. The cleavage of the trigger and the subsequent electron cascade lead to the release of an active reporter.

From the chemical point of view, the self-immolation process is normally driven by a cooperative rise in the entropy along with the formation of thermodynamically stable products. Generally speaking, self-immolative spacers can be classified in two main

groups, depending on the particular disassembling process: (1) 1,4-, 1,6-, or 1,8-Elimination; or (2) Cyclization.<sup>174</sup> Additionally, it is possible to combine both types of spacers to tune the degradation rates in self-immolative polymers.<sup>175</sup>

#### 1,4-, 1,6-, or 1,8-Elimination

These spacers are based on aromatic species that present electron donor groups in *ortho* or *para* positions and good leaving groups in benzylic positions. The electron donor group (usually amino, hydroxyl or thiol functionalities) normally leads to 1,4- or 1,6-eliminations. The cleavage of the protecting group initiates the self-immolation, leading to a free electron pair. Then, the electron donor group transmits the electron pair to the aromatic ring, starting an electronic cascade that leads to the disassembly of the spacer (Figure 2.13).

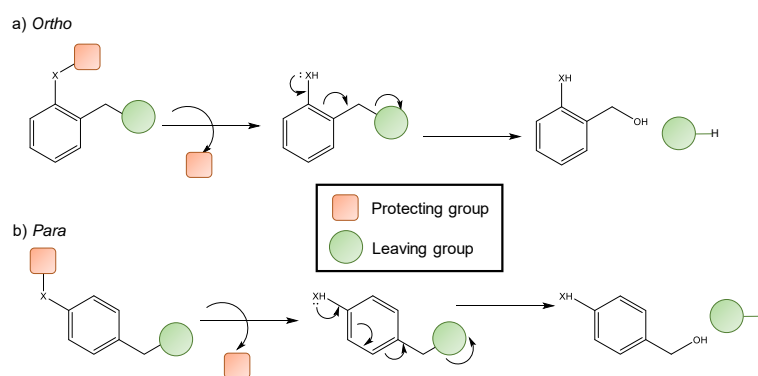


**Figure 2.13.** Spacers and elimination procedures. a) 1,4-Elimination; b) 1,6-Elimination. The protecting group is an electron donor group, normally amino, hydroxyl or thiol functionalities, that initiates the electronic cascade, leading to the reporter release.

Interestingly, in some molecules, such as naphthalene, the 1,8-elimination does not lead to the release of the leaving group. Moreover, 1,10-elimination or successive do not lead to the release of the leaving group because the electronic cascade does not take place. This behavior has not been completely elucidated although some explanations have been given. It has been associated to the excessive energy barrier that is necessary to break aromaticity and to the repulsion of the *ortho*-hydrogens that prevents the formation of the planar structure necessary for good electron delocalization.<sup>174</sup>

#### Cyclization

Spacers suffering cyclization are based on lineal alkyl chains or aromatic molecules with substituents in *ortho*. Once the trigger is cleaved, a nucleophilic attack on a carbonyl group or an electrophilic aliphatic carbon leads to the cyclization of the spacer, which provokes the release of the reporter (Figure 2.14).<sup>174</sup>



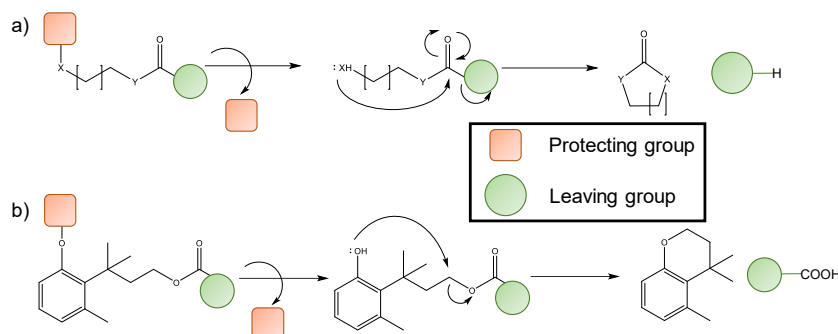


**Figure 2.14.** Spacers suffering cyclization. a) Attack to carbonyl; b) Attack to aliphatic carbon. The protecting group is an electron donor group, normally amino, hydroxyl or thiol functionalities. The cleavage of the protecting group initiates the electronic cascade, leading to the reporter release.

The applicability of the self-immolative molecule will depend on the appropriate election of the protecting group. A number of protecting groups useful in clinical scenarios have been reported. Those stimuli can be classified in three main groups: (1) chemical (hydrogen peroxide or pH); (2) enzymatic; and (3) luminescent (ultraviolet or near-infrared light). Table 2.4 summarizes the different types of stimuli-responsive protecting groups applied in the design of stimuli-responsive self-immolative spacers.

**Table 2.4.** Stimuli-responsive protecting groups used for the design of self-immolative spacers.

Protecting Group	Trigger	Refs	Protecting Group	Trigger	Refs	Protecting Group	Trigger	Refs
<b>Chemical Stimulus</b>			<b>Enzymatic Stimulus</b>			<b>Light Stimulus</b>		
	H <sub>2</sub> O <sub>2</sub>	176–181		Penicillin G-Amidase	182		Ultraviolet	178,183–190
	Acid pH	191–194		Alkaline Phosphatase	195		Near-Infrared	189,190,196
	Basic pH	197		Glutathione	176,183,198–202			
	Tetrazine	203		Glutathione	204			
				Human carboxylesterase-2	205			
				DT-Diaphorase	206			

#### 2.1.4.2. Prodrugs based on self-immolative spacers

Ideally, a prodrug would circulate throughout the body without showing therapeutic activity until arriving at the desired area, where it would suffer self-immolation and the therapeutic activity would be recovered. It is also usual the design of prodrug-like precursors that are capable of releasing dye molecules. By doing that, it is possible to monitor different processes. In this sense, the fluorescence detection indicates that the molecule has self-immolated.

For an enzymatic reaction to happen it is necessary the formation of temporary bonds between the substrate and the active site of the enzyme. Then, if an enzyme is to bind a substrate, the latter should show adequate accessibility for the active site. In that sense, it has been shown that the addition of a self-immolative spacer between the trigger and the drug increases the accessibility of the enzyme to the specific substrate. In consequence, the introduction of self-immolative fragments leads to higher rates of bioconversion and, then, higher therapeutic activity.<sup>207</sup>

There are several examples of enzymes that have been utilized in the design of this kind of molecules. Cathepsin B is a cysteine protease which is involved in many pathologies and oncogenic processes in humans.<sup>208</sup> In particular, it is overexpressed in the lysosomes of many cancer cells. The self-immolative spacer *p*-aminobenzyl alcohol has been used in combination with various of dipeptides to provide sensitivity to this enzyme. For instance, the dipeptides Phe-Lys and Lys-Lys have been used in the design of selective prodrug-inspired probes capable of releasing a fluorogenic peptide.<sup>209</sup> Besides, the Phe-Lys combination has shown great efficacy both *in vitro* and *in vivo*, showing much less toxicity in healthy areas than its active counterpart.<sup>210</sup> In order to monitor endogenous alkaline phosphatase in living cells, *p*-hydroxybenzyl alcohol has been used as spacer between a phosphate moiety (enzyme substrate) and the dye resorufin.<sup>195</sup> DT-diaphorase, an enzyme that is overexpressed in some malignant tumors, has also been used as enzymatic trigger through self-immolative linkers. In particular, the use of a quinone propionic acid-based moiety allows to incorporate two camptothecin drug molecules at a time on each prodrug.<sup>206</sup> Furthermore, there is an enzyme (human carboxyl-esterase-2) that has proved its efficacy in the cleavage of a self-immolative ester to provide the active form of the potent anticancer drug platinum-acridine.<sup>205</sup>

With regard to self-immolative prodrugs undergoing chemical activation, most of the examples involve a conversion mechanism based on the action of GSH, although designs sensitive to hydrogen peroxide have also been reported.<sup>176</sup> Besides, conjugation of self-immolative prodrugs with gold nanoparticles has also been described, leading to a system with dual drug capability and targeting ability.<sup>199</sup> In order to verify the effective drug cleavage due to the action of GSH, a dendritic system bearing one molecule of camptothecin and one of an inactive dye was reported. When GSH cleaves the trigger, both drug and dye are released in their active form, thereby obtaining a light signal only if the drug has been released.<sup>204</sup>

### 2.1.4.3. Nanocarriers based on self-immolative moieties

It is very frequent the use of single self-immolative units in order to design prodrug-like molecules, as it has been mentioned above. Nonetheless, their use is not limited to the already mentioned examples, since it is also possible to synthesize several types of nanovehicles by using self-immolative fragments in combination with other macromolecular structures.

#### ❖ *Polymer capsules*

In the last few years a number of techniques to synthesize particles or capsules out of self-immolative elements have been developed.<sup>211</sup> In that sense, the synthesis of self-immolative microcapsules composed of self-immolative polymers was accomplished in 2010 for the first time (Figure 2.15).<sup>194</sup>

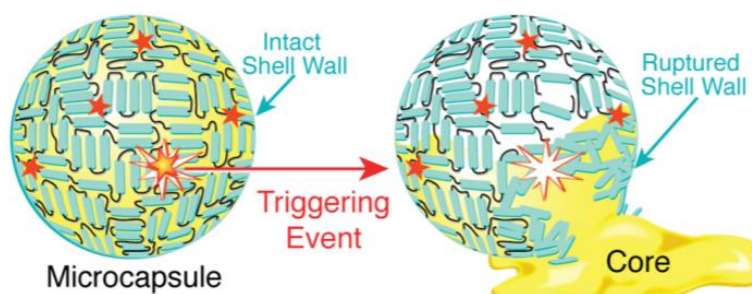


**Figure 2.15.** Microcapsule synthesized from self-immolative polymers. The cleavage of the trigger initiates the self-immolation, inducing the disruption of the wall and leading to the drug release. Reproduced from Ref 194 with permission of American Chemical Society.

The presence of triggering units throughout the wall led to the disruption of the carrier and the release of the cargo upon application of the triggering conditions. Afterward, other design of self-immolative polymer was formulated as nanoparticles. In this case, the nanocarrier was sensitive to both ultraviolet and near-infrared light (instead of to strong acid or base, as in the first example) and then, the applicability of these nanocarriers in biological scenarios was evaluated.<sup>212</sup> Furthermore, more examples comprising other designs of self-immolative polymers sensitive to various wavelengths have also been reported.<sup>188–190</sup> The introduction of aryl boronic esters within the polymer chain has led to multiple designs of hydrogen peroxide responsive polymer nanoparticles.<sup>180,181,213</sup> Moreover, dual stimuli-responsive polymer nanoparticles have also been published, including pH and light<sup>192,193</sup> or hydrogen peroxide and pH.<sup>179</sup> Finally, heat-responsive polymer nanoparticles have been recently reported. Upon heating, the carrier undergoes a retro-Diels Alder reaction that leads to a furfuryl carbamate that suffers elimination, thus inducing the degradation of the carrier.<sup>214</sup>

❖ *Polymeric micelles and polymersomes*

Self-immolative chemistry finds broad application in the synthesis of polymeric micelles and polymersomes. These nanocarriers self-assemble spontaneously from linear structures to three dimensional polymeric particles. In this sense, many self-immolative molecules have been used to synthesize block copolymers. The polymers rearrange in water and are stable until some stimulus is applied. When that happens the self-immolation starts, leading to the disassembly of the block copolymer and subsequent drug release. The use of self-immolative moieties facilitates the destabilization of the polymeric carrier because, ideally, a single event may lead to the degradation of a large self-immolative block.

There several approximations to construct self-immolative polymeric micelles. The general design normally comprises two polyethylene glycol blocks with a self-immolative fragment within them. It is common the use of a self-immolative block containing multiple triggering points along the chain. In that sense, disulfide containing polycarbonates<sup>186</sup> as well as hydrogen peroxide-responsive poly(amino ester)s<sup>187</sup> have been used as building blocks for the hydrophobic component (Figure 2.16). It is also possible to have just one triggering point. For instance, such design can be found in micelles formed from amphiphilic polymers containing a poly(ethyl glyoxylate) undergoing head-to-tail depolymerization.<sup>178</sup>

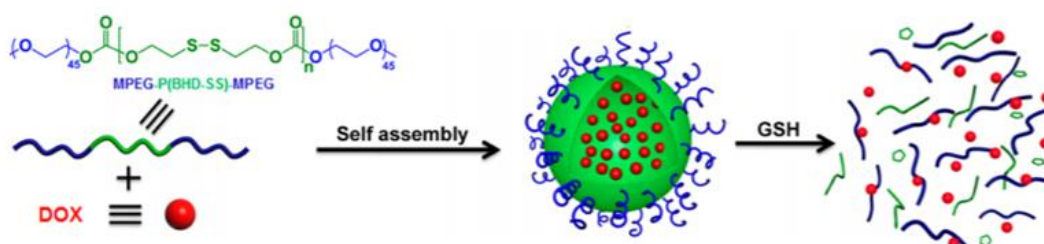


**Figure 2.16.** Redox-responsive polymeric micelle. The hydrophobic block contains periodic disulfides bonds that are cleaved by the overexpressed GSH in the cells, leading to the disassembly and the drug release. Reproduce from Ref 186 with permission of American Chemical Society.

The use of pendant self-immolative groups<sup>185</sup> or linear self-immolative polycarbamates<sup>183</sup> within the hydrophilic segments allows to synthesize light-responsive polymersomes. In addition to light, enzymes have been used to trigger the disassembly of self-immolative polymeric vesicles capable of addressing antimicrobial resistance *in vitro*.<sup>182</sup>

❖ *Nucleic acid-based nanoparticles*

There are particular three-dimensional arrangements of nucleic acids with improved properties that their linear or circular counterparts do not show, such as better cell internalization or stability against enzyme degradation. In this sense, it is possible to engineer amphiphilic blocks composed of hydrophilic DNA and a hydrophobic fragment containing hydrophobic drugs connected through a self-immolative linker. In this way, the DNA-drug complex rearranges in water and forms a micelle. The self-immolative linker is cleaved in the tumoral cells, leading to the self-immolation and subsequent drug release (Figure 2.17). Examples are the use of light<sup>-184</sup> and reductive<sup>-202</sup> responsive self-immolative moieties to synthesize the amphiphilic block.

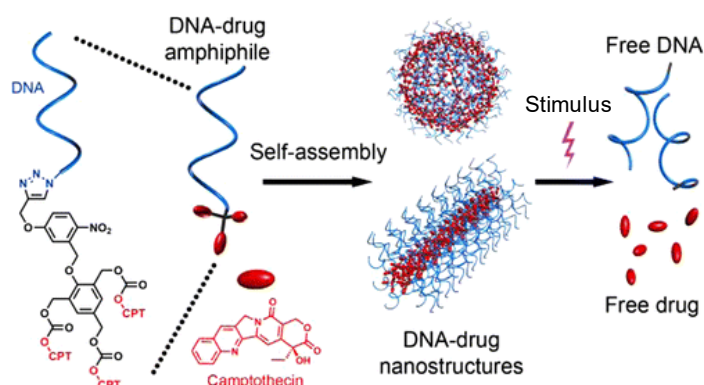


**Figure 2.17.** Micelle formed from a DNA block (hydrophilic) conjugated to the drug camptothecin (hydrophobic). The complex rearrange in water and disassembles when the stimulus is applied, leading to the self-immolation and subsequent drug release. Adapted from Ref 184 with permission of American Chemical Society.

Moreover, it is also possible the combination of miRNA with polymeric prodrugs<sup>201</sup> or polymer chains bearing pendant prodrugs<sup>200</sup> to yield particle-like polyplexes. The main advantage is that it is possible to transport drugs, in their active or inactive form, that, once the stimulus is applied, are released in combination with different nucleic acids, which also show therapeutic efficacy and biocompatibility.

### 2.1.5. Conclusions

This section has introduced several examples of nanoparticles responsive to either pH or GSH, which are known to be relevant biomarkers found in tumoral scenarios. Besides, it has been shown that self-immolative chemistry constitutes a powerful tool for the design of structures sensitive to either internal or external stimuli with application in nanomedicine. In this sense, the main purpose of this PhD thesis has been the design of

self-immolative structures and their application to mesoporous nanoparticles. In this manner, the combination of the excellent physical-chemical properties mesoporous nanocarriers with the tunability of self-immolative chemistry has led to the development of various nanocarriers with potential applicability to various diseases, such as cancer.

## References

- (1) Lee, C.-H.; Lo, L.-W.; Mou, C.-Y.; Yang, C.-S. Synthesis and Characterization of Positive-Charge Functionalized Mesoporous Silica Nanoparticles for Oral Drug Delivery of an Anti-Inflammatory Drug. *Adv. Funct. Mater.* **2008**, *18*, 3283–3292.
- (2) Papat, A.; Jambhrunkar, S.; Zhang, J.; Yang, J.; Zhang, H.; Meka, A.; Yu, C. Programmable Drug Release Using Bioresponsive Mesoporous Silica Nanoparticles for Site-Specific Oral Drug Delivery. *Chem. Commun.* **2014**, *50*, 5547–5550.
- (3) Ensign, L. M.; Cone, R.; Hanes, J. Oral Drug Delivery with Polymeric Nanoparticles: The Gastrointestinal Mucus Barriers. *Adv. Drug Deliv. Rev.* **2012**, *64*, 557–570.
- (4) Vander Heiden, M. G.; Cantley, L. C.; Thompson, C. B. Understanding the Warburg Effect: The Metabolic Requirements of Cell Proliferation. *Science.* **2009**, *324*, 1029–1033.
- (5) Kato, Y.; Ozawa, S.; Miyamoto, C.; Maehata, Y.; Suzuki, A.; Maeda, T.; Baba, Y. Acidic Extracellular Microenvironment and Cancer. *Cancer Cell Int.* **2013**, *13*, 89.
- (6) Onyango, J. O.; Chung, M. S.; Eng, C. H.; Klees, L. M.; Langenbacher, R.; Yao, L.; An, M. Noncanonical Amino Acids to Improve the pH Response of PHLIP Insertion at Tumor Acidity. *Angew. Chemie Int. Ed.* **2015**, *54*, 3658–3663.
- (7) Gao, Y.; Yang, C.; Liu, X.; Ma, R.; Kong, D.; Shi, L. A Multifunctional Nanocarrier Based on Nanogated Mesoporous Silica for Enhanced Tumor-Specific Uptake and Intracellular Delivery. *Macromol. Biosci.* **2012**, *12*, 251–259.
- (8) Xu, P.; Van Kirk, E. A.; Zhan, Y.; Murdoch, W. J.; Radosz, M.; Shen, Y. Targeted Charge-Reversal Nanoparticles for Nuclear Drug Delivery. *Angew. Chemie Int. Ed.* **2007**, *46*, 4999–5002.
- (9) Casey, J. R.; Grinstein, S.; Orłowski, J. Sensors and Regulators of Intracellular pH. *Nat. Rev. Mol. Cell Biol.* **2010**, *11*, 50–61.
- (10) Zheng, H.; Tai, C.-W.; Su, J.; Zou, X.; Gao, F. Ultra-Small Mesoporous Silica Nanoparticles as Efficient Carriers for pH Responsive Releases of Anti-Cancer Drugs. *Dalton Trans.* **2015**, *44*, 20186–20192.
- (11) Moorthy, M. S.; Bae, J. H.; Kim, M. J.; Kim, S. H.; Ha, C. S. Design of a Novel Mesoporous Organosilica Hybrid Microcarrier: A pH Stimuli-Responsive Dual-Drug-Delivery Vehicle for Intracellular Delivery of Anticancer Agents. *Part. Part. Syst. Charact.* **2013**, *30*, 1044–1055.
- (12) Ma, Y.; Zhou, L.; Zheng, H.; Xing, L.; Li, C.; Cui, J.; Che, S. pH-Responsive Mitoxantrone (MX) Delivery Using Mesoporous Silica Nanoparticles (MSN). *J. Mater. Chem.* **2011**, *21*, 9483.
- (13) Tacar, O.; Sriamornsak, P.; Dass, C. R. Doxorubicin: An Update on Anticancer Molecular Action, Toxicity and Novel Drug Delivery Systems. *J. Pharm. Pharmacol.* **2013**, *65*, 157–170.
- (14) Liu, X.; Jiang, H.; Ge, W.; Wu, C.; Chen, D.; Li, Q.; Chen, Y.; Wang, X. Green and Facile Synthesis of Highly Biocompatible Carbon Nanospheres and Their pH-

- Responsive Delivery of Doxorubicin to Cancer Cells. *RSC Adv.* **2015**, *5*, 17532–17540.
- (15) Lin, C. H.; Cheng, S. H.; Liao, W. N.; Wei, P. R.; Sung, P. J.; Weng, C. F.; Lee, C. H. Mesoporous Silica Nanoparticles for the Improved Anticancer Efficacy of Cis-Platin. *Int. J. Pharm.* **2012**, *429*, 138–147.
- (16) Zhang, P.; Kong, J. Doxorubicin-Tethered Fluorescent Silica Nanoparticles for pH-Responsive Anticancer Drug Delivery. *Talanta* **2015**, *134*, 501–507.
- (17) Lee, C. H.; Cheng, S. H.; Huang, I. P.; Souris, J. S.; Yang, C. S.; Mou, C. Y.; Lo, L. W. Intracellular pH-Responsive Mesoporous Silica Nanoparticles for the Controlled Release of Anticancer Chemotherapeutics. *Angew. Chemie Int. Ed.* **2010**, *49*, 8214–8219.
- (18) Kim, M. S.; Jeon, J. B.; Chang, J. Y. Selectively Functionalized Mesoporous Silica Particles with the PEGylated Outer Surface and the Doxorubicin-Grafted Inner Surface: Improvement of Loading Content and Solubility. *Microporous Mesoporous Mater.* **2013**, *172*, 118–124.
- (19) Cui, L.; Lin, H.; Yang, C.; Han, X.; Zhang, T.; Qu, F. Synthesis of Multifunctional Fe<sub>3</sub>O<sub>4</sub>@mSiO<sub>2</sub>@Au Core-Shell Nanocomposites for pH-Responsive Drug Delivery. *Eur. J. Inorg. Chem.* **2014**, *2014*, 6156–6164.
- (20) Chen, S.; Yang, Y.; Li, H.; Zhou, X.; Liu, M. pH-Triggered Au-Fluorescent Mesoporous Silica Nanoparticles for <sup>19</sup>F MR/Fluorescent Multimodal Cancer Cellular Imaging. *Chem. Commun.* **2014**, *50*, 283–285.
- (21) Aioub, M. S.; El-Sayed, M. a. A Real-Time Surface Enhanced Raman Spectroscopy Study of Plasmonic Photothermal Cell Death Using Targeted Gold Nanoparticles. *J. Am. Chem. Soc.* **2016**, *138*, 1258–1264.
- (22) Dai, L.; Zhang, Q.; Shen, X.; Sun, Q.; Mu, C.; Gu, H.; Cai, K. pH-Responsive Nanocontainer Based on Hydrazone-Bearing Hollow Silica Nanoparticles for Targeting Tumor Therapy. *J. Mater. Chem. B* **2016**, *4*, 4594–4604.
- (23) Schlossbauer, A.; Dohmen, C.; Schaffert, D.; Wagner, E.; Bein, T. pH-Responsive Release of Acetal-Linked Melittin from SBA-15 Mesoporous Silica. *Angew. Chemie Int. Ed.* **2011**, *50*, 6828–6830.
- (24) Liu, R.; Zhang, Y.; Zhao, X.; Agarwal, A.; Mueller, L. J.; Feng, P. pH-Responsive Nanogated Ensemble Based on Gold-Capped Mesoporous Silica through an Acid-Labile Acetal Linker. *J. Am. Chem. Soc.* **2010**, *132*, 1500–1501.
- (25) Chen, T.; Yu, H.; Yang, N.; Wang, M.; Ding, C.; Fu, J. Graphene Quantum Dot-Capped Mesoporous Silica Nanoparticles through an Acid-Cleavable Acetal Bond for Intracellular Drug Delivery and Imaging. *J. Mater. Chem. B* **2014**, *2*, 4979–4982.
- (26) Chen, M.; He, X.; Wang, K.; He, D.; Yang, S.; Qiu, P.; Chen, S. A pH-Responsive Polymer/Mesoporous Silica Nano-Container Linked through an Acid Cleavable Linker for Intracellular Controlled Release and Tumor Therapy *in vivo*. *J. Mater. Chem. B* **2014**, *2*, 428–436.
- (27) Yang, K.; Luo, H.; Zeng, M.; Jiang, Y.; Li, J.; Fu, X. Intracellular pH-Triggered, Targeted Drug Delivery to Cancer Cells by Multifunctional Envelope-Type



- Mesoporous Silica Nanocontainers. *ACS Appl. Mater. Interfaces* **2015**, *7*, 17399–17447.
- (28) Chen, Y.; Ai, K.; Liu, J.; Sun, G.; Yin, Q.; Lu, L. Multifunctional Envelope-Type Mesoporous Silica Nanoparticles for pH-Responsive Drug Delivery and Magnetic Resonance Imaging. *Biomaterials* **2015**, *60*, 111–120.
- (29) Chen, L.; Zhang, Z.; Yao, X.; Chen, X.; Chen, X. Intracellular pH-Operated Mechanized Mesoporous Silica Nanoparticles as Potential Drug Carriers. *Microporous Mesoporous Mater.* **2015**, *201*, 169–175.
- (30) Liu, J.; Luo, Z.; Zhang, J.; Luo, T.; Zhou, J.; Zhao, X.; Cai, K. Hollow Mesoporous Silica Nanoparticles Facilitated Drug Delivery via Cascade pH Stimuli in Tumor Microenvironment for Tumor Therapy. *Biomaterials* **2016**, *83*, 51–65.
- (31) Xiao, D.; Jia, H. Z.; Zhang, J.; Liu, C. W.; Zhuo, R. X.; Zhang, X. Z. A Dual-Responsive Mesoporous Silica Nanoparticle for Tumor-Triggered Targeting Drug Delivery. *Small* **2014**, *10*, 591–598.
- (32) Wang, J.; Liu, H.; Leng, F.; Zheng, L.; Yang, J.; Wang, W.; Huang, C. Z. Autofluorescent and pH-Responsive Mesoporous Silica for Cancer-Targeted and Controlled Drug Release. *Microporous Mesoporous Mater.* **2014**, *186*, 187–193.
- (33) Chen, H.; Zheng, D.; Liu, J.; Kuang, Y.; Li, Q.; Zhang, M.; Ye, H.; Qin, H.; Xu, Y.; Li, C.; *et al.* pH-Sensitive Drug Delivery System Based on Modified Dextran Coated Mesoporous Silica Nanoparticles. *Int. J. Biol. Macromol.* **2016**, *85*, 596–603.
- (34) Wang, T. T.; Lan, J.; Zhang, Y.; Wu, Z. L.; Li, C. M.; Wang, J.; Huang, C. Z. Reduced Graphene Oxide Gated Mesoporous Silica Nanoparticles as a Versatile Chemo-Photothermal Therapy System through pH Controllable Release. *J. Mater. Chem. B* **2015**, *3*, 6377–6384.
- (35) Yang, Y.; Achazi, K.; Jia, Y.; Wei, Q.; Haag, R.; Li, J. Complex Assembly of Polymer Conjugated Mesoporous Silica Nanoparticles for Intracellular pH-Responsive Drug Delivery. *Langmuir* **2016**, *32*, 12453–12460.
- (36) Fernando, I. R.; Ferris, D. P.; Frascioni, M.; Malin, D.; Strekalova, E.; Yilmaz, M. D.; Ambrogio, M. W.; Algaradah, M. M.; Hong, M. P.; Chen, X.; *et al.* Esterase- and pH-Responsive Poly( $\beta$ -Amino Ester)-Capped Mesoporous Silica Nanoparticles for Drug Delivery. *Nanoscale* **2015**, *7*, 7178–7183.
- (37) Tan, L.; Yang, M. Y.; Wu, H. X.; Tang, Z. W.; Xiao, J. Y.; Liu, C. J.; Zhuo, R. X. Glucose- and pH-Responsive Nanogated Ensemble Based on Polymeric Network Capped Mesoporous Silica. *ACS Appl. Mater. Interfaces* **2015**, *7*, 6310–6316.
- (38) Aznar, E.; Marcos, M. D.; Martínez-Mañez, R.; Sancenón, F.; Soto, J.; Amorós, P.; Guillem, C. pH- and Photo-Switched Release of Guest Molecules from Mesoporous Silica Supports. *J. Am. Chem. Soc.* **2009**, *131*, 6833–6843.
- (39) Gan, Q.; Lu, X.; Yuan, Y.; Qian, J.; Zhou, H.; Lu, X.; Shi, J.; Liu, C. A Magnetic, Reversible pH-Responsive Nanogated Ensemble Based on Fe<sub>3</sub>O<sub>4</sub> Nanoparticles-Capped Mesoporous Silica. *Biomaterials* **2011**, *32*, 1932–1942.
- (40) Luo, Z.; Cai, K.; Hu, Y.; Zhang, B.; Xu, D. Cell-Specific Intracellular Anticancer Drug Delivery from Mesoporous Silica Nanoparticles with pH Sensitivity. *Adv.*

*Healthc. Mater.* **2012**, *1*, 321–325.

- (41) Li, D.; Huang, X.; Wu, Y.; Li, J.; Cheng, W.; He, J.; Tian, H.; Huang, Y. Preparation of pH-Responsive Mesoporous Hydroxyapatite Nanoparticles for Intracellular Controlled Release of an Anticancer Drug. *Biomater. Sci.* **2015**, *5*, 36–38.
- (42) Sun, L.; Zhang, X. G.; An, J. X.; Su, C.; Guo, Q. Q.; Li, C. X. Boronate Ester Bond-Based Core-Shell Nanocarriers with pH Response for Anticancer Drug Delivery. *RSC Adv.* **2014**, *4*, 20208–20215.
- (43) Chen, X.; Yao, X.; Wang, C.; Chen, L.; Chen, X. Mesoporous Silica Nanoparticles Capped with Fluorescence-Conjugated Cyclodextrin for pH-Activated Controlled Drug Delivery and Imaging. *Microporous Mesoporous Mater.* **2015**, *217*, 46–53.
- (44) Yilmaz, M. D.; Xue, M.; Ambrogio, M. W.; Buyukcakir, O.; Wu, Y.; Frascioni, M.; Chen, X.; Nassar, M. S.; Stoddart, J. F.; Zink, J. I. Sugar and pH Dual-Responsive Mesoporous Silica Nanocontainers Based on Competitive Binding Mechanisms. *Nanoscale* **2015**, *7*, 1067–1072.
- (45) Qiu, X.-L.; Li, Q.-L.; Zhou, Y.; Jin, X.-Y.; Qi, A.-D.; Yang, Y.-W. Sugar and pH Dual-Responsive Snap-Top Nanocarriers Based on Mesoporous Silica-Coated Fe<sub>3</sub>O<sub>4</sub> Magnetic Nanoparticles for Cargo Delivery. *Chem. Commun.* **2015**, *51*, 4237–4240.
- (46) Yan, Y.; Fu, J.; Liu, X.; Wang, T.; Lu, X. Acid-Responsive Intracellular Doxorubicin Release from Click Chemistry Functionalized Mesoporous Silica Nanoparticles. *RSC Adv.* **2015**, *5*, 30640–30646.
- (47) Zhang, J.; Wu, D.; Li, M. F.; Feng, J. Multifunctional Mesoporous Silica Nanoparticles Based on Charge-Reversal Plug-Gate Nanovalves and Acid-Decomposable ZnO Quantum Dots for Intracellular Drug Delivery. *ACS Appl. Mater. Interfaces* **2015**, *7*, 26666–26673.
- (48) Xing, L.; Zheng, H.; Cao, Y.; Che, S. Coordination Polymer Coated Mesoporous Silica Nanoparticles for pH-Responsive Drug Release. *Adv. Mater.* **2012**, *24*, 6433–6437.
- (49) Zheng, H.; Huang, Z.; Che, S. Mesostructured Chitosan–Silica Hybrid as a Biodegradable Carrier for a pH-Responsive Drug Delivery System. *Dalt. Trans.* **2012**, *41*, 5038–5044.
- (50) Zheng, H.; Che, S. Amino/Quaternary Ammonium Groups Bifunctionalized Large Pore Mesoporous Silica for pH-Responsive Large Drug Delivery. *RSC Adv.* **2012**, *2*, 4421–4429.
- (51) Tarn, D.; Xue, M.; Zink, J. I. pH-Responsive Dual Cargo Delivery from Mesoporous Silica Nanoparticles with a Metal-Latched Nanogate. *Inorg. Chem.* **2013**, *52*, 2044–2049.
- (52) Dai, L.; Zhang, Q.; Li, J.; Shen, X.; Mu, C.; Cai, K. Dendrimerlike Mesoporous Silica Nanoparticles as pH-Responsive Nanocontainers for Targeted Drug Delivery and Bioimaging. *ACS Appl. Mater. Interfaces* **2015**, *7*, 7357–7372.
- (53) Chen, X.; Cheng, X.; Soeriyadi, A. H.; Sagnella, S. M.; Lu, X.; Scott, J. A.; Lowe, S. B.; Kavallaris, M.; Gooding, J. J. Stimuli-Responsive Functionalized

- Mesoporous Silica Nanoparticles for Drug Release in Response to Various Biological Stimuli. *Biomater. Sci.* **2014**, *2*, 121–130.
- (54) Kankala, R. K.; Kuthati, Y.; Liu, C.-L.; Mou, C.-Y.; Lee, C.-H. Killing Cancer Cells by Delivering a Nanoreactor for Inhibition of Catalase and Catalytically Enhancing Intracellular Levels of ROS. *RSC Adv.* **2015**, *5*, 86072–86081.
- (55) Christie, R. J.; Anderson, D. J.; Grainger, D. W. Comparison of Hydrazone Heterobifunctional Cross-Linking Agents for Reversible Conjugation of Thiol-Containing Chemistry. *Bioconjug. Chem.* **2010**, *21*, 1779–1787.
- (56) Huttunen, K. M.; Raunio, H.; Rautio, J. Prodrugs-from Serendipity to Rational Design. *Pharmacol. Rev.* **2011**, *63*, 750–771.
- (57) Qu, X.; Yang, Z. Benzoic-Imine-Based Physiological-pH-Responsive Materials for Biomedical Applications. *Chem. Asian J.* **2016**, *11*, 2633–2641.
- (58) Fang, Y.; Xue, J.; Gao, S.; Lu, A.; Yang, D.; Jiang, H.; He, Y.; Shi, K. Cleavable PEGylation: A Strategy for Overcoming the “PEG Dilemma” in Efficient Drug Delivery. *Drug Deliv.* **2017**, *24*, 22–32.
- (59) Bull, S. D.; Davidson, M. G.; Van Den Elsen, J. M. H.; Fossey, J. S.; Jenkins, A. T. A.; Jiang, Y. B.; Kubo, Y.; Marken, F.; Sakurai, K.; Zhao, J.; *et al.* Exploiting the Reversible Covalent Bonding of Boronic Acids: Recognition, Sensing, and Assembly. *Acc. Chem. Res.* **2013**, *46*, 312–326.
- (60) Zheng, H.; Xing, L.; Cao, Y.; Che, S. Coordination Bonding Based pH-Responsive Drug Delivery Systems. *Coord. Chem. Rev.* **2013**, *257*, 1933–1944.
- (61) Mourino, V.; Cattalini, J. P.; Boccaccini, A. R. Metallic Ions as Therapeutic Agents in Tissue Engineering Scaffolds: An Overview of Their Biological Applications and Strategies for New Developments. *J. R. Soc. Interface* **2012**, *9*, 401–419.
- (62) Muhammad, F.; Guo, M.; Qi, W.; Sun, F.; Wang, A.; Guo, Y.; Zhu, G. pH-Triggered Controlled Drug Release from Mesoporous Silica Nanoparticles via Intracellular Dissolution of ZnO Nanolids. *J. Am. Chem. Soc.* **2011**, *133*, 8778–8781.
- (63) Huang, X.; Wu, S.; Du, X. Gated Mesoporous Carbon Nanoparticles as Drug Delivery System for Stimuli-Responsive Controlled Release. *Carbon.* **2016**, *101*, 135–142.
- (64) Wu, S.; Huang, X.; Du, X. pH- and Redox-Triggered Synergistic Controlled Release of a ZnO-Gated Hollow Mesoporous Silica Drug Delivery System. *J. Mater. Chem. B* **2015**, *3*, 1426–1432.
- (65) Muhammad, F.; Wang, A.; Guo, M.; Zhao, J.; Qi, W.; Yingjie, G.; Gu, J.; Zhu, G. pH Dictates the Release of Hydrophobic Drug Cocktail from Mesoporous Nanoarchitecture. *ACS Appl. Mater. Interfaces* **2013**, *5*, 11828–11835.
- (66) Li, Z.; Li, H.; Liu, L.; You, X.; Zhang, C.; Wang, Y. A pH-Sensitive Nanocarrier for Co-Delivery of Doxorubicin and Camptothecin to Enhance Chemotherapeutic Efficacy and Overcome Multidrug Resistance in Vitro. *RSC Adv.* **2015**, *5*, 77097–77105.
- (67) Chen, Y.; Yin, Q.; Ji, X.; Zhang, S.; Chen, H.; Zheng, Y.; Sun, Y.; Qu, H.; Wang,

- Z.; Li, Y.; *et al.* Manganese Oxide-Based Multifunctionalized Mesoporous Silica Nanoparticles for pH-Responsive MRI, Ultrasonography and Circumvention of MDR in Cancer Cells. *Biomaterials* **2012**, *33*, 7126–7137.
- (68) Zhang, S.; Qian, X.; Zhang, L.; Peng, W.; Chen, Y. Composition-Property Relationships in Multifunctional Hollow Mesoporous Carbon Nanosystems for pH-Responsive Magnetic Resonance Imaging and on-Demand Drug Release. *Nanoscale* **2015**, *7*, 7632–7643.
- (69) Gidwani, B.; Vyas, A. A Comprehensive Review on Cyclodextrin-Based Carriers for Delivery of Chemotherapeutic Cytotoxic Anticancer Drugs. *Biomed Res. Int.* **2015**, *3*, 1–15.
- (70) Meng, H.; Xue, M.; Xia, T.; Zhao, Y. L.; Tamanoi, F.; Stoddart, J. F.; Zink, J. I.; Nel, A. E. Autonomous *in vitro* Anticancer Drug Release from Mesoporous Silica Nanoparticles by pH-Sensitive Nanovalves. *J. Am. Chem. Soc.* **2010**, *132*, 12690–12697.
- (71) Li, Z.; Clemens, D. L.; Lee, B. Y.; Dillon, B. J.; Horwitz, M. A.; Zink, J. I. Mesoporous Silica Nanoparticles with pH-Sensitive Nanovalves for Delivery of Moxifloxacin Provide Improved Treatment of Lethal Pneumonic Tularemia. *ACS Nano* **2015**, *9*, 10778–10789.
- (72) Théron, C.; Gallud, A.; Carcel, C.; Gary-Bobo, M.; Maynadier, M.; García, M.; Lu, J.; Tamanoi, F.; Zink, J. I.; Wong Chi Man, M. Hybrid Mesoporous Silica Nanoparticles with pH-Operated and Complementary H-Bonding Caps as an Autonomous Drug-Delivery System. *Chem. Eur. J.* **2014**, *20*, 9372–9380.
- (73) Pourjavadi, A.; Mazaheri Tehrani, Z.; Jokar, S. Chitosan Based Supramolecular Polypseudorotaxane as a pH-Responsive Polymer and Their Hybridization with Mesoporous Silica-Coated Magnetic Graphene Oxide for Triggered Anticancer Drug Delivery. *Polym.* **2015**, *76*, 52–61.
- (74) Liu, W. T.; Yang, Y.; Shen, P. H.; Gao, X. J.; He, S. Q.; Liu, H.; Zhu, C. S. Facile and Simple Preparation of pH-Sensitive Chitosan-Mesoporous Silica Nanoparticles for Future Breast Cancer Treatment. *Express Polym. Lett.* **2015**, *9*, 1068–1075.
- (75) Pourjavadi, A.; Shakerpoor, A.; Tehrani, Z. M.; Bumajdad, A. Magnetic Graphene Oxide Mesoporous Silica Hybrid Nanoparticles with Dendritic pH Sensitive Moieties Coated by PEGylated Alginate-Co-Poly(Acrylic Acid) for Targeted and Controlled Drug Delivery Purposes. *J. Polym. Res.* **2015**, *22*, 156.
- (76) Chen, F.; Zhu, Y. Chitosan Enclosed Mesoporous Silica Nanoparticles as Drug Nano-Carriers: Sensitive Response to the Narrow pH Range. *Microporous Mesoporous Mater.* **2012**, *150*, 83–89.
- (77) Sun, Y.; Sun, Y. L.; Wang, L.; Ma, J.; Yang, Y. W.; Gao, H. Nanoassemblies Constructed from Mesoporous Silica Nanoparticles and Surface-Coated Multilayer Polyelectrolytes for Controlled Drug Delivery. *Microporous Mesoporous Mater.* **2014**, *185*, 245–253.
- (78) Wang, L.; Liu, G.; Wang, X.; Hu, J.; Zhang, G.; Liu, S. Acid-Disintegratable Polymersomes of pH-Responsive Amphiphilic Diblock Copolymers for Intracellular Drug Delivery. *Macromolecules* **2015**, *48*, 7262–7272.

- (79) Pu, F.; Liu, X.; Yang, X.; Liu, Z.; Ren, J.; Wang, S.; Qu, X. Versatile Fluorescent Conjugated Polyelectrolyte-Capped Mesoporous Silica Nanoparticles for Controlled Drug Delivery and Imaging. *Chempluschem* **2013**, *78*, 656–662.
- (80) Ma, X.; Zhao, Y.; Ng, K. W.; Zhao, Y. Integrated Hollow Mesoporous Silica Nanoparticles for Target Drug/SiRNA Co-Delivery. *Chem. Eur. J.* **2013**, *19*, 15593–15603.
- (81) Zhang, G.; Gao, J.; Qian, J.; Zhang, L.; Zheng, K.; Zhong, K.; Cai, D.; Zhang, X.; Wu, Z. Hydroxylated Mesoporous Nanosilica Coated by Polyethylenimine Coupled with Gadolinium and Folic Acid: A Tumor-Targeted T1 Magnetic Resonance Contrast Agent and Drug Delivery System. *ACS Appl. Mater. Interfaces* **2015**, *7*, 14192–14200.
- (82) Pourjavadi, A.; Tehrani, Z. M.; Bennett, C. PEG-Co-Polyvinyl Pyridine Coated Magnetic Mesoporous Silica Nanoparticles for pH-Responsive Controlled Release of Doxorubicin. *Int. J. Polym. Mater. Polym. Biomater.* **2015**, *64*, 570–577.
- (83) Pourjavadi, A.; Tehrani, Z. M. Mesoporous Silica Nanoparticles with Bilayer Coating of Poly(Acrylic Acid-Co-Itaconic Acid) and Human Serum Albumin (HSA): A pH-Sensitive Carrier for Gemcitabine Delivery. *Mater. Sci. Eng. C* **2016**, *61*, 782–790.
- (84) Du, P.; Zhao, X.; Zeng, J.; Guo, J.; Liu, P. Layer-by-Layer Engineering Fluorescent Polyelectrolyte Coated Mesoporous Silica Nanoparticles as pH-Sensitive Nanocarriers for Controlled Release. *Appl. Surf. Sci.* **2015**, *345*, 90–98.
- (85) Feng, W.; Nie, W.; He, C.; Zhou, X.; Chen, L.; Qiu, K.; Wang, W.; Yin, Z. Effect of pH-Responsive Alginate/Chitosan Multilayers Coating on Delivery Efficiency, Cellular Uptake and Biodistribution of Mesoporous Silica Nanoparticles Based Nanocarriers. *ACS Appl. Mater. Interfaces* **2014**, *6*, 8447–8460.
- (86) Wan, X.; Zhang, G.; Liu, S. PH-Disintegrable Polyelectrolyte Multilayer-Coated Mesoporous Silica Nanoparticles Exhibiting Triggered Co-Release of Cisplatin and Model Drug Molecules. *Macromol. Rapid Commun.* **2011**, *32*, 1082–1089.
- (87) Pourjavadi, A.; Tehrani, Z. M. Mesoporous Silica Nanoparticles (MCM-41) Coated PEGylated Chitosan as a pH-Responsive Nanocarrier for Triggered Release of Erythromycin. *Int. J. Polym. Mater. Polym. Biomater.* **2014**, *63*, 692–697.
- (88) Mishra, A. K.; Pandey, H.; Agarwal, V.; Ramteke, P. W.; Pandey, A. C. Nanoengineered Mesoporous Silica Nanoparticles for Smart Delivery of Doxorubicin. *J. Nanoparticle Res.* **2014**, *16*, 2515.
- (89) Guisasola, E.; Baeza, A.; Talelli, M.; Arcos, D.; Vallet-Regí, M. Design of Thermoresponsive Polymeric Gates with Opposite Controlled Release Behaviors. *RSC Adv.* **2016**, *6*, 42510–42516.
- (90) Gao, Q.; Xu, Y.; Wu, D.; Shen, W.; Deng, F. Synthesis, Characterization, and *in vitro* pH-Controllable Drug Release from Mesoporous Silica Spheres with Switchable Gates. *Langmuir* **2010**, *26*, 17133–17138.
- (91) Xu, X.; Lü, S.; Gao, C.; Wang, X.; Bai, X.; Gao, N.; Liu, M. Facile Preparation of pH-Sensitive and Self-Fluorescent Mesoporous Silica Nanoparticles Modified

- with PAMAM Dendrimers for Label-Free Imaging and Drug Delivery. *Chem. Eng. J.* **2015**, 266, 171–178.
- (92) Pourjavadi, A.; Tehrani, Z. M.; Moghanaki, A. A. Folate-Conjugated pH-Responsive Nanocarrier Designed for Active Tumor Targeting and Controlled Release of Gemcitabine. *Pharm. Res.* **2015**, 417–432.
- (93) Tian, Y.; Glogowska, A.; Zhong, W.; Klonisch, T.; Xing, M. Polymeric Mesoporous Silica Nanoparticles as a pH-Responsive Switch to Control Doxorubicin Intracellular Delivery. *J. Mater. Chem. B* **2013**, 1, 5264–5272.
- (94) Tian, Y.; Kong, Y.; Li, X.; Wu, J.; Ko, A. C.-T.; Xing, M. Light- and pH-Activated Intracellular Drug Release from Polymeric Mesoporous Silica Nanoparticles. *Colloids Surf. B. Biointerfaces* **2015**, 134, 147–155.
- (95) Chen, T.; Wu, W.; Xiao, H.; Chen, Y.; Chen, M.; Li, J. Intelligent Drug Delivery System Based on Mesoporous Silica Nanoparticles Coated with an Ultra-pH-Sensitive Gatekeeper and Poly(Ethylene Glycol). *ACS Macro Lett.* **2016**, 5, 55–58.
- (96) Sun, J. T.; Hong, C. Y.; Pan, C. Y. Fabrication of PDEAEMA-Coated Mesoporous Silica Nanoparticles and pH-Responsive Controlled Release. *J. Phys. Chem. C* **2010**, 114, 12481–12486.
- (97) Yu, F.; Tang, X.; Pei, M. Facile Synthesis of PDMAEMA-Coated Hollow Mesoporous Silica Nanoparticles and Their pH-Responsive Controlled Release. *Microporous Mesoporous Mater.* **2013**, 173, 64–69.
- (98) Yang, M. Y.; Tan, L.; Wu, H. X.; Liu, C. J.; Zhuo, R. X. Dual-Stimuli-Responsive Polymer-Coated Mesoporous Silica Nanoparticles Used for Controlled Drug Delivery. *J. Appl. Polym. Sci.* **2015**, 132, 1–9.
- (99) Zhang, Y.; Ang, C. Y.; Li, M.; Tan, S. Y.; Qu, Q.; Luo, Z.; Zhao, Y. Polymer-Coated Hollow Mesoporous Silica Nanoparticles for Triple-Responsive Drug Delivery. *ACS Appl. Mater. Interfaces* **2015**, 7, 18179–18187.
- (100) Han, J.; Sun, J.; Bai, S.; Panezai, H.; Jin, X.; Wu, X. “Graft to” Synthesis and Ibuprofen-Loading Performance of pH-Sensitive PMAA-Silica Hybrid Nanoparticles with Controlled Bimodal Mesopores. *J. Pharm. Sci.* **2015**, 104, 4299–4306.
- (101) Zhang, H.; Bai, S.; Sun, J.; Han, J.; Guo, Y. pH-Responsive Ibuprofen Delivery in Silane-Modified Poly(Methylacrylic Acid) Coated Bimodal Mesoporous Silicas. *Mater. Res. Bull.* **2014**, 53, 266–271.
- (102) Wen, H.; Guo, J.; Chang, B.; Yang, W. pH-Responsive Composite Microspheres Based on Magnetic Mesoporous Silica Nanoparticle for Drug Delivery. *Eur. J. Pharm. Biopharm.* **2013**, 84, 91–98.
- (103) Xing, R.; Lin, H.; Jiang, P.; Qu, F. Biofunctional Mesoporous Silica Nanoparticles for Magnetically Oriented Target and pH-Responsive Controlled Release of Ibuprofen. *Colloids Surfaces A Physicochem. Eng. Asp.* **2012**, 403, 7–14.
- (104) Chang, B.; Chen, D.; Wang, Y.; Chen, Y.; Jiao, Y.; Sha, X.; Yang, W. Bioresponsive Controlled Drug Release Based on Mesoporous Silica Nanoparticles Coated with Reductively Sheddable Polymer Shell. *Chem. Mater.*

2013, 25, 574–585.

- (105) Zhang, X.; Yang, P.; Dai, Y.; Ma, P.; Li, X.; Cheng, Z.; Hou, Z.; Kang, X.; Li, C.; Lin, J. Multifunctional Up-Converting Nanocomposites with Smart Polymer Brushes Gated Mesopores for Cell Imaging and Thermo/pH Dual-Responsive Drug Controlled Release. *Adv. Funct. Mater.* **2013**, 23, 4067–4078.
- (106) Lv, R.; Yang, P.; He, F.; Gai, S.; Yang, G.; Dai, Y.; Hou, Z.; Lin, J. An Imaging-Guided Platform for Synergistic Photodynamic/Photothermal/Chemo-Therapy with pH/Temperature-Responsive Drug Release. *Biomaterials* **2015**, 63, 115–127.
- (107) Peng, H.; Dong, R.; Wang, S.; Zhang, Z.; Luo, M.; Bai, C.; Zhao, Q.; Li, J.; Chen, L.; Xiong, H. A pH-Responsive Nano-Carrier with Mesoporous Silica Nanoparticles Cores and Poly(Acrylic Acid) Shell-Layers: Fabrication, Characterization and Properties for Controlled Release of Salidroside. *Int. J. Pharm.* **2013**, 446, 153–159.
- (108) Samart, C.; Prawingwong, P.; Amnuaypanich, S.; Zhang, H.; Kajiyoshi, K.; Reubroycharoen, P. Preparation of Poly(Acrylic Acid) Grafted-Mesoporous Silica as pH-Responsive Releasing Material. *J. Ind. Eng. Chem.* **2014**, 20, 2153–2158.
- (109) Hong, C.-Y.; Li, X.; Pan, C.-Y. Fabrication of Smart Nanocontainers with a Mesoporous Core and a pH-Responsive Shell for Controlled Uptake and Release. *J. Mater. Chem.* **2009**, 19, 5155–5160.
- (110) Yuan, L.; Tang, Q.; Yang, D.; Zhang, J. Z.; Zhang, F.; Hu, J. Preparation of pH-Responsive Mesoporous Silica Nanoparticles and Their Application in Controlled Drug Delivery. *J. Phys. Chem. C* **2011**, 115, 9926–9932.
- (111) Wu, H.; Tang, L.; An, L.; Wang, X.; Zhang, H.; Shi, J.; Yang, S. pH-Responsive Magnetic Mesoporous Silica Nanospheres for Magnetic Resonance Imaging and Drug Delivery. *React. Funct. Polym.* **2012**, 72, 329–336.
- (112) Zhang, Y.; Han, L.; Hu, L.-L.; Chang, Y.-Q.; He, R.-H.; Chen, M.-L.; Shu, Y.; Wang, J.-H. Mesoporous Carbon Nanoparticles Capped with Poly(Acrylic Acid) as Drug Carrier for Bi-Trigger Continuous Drug Release. *J. Mater. Chem. B* **2016**, 4, 5178–5184.
- (113) Bilalis, P.; Tziveleka, L.-A.; Varlas, S.; Iatrou, H. pH-Sensitive Nanogates Based on Poly(l-Histidine) for Controlled Drug Release from Mesoporous Silica Nanoparticles. *Polym. Chem.* **2016**, 7, 1475–1485.
- (114) Liu, R.; Liao, P.; Liu, J.; Feng, P. Responsive Polymer-Coated Mesoporous Silica as a pH-Sensitive Nanocarrier for Controlled Release. *Langmuir* **2011**, 27, 3095–3099.
- (115) Rafi, A. A.; Mahkam, M.; Davaran, S.; Hamishehkar, H. A Smart PH-Responsive Nano-Carrier as a Drug Delivery System: A Hybrid System Comprised of Mesoporous Nanosilica MCM-41 (as a Nano-Container) & a pH-Sensitive Polymer (as Smart Reversible Gatekeepers): Preparation, Characterization and *in vitro* Release. *Eur. J. Pharm. Sci.* **2016**, 93, 64–73.
- (116) Niedermayer, S.; Weiss, V.; Herrmann, A.; Schmidt, A.; Datz, S.; Müller, K.; Wagner, E.; Bein, T.; Bräuchle, C. Multifunctional Polymer-Capped Mesoporous Silica Nanoparticles for pH-Responsive Targeted Drug Delivery. *Nanoscale* **2015**,

- 7, 7953–7964.
- (117) Xi, J.; Qin, J.; Fan, L. Chondroitin Sulfate Functionalized Mesostructured Silica Nanoparticles as Biocompatible Carriers for Drug Delivery. *Int. J. Nanomedicine* **2012**, *7*, 5235–5247.
- (118) Chang, B.; Sha, X.; Guo, J.; Jiao, Y.; Wang, C.; Yang, W. Thermo and pH Dual Responsive, Polymer Shell Coated, Magnetic Mesoporous Silica Nanoparticles for Controlled Drug Release. *J. Mater. Chem.* **2011**, *21*, 9239–9247.
- (119) Chen, Y.; Yang, W.; Chang, B.; Hu, H.; Fang, X.; Sha, X. *In vivo* Distribution and Antitumor Activity of Doxorubicin-Loaded N-Isopropylacrylamide-Co-Methacrylic Acid Coated Mesoporous Silica Nanoparticles and Safety Evaluation. *Eur. J. Pharm. Biopharm.* **2013**, *85*, 406–412.
- (120) Liu, X.; Yu, D.; Jin, C.; Song, X.; Cheng, J.; Zhao, X.; Qi, X.; Zhang, G. A Dual Responsive Targeted Drug Delivery System Based on Smart Polymer Coated Mesoporous Silica for Laryngeal Carcinoma Treatment. *New J. Chem.* **2014**, *38*, 4830–4836.
- (121) Wu, X.; Wang, Z.; Zhu, D.; Zong, S.; Yang, L.; Zhong, Y.; Cui, Y. pH and Thermo Dual-Stimuli-Responsive Drug Carrier Based on Mesoporous Silica Nanoparticles Encapsulated in a Copolymer-Lipid Bilayer. *ACS Appl. Mater. Interfaces* **2013**, *5*, 10895–10903.
- (122) Chen, L.; Di, J.; Cao, C.; Zhao, Y.; Ma, Y.; Luo, J.; Wen, Y.; Song, W.; Song, Y.; Jiang, L. A pH-Driven DNA Nanoswitch for Responsive Controlled Release. *Chem. Commun.* **2011**, *47*, 2850–2852.
- (123) Chen, M.; Yang, S.; He, X.; Wang, K.; Qiu, P.; He, D. Co-Loading of Coralyne and Indocyanine Green into Adenine DNA-Functionalized Mesoporous Silica Nanoparticles for pH- and near-Infrared-Responsive Chemothermal Treatment of Cancer Cells. *J. Mater. Chem. B* **2014**, *2*, 6064–6071.
- (124) He, D. G.; He, X. X.; Wang, K. M.; Chen, M. A.; Zhao, Y. X.; Zou, Z. Intracellular Acid-Triggered Drug Delivery System Using Mesoporous Silica Nanoparticles Capped with T-Hg<sup>2+</sup>-T Base Pairs Mediated Duplex DNA. *J. Mater. Chem. B* **2013**, *1*, 1552–1560.
- (125) Murai, K.; Higuchi, M.; Kinoshita, T.; Nagata, K.; Kato, K. Design of a Nanocarrier with Regulated Drug Release Ability Utilizing a Reversible Conformational Transition of a Peptide, Responsive to Slight Changes in pH. *Phys. Chem. Chem. Phys.* **2013**, *15*, 11454–11460.
- (126) Chen, C.; Pu, F.; Huang, Z.; Liu, Z.; Ren, J.; Qu, X. Stimuli-Responsive Controlled-Release System Using Quadruplex DNA-Capped Silica Nanocontainers. *Nucleic Acids Res.* **2011**, *39*, 1638–1644.
- (127) Xue, M.; Findenegg, G. H. Lysozyme as a pH-Responsive Valve for the Controlled Release of Guest Molecules from Mesoporous Silica. *Langmuir* **2012**, *28*, 17578–17584.
- (128) Traverso, N.; Ricciarelli, R.; Nitti, M.; Marengo, B.; Furfaro, A. L.; Pronzato, M. A.; Marinari, U. M.; Domenicotti, C. Role of Glutathione in Cancer Progression and Chemoresistance. *Oxid. Med. Cell. Longev.* **2013**, *2013*.



- (129) Estrela, J. M.; Ortega, A.; Obrador, E. Glutathione in Cancer Biology and Therapy. *Crit. Rev. Clin. Lab. Sci.* **2006**, *43*, 143–181.
- (130) Balendiran, G. K.; Dabur, R.; Fraser, D. The Role of Glutathione in Cancer. *Cell Biochem. Funct.* **2004**, *22*, 343–352.
- (131) Cheng, R.; Feng, F.; Meng, F.; Deng, C.; Feijen, J.; Zhong, Z. Glutathione-Responsive Nano-Vehicles as a Promising Platform for Targeted Intracellular Drug and Gene Delivery. *J. Control. Release* **2011**, *152*, 2–12.
- (132) Guo, X.; Cheng, Y.; Zhao, X.; Luo, Y.; Chen, J.; Yuan, W. E. Advances in Redox-Responsive Drug Delivery Systems of Tumor Microenvironment. *J. Nanobiotechnology* **2018**, *16*.
- (133) Sternberg, P.; Mody, V. C.; Carlson, J. L.; Jones, D. P.; Cai, J.; Lynn, M. J. Redox State of Glutathione in Human Plasma. *Free Radic. Biol. Med.* **2002**, *28*, 625–635.
- (134) Han, L.; Zhang, X. Y.; Wang, Y. L.; Li, X.; Yang, X. H.; Huang, M.; Hu, K.; Li, L. H.; Wei, Y. Redox-Responsive Theranostic Nanoplatfoms Based on Inorganic Nanomaterials. *J. Control. Release* **2017**, *259*, 40–52.
- (135) Huo, M.; Yuan, J.; Tao, L.; Wei, Y. Redox-Responsive Polymers for Drug Delivery: From Molecular Design to Applications. *Polym. Chem.* **2014**, *5*, 1519–1528.
- (136) Sun, H.; Guo, B.; Cheng, R.; Meng, F.; Liu, H.; Zhong, Z. Biodegradable Micelles with Sheddable Poly(Ethylene Glycol) Shells for Triggered Intracellular Release of Doxorubicin. *Biomaterials* **2009**, *30*, 6358–6366.
- (137) Kataoka, K.; Harada, A.; Nagasaki, Y. Block Copolymer Micelles for Drug Delivery: Design, Characterization and Biological Significance. *Adv. Drug Deliv. Rev.* **2001**, *47*, 113–131.
- (138) Sun, H.; Guo, B.; Li, X.; Cheng, R.; Meng, F.; Liu, H. Shell-Sheddable Micelles Based on Dextran-SS-Poly ( $\epsilon$ -Caprolactone) Diblock Copolymer for Efficient Intracellular Release of Doxorubicin. *Biomacromolecules* **2010**, *11*, 848–854.
- (139) Tang, L.; Wang, Y.; Li, Y.; Du, J.; Wang, J. Shell-Detachable Micelles Based on Disulfide-Linked Block Copolymer As Potential Carrier for Intracellular Drug Delivery. *Bioconjug. Chem.* **2009**, *20*, 1095–1099.
- (140) Klaikherd, A.; Nagamani, C.; Thayumanavan, S. Multi-Stimuli Sensitive Amphiphilic Block Copolymer Assemblies. *J. Am. Chem. Soc.* **2009**, *131*, 4830–4838.
- (141) Park, K. M.; Lee, D.; Sarkar, B.; Jung, H.; Kim, J.; Ko, H.; Lee, K. E.; Jeon, H.; Kim, K. Reduction-Sensitive, Robust Vesicles with a Non-Covalently Modifiable Surface as a Multifunctional Drug-Delivery Platform. *Small* **2010**, *6*, 1430–1441.
- (142) Hell, A. J. Van; Fretz, M. M.; Crommelin, D. J. A.; Hennink, W. E.; Mastrobattista, E. Peptide Nanocarriers for Intracellular Delivery of Photosensitizers. *J. Control. Release* **2010**, *141*, 347–353.
- (143) Hell, A. J. Van; Crommelin, D. J. A.; Hennink, W. E.; Mastrobattista, E. Stabilization of Peptide Vesicles by Introducing Inter-Peptide Disulfide Bonds. *Pharm. Res.* **2009**, *26*, 2186–2193.

- (144) Xu, H.; Meng, F.; Zhong, Z. Reversibly Crosslinked Temperature-Responsive Nano-Sized Polymersomes: Synthesis and Triggered Drug Release. *J. Mater. Chem.* **2009**, *19*, 4183–4190.
- (145) Sexton, A.; Whitney, P. G.; Chong, S.; Zelikin, A. N.; Johnston, A. P. R.; Rose, R. De; Brooks, A. G.; Caruso, F.; Kent, S. J. A Protective Vaccine Delivery System for *in vivo* T Cell Stimulation Using Nanoengineered Polymer Hydrogel Capsules. *ACS Nano* **2009**, *3*, 3391–3400.
- (146) Sivakumar, B. S.; Bansal, V.; Cortez, C.; Chong, S.; Zelikin, A. N.; Caruso, F. Degradable, Surfactant-Free, Monodisperse Polymer-Encapsulated Emulsions as Anticancer Drug Carriers. *Adv. Mater.* **2009**, *21*, 1820–1824.
- (147) Ma, X.; Özliseli, E.; Zhang, Y.; Pan, G.; Wang, D.; Zhang, H. Fabrication of Redox-Responsive Doxorubicin and Paclitaxel Prodrug Nanoparticles with Microfluidics for Selective Cancer Therapy. *Biomater. Sci.* **2019**, *7*, 634–644.
- (148) Pauletti, G. M.; Cai, X.; Shi, D.; Li, Y. Self-Assembling Nanomicelles of a Novel Camptothecin Prodrug Engineered with a Redox-Responsive Release Mechanism. *Chem. Commun.* **2011**, *47*, 8647–8649.
- (149) Navath, R. S.; Wang, B.; Kannan, S.; Romero, R.; Kannan, R. M. Stimuli-Responsive Star Poly(Ethylene Glycol) Drug Conjugates for Improved Intracellular Delivery of the Drug in Neuroinflammation. *J. Control. Release* **2010**, *142*, 447–456.
- (150) Kurtoglu, Y. E.; Navath, R. S.; Wang, B.; Kannan, S.; Romero, R.; Kannan, R. M. Poly(Amidoamine) Dendrimer–Drug Conjugates with Disulfide Linkages for Intracellular Drug Delivery. *Biomaterials* **2009**, *30*, 2112–2121.
- (151) Navath, R. S.; Kurtoglu, Y. E.; Wang, B.; Kannan, S.; Romero, R.; Kannan, R. M. Dendrimer–Drug Conjugates for Tailored Intracellular Drug Release Based on Glutathione Levels. *Bioconjug. Chem.* **2008**, *19*, 2446–2455.
- (152) Jung, S.; Lee, S. H.; Mok, H.; Chung, H. J.; Park, T. G. Gene Silencing Efficiency of SiRNA-PEG Conjugates: Effect of PEGylation Site and PEG Molecular Weight. *J. Control. Release* **2010**, *144*, 306–313.
- (153) Takemoto, H.; Ishii, A.; Miyata, K.; Nakanishi, M.; Oba, M.; Ishii, T.; Yamasaki, Y.; Nishiyama, N.; Kataoka, K. Polyion Complex Stability and Gene Silencing Efficiency with a SiRNA-Grafted Polymer Delivery System. *Biomaterials* **2010**, *31*, 8097–8105.
- (154) Li, Z.; Zhang, C.; Wang, B.; Wang, H.; Chen, X.; Möhwald, H.; Cui, X. Sonochemical Fabrication of Dual-Targeted Redox-Responsive Smart Microcarriers. *ACS Appl. Mater. Interfaces* **2014**, *6*, 22166–22173.
- (155) Luo, Z.; Cai, K.; Hu, Y.; Li, J.; Ding, X.; Zhang, B.; Xu, D.; Yang, W.; Liu, P. Redox-Responsive Molecular Nanoreservoirs for Controlled Intracellular Anticancer Drug Delivery Based on Magnetic Nanoparticles. *Adv. Mater.* **2012**, *24*, 431–435.
- (156) Tao, Y.; Han, J.; Ye, C.; Thomas, T.; Dou, H. Reduction-Responsive Gold-Nanoparticle-Conjugated Pluronic Micelles: An Effective Anti-Cancer Drug Delivery System. *J. Mater. Chem.* **2012**, *22*, 18864–18871.

- (157) Hong, R.; Han, G.; Fernández, J. M.; Kim, B.; Forbes, N. S.; Rotello, V. M. Glutathione-Mediated Delivery and Release Using Monolayer Protected Nanoparticle Carriers. *J. Am. Chem. Soc.* **2006**, *128*, 1078–1079.
- (158) Yang, S.; Sun, J.; He, P.; Deng, X.; Wang, Z.; Hu, C.; Ding, G.; Xie, X. Selenium Doped Graphene Quantum Dots as an Ultrasensitive Redox Fluorescent Switch. *Chem. Mater.* **2015**, *27*, 2004–2011.
- (159) Li, D.; He, J.; Cheng, W.; Wu, Y.; Hu, Z.; Tian, H.; Huang, Y. Redox-Responsive Nanoreservoirs Based on Collagen End-Capped Mesoporous Hydroxyapatite Nanoparticles for Targeted Drug Delivery. *J. Mater. Chem. B* **2014**, *2*, 6089–6096.
- (160) Luo, Z.; Ding, X.; Hu, Y.; Wu, S.; Xiang, Y.; Zeng, Y.; Zhang, B.; Yan, H.; Zhang, H.; Zhu, L.; *et al.* Engineering a Hollow Nanocontainer Platform with Multifunctional Molecular Machines for Tumor-Targeted Therapy *in vitro* and *in vivo*. *ACS Nano* **2013**, *7*, 10271–10284.
- (161) Zhang, J.; Yuan, Z.-F.; Wang, Y.; Chen, W.-H.; Luo, G.-F.; Cheng, S.-X.; Zhuo, R.-X.; Zhang, X.-Z. Multifunctional Envelope-Type Mesoporous Silica Nanoparticles for Tumor-Triggered Targeting Drug Delivery. *J. Am. Chem. Soc.* **2013**, *135*, 5068–5073.
- (162) Luo, Z.; Cai, K.; Hu, Y.; Zhao, L.; Liu, P.; Duan, L.; Yang, W. Mesoporous Silica Nanoparticles End-Capped with Collagen: Redox-Responsive Nanoreservoirs for Targeted Drug Delivery. *Angew. Chemie Int. Ed.* **2011**, *50*, 640–643.
- (163) Cui, Y.; Dong, H.; Cai, X.; Wang, D.; Li, Y. Mesoporous Silica Nanoparticles Capped with Disulfide-Linked PEG Gatekeepers for Glutathione-Mediated Controlled Release. *ACS Appl. Mater. Interfaces* **2012**, *4*, 3177–3183.
- (164) Li, Z.-Y.; Hu, J.-J.; Xu, Q.; Chen, S.; Jia, H.-Z.; Sun, Y.-X.; Zhuo, R.-X.; Zhang, X.-Z. A Redox-Responsive Drug Delivery System Based on RGD Containing Peptide-Capped Mesoporous Silica Nanoparticles. *J. Mater. Chem. B* **2015**, *3*, 39–44.
- (165) Zhang, B.; Luo, Z.; Liu, J.; Ding, X.; Li, J.; Cai, K. Cytochrome c End-Capped Mesoporous Silica Nanoparticles as Redox-Responsive Drug Delivery Vehicles for Liver Tumor-Targeted Triplex Therapy *in vitro* and *in vivo*. *J. Control. Release* **2014**, *192*, 192–201.
- (166) Sun, X.; Zhao, Y.; Lin, V. S.-Y.; Slowing, I. I.; Trewyn, B. G. Luciferase and Luciferin Co-Immobilized Mesoporous Silica Nanoparticle Materials for Intracellular Biocatalysis. *J. Am. Chem. Soc.* **2011**, *133*, 18554–18557.
- (167) Muhammad, F.; Wang, A.; Qi, W.; Zhang, S.; Zhu, G. Intracellular Antioxidants Dissolve Man-Made Antioxidant Nanoparticles: Using Redox Vulnerability of Nanocerium to Develop a Responsive Drug Delivery System. *ACS Appl. Mater. Interfaces* **2014**, *6*, 19424–19433.
- (168) Li, H.; Zhang, J. Z.; Tang, Q.; Du, M.; Hu, J.; Yang, D. Reduction-Responsive Drug Delivery Based on Mesoporous Silica Nanoparticle Core with Crosslinked Poly(Acrylic Acid) Shell. *Mater. Sci. Eng. C* **2013**, *33*, 3426–3431.
- (169) Croissant, J. G.; Fatieiev, Y.; Khashab, N. M. Degradability and Clearance of Silicon, Organosilica, Silsesquioxane, Silica Mixed Oxide, and Mesoporous Silica

- Nanoparticles. *Adv. Mater.* **2017**, *29*, 1604634.
- (170) Xiong, H.; Guo, Z.; Zhang, W.; Zhong, H.; Liu, S.; Ji, Y. Redox-Responsive Biodegradable PEGylated Nanographene Oxide for Efficiently Chemo-Photothermal Therapy: A Comparative Study with Non-Biodegradable PEGylated Nanographene Oxide. *J. Photochem. Photobiol. B Biol.* **2014**, *138*, 191–201.
- (171) Al-Nahain, A.; Lee, S. Y.; In, I.; Lee, K. D.; Park, S. Y. Triggered PH/Redox Responsive Release of Doxorubicin from Prepared Highly Stable Graphene with Thiol Grafted Pluronic. *Int. J. Pharm.* **2013**, *450*, 208–217.
- (172) Amir, R. J.; Pessah, N.; Shamis, M.; Shabat, D. Self-Immolative Dendrimers. *Angew. Chemie Int. Ed.* **2003**, *42*, 4494–4499.
- (173) Sagi, A.; Weinstain, R.; Karton, N.; Shabat, D. Self-Immolative Polymers. *J. Am. Chem. Soc.* **2008**, *8*, 5434–5435.
- (174) Alouane, A.; Saux, T. Le; Schmidt, F.; Jullien, L. Self-Immolative Spacers: Kinetic Aspects, Structure–Property Relationships, and Applications. *Angew. Chemie Int. Ed.* **2015**, *54*, 7492–7509.
- (175) Chen, E. K. Y.; McBride, R. A.; Gillies, E. R. Self-Immolative Polymers Containing Rapidly Cyclizing Spacers: Toward Rapid Depolymerization Rates. *Macromolecules* **2012**, *45*, 7364–7374.
- (176) Walther, R.; Rautio, J.; Zelikin, A. N. Prodrugs in Medicinal Chemistry and Enzyme Prodrug Therapies. *Adv. Drug Deliv. Rev.* **2017**, *118*, 65–77.
- (177) Gondi, C. S.; Rao, J. S. Cathepsin B as a Cancer Target. *Expert Opin. Ther. Targets* **2013**, *17*, 281–291.
- (178) Chowdhury, M. A.; Moya, I. A.; Bhilocha, S.; Mcmillan, C. C.; Vigliarolo, B. G.; Zehbe, I.; Phenix, C. P. Prodrug-Inspired Probes Selective to Cathepsin B over Other Cysteine Cathepsins. *J. Med. Chem.* **2014**, *57*, 6092–6104.
- (179) Shao, L.-H.; Liu, S.-P.; Hou, J.-X.; Zhang, Y.-H.; Peng, C.-W.; Zhong, Y.-J.; Liu, X.; Liu, X.-L.; Hong, Y.-P.; Firestone, R. A.; *et al.* Cathepsin B Cleavable Novel Prodrug Ac-Phe-Lys-PABC-ADM Enhances Efficacy at Reduced Toxicity in Treating Gastric Cancer Peritoneal Carcinomatosis. *Cancer* **2012**, *118*, 2986–2996.
- (180) Zhang, H.; Xu, C.; Liu, J.; Li, X.; Guo, L.; Li, X. Enzyme-Activatable Probe with a Self-Immolative Linker for Rapid and Sensitive Alkaline Phosphatase Detection and Cell Imaging through Cascade Reaction. *Chem. Commun.* **2015**, *51*, 7031–7034.
- (181) Li, B.; Liu, P.; Yan, D.; Zeng, F.; Wu, S. A Self-Immolative and DT-Diaphorase-Activatable Prodrug for Drug-Release Tracking and Therapy. *J. Mater. Chem. B* **2017**, *5*, 2635–2643.
- (182) Ding, S.; Pickard, A. J.; Kucera, G. L.; Bierbach, U. Design of Enzymatically Cleavable Prodrugs of a Potent Platinum-Containing Anticancer Agent. *Chem. Eur. J.* **2014**, *20*, 16164–16173.
- (183) Redy-Keisar, O.; Ferber, S.; Satchi-Fainaro, R.; Shabat, D. NIR Fluorogenic Dye as a Modular Platform for Prodrug Assembly: Real-Time *in vivo* Monitoring of

- Drug Release. *ChemMedChem* **2015**, *10*, 999–1007.
- (184) Latorre, A.; Posch, C.; Garcimart, Y.; Celli, A.; Sanlorenzo, M.; Vujic, I.; Ma, J.; Zekhtser, M.; Rappersberger, K.; Ortiz-Urda, S.; *et al.* DNA and Aptamer Stabilized Gold Nanoparticles for Targeted Delivery of Anticancer Therapeutics. *Nanoscale* **2014**, *6*, 7436–7442.
- (185) Wang, Z.; Wu, H.; Liu, P.; Zeng, F.; Wu, S. A Self-Immolative Prodrug Nanosystem Capable of Releasing a Drug and a NIR Reporter for *in vivo* Imaging and Therapy. *Biomaterials* **2017**, *139*, 139–150.
- (186) Rao, J. P.; Geckeler, K. E. Polymer Nanoparticles: Preparation Techniques and Size-Control Parameters. *Prog. Polym. Sci.* **2011**, *36*, 887–913.
- (187) Esser-Kahn, A. P.; Sottos, N. R.; White, S. R.; Moore, J. S. Programmable Microcapsules from Self-Immolative Polymers. *J. Am. Chem. Soc.* **2010**, *132*, 10266–10268.
- (188) Fomina, N.; Mcfearin, C.; Sermsakdi, M.; Edigin, O.; Almutairi, A. UV and Near-IR Triggered Release from Polymeric Nanoparticles. *J. Am. Chem. Soc.* **2010**, *132*, 9540–9542.
- (189) Ma, L.; Baumgartner, R.; Zhang, Y.; Song, Z.; Cai, K.; Cheng, J. UV-Responsive Degradable Polymers Derived from 1-(4-Aminophenyl). *J. Polym. Sci. Part A Polym. Chem.* **2015**, *53*, 1161–1168.
- (190) Fomina, N.; McFearin, C.; Sermsakdi, M.; Edigin, O.; Almutairi, A. UV and Near-IR Triggered Release from Polymeric Nanoparticles. *J. Am. Chem. Soc.* **2010**, *132*, 9540–9542.
- (191) Lux, C. D. G.; Mcfearin, C. L.; Joshi-Barr, S.; Sankaranarayanan, J.; Fomina, N.; Almutairi, A. Single UV or Near IR Triggering Event Leads to Polymer Degradation into Small Molecules. *ACS Macro Lett.* **2012**, *1*, 922–926.
- (192) Jäger, E.; Höcherl, A.; Janou, O.; Jäger, A.; Hrubý, M.; Netopilik, M.; Miroslav, Š.; Ulbrich, K.; Petr, Š. Fluorescent Boronate-Based Polymer Nanoparticles with Reactive Oxygen Species (ROS)-Triggered Cargo Release for Drug-Delivery Applications. *Nanoscale* **2016**, *8*, 6958–6963.
- (193) Cui, Y.; Zhang, M.; Du, F.; Li, Z. Facile Synthesis of H<sub>2</sub>O<sub>2</sub>-Cleavable Poly(Ester-Amide)s by Passerini Multicomponent Polymerization. *ACS Macro Lett.* **2017**, *6*, 11–15.
- (194) De Gracia Lux, C.; Joshi-Barr, S.; Nguyen, T.; Mahmoud, E.; Schopf, E.; Fomina, N.; Almutairi, A. Biocompatible Polymeric Nanoparticles Degrade and Release Cargo in Response to Biologically Relevant Levels of Hydrogen Peroxide. *J. Am. Chem. Soc.* **2012**, *134*, 15758–15764.
- (195) Lux, C. D. G.; Almutairi, A. Intramolecular Cyclization for Stimuli-Controlled Depolymerization of Polycaprolactone Particles Leading to Disassembly and Payload Release. *ACS Macro Lett.* **2013**, *2*, 432–435.
- (196) De Gracia Lux, C.; Olejniczak, J.; Fomina, N.; Viger, M. L.; Almutairi, A. Intramolecular Cyclization Assistance for Fast Degradation of Ornithine-Based Poly(Ester Amide)s. *J. Polym. Sci. Part A Polym. Chem.* **2013**, *51*, 3783–3790.

- (197) Wang, Z.; Sun, J.; Jia, X. Self-Immolative Nanoparticles Triggered by Hydrogen Peroxide and PH. *J. Polym. Sci. Part A Polym. Chem.* **2014**, *52*, 1962–1969.
- (198) Gillies, E. R.; Fan, B.; Trant, J. F.; Gillies, E. R. Thermo-Responsive Self-Immolative Nanoassemblies: Direct and Indirect Triggering. *Chem. Commun.* **2017**, *53*, 12068–12071.
- (199) Xu, Z.; Liu, S.; Kang, Y.; Wang, M. Glutathione-Responsive Polymeric Micelles Formed by a Biodegradable Amphiphilic Triblock Copolymer for Anticancer Drug Delivery and Controlled Release. *ACS Biomater. Sci.* **2015**, *1*, 585–592.
- (200) Song, C.; Ji, R.; Du, F.; Li, Z. Oxidation-Responsive Poly(Amino Ester)s Containing Arylboronic Ester and Self-Immolative Motif: Synthesis and Degradation Study. *Macromolecules* **2013**, *46*, 8416–8425.
- (201) Fan, B.; Gillies, E. R. Poly(Ethyl Glyoxylate)-Poly(Ethylene Oxide) Nanoparticles: Stimuli- Responsive Drug Release via End-to-End Polyglyoxylate Depolymerization. *Mol. Pharm.* **2017**, *14*, 2548–2559.
- (202) Wang, X.; Liu, G.; Hu, J.; Zhang, G.; Liu, S. Concurrent Block Copolymer Polymersome Stabilization and Bilayer Permeabilization by Stimuli-Regulated “Traceless” Crosslinking. *Angew. Chemie Int. Ed.* **2014**, *53*, 3138–3142.
- (203) Liu, G.; Wang, X.; Hu, J.; Zhang, G.; Liu, S. Self-Immolative Polymersomes for High-Efficiency Triggered Release and Programmed Enzymatic Reactions. *J. Am. Chem. Soc.* **2014**, *136*, 7492–7497.
- (204) Li, Y.; Liu, G.; Wang, X.; Hu, J.; Liu, S. Polymeric Vesicles Enzyme-Responsive Polymeric Vesicles for Bacterial-Strain-Selective Delivery of Antimicrobial Agents. *Angew. Chemie Int. Ed.* **2016**, *55*, 1760–1764.
- (205) Tan, X.; Li, B. B.; Lu, X.; Jia, F.; Santori, C.; Menon, P.; Li, H.; Zhang, B.; Zhao, J. J.; Zhang, K. Light-Triggered , Self-Immolative Nucleic Acid-Drug Nanostructures. *J. Am. Chem. Soc.* **2015**, *137*, 6112–6115.
- (206) Tan, X.; Lu, X.; Jia, F.; Liu, X.; Sun, Y.; Logan, J. K.; Zhang, K.; Tan, X.; Lu, X.; Jia, F.; *et al.* Blurring the Role of Oligonucleotides: Spherical Nucleic Acids as a Drug Delivery Vehicle. *J. Am. Chem. Soc.* **2016**, *138*, 10834–10837.
- (207) Xie, Y.; Murray-stewart, T.; Wang, Y.; Yu, F.; Li, J.; Marton, L. J.; Casero, R. A.; Oupický, D. Self-Immolative Nanoparticles for Simultaneous Delivery of MicroRNA and Targeting of Polyamine Metabolism in Combination Cancer Therapy. *J. Control. Release* **2017**, *246*, 110–119.
- (208) Peng, Z.; Xie, Y.; Wang, Y.; Li, J.; Oupicky, D. Dual-Function Polymeric HPMA Prodrugs for the Delivery of MiRNA. *Mol. Pharm.* **2017**, *14*, 1395–1404.

## 2.2. Self-Immolative Polymers as Novel pH-Responsive gatekeepers for Mesoporous Silica Nanoparticles

### 2.2.1. Introduction

This first piece of research consisted in developing a smart stimuli-responsive drug delivery system using mesoporous silica nanoparticles as carriers and a polymeric coating as gatekeeper.

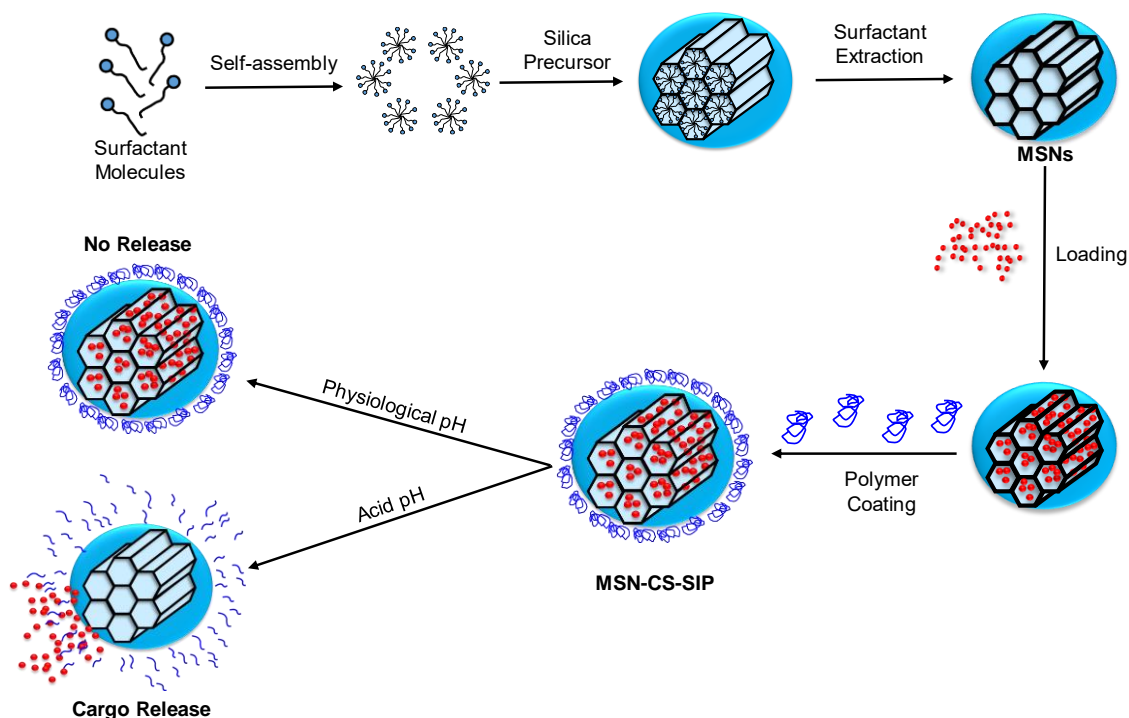
Mesoporous silica nanoparticles were synthesized following a modification of the well-known Stöber method and their successful synthesis was verified through several characterization techniques.

Regarding the responsive behavior, pH was selected as trigger owing to the differences found through the organism. Then, the gatekeeper should be able to change its conformation upon variations in pH. In this sense, the possibility of using a self-immolative polymer to obtain such behavior was explored. The idea was to use a polymer that would maintain its integrity at physiological pH, and when exposed to an acid environment it would disassemble into its functional units.

The synthesis of the here employed self-immolative polymer involved many modifications of a previously reported method. The monomer was easily synthesized but the polymerization required several attempts. During this process, two main interrelated challenges were found: (1) being able to introduce a significant amount of pH-responsive trigger into the polymeric chain and (2) being able to synthesize a polymeric chain long enough to close the mesopores. For such reason, three different protocols were developed and, finally, a synthetic pathway that yielded *ca.* 100% of the chains bearing the trigger was obtained.

The surface coating was performed in two steps. First, the surface of the particles was modified with a chloro alkoxysilane that would act as a linker. Then, the polymer was added and the final material was characterized through different techniques.

A summary of the synthetic work carried out here and the hypothesized pH-responsive behavior is depicted in Scheme 2.2.



**Scheme 2.2.** Schematic representation of the synthesis of the polymer-coated nanoparticles and their pH-responsive evaluation. The nanoparticles were synthesized using the *sol-gel* method. The template was removed to yield hollow mesopores. Then, the surface was modified with a linker and the particles were loaded with a model fluorophore to then graft the polymer on the surface. Finally, the pH-responsiveness was evaluated at two representative pH values.

Once synthesized, the particles were loaded with a ruthenium complex and an *in vial* release experiment was carried out to test the pH-responsiveness. The experiment was performed at two pH values, 7.4 (physiological pH) and 5 (lysosomal pH).

Finally, some preliminary biological experiments were carried out. The behavior of the system with healthy cells was evaluated to determine the potential intrinsic cytotoxicity of the material. Then, their ability to be internalized by tumoral cells was evaluated using prostate cancer cells.



## 2.2.2. Materials and Methods

The following compounds were purchased from Sigma-Aldrich Inc.: Tetraethyl orthosilicate (TEOS); Ammonium nitrate; Cetyltrimethylammonium bromide (CTAB); Fluorescein isothiocyanate isomer I (FITC); 3-(Aminopropyl)triethoxysilane (APTES); 4-Aminobenzyl alcohol (ABA); Phenyl chloroformate; N,N-Diisopropylethylamine (DIPEA); Dibutyltin dilaurate (DBTL); *tert*-butanol (*t*BuOH); 4-Dimethylaminopyridine (DMAP); Tris(2,2'-bipyridyl)dichlororuthenium(II) hexahydrate (Ru) ; (3-chloropropyl)triethoxysilane; Di-*tert*-butyl dicarbonate (BOC<sub>2</sub>O); Dimethyl sulfoxide (DMSO); N,N-Dimethylformamide (DMF); Tetrahydrofuran (THF); Dichloromethane (DCM). The rest of the chemicals (ethanol, heptane, etc) were of the best quality and were employed as received.

### 2.2.2.1. Mesoporous Silica Nanoparticles

Mesoporous silica nanoparticles were synthesized following a modification of the Stöber method.<sup>1</sup> Briefly, to a 1L flask containing CTAB (1 g, 2.74 mmol), H<sub>2</sub>O (480 mL) and NaOH (3.5 mL) were added and the solution was stirred until the surfactant was dissolved. Then, the solution was heated to 80°C and TEOS (5 mL, 22.39 mmol) was added dropwise over 20 minutes. Afterward, the solution was heated for further 2 hours at 80°C under magnetic stirring. Finally, the precipitate was centrifuged and washed twice with water and once with ethanol.

The surfactant was removed by ionic exchange using 500 mL of a solution of 10 mg/mL of NH<sub>4</sub>NO<sub>3</sub> in ethanol (95%) at 75°C for 2 hours. The process was repeated two more times. Finally, the nanoparticles were centrifuged, washed twice with water and once with ethanol and subsequently stored in absolute ethanol.

To synthesize fluorescein-labeled MSNs (MSN-F), FITC (1 mg, 0.002 mmol) was reacted with APTES (2.2 μL, 0.009 mmol) in ethanol (40 μL) for 2 hours. Then, TEOS was added and the whole solution was gently shaken. After that, the procedure was carried out as previously described.

The as-produced particles were characterized in terms of X-Ray Diffraction (XRD), Fourier Transformed Infrared (FTIR) spectroscopy, Thermogravimetric Analysis (TGA analysis) N<sub>2</sub> adsorption analysis, Scanning Electron Microscopy (SEM), Transmission Electron Microscopy (TEM), Dynamic Light Scattering (DLS) and Zeta potential.

### 2.2.2.2. pH-Responsive Self-Immolative Polymers

#### ❖ *Phenyl(4-(hydroxymethyl)phenyl)carbamate (1)*

To a N<sub>2</sub>-purged flask containing ABA (1 g, 8.12 mmol), dry DMF (15 mL) and dry DIPEA (1.7 mL, 9.76 mmol) were added and the solution was magnetically stirred until the powder was completely dissolved. Then, the flask was placed in an ice bath and phenyl chloroformate (1.12 mL, 8.83 mmol) was added dropwise. After 15 minutes the ice bath was removed and the reaction was controlled to completion by thin layer chromatography. Afterward, the organic phase was extracted in ethyl acetate, washed with saturated ammonium chloride solution and finally dried over sodium sulfate. Finally, the solvent was partially removed and the resultant solution was precipitated in cold heptane and centrifuged twice to yield compound **1** as a whitish solid that was dried under vacuum. The product was characterized by <sup>1</sup>H-NMR.

#### ❖ *Tert-butyl(4-(hydroxymethyl)phenyl)carbamate (2)*

To a N<sub>2</sub>-purged flask containing ABA (1 g, 8.12 mmol) and BOC<sub>2</sub>O (1.8 g, 8.12 mmol), dry THF (80 mL) and dry DIPEA (1.4 mL, 8.12 mmol) were added and the solution was stirred until the powder was completely dissolved. Then, the mixture was refluxed overnight and subsequently evaporated to yield a yellow oil. The oil was dissolved in a small amount of ethyl acetate and precipitated in cold heptane to yield compound **2** as a whitish solid, which was filtered off and dried under vacuum. The product was characterized by <sup>1</sup>H-NMR.

#### ❖ *Poly(phenyl(4-(hydroxymethyl)phenyl)carbamate) (3)*

The synthesis of compound **3** was attempted through various synthetic pathways based on a previously reported method.<sup>2</sup> Protocol A and B were carried out for 150 mg of monomer while protocol C was adapted to 1 g of starting material.

Protocol A: To a N<sub>2</sub>-purged vial containing compound **1** (0.15 g, 0.618 mmol), dry DMSO (0.5 mL) was added and the solution was heated to 80°C under magnetic stirring. Then, DBTL (13% mol with respect to **1**) was added and the reaction mixture was subsequently stirred for 90 minutes at 80°C. Then, dry DMSO (1.5 mL) and *t*BuOH (1.5 mL, 18 mmol) were mixed in a N<sub>2</sub>-purged vial and the mixture was added in 6 times (0.5 mL of the mixture each time). Afterward, the reaction was further stirred for 2 hours and finally allowed to cool down to room temperature (rt). After that, the mixture was precipitated in cold methanol, centrifuged and washed 3 times with methanol to yield compound **3** as a dark yellow solid that was dried under vacuum.

**Protocol B:** To a N<sub>2</sub>-purged vial containing compound **1** (0.15 g, 0.618 mmol), dry DMSO (0.5 mL) was added and the solution was heated to 80°C with stirring. Then, DBTL (5% mol) was added and the reaction mixture was subsequently stirred for 90 minutes at 80°C. Then, to a N<sub>2</sub>-purged vial containing different amounts DMAP and dry DMSO (1 mL), different amounts of *t*BuOH were added. This vial was added to the initial reaction mixture in several steps. Afterward, the reaction was further stirred for 2 hours and, finally, it was allowed to cool down to rt. After that, the mixture was precipitated in cold methanol, centrifuged and washed 3 times with methanol to yield compound **3** as a dark yellow solid that was dried under vacuum.

**Protocol C:** To a N<sub>2</sub>-purged vial containing compound **1** (1 g, 4.12 mmol), dry DMSO (1.62 mL) was added and the solution was heated to 85°C with stirring. Then, DBTL (5% mol) was added and the reaction mixture was subsequently stirred for 2h 30 minutes at 85°C. After that, compound **2** (223 mg, 1 mmol) in dry DMSO (0.5 mL) was injected and the solution was heated for further 2 hours. Finally, the crude reaction mixture was precipitated in cold methanol, centrifuged and washed 3 times with methanol to yield compound **3** as a yellowish solid that was dried under vacuum.

The compounds obtained through the different approximations were all characterized by <sup>1</sup>H-NMR.

### 2.2.2.3. SIP-Coated Mesoporous Silica Nanoparticles

❖ *Mesoporous Silica Nanoparticles Functionalized with (3-chloropropyl) triethoxysilane (MSN-CS)*

First, to a N<sub>2</sub>-purged flask containing MSNs (175 mg), dry toluene (30 mL) was added and the solution was sonicated until no aggregates could be observed. Then, (3-chloropropyl)triethoxysilane (100 μL, 0.04 mmol) was added and the mixture was refluxed overnight. After that, the particles were centrifuged, washed with toluene and ethanol and dried under vacuum.

❖ *SIP-Coated Mesoporous Silica Nanoparticles (MSN-CS-SIP)*

First, to a N<sub>2</sub>-purged flask containing MSN-CS (175 mg), dry DMSO (25 mL) was added and the particles were dispersed with the aid of an ultrasonicator. Separately, to a N<sub>2</sub>-purged flask containing compound **3** (0.33 g, 0.1 mmol), dry DMSO (2.5 mL) and dry DIPEA (25.6 μL, 0.15 mmol) were added and the solution was stirred for 2 hours for alcohol activation. After that, the latter solution was added dropwise to the nanoparticles

solution and the mixture was heated to 80°C. Afterward, a second vial containing compound **3** in DMSO was activated for 2 hours with dry DIPEA and subsequently added to the nanoparticles solution. Finally, a third vial containing compound **3** in DMSO was activated with dry DIPEA and added to the nanoparticles solution. After the third addition of activated compound **3**, the whole reaction mixture was allowed to react overnight at 80°C. Finally, the product was centrifuged, thoroughly washed with DMSO, water and ethanol and dried under vacuum.

Both materials were characterized in terms of XRD, FTIR spectroscopy, TGA analysis N<sub>2</sub> adsorption analysis, DLS and Zeta potential.

#### 2.2.2.4. Release Experiment from MSN-CS-SIP

##### ❖ *MSN-CS-SIP Loaded with Ru (MSN-CS-SIP-Ru)*

First, to a N<sub>2</sub>-purged flask containing MSN-CS (175 mg), a solution of Ru (260 mg, 0.33 mmol) in dry DMSO (25 mL) was added and the solution was stirred overnight at rt. After that, the functionalization with the SIP was carried out as described in Section 2.2.2.3. A control group without SIP coating was prepared soaking MSNs in a saturated solution containing the Ru dye (MSNs-Ru).

##### ❖ *Release Experiments*

The pH-responsive capabilities of MSNs-Ru and MSN-CS-SIP-Ru were tested *in vial* using Transwells® and at two different pH values: 7.4 (0.01 M phosphate buffer) and 5 (0.01 M acetate buffer). The general protocol was carried out as follows. A vial containing 10 mg of the corresponding group of particles was prepared for each pH (two vials of 10 mg for either MSNs-Ru or MSN-CS-SIP-Ru). Then, 1.8 mL of phosphate buffer (pH 7.4) were added to each vial. After that, 0.5 mL of nanoparticles suspension (*ca.* 3 mg of particles) were placed on a Transwell® permeable support with 0.4 µm of polycarbonate membrane. Three Transwell® support were prepared from each vial (6 Transwell® in total for either MSNs-Ru or MSN-CS-SIP-Ru). The external well was filled with 1.5 mL of phosphate buffer (pH 7.4) and the suspension was kept under orbital shaking at 100 rpm and 37°C for all the experiment. After 2 hours, the phosphate buffer (pH 7.4) of three of the Transwell® was replaced by the acetate buffer (pH 5). The group at pH 5 received this solution for the rest of the experiment. At every time point evaluated, the solution from the external well of the Transwell® was taken out, measured by fluorescence spectrometry to determine the amount of Ru released and replaced with the corresponding fresh medium

### 2.2.2.5. Cell Experiments

#### ❖ Cell Cultures

Cell culture tests were performed using the well-characterized mouse osteoblastic cell line MC3T3-E1 (subclone 4, CRL-2593) and an androgen-sensitive LNCaP cells, a human prostate cancer cell line (CRL-1740; ATCC). MC3T3-E1 and LNCaP cells were then plated at a density of 20,000 cells cm<sup>2</sup> in 1 mL of alpha-minimum essential medium or Dulbecco's modified Eagle's medium (DMEM, Sigma Chemical Company), respectively, containing 10% of heat-inactivated fetal bovine serum (FBS, Thermo Fisher Scientific) and 1% penicillin–streptomycin (BioWhittaker Europe) at 37°C in a humidified atmosphere of 5% CO<sub>2</sub>. Then, nanoparticles were placed at different concentrations and incubated for different periods of time.

#### ❖ Cell Viability

Cell proliferation was determined by addition of Alamar Blue solution (AbD Serotec) at 10% (v/v) to the cell culture at 24, 48 and 72 hours, following manufacturer instructions. After 4 hours, 200 µL aliquots were added to 96-well plates, and the absorbance intensity was measured using excitation emission wavelengths of 570 and 600 nm, respectively, in a Unicam UV-500 UV–visible spectrophotometer.

#### ❖ Internalization studies

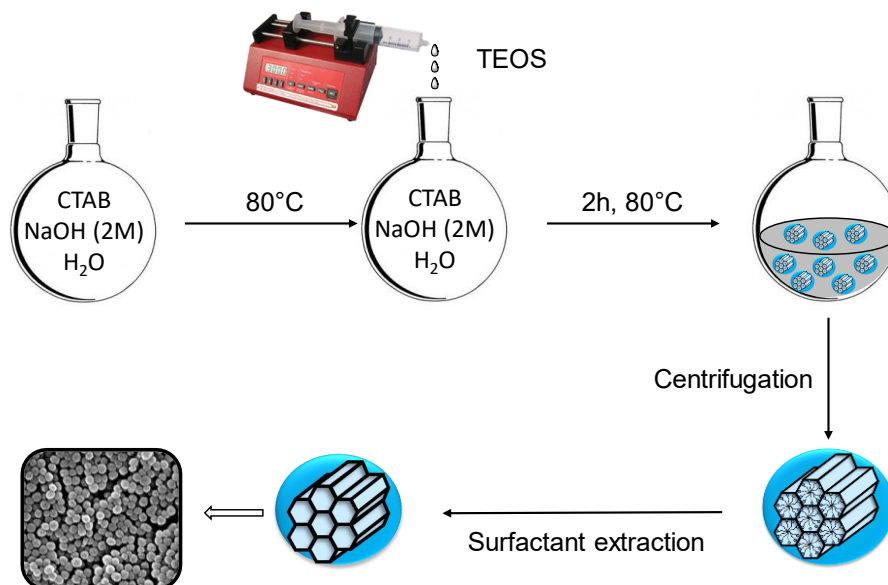
For the fluorescence microscopy, LNCaP cells were incubated with the nanoparticles (100 µg/mL) for 2h in serum-free culture medium. Then, the medium was withdrawn and cells were washed with phosphate buffered saline (PBS) three times. Cells were fixed with ethanol for 2 min and stained with DAPI. Fluorescence microscopy was carried out in order to evaluate nanoparticle uptake. Green channel was used for nanoparticles and blue for cell nucleus, in a Evos FL Cell Imaging System equipped with three Led Lights Cubes (IEX (nm); IEM (nm)): DAPI (357/44; 447/60), GFP (470/22; 525/50), RFP (531/40; 593/40) from AMG (Advance Microscopy Group).

## 2.2.3. Results and Discussion

### 2.2.3.1. Synthesis of Mesoporous Silica Nanoparticles

The synthesis of MSNs was accomplished through a modification of the Stöber method.<sup>1</sup> In particular, MSNs were synthesized using the *sol-gel* method under basic and very diluted conditions, employing CTAB as structure directing agent and TEOS as silica precursor. The template was removed by solvent extraction to obtain empty pores

(Scheme 2.3). The as-produced nanoparticles were characterized through TGA, XRD, FTIR spectroscopy, N<sub>2</sub> adsorption analysis, SEM, TEM, DLS and Zeta potential.



**Scheme 2.3.** Schematic representation of the synthesis of mesoporous silica nanoparticles. The silica precursor was added to the self-assembled surfactant molecules to form the silica backbone. Then, the template was removed using a solvent extraction to yield mesoporous silica nanoparticles with empty pores.

The produced nanoparticles were analyzed through TGA analysis to ensure the correct removal of the surfactant and to determine the amount of residual surfactant present within the pores after the extraction (Figure 2.18).

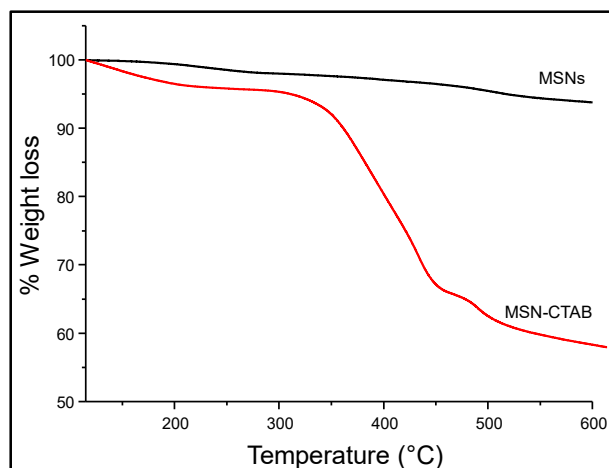


**Figure 2.18.** TGA measurement of MSNs and MSN-CTAB. The as-produced (MSN-CTAB) showed *ca.* 40% of weight loss associated to the presence of the template. The successive extraction steps yielded nanoparticles showing *ca.* 3% of weight loss, confirming the correct template removal.

Figure 2.18 shows *ca.* 40% of weight loss in the as-produced nanoparticles, indicating the presence of the surfactant template filling the pores. However, after carrying out several extraction steps, only *ca.* 3% of weight loss could be observed, confirming the successful extraction and yielding nanoparticles with empty pores.

The correct removal of the template as well as the proper formation of the silica backbone was determined through FTIR spectroscopy measurements (Figure 2.19).

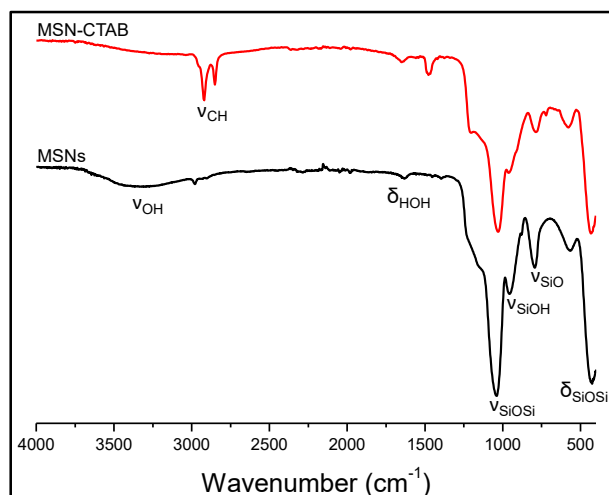


**Figure 2.19.** FTIR spectroscopy before and after the template removal. The presence of the C-H band in MSN-CTAB indicated the presence of the organic template. The indicated bands in MSNs demonstrated the proper hydrolysis, condensation and polymerization processes of the silica precursor and the presence of silanol groups on the surface. The disappearance of the C-H vibration bands confirmed the template removal.

Figure 2.19 shows the representative stretching ( $\delta$ ) and bending ( $\nu$ ) bands of the as-produced material. The presence of the C-H vibration bands in MSN-CTAB indicated the presence of the organic template within the pores. However, after carrying out several extraction steps, that bands disappeared in MSNs, confirming again the successful template removal. Furthermore, the Si-O-Si vibration bands confirmed the proper hydrolysis, condensation and subsequent polymerization of the silica precursors during the synthesis, leading to a network of Si-O-Si bonds as backbone. In addition, the Si-OH bands confirmed the expected presence of silanol groups on surface of MSNs.

The structure of the MSNs was determined through XRD measurements. These materials are composed of amorphous silica. This means that they are amorphous on an atomic level. However, their porosity present certain symmetry and this is why the XRD are carried out at low angle (Figure 2.20).

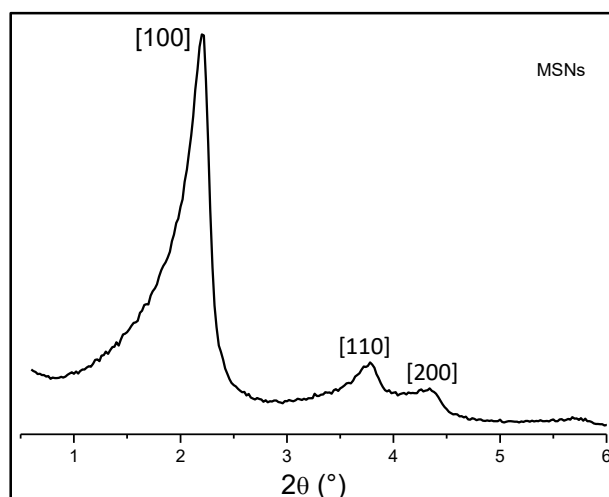


**Figure 2.20.** XRD diffractogram of MSNs. The maxima obtained demonstrated the hexagonal pore symmetry, as expected in a MCM-41-like material.

The maxima shown in the diffractogram, ([100], [110] and [200]), confirmed the hexagonally ordered pore distribution with  $p6mm$  spatial group typical of MCM-41-like materials.<sup>3,4</sup>

MSNs were subjected to  $N_2$  adsorption analysis to determine the textural properties, including the morphology and size of the above-confirmed honeycomb-patterned pores. (Figure 2.21).

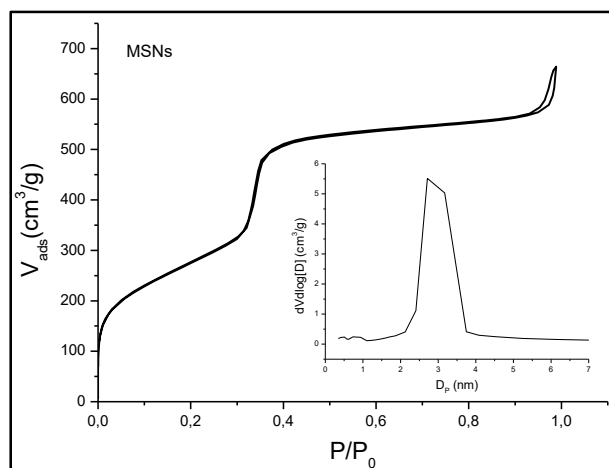


**Figure 2.21.**  $N_2$  adsorption analysis of MSNs. The type-IV isotherm confirmed the presence of cylindrical mesopores with a diameter of *ca.* 2.7 nm.

The  $N_2$  adsorption analysis confirmed the excellent textural properties of this kind of material, showing a surface area of *ca.* 1000 m<sup>2</sup>/g and pore width and volume of 2.74 nm and 1.05 cm<sup>3</sup>/g, respectively. The pore size would allow the loading of therapeutic compounds, such as the typical anticancer drugs.<sup>5</sup> The shape of the isotherm provides structural information about the material. According to the IUPAC classification, Figure 2.21 showed the type-IV isotherm typical of mesoporous materials,<sup>6</sup> although some



authors consider this type of isotherm where hysteresis can barely be observed as type-IVc isotherm.<sup>7</sup> In addition, MSNs mainly presented a highly ordered distribution of cylindrical mesopores ( $2 \text{ nm} < \text{pore size} < 50 \text{ nm}$ ).<sup>8,9</sup>

The morphology of MSNs was observed through different electron microscopy techniques (Figure 2.22).

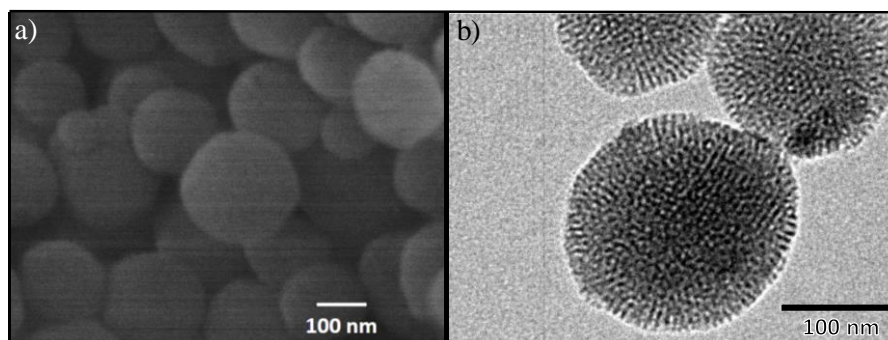


**Figure 2.22.** Micrographs of MSNs. a) SEM. b) TEM. The observations under the electronic microscopes demonstrated the nearly spherical homogeneous shape and the porosity of MSNs.

The observation of the MSNs through the SEM and TEM microscopes confirmed the almost spherical and homogeneous shape of the particles with size of *ca.* 160-190 nm. In addition, it could be observed that the particles were well dispersed. Moreover, the analysis through the TEM microscope demonstrated the presence of porosity in the as-synthesized nanoparticles.

The surface charge of MSNs was analyzed through Zeta potential measurements. Silanol groups on the surface of MSNs are deprotonated at neutral pH, so a negative value for surface charge was expected. In this sense, the measurements on MSNs yielded a value of -35.3 mV, confirming the chemical nature of this material.

The size distribution of MSNs in aqueous solution was analyzed through DLS measurements (Figure 2.23).

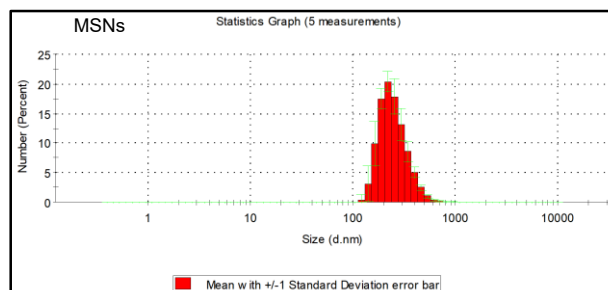


**Figure 2.23.** DLS measurements of MSNs. The analysis showed a homogenous distribution centered at 220 nm and well dispersed, in agreement with the electronic micrographs.

As observed in Figure 2.23, the distribution was centered at *ca.* 220 nm. The DLS technique provides the hydrodynamic size of the particles because the water molecules bind their surface. In consequence, the size distribution was centered at slightly higher values than the observed in the electronic micrographs. In addition, there were no aggregates, confirming the suitability of the particles for their biological application.

### 2.2.3.2. Synthesis of pH-Responsive Self-Immolative Polymers

The synthesis of the SIPs was based on the use of ABA as building block. This molecule has been widely explored in the design of prodrugs owing to their self-immolative properties.<sup>10-12</sup> The synthesis of compound **1** was accomplished straightforwardly through the reaction of ABA with phenyl chloroformate. The compound was characterized through <sup>1</sup>H-NMR (Figure 2.24).

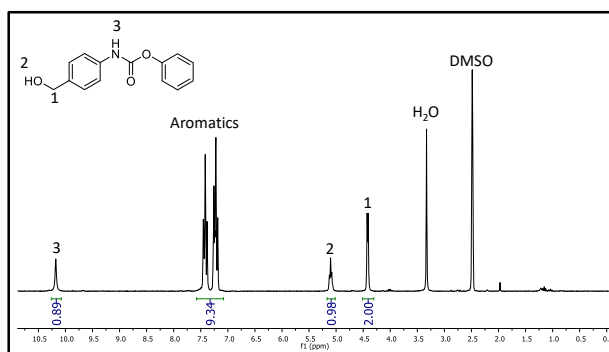


**Figure 2.24.** The presence of the expected signals confirmed the correct synthesis of compound **1**. (250 MHz, DMSO)  $\delta$  10.20 (s, 1H), 7.25-7.45 (m, 9H), 5.12 (t, 1H), 4.45 (d, 2H).

The synthesis of the polymer was accomplished through modifications of a previously reported method.<sup>2</sup> The polymerization was based on the addition of the alcohol group of one monomer to the carbamate of another monomer. This process was catalyzed by DBTL, which is a catalyst widely used in the synthesis of polyurethanes.<sup>13</sup>

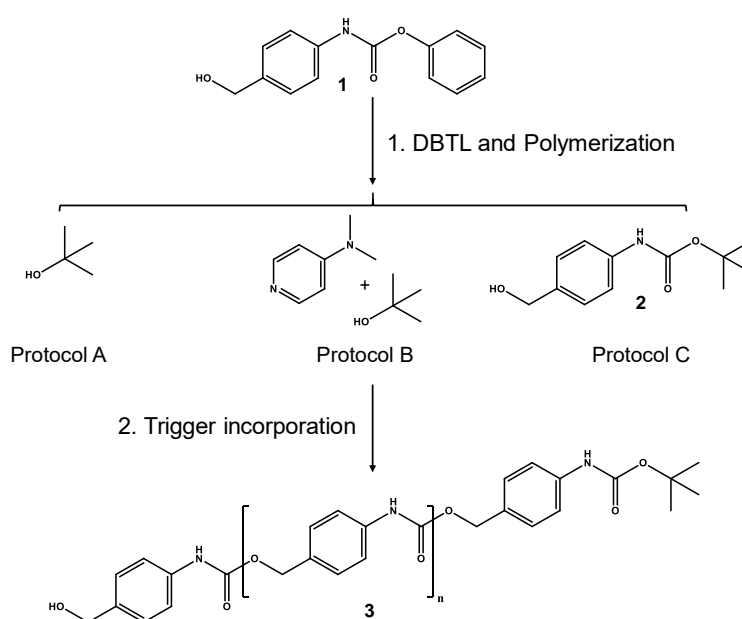
Different experimental conditions in terms of monomer and catalyst concentrations were evaluated to produce polymer chains with different lengths. Additionally, different solvents were also evaluated, such as *N,N*-dimethylformamide and dimethyl sulfoxide. When using the former, the polymer tended to precipitate during the reaction, leaving the latter as best candidate.

It was observed that for a fixed monomer concentration, the higher the amount of catalyst, the lower the molecular weight of the polymer. The reason for that was that a high catalyst concentration would lead to several polymer chains starting at the same time.

In consequence, less single monomers would be available to be sequentially incorporated into each polymer chain, and the molecular weight would be lower.

Moreover, it was observed that there was a lower limit for the catalyst concentration, below which the polymer could not be synthesized regardless of the temperature or the reaction time. This was ascribed to a too low amount of monomers activated as a consequence of a too low presence of the catalyst in the medium.

The incorporation of the pH-responsive trigger was explored through three different approximations (Scheme 2.4).



Scheme 2.4. Strategies for the incorporation of the pH-responsive trigger. Left: Direct addition of *tert*-butanol (protocol A); Center: Activation of *tert*-BuOH with DMAP (protocol B); Right: Triggering monomer (protocol C).

The initial approach (Protocol A) consisted in following the previously reported method,<sup>2</sup> which was based on the direct addition of *tert*-BuOH to end-cap the preformed polymeric chain. Despite several experimental conditions were explored, such as adding the trigger in several steps or increasing the total amount of *tert*-BuOH, the maximum amount of the molecule that could be incorporated was 15%. This value was determined using <sup>1</sup>H-NMR (Figure 2.25).

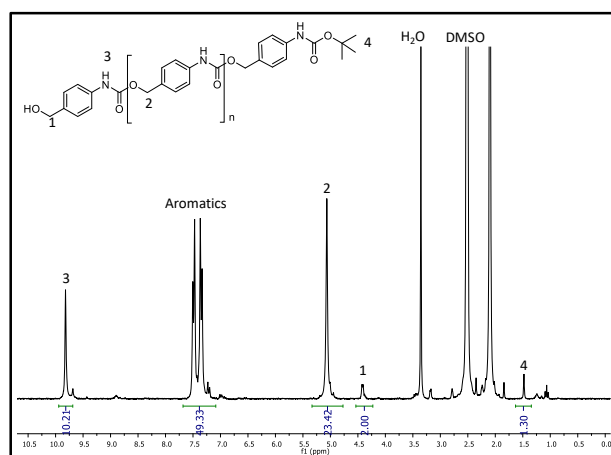


**Figure 2.25.**  $^1\text{H-NMR}$  of compound **3** synthesized through protocol A. (250 MHz, DMSO)  $\delta$  9.82 (s, 10H), 7.56-7.15 (m, 49H), 5.15(s, 23H), 4.43 (d, 2H), 1.48 (s, 1H). The ratio between integrals of peaks 2 and 1 provided the number of monomers in the chain. Signal 4 integral provided the amount of trigger incorporated.

The low percentage of trigger grafting might be ascribed to the low reactivity of the alcohol group from *t*BuOH. Hence, the possibility of pre-activating it with a base prior to the addition was explored (Protocol B). Different amounts of DMAP and *t*BuOH were employed, increasing the trigger presence up to 40% (Figure 2.26).

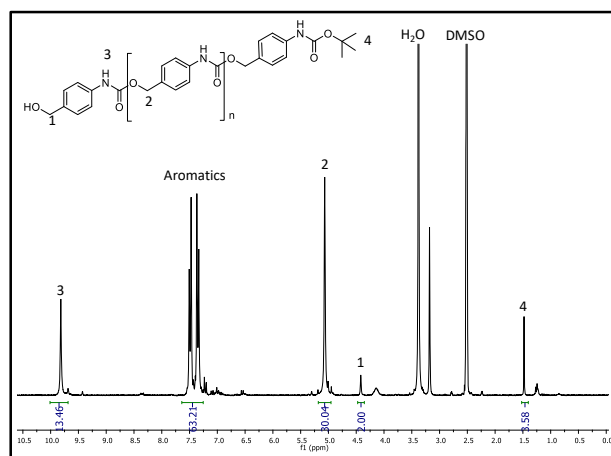


**Figure 2.26.**  $^1\text{H-NMR}$  of compound **3** synthesized through protocol B. (250 MHz, DMSO)  $\delta$  9.82 (s, 13H), 7.56-7.15 (m, 63H), 5.15(s, 30H), 4.43 (d, 2H), 1.48 (s, 4H). The amount of trigger incorporated was calculated in a similar way than in Figure 2.25.

In view of this results, the next approach (Protocol C) consisted in producing an analog of compound **1** with the trigger already incorporated. Compound **2** was obtained through the reaction of ABA with  $\text{BOC}_2\text{O}$  and the product was characterized by  $^1\text{H-NMR}$ , confirming the successful synthesis of the monomer with the trigger already incorporated (Figure 2.27).

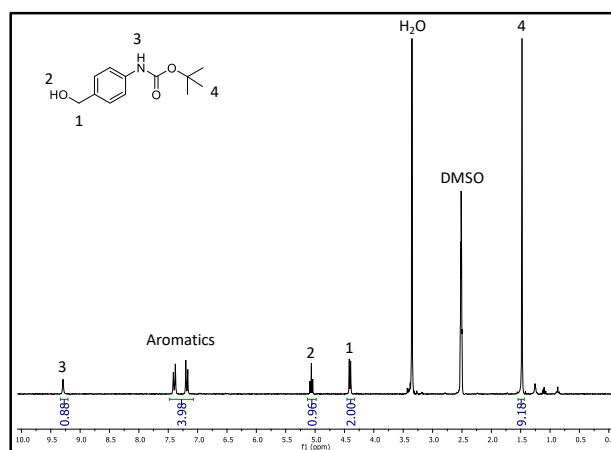


**Figure 2.27.** The presence of the expected signals verified the success of the synthesis of compound **2**. (250 MHz, DMSO)  $\delta$  9.29 (s, 1H), 7.17-7.41 (m, 4H), 5.05 (t, 1H), 4.40 (d, 2H), 1.48 (s, 9H).

In this way, the trigger and the monomers would show the same reactivity and it would be more easily introduced as end-cap for the polymer chains. This approximation yielded self-immolative chains with *ca.* 100% of the chains bearing the pH-responsive moiety (Figure 2.28).

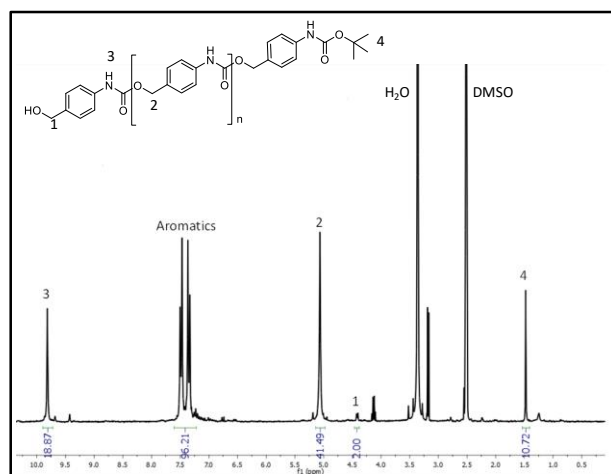


**Figure 2.28.**  $^1\text{H-NMR}$  of compound **3** synthesized through protocol C. (250 MHz, DMSO)  $\delta$  9.82 (s, 19H), 7.56-7.15 (m, 96H), 5.15 (s, 41H), 4.43 (d, 2H), 1.48 (s, 9H).

The molecular weight was calculated from the  $^1\text{H-NMR}$  spectrum. The number of monomer units per polymer chain was determined through the ratio “benzylic hydrogens at the molecule tail vs those in the polymeric chain”. An average synthesis led to SIPs with *ca.* 20 units, which translated into a molecular weight of *ca.* 3,300 g/mol.

It was found that when the SIPs produced using Protocol C presented more than 20-25 units before the addition of compound **2**, the process of end-capping reduced the final number of monomers to *ca.* 20 units (Figure 2.29).

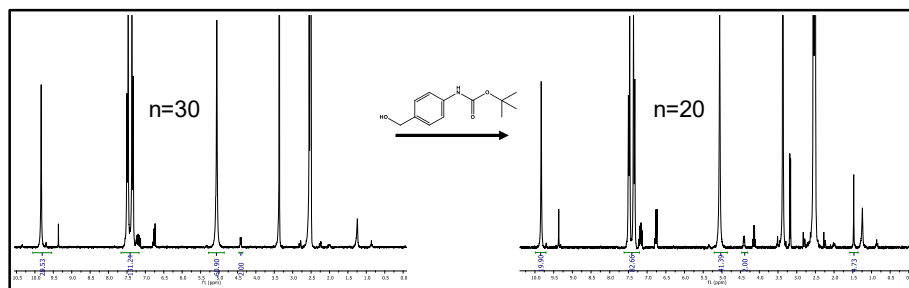


**Figure 2.29.** Effect of the addition of compound 2 (Protocol C) on chains presenting  $n > 20$ -25 units. It was observed that for this sizes, the addition of the trigger decreased the final molecular weight of the polymer.

The reason for that might be that for a longer polymer chain, it would be more difficult for the trigger to react at the end of the chain, being easier the attack somewhere along the chain, leading to two separated chains, some of the bearing the pH-responsive fragment. Consequently, it was possible to cap all the polymer chains with a pH-responsive moiety, although those chains were not particularly large.

In a final step, the as-produced SIP was exposed to trifluoroacetic acid, which is known to cleave BOC-protected amines, to evaluate its response to acid environment. Figure 2.30 shows the <sup>1</sup>H-NMR of the SIP before and after acid treatment.

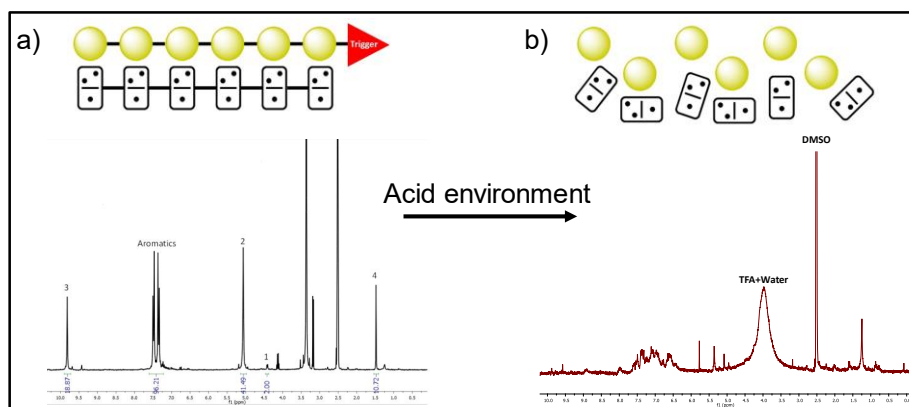
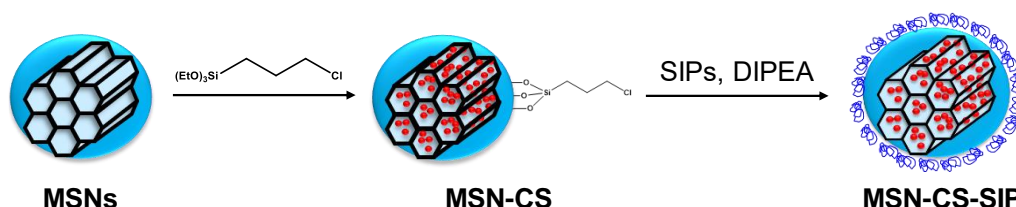


**Figure 2.30.** Verification of the pH-sensitivity of compound 3. a) <sup>1</sup>H-NMR of compound 3. b) <sup>1</sup>H-NMR of compound 3 treated with trifluoroacetic acid (TFA). The acid environment induced the degradation of the polymer and the signals observed for the SIPs were lost.

As observed in Figure 2.30, the structure of the polymer was completely lost after few drops of trifluoroacetic acid, which could be ascribed to the expected self-immolation process. This observation confirmed the responsive behavior to acid pH of the self-immolative chain here produced.

### 2.2.3.3. Synthesis of SIP-Coated Mesoporous Silica Nanoparticles

The functionalization of the MSNs with the pH-responsive self-immolative coating was carried out following a two-step synthetic strategy based on activating the surface of the MSNs and then anchoring the SIPs (Scheme 2.5).



**Scheme 2.5.** Schematic representation of the two-step process for the coating of the MSNs with the SIPs. First, the nanoparticles surface was modified with a chloroalkoxysilane (MSN-CS) to then graft the SIP, leading SIP-coated MSNs (MSN-CS-SIP).

First, a chloroalkoxysilane linker was anchored to the surface to activate the surface of MSNs. Once verified its successful grafting, the alcohol group of the polymer was activated with DIPEA, added to the nanoparticles and allowed to react to accomplish a Williamson etherification.<sup>14</sup> Both processes, MSNs activation to produce MSN-CS and SIP grafting to obtain MSN-CS-SIP, were confirmed through different characterization techniques.

The effect of the successive functionalization steps on the ordered mesostructure was evaluated through XRD measurements (Figure 2.31).

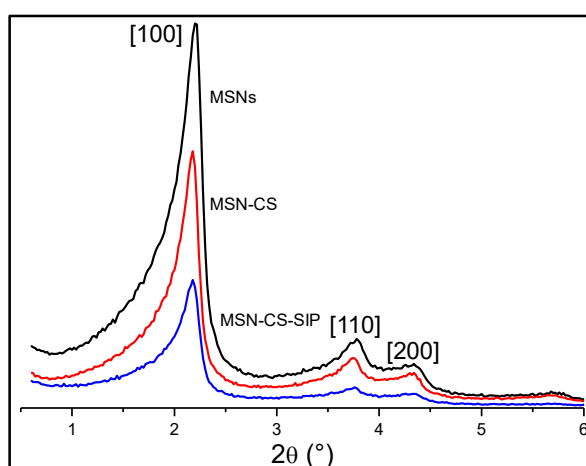


**Figure 2.31.** XRD diffractogram of MSNs, MSN-CS and MSN-CS-SIP. The typical diffraction pattern of a MCM-41-like material could be observed in MSN-CS and MSN-CS-SIP, indicating the preservation of the ordered porosity after the subsequent functionalization steps.

As shown in Figure 2.31, the diffraction pattern obtained for MSNs was still observable in the functionalized samples. This indicated that the mild synthetic protocols employed for the subsequent functionalization maintained the hexagonally ordered

porosity of the starting material. Moreover, the maxima intensity decreased as the degree of functionalization increased. This could be ascribed to the partial filling of the pores owing to the grafting of the chloro alkoxy silane and the SIPs within them.<sup>15</sup>

All materials were subjected to TGA analysis to determine the amount of additional organic matter incorporated in the samples after the different modification steps (Figure 2.32).

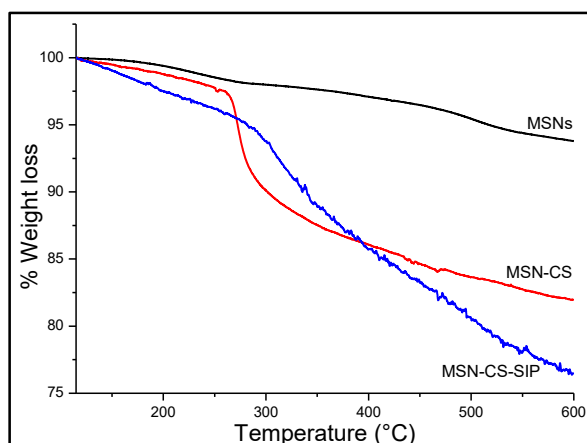


**Figure 2.32.** TGA analysis of MSNs, MSN-CS and MSN-CS-SIP. The functionalization of MSNs with the alkoxy silane introduced an additional 9% of organic matter. The modification with the SIPs increased the weight loss up to 15%, confirming the success of the functionalization steps.

Figure 2.32 shows that the modification of MSNs with the alkoxy silane led to an increment of *ca.* 9% in the weight loss. The subsequent addition of the self-immolative coating increased the weight loss up to *ca.* 15%, compared to their pristine counterpart. These observations confirmed the presence of additional organic matter on the surface that was ascribed to the presence of the SIPs. The presence of organic matter was further analyzed through elemental analysis. The amount of N in MSN-CS-SIP was found to be 0.53%, which was significantly higher than that observed in the MSNs (0.06%), confirming the presence of the polymeric coating. The samples were analyzed through FTIR spectroscopy to evaluate whether the successive functionalization steps introduced new functional groups in the nanoparticles (Figure 2.33).



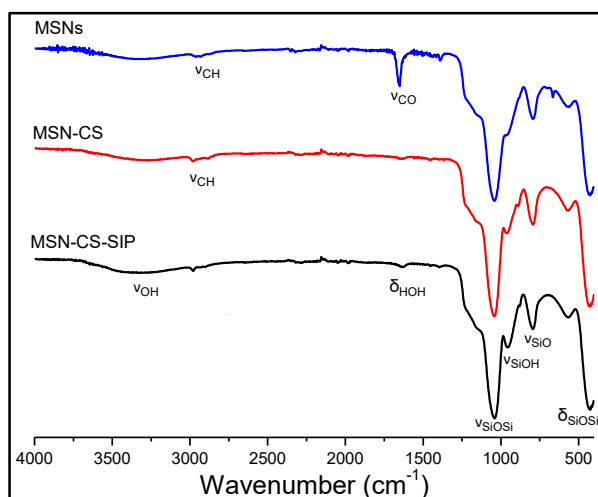


**Figure 2.33.** FTIR spectroscopy of MSNs, MSN-CS and MSN-CS-SIP. The presence of C-H vibration bands at  $2900\text{ cm}^{-1}$  confirmed the successful grafting of the alkoxy silane. The incorporation of the polymer was validated through the presence of the C-O stretching vibration at  $1650\text{ cm}^{-1}$ , ascribed to the carbamates from the polymer chain.

The successful preparation of MSN-CS was confirmed by the presence of the stretching band C-H at  $2900\text{ cm}^{-1}$  associated to the  $\text{CH}_2$  groups of the organosilane. The subsequent functionalization of MSN-CS with the polymer was confirmed by the presence of the C-O stretching vibration at  $1650\text{ cm}^{-1}$ , ascribed to the carbamate groups of the polymeric chain.

The effect of the surface modification with the organosilane and the subsequent SIP grafting on the textural properties of the samples was determined through  $\text{N}_2$  adsorption (Figure 2.34).

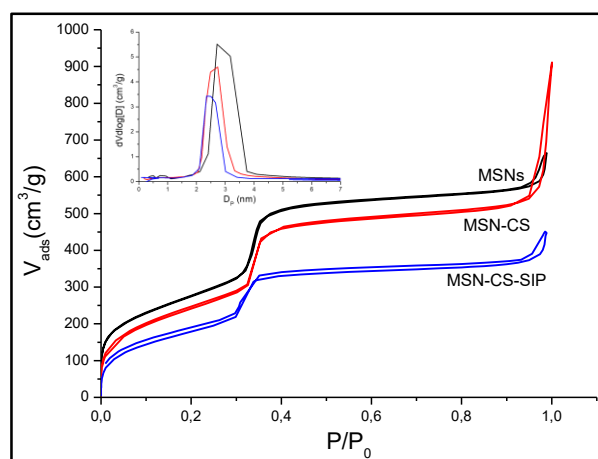


**Figure 2.34.**  $\text{N}_2$  adsorption analysis of MSNs, MSN-CS and MSN-CS-SIP. Inset: Pore size distribution. Both functionalization steps decreased the specific surface area, especially after grafting the SIPs, which was *ca.* 40%. The pore size also decreased as the functionalization was carried out, as expected.

The shape of the isotherms displayed in Figure 2.34 confirmed that the samples maintained their cylindrical mesopores after the functionalization steps. This observation,

together with maintenance of the hexagonally ordered mesostructure, confirmed that the integrity of the mesoporous silica matrix remained unaffected by the successive functionalization steps. The values obtained from the N<sub>2</sub> adsorption analysis are summarized in Table 2.5.

**Table 2.5.** Summary of the values obtained from the N<sub>2</sub> adsorption analysis of MSNs, MSN-CS and MSN-CS-SIP. The significant variations in MSN-CS-SIP confirmed the successful functionalization of MSNs with the SIPs.

	MSNs	MSN-CS	MSN-CS-SIP
Surface area (m <sup>2</sup> /g)	1053	914	671
Pore volume (cm <sup>3</sup> /g)	1.05	1.02	0.60
Pore diameter (nm)	2.74	2.66	2.19

The addition of the organosilane barely modified the textural properties. The slight changes in the pore width and volume were ascribed to residual organosilane molecules grafted within the pores, in agreement with the XRD pattern. On the contrary, the functionalization with the self-immolative coating induced a significant reduction in most of the textural properties. The specific surface area decreased *ca.* 40% after the SIP grafting, clearly indicating the presence of the polymer. In addition, the reduction of the pore width and volume would confirm the partial filling of the mesopores with the SIP chains, in agreement with XRD pattern. This is another confirmation of the successful functionalization of MSNs with self-immolative polymers.

Finally, the size distribution and the surface charge of the samples were analyzed through DLS and Zeta potential measurements. The size of MSN-CS and MSN-CS-SIP remained unaffected after the successive functionalization steps, probably due to the low molecular weight of the polymers. Nevertheless, the changes in the zeta potential as the linker and the polymer were incorporated (-29.0 mV and -23.8 mV, respectively, *vs* -35.3 mV of MSNs) confirmed the successful functionalization.

In conclusion, the different characterization techniques confirmed the correct functionalization of the mesoporous silica nanoparticles with the previously produced self-immolative polymers.

#### 2.2.3.4. Release Experiments

In a first approach, different MSNs:SIP ratios were explored to determine the amount of SIP able to effectively close the pore entrances. Each MSN-CS-SIP and MSNs were

loaded with a model ruthenium fluorophore and an *in vial* release experiment at physiological pH was carried out (Figure 2.35).

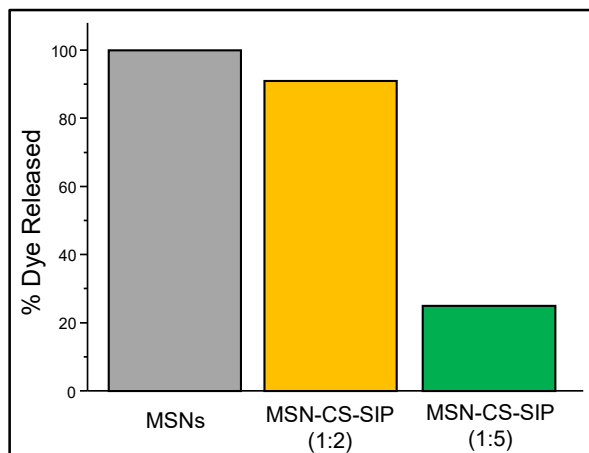


**Figure 2.35.** % Dye Released at physiological pH after 100 hours for MSNs, MSN-CS-SIP (1:2), MSN-CS-SIP (1:5). The experiment demonstrated that a ratio 1:5 was able to effectively seal the mesopores, leading to only 25% of release.

As shown in Figure 2.35, the percentage of dye released by MSN-CS-SIP (1:2) was almost the same as that of MSNs, indicating that a ratio 1:2 was unable to close the pore entrances, which led to the cargo release. However, the ratio 1:5 only released *ca.* 25% of the dye after 100 hours of experiment, demonstrating a more effective sealing of the mesopores.

After achieving an adequate closing of the mesopores at physiological pH, the next step was to evaluate the pH-responsiveness of the self-immolative polymeric coating at acid pH. For such purpose, two solutions at pH 7.4 and pH 5 were used to mimic the pH of the bloodstream and that of the lysosomes, respectively. As a control, a release experiment of naked mesoporous silica nanoparticles was performed (Figure 2.36).

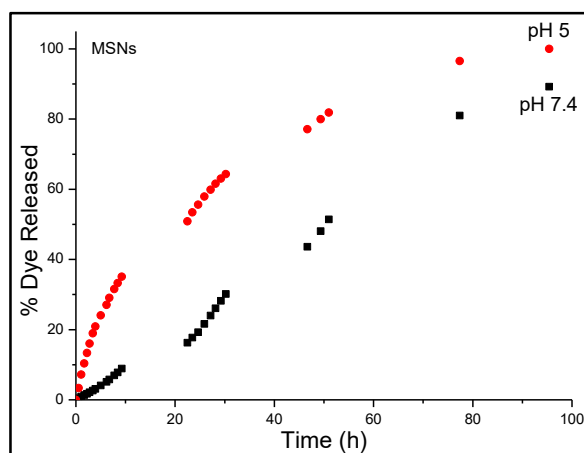


**Figure 2.36.** Release experiment of Ru-loaded MSNs at pH 7.4 and pH 5. The group at pH 5 released a slightly higher amount of dye, which was ascribed to the effect of pH on the host-guest interactions.

As shown in Figure 2.36, the amount of dye released at acid pH from MSNs was slightly higher than that at pH 7.4. The reason for this small difference was the effect that pH has on the interactions between the silica matrix and the guest molecules. Silanol groups protonate at acid pH and the strength of the interaction with the Ru dye weakens, leading to an enhanced release. In this case, the cargo was released independently of the pH, demonstrating the need for gatekeepers to avoid premature release.

The pH-responsiveness of MSN-CS-SIP was evaluated at physiological and acid pH, as it can be observed in Figure 2.37. In this experiment both groups were initially soaked at physiological pH to then change one of them to pH 5.

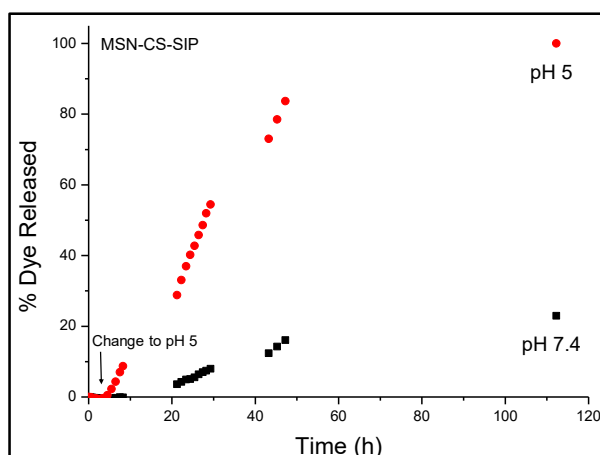


**Figure 2.37.** Release experiment of Ru-loaded MSN-CS-SIP at pH 7.4 and pH 5. The SIPs could close the pore entrances at pH 7.4. However, at pH 5 the release was significantly higher, demonstrating the pH-responsivity of the carrier.

As shown in Figure 2.37, the carrier at physiological pH released less than 10% of the cargo within the first couple of days, demonstrating the efficiency of the SIP to close the pore entrances. The residual release could be ascribed to the cargo molecules entrapped

within the polymer network. The carrier at acid pH showed a five-fold difference in the release compared to pH 7.4, demonstrating the sensitivity of the designed nanocarrier to acid pH.

### 2.2.3.5. Cell Experiments

Having confirmed the successful functionalization with the SIPs and the pH-responsive behavior, the next step was to evaluate the biocompatibility with cells. To assess that, the pre-osteoblastic MC3T3-E1 cell line was exposed to different concentrations of MSN-CS-SIP to evaluate their potential cytotoxicity in case of interaction with healthy cells on their way to the tumor (Figure 2.38).

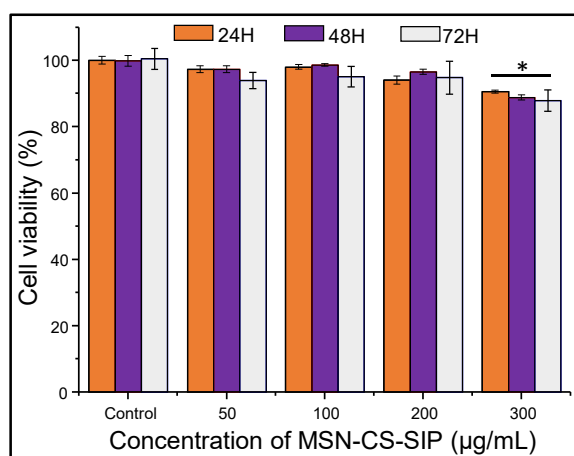


**Figure 2.38.** MC3T3-E1 cell viability upon exposure with different concentrations of MSN-CS-SIP at 24, 48 and 72 hours. \* $p < 0.05$  vs. control. The material was biocompatible for all concentrations except for the highest one, which was used as positive death control.

As shown in figure 2.38, the material did not induce any significant cytotoxicity for any of the concentrations, except for 300 µg/mL, which was intentionally used as positive death control. This results clearly indicated that, regardless of the concentration, neither the SIP-coated nanoparticles nor the self-immolation by-products were cytotoxic, which is of vital importance for the final application of the nanocarrier.

Finally, an internalization study was carried out to test the behavior of the SIP-coated nanoparticles with cancer cells. For this purpose, MSN-CS-SIP were incubated with LNCaP prostate cancer cells, and then, after thoroughly washing the non-internalized nanoparticles, the samples were observed through fluorescence microscopy (Figure 2.39).

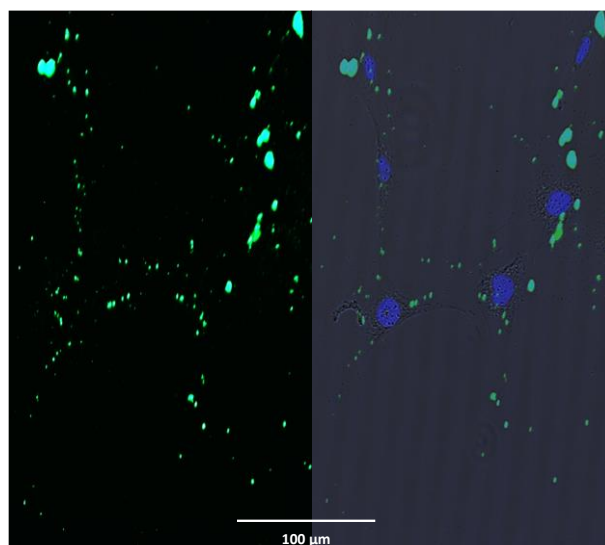


**Figure 2.39.** Internalization of MSN-CS-SIP in LNCaP cells after incubation for 2 hours. a) MSN-CS-SIP; b) MSN-CS-SIP + Bright field (Nanoparticles labelled with FITC and nuclei stained with DAPI). The hybrid nanoparticles were located within the cytoplasm, confirming their proper internalization in tumoral cells.

As observed in Figure 2.39, MSN-CS-SIP distributed along the cytoplasm of tumoral cells, indicating that they could be passively engulfed by the tumoral cells. This confirmed that the functionalization of the MSNs with a self-immolative polymer had no effects on their ability to be internalized. The successful uptake by cancer cells together with all the data here shown indicated the suitability of the SIPs as gatekeepers for mesoporous nanocarriers.

#### 2.2.4. Conclusions

The objective of this first work was to develop a stimuli-responsive system with potential applicability in cancer therapy. Taking advantage of the difference in pH between the bloodstream (pH 7.4) and the lysosomes (pH 5), a system based on mesoporous silica nanoparticles and pH-responsive self-immolative polymers acting as gatekeepers was devised.

The MSNs were synthesized following a modification of the Stöber method, yielding nearly spherical homogenous mesoporous nanoparticles with convenient size for their application in a biological scenario.

The SIPs were synthesized through progressive modifications of a previously reported method. These improvements made possible the development of a synthetic method that yielded polymers with an average molecular weight of *ca.* 3300 g/mol. In addition, the amount of trigger incorporated into the polymer chains increased from barely 1-2% to

100%. This was made possible through the synthesis of a triggering monomer that polymerized in the same way as the monomers.

A synthetic method to graft the SIPs on the MSNs was developed and optimized. Two ratios MSNs:SIP (1:2 and 1:5) were explored to determine the amount of polymer able to close the pore entrances. In a first approach, both MSN-CS-SIP batches and naked MSNs were loaded with a model molecule and subjected to a release experiment at physiological pH, demonstrating that only the ratio 1:5 was able to close the mesopores. Then, a release experiment at physiological and acid pH was carried out on MSNs and MSN-CS-SIP (1:5), clearly showing that only the SIP-coated nanoparticles were able to hamper the release at pH 7.4 and trigger it at pH 5.

Finally, some preliminary cellular experiments were performed. The biocompatibility of MSN-CS-SIP was evaluated using healthy cells, showing no cytotoxic effect except for the higher concentration used as positive death control. Then, their ability to be internalized by cancer cells was evaluated using LNCaP prostate cancer cells. This experiment showed that the SIP-coated nanoparticles could be effectively engulfed by this cells, laying the foundations for future and more complex biological experiments.

## References

- (1) Baeza, A.; Guisasola, E.; Torres-Pardo, A.; González-Calbet, J. M.; Melen, G. J.; Ramírez, M.; Vallet-Regí, M. Hybrid Enzyme-Polymeric Capsules/Mesoporous Silica Nanodevice for in Situ Cytotoxic Agent Generation. *Adv. Funct. Mater.* **2014**, *24*, 4625–4633.
- (2) Sagi, A.; Weinstain, R.; Karton, N.; Shabat, D. Self-Immolative Polymers. *J. Am. Chem. Soc.* **2008**, *8*, 5434–5435.
- (3) Vallet-Regí, M. Nanostructured Mesoporous Silica Matrices in Nanomedicine. *J. Intern. Med.* **2010**, *267*, 22–43.
- (4) Manzano, M.; Aina, V.; Areán, C. O.; Balas, F.; Cauda, V.; Colilla, M.; Delgado, M. R.; Vallet-Regí, M. Studies on MCM-41 Mesoporous Silica for Drug Delivery: Effect of Particle Morphology and Amine Functionalization. *Chem. Eng. J.* **2008**, *137*, 30–37.
- (5) Tang, L.; Yang, X.; Yin, Q.; Cai, K.; Wang, H.; Chaudhury, I.; Yao, C.; Zhou, Q.; Kwon, M.; Hartman, J. A.; *et al.* Investigating the Optimal Size of Anticancer Nanomedicine. *Proc. Natl. Acad. Sci.* **2014**, *111*, 15344–15349.
- (6) Sing, K. S. W.; Everett, D. H.; Haul, R. A. W.; Moscou, L.; Pierotti, R. A.; Rouquérol, J.; T.Siemieniewska. Reporting Physisorption Data For GAS/SOLID SYSTEMS with Special Reference to the Determination of Surface Area and Porosity. *Pure Appl. Chem.* **1985**, *57*, 603–619.
- (7) Kruk, M.; Jaroniec, M. Gas Adsorption Characterization of Ordered Organic-Inorganic Nanocomposite Materials. *Chem. Mater.* **2001**, *13*, 3169–3183.
- (8) Kruk, M.; Jaroniec, M.; Sayari, A. Relations between Pore Structure Parameters and Their Implications for Characterization of MCM-41 Using Gas Adsorption and X-Ray Diffraction. *Chem. Mater.* **1999**, *11*, 492–500.
- (9) Kruk, M.; Jaroniec, M.; Kim, J. M.; Ryong Ryoo. Characterization of Highly Ordered MCM-41 Silicas Using X-Ray Diffraction and Nitrogen Adsorption. *Langmuir* **1999**, *15*, 5279–5284.
- (10) Müller, I. A.; Kratz, F.; Jung, M.; Warnecke, A. Schiff Bases Derived from p-Aminobenzyl Alcohol as Trigger Groups for pH-Dependent Prodrug Activation. **2010**, *51*, 4371–4374.
- (11) Toki, B. E.; Cerveny, C. G.; Wahl, A. F.; Senter, P. D. Protease-Mediated Fragmentation of p-Amidobenzyl Ethers: A New Strategy for the Activation of Anticancer Prodrugs. *J. Org. Chem.* **2002**, *67*, 1866–1872.
- (12) Giang, I.; Boland, E. L.; Poon, G. M. K. Prodrug Applications for Targeted Cancer Therapy. *AAPS J.* **2014**, *16*, 899–913.
- (13) Delebecq, E.; Pascault, J.; Boutevin, B.; Ganachaud, F. On the Versatility of Urethane/Urea Bonds: Reversibility, Blocked Isocyanate, and Non-Isocyanate Polyurethane. *Chem. Rev.* **2013**, *113*, 80–118.
- (14) Mandal, S.; Mandal, S.; Ghosh, S. K.; Sar, P.; Ghosh, A.; Saha, R.; Saha, B. A Review on the Advancement of Ether Synthesis from Organic Solvent to Water.



*RSC Adv.* **2016**, *6*, 69605–69614.

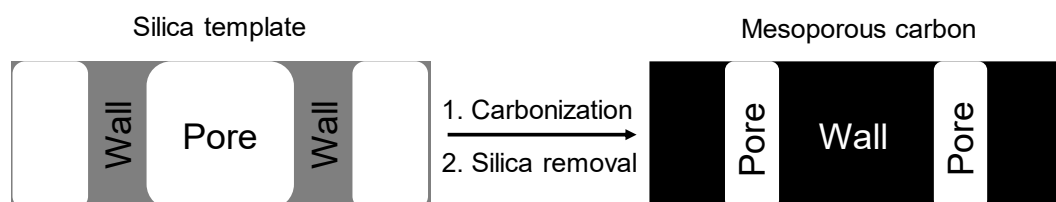
- (15) González, B.; Colilla, M.; De Laorden, C. L.; Vallet-Regí, M. A Novel Synthetic Strategy for Covalently Bonding Dendrimers to Ordered Mesoporous Silica: Potential Drug Delivery Applications. *J. Mater. Chem.* **2009**, *19*, 9012–9024.

## 2.3. Engineered pH-Responsive Mesoporous Carbon Nanoparticles for Drug Delivery

### 2.3.1. Introduction

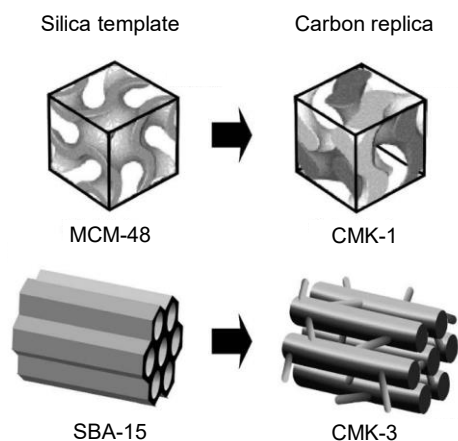
The field of mesoporous carbon is still at its early stage in comparison with the widely studied MSNs. In consequence, the possibilities that they might offer have not been explored in detail so far. Some properties, such as their textural properties, stand out over those of their silica counterpart. While conventional MSNs exhibit a specific surface area of *ca.* 1,000 m<sup>2</sup>/g and an average pore volume of *ca.* 1 cm<sup>3</sup>/g, mesoporous carbons can reach values of up to 2,000 m<sup>2</sup>/g and 1.5 cm<sup>3</sup>/g, respectively. In addition, mesoporous carbons show excellent biocompatibility, allow significant loading of poorly soluble and/or hydrophobic drugs, produce heat upon near-infrared irradiation and provide potential supramolecular  $\pi$ - $\pi$  stacking possibilities, which may be particularly beneficial for aromatic drugs, as many therapeutics are.<sup>1-5</sup>

The synthesis of this type of nanomaterials is based on the use of a silica template, produced through the *sol-gel* method, and the subsequent deposition and carbonization of an organic precursor. Then, the inorganic template is removed to yield carbon nanoparticles with empty pores. Interestingly, the pore network structure of these carbon materials is the negative of that from the silica template (Scheme 2.6).



**Scheme 2.6.** Schematic representation of the pore structure of carbon particles synthesized from mesoporous silica templates. The carbon nanoparticles represent the negative of the mesoporous silica, showing porosity where there was silica in the template.

Representative examples of mesoporous carbons are CMK-1 type and CMK-3 type, which are synthesized using MCM-48 and SBA-15 silica particles as templates, respectively (Scheme 2.7).



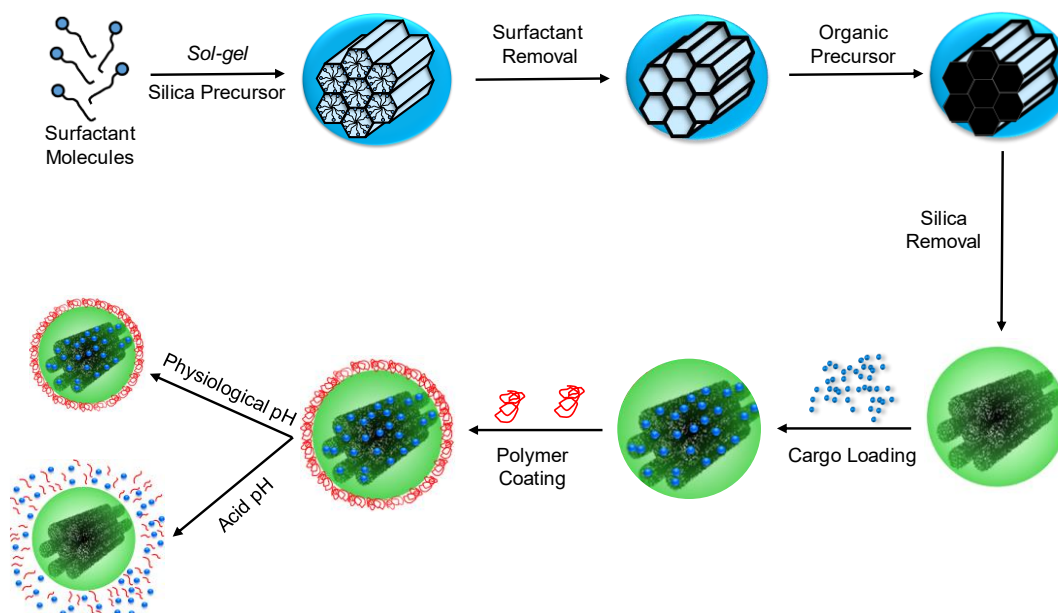
**Scheme 2.7.** Representative examples of mesoporous carbons. CMK-1 is synthesized using MCM-48 silica as template, while CMK-3 is synthesized from SBA-15 mesoporous silica. Adapted from Ref 6 with permission of Taylor & Francis Online.

Nonetheless, their open porous structure presents similar drawbacks as that of mesoporous silica, *i.e.*, premature and nonspecific drug release. Therefore, it is necessary to close the pore entrances with responsive gates to control the cargo release. Based on our previous experience, the different pH values found in the organism were employed as stimulus and the previously employed self-immolative technology was adapted to the carbon carriers. In this sense, the synthesis of pH-responsive self-immolative polymers was optimized and a grafting protocol to mesoporous carbons was developed. In this way, the mesoporous carbons would have a self-immolative polymeric layer on the surface that would disassembly upon a drop in the pH, opening the pores and triggering the drug release.

In particular, two types of mesoporous carbons, CMK-3 and CMK-1, have been synthesized. Their loading capacity has been evaluated and compared to that of mesoporous silica nanoparticles. Then, a method for the SIP coating has been developed and the pH-responsive behavior has been explored using *in vial*, *in vitro* and *in vivo* set-ups.

In addition, the biocompatibility of these materials has been studied *in vitro* and *in vivo*. Furthermore, the carriers have been loaded with a cytotoxic compound and their biological performance has been evaluated.

A summary of the synthetic work carried out here and the hypothesized pH-responsive behavior is depicted in Scheme 2.8.



**Scheme 2.8.** Schematic representation of the synthesis of mesoporous carbons coated with a pH-responsive self-immolative polymer. First, a silica template is synthesized with a silica precursor using the *sol-gel* method. After surfactant removal, the mold is impregnated with an organic precursor that is subsequently carbonized. After that the silica template is removed, yielding the mesoporous carbon matrix. Then, these particles are loaded and subsequently coated with the SIPs. Finally, it is hypothesized that the release would only be triggered at acid pH.

## 2.3.2. Materials and methods

The following compounds were purchased from Sigma-Aldrich Inc.: TEOS; CTAB; Pluronic P123 (Ethylene oxide<sub>20</sub> Propylene oxide<sub>70</sub> Ethylene oxide<sub>20</sub>, EO<sub>20</sub>PO<sub>70</sub>EO<sub>20</sub>); Pluronic F127 (Ethylene oxide<sub>106</sub> Propylene oxide<sub>70</sub> Ethylene oxide<sub>106</sub>, EO<sub>106</sub>PO<sub>70</sub>EO<sub>106</sub>); ABA; Phenyl chloroformate; DIPEA; DBTL; Ru; BOC<sub>2</sub>O; THF; DMSO; DMF; DCM. The rest of the chemicals (ethanol, heptane, etc) were of the best quality and were employed as received.

### 2.3.2.1. Mesoporous Carbon Nanoparticles

#### ❖ CMK-3 type ordered mesoporous carbon nanoparticles (C3)

The CMK-3-type ordered mesoporous carbon was prepared following a nanocasting procedure, using sucrose as carbon source and SBA-15 mesoporous silica as template. SBA-15 was synthesized using TEOS as silica source and triblock copolymer Pluronic P123 as template.<sup>7-9</sup> Then, the carbon replica was obtained by infiltration of SBA-15 with an acidic sucrose solution and subsequent carbonization of the composite material at 900°C. Then, the silica template was removed using hydrofluoric acid to yield a carbon replica with empty pores.

❖ *CMK-1 type ordered mesoporous carbon nanospheres (C1Sph)*

The CMK-1-type mesoporous carbons were synthesized following a similar procedure, using sucrose as carbon source and MCM-48 mesoporous silica as template. The MCM-48 spheres were prepared following a modified Stöber method, using a mixture of surfactants in a H<sub>2</sub>O/NH<sub>3</sub>/ethanol solution at rt and static conditions. The cationic surfactant CTAB was used as template and a nonionic surfactant (triblock copolymer Pluronic F127) as suppressant of the grain growth of the silica particles. TEOS was used as silica source.<sup>3</sup> The carbon replica was obtained through infiltration of the silica template with an acidic sucrose solution, followed by thermopolymerization and carbonization at high temperatures. Finally, the silica template was removed using hydrofluoric acid.

### 2.3.2.2. Determination of the Loading Capacity

Each nanocarrier (15 mg) was dispersed in a saturated solution of Ru (34 mg, 0.04 mmol) in ethanol (2 mL) and subsequently stirred for 24 hours. After that, each batch of particles was filtered, rinsed with 40 mL of ethanol and dried under vacuum. The loading capacity was determined by comparing the thermogravimetric analysis of the Ru-loaded samples with their respective unloaded counterpart.

### 2.3.2.3. pH-responsive Self-Immolative Polymers

❖ *Phenyl(4-(hydroxymethyl)phenyl) carbamate (1)*

Compound **1** was synthesized following a previously reported method with slight modifications.<sup>10</sup> Briefly, to a flask containing 4-aminobenzyl alcohol (6 g, 48.7 mmol), a 2:2:1 mixture of THF/saturated aqueous sodium bicarbonate/water (240 mL) was added. Then, phenyl chloroformate (7 mL, 55.8 mmol) was added dropwise at rt under magnetic stirring and the reaction was controlled to completion by thin layer chromatography. Afterward, the organic phase was extracted in ethyl acetate, washed twice with saturated aqueous sodium bicarbonate and dried over sodium sulfate. Finally, the solvent was evaporated under reduced pressure and subsequently subjected to recrystallization in chloroform, yielding compound **1** as a white powder. The product was characterized by <sup>1</sup>H-NMR.

❖ *Tert-butyl(4-(hydroxymethyl)phenyl) carbamate (2)*

Compound **2** was synthesized following a previously reported method.<sup>11</sup> Briefly, to a flask containing 4-aminobenzyl alcohol (1 g, 8.12 mmol), dichloromethane (14 mL) was

added. Then, di-tert-butyl dicarbonate (1.94 g, 8.75 mmol) in dichloromethane (3 mL) was added and the mixture was left to react overnight at rt. After that, the solvent was removed under reduced pressure and the product was purified in a silica column (ethyl acetate/heptane, 1:1) to give compound **2** as an orange powder. The product was characterized by <sup>1</sup>H-NMR.

❖ *Poly(phenyl(4-(hydroxymethyl)phenyl) carbamate) (3)*

Compound **3** was synthesized following a previously reported method with modifications.<sup>12</sup> To a N<sub>2</sub>-purged vial containing compound **1** (1 g, 4.12 mmol), dry DMSO (2.1 mL) was added and the solution was heated to 85°C under magnetic stirring. Then, DBTL (3% mol) was added and the reaction mixture was subsequently stirred for 2 hours at 85°C. After that, the reaction mixture was cooled down to 40°C and compound **2** (223 mg, 1 mmol) dissolved in dry DMSO (0.5 mL) was added dropwise over 5 minutes. After being stirred at 40°C for 15 minutes, the mixture was heated at 85°C again for further 2 hours. Finally, the crude reaction mixture was precipitated in cold methanol, centrifuged and washed twice with methanol to obtain compound **3** as a yellowish solid that was dried under vacuum and characterized by <sup>1</sup>H-NMR.

#### 2.3.2.4. SIP-Coated Carbon Nanoparticles

First, to a N<sub>2</sub>-purged vial containing 30 mg of each type of particles (C3 and C1Sph) dry DMF (3 mL) was added. Meanwhile, in a separated N<sub>2</sub>-purged vial containing compound **3** (300 mg, 0.09 mmol), dry DMF (2 mL) and dry DIPEA (31 μL, 0.17 mmol) were added and stirred at rt for 30 minutes. After that, that solution was added to each batch of particles and subsequently stirred at 80°C for 24 hours. Then, the produced hybrid carbons were filtered, washed with DMF, water and ethanol and finally dried under vacuum. Both materials were characterized by means of TGA analysis, N<sub>2</sub> adsorption analysis, X-ray Photoelectron Spectroscopy (XPS) and TEM microscopy.

#### 2.3.2.5. Release Experiments from SIP-Coated Carbon Nanoparticles

❖ *SIP-coated carbon nanoparticles loaded with Ru*

To a N<sub>2</sub>-purged vial containing each type of particles (30 mg), a saturated solution of Ru (40 mg, 0.05 mmol) in dry DMF (3 mL) was added and stirred for 24 hours at rt. After that, the grafting protocol for the SIP coating described in Section 2.3.2.4 was carried out on the loaded materials.

❖ *Release experiments*

The pH-responsive responsiveness of both hybrid carbons was tested *in vial* using the same protocol previously described in Section 2.2.2.4 for SIP-coated MSNs. Briefly, the particles were dispersed in a solution either at physiological or acid pH and placed in Tranwell® at 37°C with orbital stirring. The media were removed every time point and measured in a fluorimeter to determine the amount of Ru released. Fresh medium at the corresponding pH was added and the procedure was repeated for every time point.

### 2.3.2.6. Cell Experiments

❖ *Cell Cultures*

Cell culture tests were performed using HOS cells derived from a human osteosarcoma (CRL-1543; ATCC). HOS cells were then plated at a density of 20,000 cells cm<sup>2</sup> in 1 mL of Dulbecco's modified Eagle's medium (DMEM, Sigma Chemical Company) containing 10% of heat-inactivated fetal bovine serum (FBS, Thermo Fisher Scientific) and 1% penicillin–streptomycin (BioWhittaker Europe) at 37°C in a humidified atmosphere of 5% CO<sub>2</sub>. Then, hybrid carbon nanoparticles were placed at different concentrations and incubated for different periods of time.

❖ *Cell Viability*

Cell proliferation was determined by addition of Alamar Blue solution following the protocol described in Section 2.2.2.5.

### 2.3.2.7. Short-Term Release Experiments from C1Sph-SIP

In view of a subsequent *in vivo* experiment, a second validation of the pH-responsive behavior was carried out on Ru-loaded C1Sph-SIP. In this case, the material was dispersed in a physiological solution (Sterofundin®), whose pH was adjusted to 4 or 7.4, respectively. Then, the particles were incubated at 37°C for 30 minutes or 24 hours at pH 4 or for 24 hours at pH 7.4. After each triggering period, the particles were centrifuged and the supernatant was collected and re-centrifuged to remove residual particles. The particles were imaged using the IVIS® Lumina (Caliper LifeSciences, MA; ex/em filter: 465 nm/ Cy5.5) and the supernatants measured in a plate reader (Tecan Infinite Pro 200, ex/em 450/620 nm). All the precipitated particles were re-suspended in pH 7.4 solution and incubated for an additional 24 hours at 37°C. Afterward, centrifugation, supernatant imaging and quantification was carried out as previously described.

### 2.3.2.8. *In Vivo* Study

#### ❖ *pH-responsive Ru release from Ru-loaded C1Sph-SIP*

The *in vivo* study was performed in Germany, in accordance with the German Animal Welfare Act and was approved by the local animal protection authorities (LaGeSo; permit numbers: G 0293/17). During the procedures, animals were anesthetized by inhalation of Isoflurane (2%).

C57BL/6 mice received Ru-loaded C1Sph-SIP hybrid systems at a concentration of 3 mg/200  $\mu$ l *via* subcutaneous injection through a 20 G needle (Sterican) or dwelling canula (Vasofix®), respectively. The mice were shaved before the administration to prevent interference of the hair with the imaging system. The animals received an injection of physiological solution with either pH 4 or 7.4 (Sterofundin® adjusted with NaOH or HCl). Prior to the treatment, the animals received 0.015 mg/kg of buprenorphine solution (Temgesic®) as analgesic.

The imaging was performed using an IVIS® Lumina (Caliper LifeSciences) in conjunction with Living Image® 3.1 software. All images shown were generated with excitation/ emission filters of 465 nm and Cy5.5, respectively. Exposure time was 15 s. Images shown are overlay images of bright field and fluorescent images. The final imaging was performed in deep anesthesia achieved by injection of medetomidine and ketamine (medetomidine 1 mg/kg BW (Cepetor®, CP-Pharma) and ketamin 75 mg/kg BW (Inresa Arzneimittel). Animals were sacrificed afterward and the injections site were harvested for further analysis.

#### ❖ *Histological analysis of injection sites from mice*

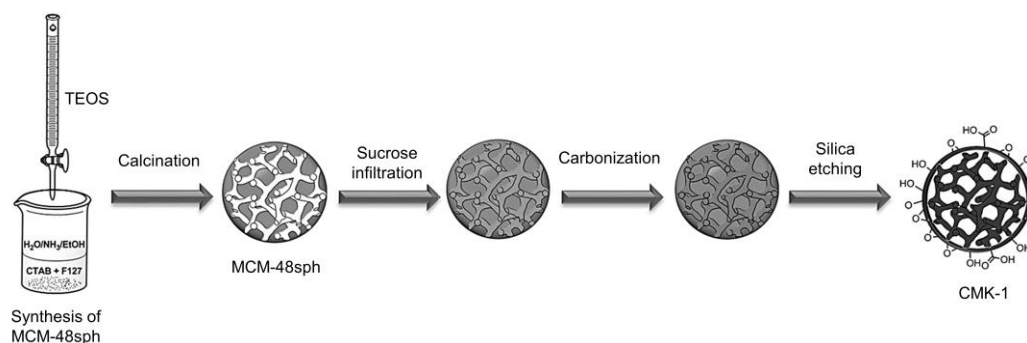
The explanted injection sites were sewed onto histological embedding cassettes (Tissue-Tec, Sacura Finetec) to prevent rolling up of the tissue. Fixation was performed in paraformaldehyde (4%) for 24 hours. Afterward, the tissue was dehydrated and embedded in paraffin. Then, 5  $\mu$ m thick tissue sections were stained with hematoxylin and eosin to visualize the tissue and the injected hybrid systems. Images were taken at given magnifications (10x and 40x) under bright field conditions.



### 2.3.3. Results and Discussion

#### 2.3.3.1. Synthesis of Mesoporous Carbon Nanoparticles

The synthesis of C3 and C1Sph mesoporous carbons was accomplished through a nanocasting procedure, *i.e.*, the use of a template and its subsequent filling with another material.<sup>13</sup> In particular, SBA-15 and MCM-48 silica nanoparticles were used as templates, respectively. The silica molds were synthesized through the *sol-gel* method using a surfactant as structure directing agent and the calcination approach to remove the surfactant. Then, both samples were infiltrated with an organic carbon source that was subsequently polymerized/carbonized. Finally, the carbonized materials were treated with hydrofluoric acid to remove the silica template, yielding mesostructured carbon nanoparticles (Scheme 2.9).



**Scheme 2.9.** Representative example of the synthesis of mesoporous carbons (C1Sph) through nanocasting. The MCM-48 silica template was synthesized using the *sol-gel* method and the surfactant was removed through calcination. The obtained silica mold was impregnated with a sucrose solution as organic precursor which was subsequently carbonized. Finally, the silica template was removed using hydrofluoric acid to yield mesostructured carbon nanoparticles.

MCM-48 was used because it presents a cubic phase structure that assures the connectivity of the cavity networks after carbonization. SBA-15 was used owing to their large mesopores connected through micropores, which also assures the homogeneous carbonization. In this sense, MCM-41 presents isolated hexagonal symmetry, which prevents their use as template for mesoporous carbons.<sup>6</sup>

The as-produced carbon materials were characterized by means of XRD, N<sub>2</sub> adsorption analysis and SEM microscopy.

The structure of the carbon nanoparticles was analyzed through XRD measurements. As it happened for the MSNs, these materials are amorphous at the atomic level. Therefore, the maxima observed in the diffractogram are related to the symmetry of the pores (Figure 2.40).

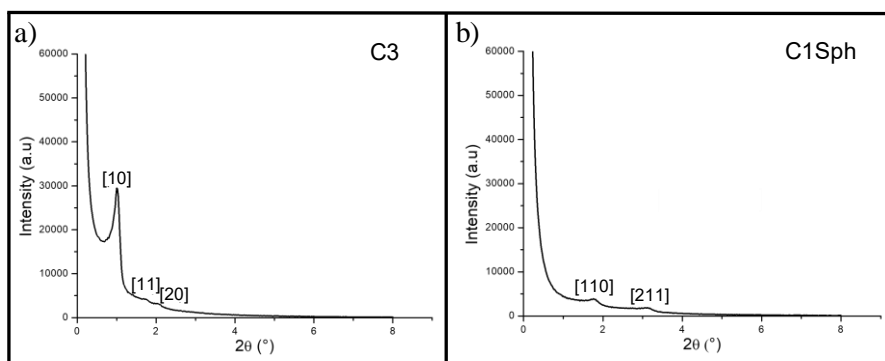


**Figure 2.40.** XRD diffractograms. a) C3. b) C1Sph. The maxima obtained demonstrated the hexagonal pore symmetry of C3 and 3D cubic structure of C1Sph, as expected for these materials.

The x-ray pattern of C3 (Figure 2.40a) shows three maxima that can be ascribed to the [10], [11], and [20] reflections typical of a 2-D hexagonal ordered arrangement ( $p6mm$  space group), in agreement with SBA-15 materials.<sup>14,15</sup> On the other hand, figure 2.40b shows the x-ray pattern of C1Sph, where the maxima [110] and [211] can be observed. This would be in agreement with the 3D cubic structure ( $I4_132$  space group), as expected.<sup>16</sup>

The textural properties of the as-produced mesoporous carbons were determined through N<sub>2</sub> adsorption analysis (Figure 2.41).

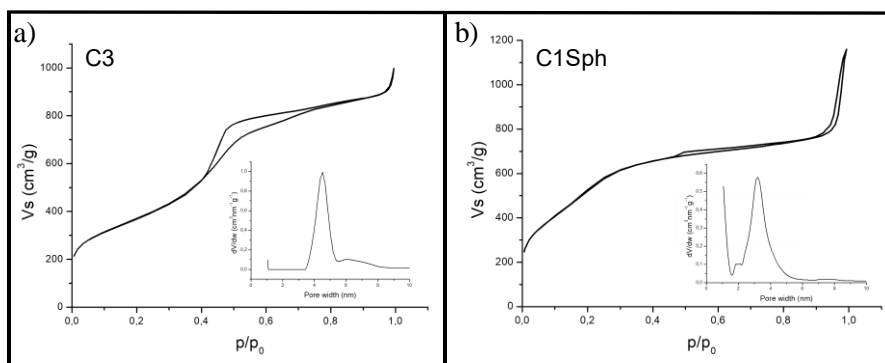


**Figure 2.41.** N<sub>2</sub> adsorption analysis. a) C3. b) C1Sph. C3 showed a type-IV isotherm typical of CMK-3 materials showing mesoporosity. C1Sph showed a stepwise behavior typical of CMK-1 materials with mesopores.

The adsorption analysis of C3 (Figure 2.41a) showed a type-IV isotherm with H2 hysteresis loop, typical of CMK-3-type mesoporous materials with uniform cylindrical mesopores of *ca.* 4.5 nm.<sup>14,15</sup> On the other hand, the isotherm of C1Sph (Figure 2.41b) exhibited a stepwise behavior, typical of CMK-1-type mesoporous materials with narrow mesopores of *ca.* 3.2 nm disposed as a helical structure of two interweaved worm-like pore systems.<sup>16-18</sup> The textural properties are summarized in table 2.6.

**Table 2.6.** Summary of the textural properties of C3 and C1Sph. Both materials showed greater textural properties than the MSNs (Specific surface area *ca.* 1,000 m<sup>2</sup>/g and pore volume *ca.* 1 cm<sup>3</sup>/g).

	Specific surface area (m <sup>2</sup> /g)	Pore volume (cm <sup>3</sup> /g)	Pore width (nm)
C3	1,340	1.4	4.5
C1Sph	1,650	1.2	3.2

As observed in Table 2.7, both mesoporous carbons showed improved textural properties compared to the well-studied MSNs, which usually show values of specific surface area *ca.* 1,000 m<sup>2</sup>/g and pore volume *ca.* 1 cm<sup>3</sup>/g. The morphology of C3 and C1Sph was evaluated in the SEM microscope (Figure 2.42).

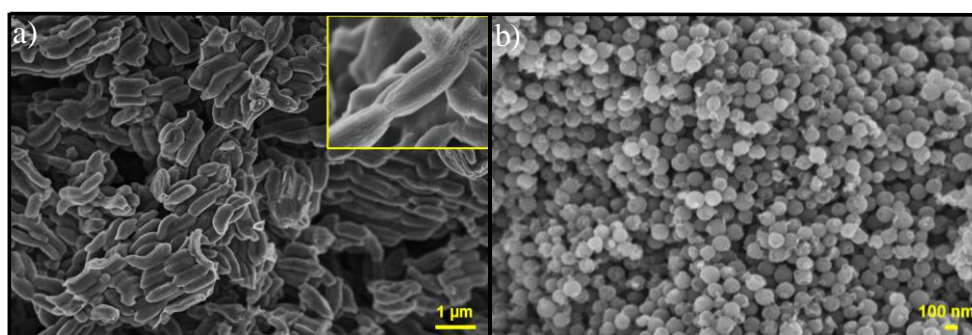


**Figure 2.42.** SEM. a) C3 (Inset: zoom). b) C1Sph. C3 exhibited a rod-like elongated morphology with dimensions 0.2-0.3 x 0.5-1 µm. C1 consisted of well-defined spheres with size *ca.* 150 nm.

C3 consisted of agglomerated rod-like elongated carbon particles (Figure 2.42a), typical of CMK-3 type carbons,<sup>19</sup> with diameter of 0.2-0.3 µm and length of 0.5-1 µm. On the other hand, the C1Sph nanoparticles exhibited a well-defined spherical morphology with a mean particle size of *ca.* 150 nm (Figure 2.42b).

### 2.3.3.2. Determination of the Loading Capacity

The next step was to evaluate the loading capacity of these carriers and find out if they could load higher amounts of molecules than their mesoporous silica nanoparticles counterparts. In this sense, C3, C1Sph and MSNs were loaded with the Ru dye and subjected to thermogravimetric analysis to measure the organic content, which translated into the amount of cargo loaded (Figure 2.43).

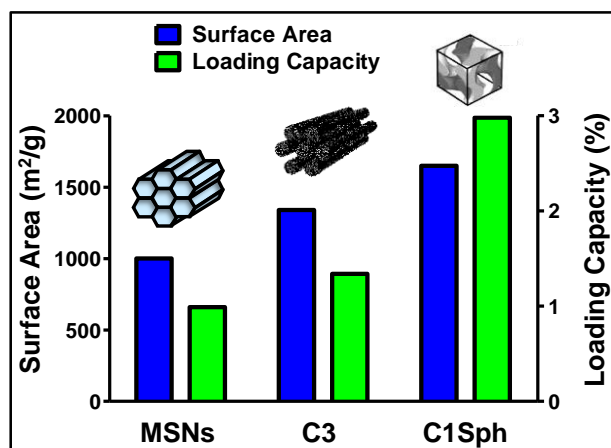


**Figure 2.43.** Surface Area and Loading Capacity of MSNs vs mesoporous carbon matrices (C3 and C1Sph). Both carbon nanoparticles showed greater loading capacity, specially C1Sph, which triplicated the silica loading capacity.

As shown in Figure 2.43, both carbons performed better than MSNs. It should be highlighted that C1Sph showed remarkable loading capacity, triplicating the amount of cargo loaded by the MSNs. These results would confirm (1) that the adsorption capacity is related to the surface area and (2) that the  $\pi$ - $\pi$  stacking could be useful for the loading of aromatic molecules, as many therapeutic drugs are.

### 2.3.3.3. Synthesis of pH-Responsive Self-Immolative Polymers

Once the initial hypothesis of the higher loading capacity was confirmed, the next step was to provide C3 and C1Sph with smart stimuli-responsive behavior. An interesting approximation to obtain such on-demand release would be the translation of the previously described self-immolative technology to these carbon materials.

In view of a potential scale-up of this technology within the frame of MOZART, the next steps were headed towards the optimization of the SIP synthesis. In this sense, new synthetic approximations for the synthesis of compounds **1** and **2** were carried out and the synthesis of compound **3** was optimized to obtain higher yields.

The synthesis of compound **1** was adapted from a previously reported method and scaled up to 6 g of starting ABA.<sup>10</sup> In addition, the purification was changed to a fast crystallization in chloroform that provided excellent results. The synthesis of compound **2** was reproduced from a reported method,<sup>11</sup> avoiding the use of refluxing temperatures and providing better yields.

The method for the synthesis of compound **3** described in section 2.2.2.2 was thoroughly modified to improve the yield of the SIP synthesis. First, different experimental conditions such as catalyst and reactant concentrations were explored to maximize the molecular weight of the polymer (Table 2.7). The trigger was not added until the highest molecular weight possible was achieved.

**Table 2.7.** Optimization of the SIP molecular weight as a function of the catalyst and monomer concentration. \*Referred to compound **1**.

% DBTL*	Molarity*	Number of monomers	Reaction conditions
5	1	10	
4	1	12	
3	1	14	2.5 hours
3	1.5	17	
2	1.5	18	85°C
2	2	12	
3	2	20-40	

The best results in terms of number of units and, consequently, molecular weight were obtained with the condition: 3% DBTL, 2M, 85°C, 2.5 hours. An average synthesis using these conditions led to SIPs with *ca.* 20 units, although polymers with up to 40 units were obtained, as shown in Table 2.7.

Then, the next step was to introduce the trigger to provide the chain with pH-responsive stimuli-responsive behavior. It was observed that the addition of compound **2** at the reaction temperature (85°C) led to the degradation of the preformed polymeric chains synthesized as stated in table 2.7. A possible explanation might be that compound **2** would be too reactive at such temperature and might react throughout the polymer chain, rather than at its end. For that reason, the possibility of reducing the temperature to add the trigger and then increase it again was explored. In this way, the temperature progressively increased and compound **2** would react in a milder way. This approach provided SIPs composed of *ca.* 20 units and *ca.* 70-80% of incorporation of the pH-responsive trigger (Figure 2.44). Regardless of temperature, the behavior shown in Figure 2.30 (polymer degradation upon trigger addition if size > 20-25 units) was also observed.

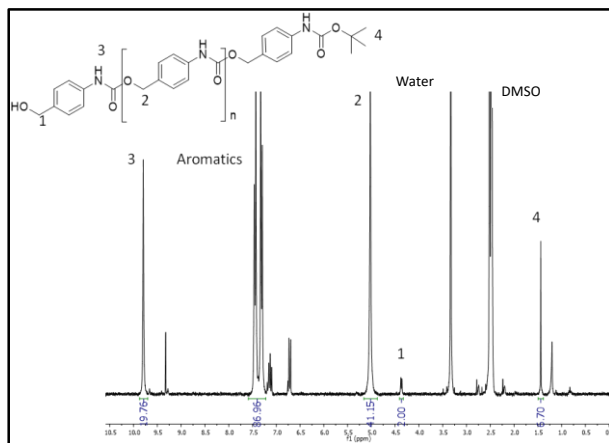


**Figure 2.44.**  $^1\text{H-NMR}$  of compound **3** synthesized through the protocol described in section 2.3.2.3. (250 MHz, DMSO)  $\delta$  9.82 (s, 20H), 7.56-7.15 (m, 87H), 5.15(s, 41H), 4.43 (d, 2H), 1.48 (s, 7H).

As shown in Figure 2.44, the SIP could be effectively synthesized, achieving the maximum molecular weight possible and the incorporation of a significant amount of trigger. Overall, the optimization of the SIP synthesis led to SIPs with molecular weight *ca.* 3,300 g/mol and average yield *ca.* 90%, which was much greater than that obtained using the protocol described in Section 2.2.2.2 (*ca.* 30%).

#### 2.3.3.4. Synthesis of SIP-Coated Carbon Nanoparticles

The carbons were characterized by XPS to unravel the chemical groups on the surface and design a synthetic protocol to graft the self-immolative coating (Figure 2.45).

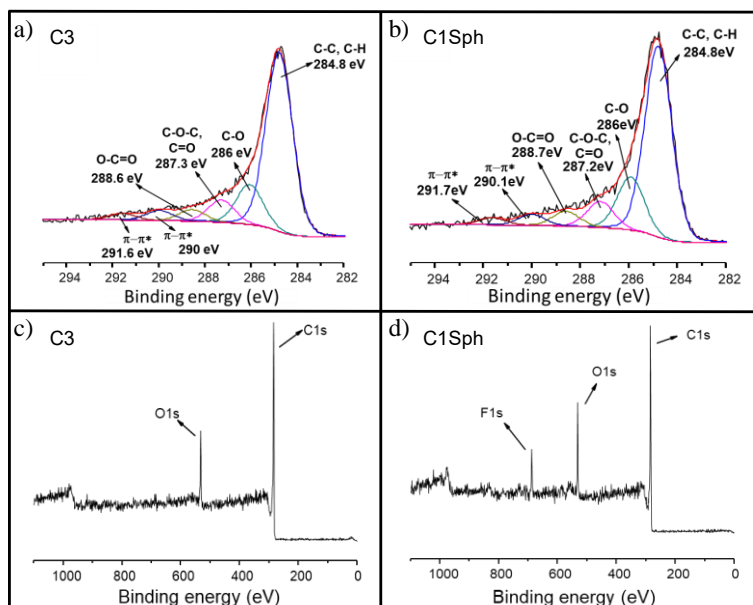


**Figure 2.45.** Top: XPS analysis; Bottom: Survey spectrum. a) XPS analysis of C3. b) XPS analysis of C1Sph. c) Survey spectrum of C3. d) Survey spectrum of C1Sph. The XPS analysis demonstrated the presence of hydroxyl, carboxylic acid and epoxy groups on the surface.

The spectrum of C3 (figure 2.45a) can be decomposed into six peaks: 284.8 eV, 286.0 eV, 287.3 eV, 288.6 eV, 290.0 eV and 291.6 eV. The carbon-carbon bonds are located at 284.8 eV. The second peak is associated to the C-O bonds. The peak at 287.3 eV can be ascribed to the epoxy/ether and carbonyl groups. Finally, the last two peaks may be related to the  $\pi$ - $\pi^*$  (HOMO-LUMO) transition of the turbostratic structure of the carbon backbone.<sup>20</sup> However, it should be mentioned that signals at 290.0 eV have been also related in the literature to C bonded as  $\text{CO}_3^{2-}$  (surface carbonates)<sup>21-23</sup> Additionally, a residual rests of the etching agent (HF) employed to remove the silica template were detected in the survey of C1Sph (Figure 2.45d).

The spectrum of C1Sph (Figure 2.45b) can be decomposed again into six peaks located at 284.8 eV, 286.0 eV, 287.2 eV, 288.7 eV, 290.1 eV and 291.7 eV. The first peak can be ascribed to the aliphatic C-C and/or C-H bonds of the main  $\text{sp}^3$  carbon frame. The peak at 286 eV represents the C-OH bonds on the surface of the plain carbon. The peak at 287.2 eV represents the contribution of C-O-C epoxy/ether and C=O carbonyl groups present on the surface (the instrumental resolution does not allow the distinction of these groups).<sup>24</sup> The peak at 288.7 eV represent the carboxylic acid groups present on the surface of C1Sph. Finally, the peaks at 290.1 and 291.7 eV may be ascribed to the  $\pi$ - $\pi^*$  features of the carbon matrix.<sup>20,22,24,25</sup>

In view of the results, the most abundant functional groups in the samples were hydroxyl (OH), carboxylic acid (COOH) and epoxy (C-O-C) groups. In consequence, the direct addition of the hydroxyl functionality of the SIPs to form C-O-C ether groups with the epoxy groups of the surface was explored. The correct grafting of the SIPs on the surface of C3 and C1Sph was characterized in terms of TGA,  $\text{N}_2$  adsorption analysis, XPS measurements and TEM microscopy.

The samples were subjected to TGA analysis to determine the amount of additional organic matter present in the samples after the SIP coating (Figure 2.46).

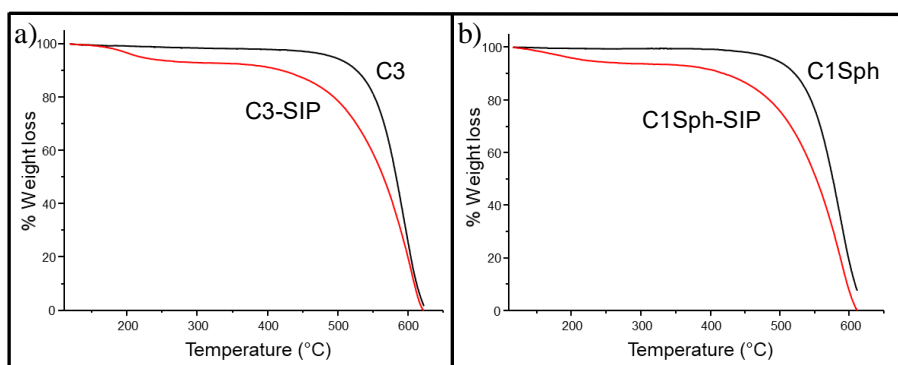


**Figure 2.46.** TGA analysis. a) C3 vs C3-SIP. b) C1Sph vs C1Sph-SIP. In both cases, the addition of the SIP led to *ca.* 15% of weight loss, confirming the presence of the SIP.

The TGA analysis of the SIP-coated samples showed a difference of *ca.* 15% in the weight loss for each SIP-coated material, measured in the range 150-450°C. This organic content could be ascribed to the presence of the polymer, confirming the functionalization the carbons surface.

The effect of the functionalization with the pH-responsive polymer on the textural properties of the samples was determined through N<sub>2</sub> adsorption analysis (Figure 2.47).

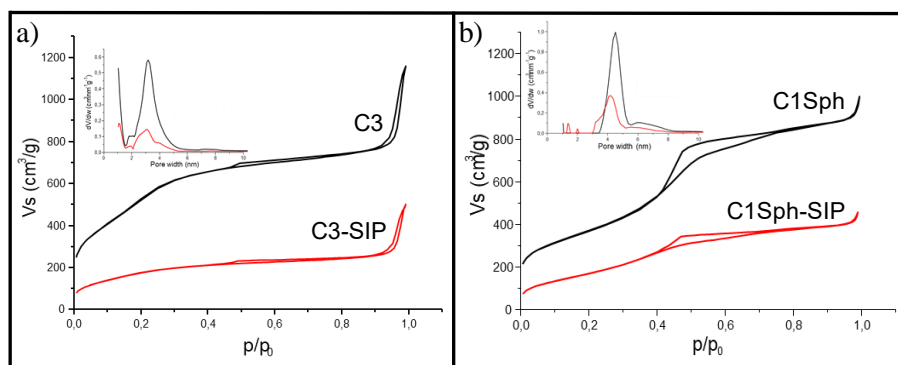


**Figure 2.47.** N<sub>2</sub> adsorption analysis. (Inset: Pore size distribution). a) C3 vs C3-SIP. b) C1Sph vs C1Sph-SIP. The SIP coating of C3 and C1Sph led to a decrease of *ca.* 55% and *ca.* 65% in the specific surface area, respectively, confirming the successful grafting of the polymer.

The functionalization of C3 with the SIPs led to a reduction of *ca.* 55% in the specific surface area (Figure 2.47a), while inducing a decrease of *ca.* 65% in the specific surface area of C1Sph. These results confirmed the successful functionalization of both mesoporous carbons with the self-immolative polymeric coating. In addition, the shape of the isotherms of the SIP-coated mesoporous carbons remained after the functionalization, indicating that the mesostructure was unaffected by the selected synthetic protocol. The results derived from the TGA and the N<sub>2</sub> adsorption analysis are summarized in Table 2.8.



**Table 2.8.** Summary of the TGA analysis and the textural properties of the mesoporous carbon materials. The differences between the coated and non-coated materials (increase of weight loss and decrease of textural properties) confirm the successful functionalization. \*Weight loss with respect to the pristine materials.

	Specific surface area (m <sup>2</sup> /g)	Pore volume (cm <sup>3</sup> /g)	Pore width (nm)	% Weight loss
C3	1340	1.4	4.5	-
C3-SIP	620	0.6	4.1	14.8*
C1Sph	1650	1.2	3.2	-
C1Sph-SIP	560	0.4	3.0	14.9*

As shown in Table 2.8, the SIP grafting induced a reduction of the pore volume, as it happened for MSN-CS-SIP (Table 2.5). This would be ascribed again to the partial filling of the mesopores with the SIPs.

The SIP-coated samples were analyzed through XPS to determine if the functional groups of the polymer were present (Figure 2.48).

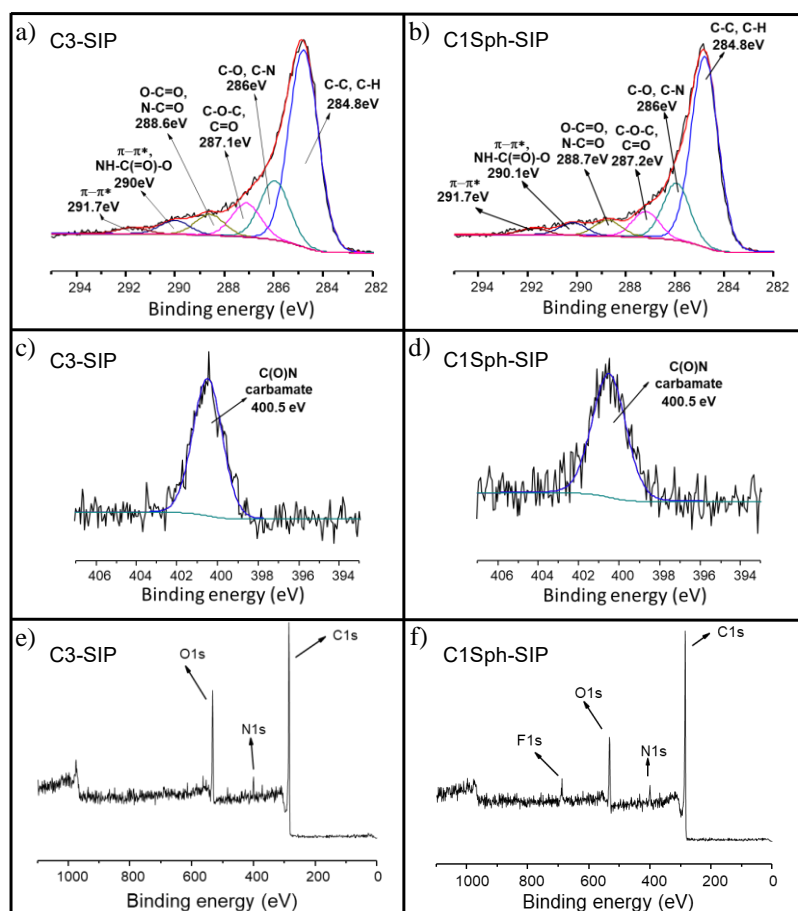


**Figure 2.48.** a) XPS analysis of C3-SIP. b) XPS analysis of C1Sph-SIP. c) XPS carbamate signal of C3-SIP. d) XPS carbamate signal of C1Sph-SIP. e) Survey spectrum of C3-SIP. f) Survey spectrum of C1Sph-SIP. The appearance of signals associated to the carbamates of the SIPs confirmed the successful synthesis of the SIP-coated carbons.

In more detail, after the functionalization the percentage of C-C/C-H peaks decreased whereas the peaks that may be ascribed to C-N bonds (amines at 286.0 eV,<sup>22–28</sup> and carbamates at 290.1 eV<sup>24,27</sup>), increased in general. An additional confirmation of the successful functionalization was the appearance of the N1s photoelectron peak at 400.5 eV<sup>22,26–28</sup> for both C1Sph-SIP and C3-SIP (figures 2.48c and d), which would be attributed to the carbamate groups of the polymer. A detailed summary of the XPS measurements is shown in table 2.9.

**Table 2.9.** Analysis of the XPS measurements of unmodified and SIP-coated samples.

Peak Assignment	Binding Energy (eV)	C1sph (at. %)	C1sph-SIP (at. %)	C3 (at. %)	C3-SIP (at. %)
C-C / C-H	284.8	63.0	61.7	66.4	59.5
C-O / C-N	286.0	17.6	18.5	14.8	17.9
C-O-C / C=O	287.2	8.5	8.5	8.3	10.2
O-C=O / N-C=O	288.7	4.8	5.1	4.3	6.4
CO <sub>3</sub> <sup>2-</sup> / $\pi$ - $\pi^*$ / NH-C(=O)-O	290.1	3.8	4.0	3.8	4.1
$\pi$ - $\pi^*$ / CF <sub>2</sub>	291.7	2.3	2.2	2.4	1.9

The correct SIP coating of the carbons was confirmed through the increment of the peaks ascribed to the presence of nitrogen in Table 2.9, such as N-C=O and NH-C(=O)-O, which would be ascribed to the carbamate of the SIPs.

One of the main drawbacks of the nanocasting procedure is the difficulty to obtain hydrophilic samples.<sup>13</sup> In this sense, the aqueous dispersibility of the samples improved after grafting the SIP, probably due to the presence of the carbamate groups. The experimental evidence was that when the pristine carbons were added to an aqueous solution they remained on the top of the surface, as a consequence of the highly hydrophobic nature of the samples (a slight degree of dispersion after sonication could be observed). On the contrary, when doing the same experiment with the SIP-coated nanocarriers, they could be properly dispersed after a short period of sonication. Indeed, the hybrids remained dispersed for longer periods of time after sonication (Figure 2.49).

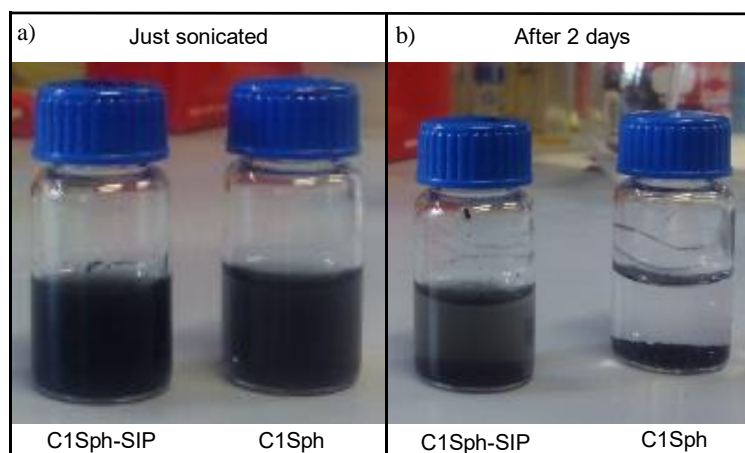


**Figure 2.49.** Representative example of the aqueous dispersibility of the carbons before and after functionalization. a) Right after sonicating the samples. b) After two days. In general, the SIP-coated materials were better dispersed than their pristine counterparts.

Finally, TEM analysis was carried out to evaluate whether there was presence of organic matter on the surface of the SIP-coated carbons. For that purpose, the pristine and modified materials were stained with phosphotungstic acid and observed under the microscope (Figure 2.50).

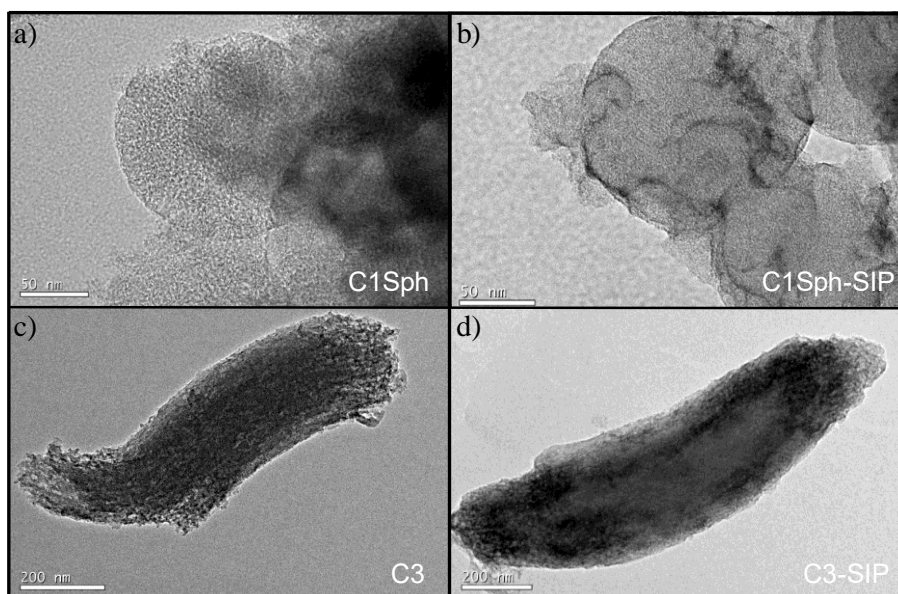


**Figure 2.50.** TEM visualization of samples stained with phosphotungstic acid. a) C1Sph. b) C1Sph-SIP. c) C3. d) C3-SIP. The blurrier surface in the SIP-coated samples was indicative of the presence of organic matter on the surface, as a consequence of a successful SIP grafting.

Phosphotungstic acid binds to the organic matter present in a sample and allows its visualization under the electronic microscope.<sup>29</sup> In this sense, the SIP-coated samples (Figures 2.50b and d) showed a blurry shade on the surface, typical of functionalizations with organic compounds, confirming the successful grafting of self-immolative polymeric coating.

### 2.3.3.5. Release Experiments from SIP-Coated Carbon Nanoparticles

Mesoporous carbons were loaded with a model fluorophore prior to the SIP coating. The release experiments were carried out in Transwells® at pH 7.4 and 5 to mimic the pH of the bloodstream and the lysosomes, respectively (Figure 2.51).

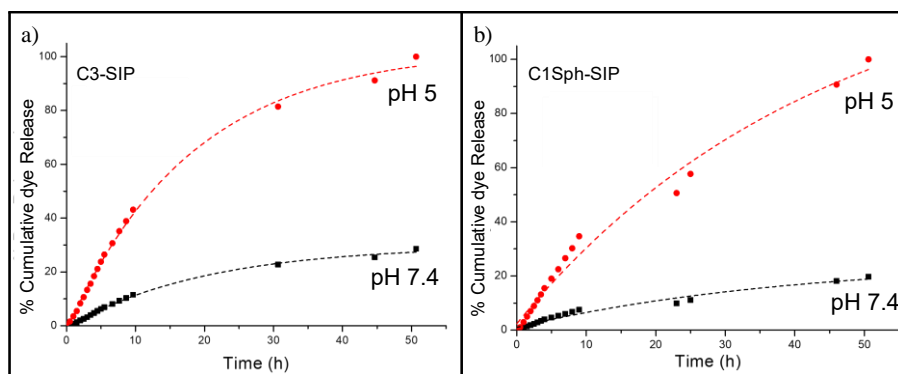


**Figure 2.51.** Release experiments at physiological and acid pH. a) C3-SIP; b) C1Sph-SIP. At physiological pH, the SIPs blocked the pore entrances, hampering the release. However, at acid pH the SIPs degraded, opening the pores and inducing the release.

Overall, both release experiments clearly showed that the SIPs maintained their integrity at physiological pH, blocking the mesopores and hampering the release, as initially hypothesized. However, at acid pH the polymeric gatekeeper self-immolated, opening the pores and leading to the release.

In more detail, the release experiment of C3-SIP (Figure 2.51a) showed residual release of dye (*ca.* 28%) at physiological pH after 50 hours, which was partially ascribed to dye molecules entrapped within the polymeric network. However, a more than four-fold release at acid pH was observed, confirming the sensitivity of the polymer to acid environments. The release kinetics for C1Sph-SIP (Figure 2.51b) showed a similar trend. In this case, only 20% of dye was released at physiological pH, indicating better performance of the polymeric coating. This could probably be ascribed to (1) the smaller pore size of C1Sph that would be easier to cap with the SIPs and (2) the smaller size of C1Sph that might lead to more homogenous SIP coating. On the other hand, the sample at acid pH showed a five-fold release, clearly indicating the pH-responsiveness of the coating.

### 2.3.3.6. Cell Experiments

The *in vitro* biocompatibility and cytotoxicity of the SIP-coated mesoporous carbon materials were assessed on human osteosarcoma (HOS) cells. Three concentrations (25,

50 and 100  $\mu\text{g/mL}$ ) and two time points (24 and 48 hours) were studied. The biocompatibility was tested using unloaded SIP-coated carbons (C3-SIP and C1Sph-SIP). To assess the cytotoxicity, the two carbons were loaded with doxorubicin (C3-DOX-SIP and C1Sph-DOX-SIP) before the SIP coating. DOX was selected because it is currently used for the treatment of osteosarcoma in the clinic.<sup>30</sup> In order to verify that the SIP coating actually degrades upon acid pH and behaves as responsive and effective gatekeeper, another series of samples were prepared by loading the two carbons with doxorubicin and then coating them with the same polymer backbone but without the pH-responsive trigger (C3-DOX-NOBOC and C1Sph-DOX-NOBOC). The results are depicted in figure 2.52.

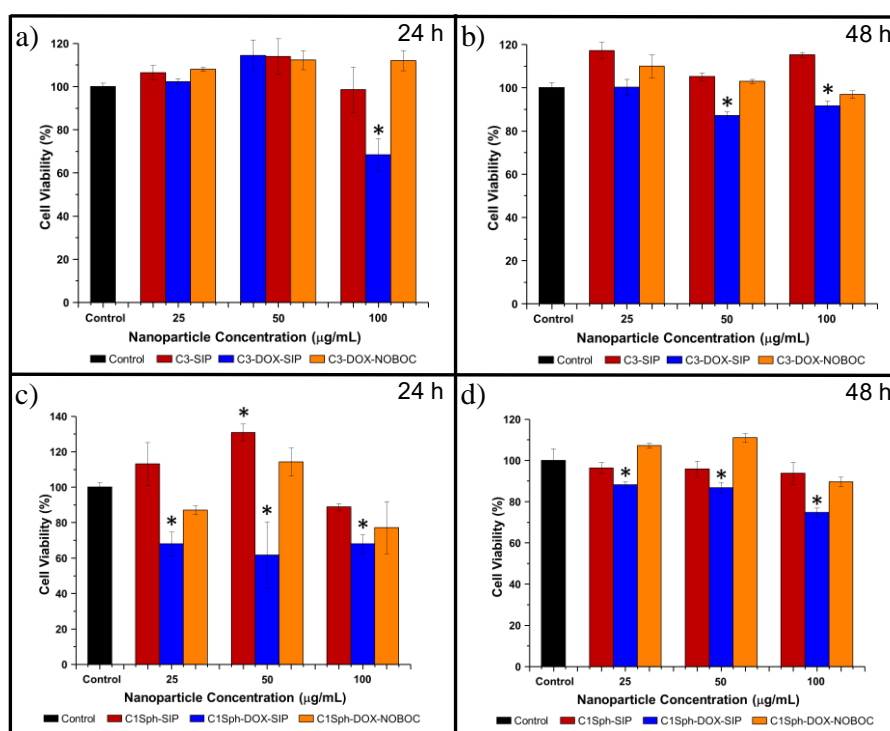


**Figure 2.52.** Cytotoxicity assay in HOS cells. a) C3-SIP and derivatives at 24 hours. b) C3-SIP and derivatives at 48 hours. c) C1Sph-SIP and derivatives at 24 hours. d) C1Sph-SIP and derivatives at 48 hours. Data are mean  $\pm$  SEM of 3 independent experiments performed in duplicate. \* $p < 0.05$  vs. corresponding SIP-coated carbon and control. None of the unloaded carriers induced toxicity for any of the times or concentrations. The highest cytotoxic effects were observed for C1Sph-DOX-SIP, while only the higher concentrations of C3-DOX-SIP inhibited the cell viability when using this material. None of the groups bearing the non-sensitive SIPs exerted cytotoxic effects, demonstrating the pH-sensitivity of the SIPs.

Overall, neither C3-SIP nor C1Sph-SIP induced any cytotoxic effect to the cells, regardless of the time point or concentration. Interestingly, for lower concentrations of C1Sph-SIP, in particular 50  $\mu\text{g/mL}$ , a significant increase of cell proliferation at 24 hours

was observed due to the presence of the material (Figure 2.52c). This behavior has been previously reported in the literature for carbon nanotubes on several cell lines.<sup>31,32</sup> In the case of C3-SIP particles a slightly positive effect (but still not significant) on the proliferation of the cells was found at 24 hours when using a concentration of 25 and 50  $\mu\text{g}/\text{mL}$  (Figure 2.52a). In addition, and what is more important for the present work, this confirmed that the polymeric coating and their degradation by-products, generated as a consequence of the acid pH in the lysosomes, were biocompatible.

The drug-loaded C1Sph-DOX-SIP was able to induce significant cytotoxicity at 24 and 48 hours, which appeared to be more pronounced at 24 hours. However, the overall cytotoxicity effect of C3-SIP was much lower than that of C1Sph-SIP. A reasonable hypothesis would be that, in general, small nanoparticles (C1Sph-SIP) are engulfed more easily than the bigger ones (C3-SIP). This would lead to a lower total amount of released drug and then a lower effect on cell viability. At 24 hours only the 100  $\mu\text{g}/\text{mL}$  condition was able to reduce the cell viability while at 48 hours the particles at 50  $\mu\text{g}/\text{mL}$  showed the first cytotoxic effect. Aside from the size, the fact that C1Sph shows higher release capacity than C3 might also be a reason for the enhanced cytotoxicity of the C1Sph materials.

Once the biocompatibility and cytotoxicity of the SIP-coated nanocarriers was confirmed, the next step was to verify the responsivity to acid pH *in vitro*. For that purpose, a polymer with the same backbone without the pH-responsive trigger was synthesized (same protocol but without the addition of compound 2) and further grafted on the doxorubicin-loaded mesoporous carbons. As observed in figure 2.52, any of these groups (C3-DOX-NOBOC and C1Sph-DOX-NOBOC) induced any cytotoxic effects on the cells for any concentration or time point. This is a confirmation of the need of a pH-responsive trigger to initiate the self-immolation and, consequently, trigger the drug release. This means that the polymeric coating maintained its integrity, closing the pore entrances of the non-responsive mesoporous carbons and avoiding the drug release.

#### 2.3.3.7. Short-Term Release Experiments from C1Sph-SIP

The promising *in vial* and *in vitro* experiments called for an *in vivo* proof of concept validation of the system. C1Sph-SIP was chosen for such experiments because it was observed to be the best candidate in terms of textural properties, responsive release profile and cytotoxic effects. The experiments were carried out in mice exposed to either acid or

neutral solution in a pocket under the skin. During these experiments, a pH 4 solution was employed to delay pH homeostasis that could interfere with our responsive carrier.

Prior to the *in vivo* experiments, the responsiveness of the Ru-loaded C1Sph-SIP to short-term pH-triggering was evaluated *in vial* (Figure 2.53).

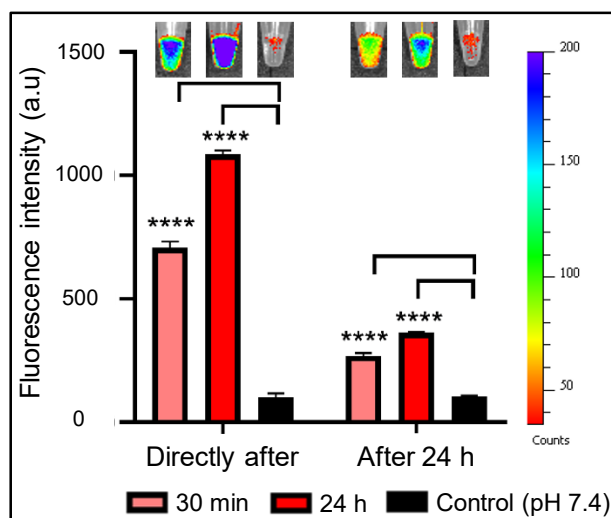


**Figure 2.53.** Short-term pH-triggering *in vial* release experiment of Ru-loaded C1Sph-SIP. The samples were exposed to pH 4 (red) or 7.4 (black) and the supernatants were measured in the IVIS®. Then, all the samples were dispersed in a 7.4 solution and measured again after 24 hours. The experiment demonstrated that only the particles previously exposed to acid pH were able to induce significant and continuous release. Images at the top are representative IVIS® images per condition. Color bar is shown on the right. Data are mean  $\pm$  SD of  $n=3$  (for 24 h trigger  $n=2$ ). Statistics: unpaired, two-tailed t-test,  $p^* \leq 0.05$ , conditions always compared to control per time point.

As shown in Figure 2.53, only the samples soaked at pH 4 (red), for either 30 minutes or 24 hours, resulted in substantial Ru release. This meant that 30 minutes was long enough to trigger the cargo release, highlighting the fast responsive behavior of the designed system. In consequence, C1Sph-SIP should be unaffected by any potential *in vivo* homeostasis and the triggering could be performed *in vivo*.

After that experiment, the above-mentioned samples were dispersed in a 7.4 pH solution for further 24 hours and the supernatants were measured again, observing that only the previously triggered groups kept releasing the cargo. On the other hand, carriers at physiological pH showed negligible release, which confirms the pore blocking stability and highlights the unquestionable pH-responsiveness of the here designed nanocarrier.

### 2.3.3.8. *In Vivo* Study: pH-Responsive Ru Release and Biocompatibility of C1Sph-SIP

This *in vivo* study was conceived to provide answers to three questions: (1) despite both release experiments (I and II) seemed to indicate that the SIP coating maintained its integrity at physiological pH, would it survive when placed in a more realistic scenario with mice? (2) despite not being cytotoxic *in vitro*, would C1Sph-SIP induce an immune response when administered under the skin to the mice? and (3) would it be possible to open the pores despite the effects of the potential immune response?

Ru-loaded C1Sph-SIP particles were administered subcutaneously to the mice in a physiological solution at pH 7.4 and then, the animals were imaged longitudinally in the IVIS® prior and just after the injection, and 24, 48 and 96 hours post injection (Figure 2.54).

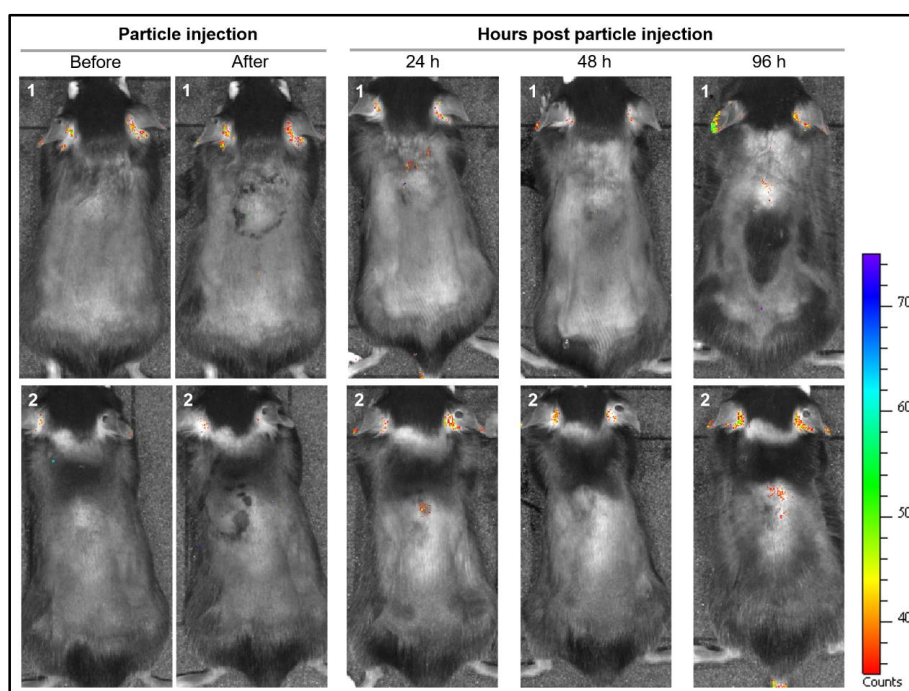


**Figure 2.54.** Longitudinal IVIS® imaging of the dorsal site of two mice. Left: Before and just after injection; Right: 24, 48 and 96 h post injection. Even after 96 hours the SIPs on the surface remain unaffected since almost no fluorescence can be detected.

As shown in figure 2.54, only a small amount of fluorophore could be detected after 96 hours. This clearly demonstrated that the SIP coating could survive at physiological pH inside an animal. In consequence, the pores would remain closed during a potential systemic administration, thus avoiding premature release and confirming the pH-sensitivity of the coating.



To study the general biocompatibility of C1Sph-SIP the animals were visually inspected on a daily basis for irritations in the injection site, overall appearance and behavior. After imaging at 96 h, the animals were sacrificed, the injection site was explanted and prepared for histology (hematoxylin and eosin staining, H&E). (Figure 2.55).

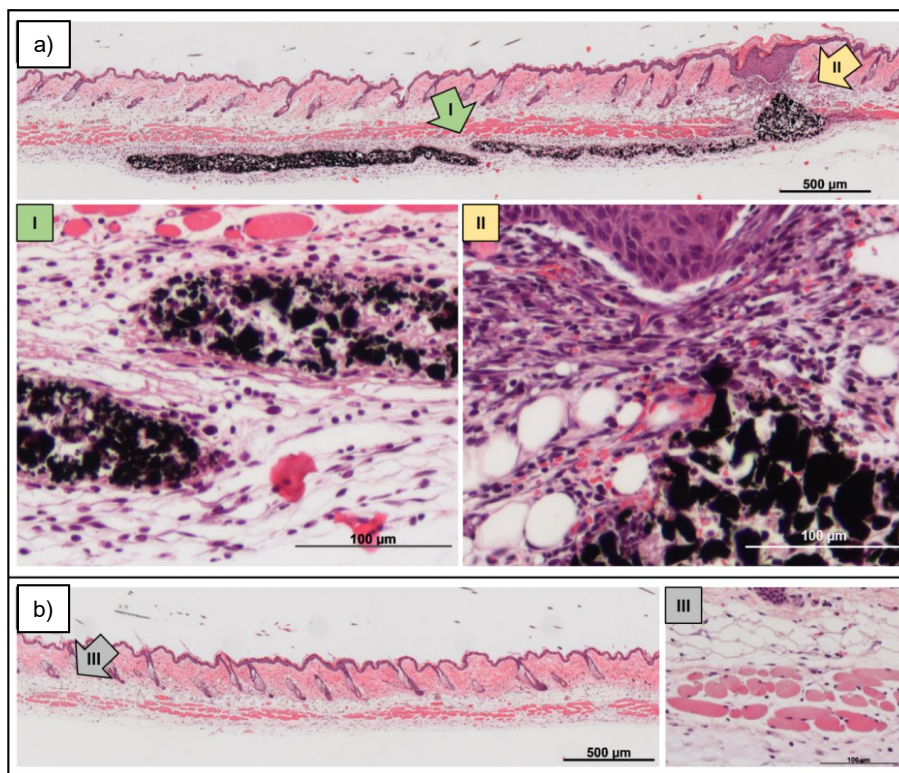


**Figure 2.55.** H&E-stained sections of paraffin-embedded skin tissue. a) Injected mouse; b) Non-injected mouse. I (administered nanoparticles), II (injection site) and III (control tissue) represent areas of a) and b) with higher magnification. Black: C1Sph-SIP; Purple: Nuclei; Light pink: Cytoplasm and connective tissue; Dark pink: Muscle tissue. The SIP-coated carriers did not induce a significant immune response, and a similar aspect as that of the non-injected tissue could be observed.

As shown in figure 2.55a, none of the injected animals exhibited adverse reactions to the carbon material. The organism reacted to the injection of C1Sph-SIP by moderate formation of a capsule around the particles and only minor infiltration of immune cells (figure 2.55a.I) compared to the non-injected skin (figure 2.55b.III). This clearly demonstrated the high biocompatibility of C1Sph-SIP and its potential to be translated to the clinic.

Once the absence of adverse immune reaction *in vivo* was demonstrated, the next objective was to evaluate whether the self-immolation could be triggered *in vivo* by the application of an exogenous pH trigger (pH 4). As a control, physiological pH solution

was evaluated. The animals were imaged with the IVIS® before, during and after the triggering period, and again at 24 and 72 hours post triggering. (Figure 2.56)

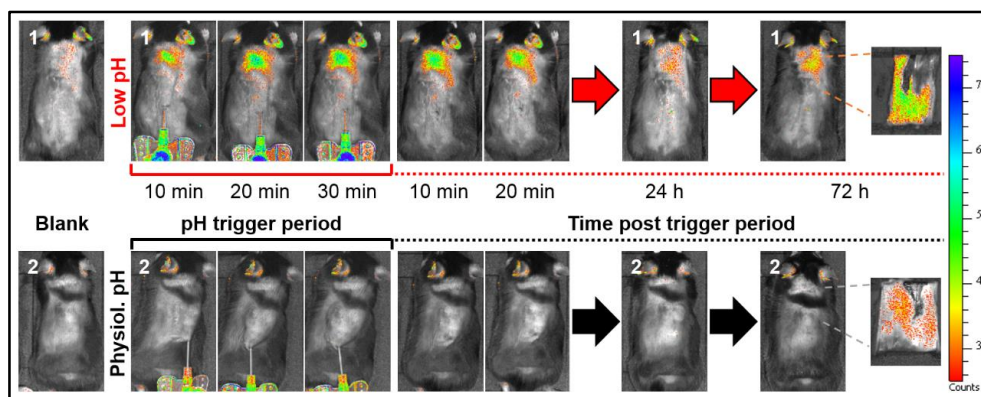


**Figure 2.56.** Longitudinal IVIS® imaging over 72 h (from 10 min after injection up to 72 h). Top: pH 4; Bottom: pH 7.4. The animals were sacrificed, the injection sites harvested, inverted and imaged again (zoom in the right). Only the animals receiving the solution at acid pH showed significant levels of fluorescence.

As shown in Figure 2.56, only the animals receiving the acid solution (top) showed a significant Ru release. After the initial triggering, the fluorescence signal could be consistently detected during the entire testing period for the group at pH 4 while only a low signal could be detected under pH 7.4 conditions.

After 72 hours, the animals were euthanized and the injection site explanted, inverted and imaged. In this case, only the group receiving the pH 4 solution showed a strong fluorescent signal, while only minor signals were detected for the animals treated with the pH 7.4 solution.

This results confirmed that (1) the polymeric coating maintained its integrity at physiological pH and (2) only the acid environment was able to trigger the degradation of the polymers and the subsequent dye release, clearly demonstrating the feasibility of triggering the release in an *in vivo* scenario.

### 2.3.4. Conclusions

The objective of this work was to develop smart stimuli-responsive nanocarriers based on mesoporous carbons for cancer treatment. For that purpose, the differences in pH found in the organism were selected again as stimulus to trigger the release from the mesopores. In this sense, the pH-responsive self-immolative technology developed in the previous work was adapted to these materials.

Since mesoporous carbons showed even better textural properties than MSNs, the loading capacity of these materials was determined to find out if larger specific surface areas translated into greater loading capacities. In this sense, both carbon materials outperformed the MSNs, in particular C1Sph which triplicated the silica storage capacity, demonstrating the influence of the specific surface area on the loading ability.

In view of a future scale-up within the MOZART framework, the synthetic protocols reported in the previous work for the synthesis of compounds **1**, **2** and **3** were optimized, leading to higher yields. Additionally, a synthetic method for the grafting of the SIPs on the carbons was developed, based on the analysis of the chemical groups present on the surface of the carbon materials.

The pH-responsiveness was validated *in vial*, *in vitro* and *in vivo*, showing unequivocally that the polymeric coating could maintain its integrity at physiological pH and undergo self-immolation at acid pH, thus opening the pores and triggering the drug release.

The *in vial* release experiments showed that the C1Sph-SIP could close more effectively the pore entrances at physiological pH, which translated in lower premature release. The *in vitro* experiment was carried out using doxorubicin-loaded carbons with a non-responsive self-immolative-like polymeric coating. In this case, the viability of the cells in contact with these materials was unaffected, clearly showing the need of the pH-responsive trigger as end-cap for the polymeric backbone. The pH-responsive *in vivo* experiment demonstrated (1) that the self-immolative polymers maintained their integrity at physiological pH inside an animal and (2) the induction of an acidic environment within the animals could trigger the release, thus confirming the pH-responsive nature of the SIP-coated carbon materials within an animal.

The biocompatibility of the SIP-coated mesoporous carbons was evaluated *in vitro* and *in vivo*. The *in vitro* experiments showed that the unloaded SIP-coated materials did not exert any cytotoxic effect on the cells. Moreover, the doxorubicin-loaded mesoporous carbons were able to inhibit the cell viability. In particular, C1Sph-SIP could exert a much higher cytotoxic effect. The *in vivo* biocompatibility was carried out in mice, where it could clearly be observed that the administration of the SIP-coated carbons induced only minor immune response, clearly demonstrating the potential applicability of these mesoporous carbons in further *in vivo* experiments.

## References

- (1) Yudasaka, M.; Yomogida, Y.; Zhang, M.; Tanaka, T.; Nakahara, M.; Kobayashi, N.; Okamatsu-Ogura, Y.; Machida, K.; Ishihara, K.; Saeki, K.; *et al.* Near-Infrared Photoluminescent Carbon Nanotubes for Imaging of Brown Fat. *Sci. Rep.* **2017**, *7*, 44760.
- (2) Yan, A.; Lau, B. W.; Weissman, B. S.; Külaots, I.; Yang, N. Y. C.; Kane, A. B.; Hurt, R. H. Biocompatible, Hydrophilic, Supramolecular Carbon Nanoparticles for Cell Delivery. *Adv. Mater.* **2006**, *18*, 2373–2378.
- (3) Kim, T.; Chung, P.; Slowing, I. I.; Tsunoda, M.; Yeung, E. S.; Lin, V. S. Structurally Ordered Mesoporous Carbon Nanoparticles as Transmembrane Delivery Vehicle in Human Cancer Cells. *Nano Lett.* **2008**, *8*, 3724–3727.
- (4) Gu, J.; Su, S.; Li, Y.; He, Q.; Shi, J. Hydrophilic Mesoporous Carbon Nanoparticles as Carriers for Sustained Release of Hydrophobic Anti-Cancer Drugs. *Chem. Commun.* **2011**, *47*, 2101–2103.
- (5) Saha, D.; Warren, K. E.; Naskar, A. K. Soft-Templated Mesoporous Carbons as Potential Materials for Oral Drug Delivery. *Carbon.* **2014**, *71*, 47–57.
- (6) Vinu, A.; Mori, T.; Ariga, K.; Vinu, A.; Mori, T.; Ariga, K. New Families of Mesoporous Materials. *Sci. Technol. Adv. Mater.* **2006**, *7*, 753–771.
- (7) Lu, A. H.; Li, W. C.; Schmidt, W.; Schüth, F. Template Synthesis of Large Pore Ordered Mesoporous Carbon. *Microporous Mesoporous Mater.* **2005**, *80*, 117–128.
- (8) Shin, H. J.; Ryoo, R.; Jaroniec, M. Modification of SBA-15 Pore Connectivity by High-Temperature Calcination Investigated by Carbon Inverse Replication. *Chem. Commun.* **2001**, 349–350.
- (9) Zhao, D.; Zhao, D.; Feng, J.; Huo, Q.; Melosh, N.; Fredrickson, G. H.; Chmelka, B. F.; Stucky, G. D. Triblock Copolymer Syntheses of Mesoporous Silica with Periodic 50 to 300 Angstrom Pores Triblock Copolymer. *Science.* **1998**, *279*, 548–552.
- (10) Robbins, J. S.; Schmid, K. M.; Phillips, S. T. Effects of Electronics, Aromaticity, and Solvent Polarity on the Rate of Azaquinone-Methide-Mediated Depolymerization of Aromatic Carbamate Oligomers. *J. Org. Chem.* **2013**, *78*, 3159–3169.
- (11) Lin, C.; Stedronsky, E. R.; Regen, S. L. pKa-Dependent Facilitated Transport of CO<sub>2</sub> across Hyperthin Polyelectrolyte Multilayers. *ACS Appl. Mater. Interfaces* **2017**, *9*, 19525–19528.
- (12) Sagi, A.; Weinstain, R.; Karton, N.; Shabat, D. Self-Immolative Polymers. *J. Am. Chem. Soc.* **2008**, *8*, 5434–5435.
- (13) Chen, Y.; Shi, J. Mesoporous Carbon Biomaterials. *Sci. China Mater.* **2015**, *58*, 241–257.
- (14) Giasafaki, D.; Bourlinos, A.; Charalambopoulou, G.; Stubos, A.; Steriotis, T. Nanoporous Carbon - Metal Composites for Hydrogen Storage. *Cent. Eur. J.*

*Chem.* **2011**, *9*, 948–952.

- (15) Giasafaki, D.; Bourlinos, A.; Charalambopoulou, G.; Stubos, A.; Steriotis, T. Synthesis and Characterisation of Nanoporous Carbon-Metal Composites for Hydrogen Storage. *Microporous Mesoporous Mater.* **2012**, *154*, 74–81.
- (16) Ryoo, R.; Joo, S. H.; Jun, S. Synthesis of Highly Ordered Carbon Molecular Sieves via Template-Mediated Structural Transformation. *J. Phys. Chem. B* **1999**, *103*, 7743–7746.
- (17) Ryoo, B. R.; Joo, S. H.; Kruk, M.; Jaroniec, M. Ordered Mesoporous Carbons. *Adv. Mater.* **2001**, *13*, 677–681.
- (18) Kruk, M.; Jaroniec, M.; Ryoo, R.; Joo, S. H. Characterization of Ordered Mesoporous Carbons Synthesized Using MCM-48 Silicas as Templates. *J. Phys. Chem. B* **2000**, *104*, 7960–7968.
- (19) Karavasili, C.; Amanatiadou, E. P.; Sygellou, L.; Giasafaki, D. K.; Steriotis, T. A.; Charalambopoulou, G. C. Development of New Drug Delivery System Based on Ordered Mesoporous Carbons: Characterisation and Cytocompatibility Studies. *J. Mater. Chem. B* **2013**, *1*, 3167–3174.
- (20) Giasafaki, D.; Charalambopoulou, G.; Tampaxis, C.; Dimos, K.; Gournis, D.; Stubos, A.; Steriotis, T. Comparing Hydrogen Sorption in Different Pd-Doped Pristine and Surface-Modified Nanoporous Carbons. *Carbon*. **2016**, *98*, 1–14.
- (21) Webb, M. J.; Palmgren, P.; Pal, P.; Karis, O.; Grennberg, H. A Simple Method to Produce Almost Perfect Graphene on Highly Oriented Pyrolytic Graphite. *Carbon*. **2011**, *49*, 3242–3249.
- (22) VanDelinder, V.; Wheeler, D. R.; Small, L. J.; Brumbach, M. T.; Spoeerke, E. D.; Henderson, I.; Bachand, G. D. Simple, Benign, Aqueous-Based Amination of Polycarbonate Surfaces. *ACS Appl. Mater. Interfaces* **2015**, *7*, 5643–5649.
- (23) Moulder, J. F.; William F. Stickle; Sobol, P. E.; Bomben, K. D. *Handbook of X-Ray Photoelectron Spectroscopy*; Perkin-Elmer Corporation, 1992.
- (24) Ederer, J.; Janoš, P.; Ecorchard, P.; Tolasz, J.; Štengl, V.; Beneš, H.; Perchacz, M.; Pop-Georgievski, O. Determination of Amino Groups on Functionalized Graphene Oxide for Polyurethane Nanomaterials: XPS Quantitation vs. Functional Speciation. *RSC Adv.* **2017**, *7*, 12464–12473.
- (25) Spyrou, K.; Calvaresi, M.; Diamanti, E. K.; Tsoufis, T.; Gournis, D.; Rudolf, P.; Zerbetto, F. Graphite Oxide and Aromatic Amines: Size Matters. *Adv. Funct. Mater.* **2015**, *25*, 263–269.
- (26) Briggs, D. *Surface Analysis of Polymers by XPS and Static SIMS*; Briggs, D., Ed.; Cambridge Solid State Science Series; Cambridge University Press: Cambridge, 1998
- (27) Benne, D.; Maccallini, E.; Rudolf, P.; Sooambar, C.; Prato, M. X-Ray Photoemission Spectroscopy Study on the Effects of Functionalization in Fulleropyrrolidine and Pyrrolidine Derivatives. *Carbon*. **2006**, *44*, 2896–2903.
- (28) Nie, Y.; Wang, W. N.; Jiang, Y.; Fortner, J.; Biswas, P. Crumpled Reduced

- Graphene Oxide-Amine-Titanium Dioxide Nanocomposites for Simultaneous Carbon Dioxide Adsorption and Photoreduction. *Catal. Sci. Technol.* **2016**, *6*, 6187–6196.
- (29) Guisasola, E.; Baeza, A.; Talelli, M.; Arcos, D.; Moros, M.; de la Fuente, J. M.; Vallet-Regí, M. Magnetic-Responsive Release Controlled by Hot Spot Effect. *Langmuir* **2015**, *31*, 12777–12782.
- (30) Lamplot, J. D.; Denduluri, S.; Qin, J.; Li, R.; Liu, X.; Zhang, H.; Chen, X.; Wang, N.; Pratt, A.; Shui, W.; *et al.* The Current and Future Therapies for Human Osteosarcoma. *Curr. Cancer Ther. Rev.* **2016**, *9*, 55–77.
- (31) Unfried, K.; Sydlik, U.; Bierhals, K.; Weissenberg, A.; Abel, J. Carbon Nanoparticle-Induced Lung Epithelial Cell Proliferation Is Mediated by Receptor-Dependent Akt Activation. *Am. J. Physiol. Lung Cell. Mol. Physiol.* **2008**, *294*, L358-L367.
- (32) Zanello, L. P.; Zhao, B.; Hu, H.; Haddon, R. C. Bone Cell Proliferation on Carbon Nanotubes. *Nano Lett.* **2006**, *6*, 562–567.

## 2.4. Design of pH-Responsive Mesoporous Silica and Mesoporous Bioactive Glasses

### 2.4.1. Introduction

The work here presented consisted in applying the pH-responsive self-immolative technology to different MOZART mesoporous nanomatrices. The particles would be coated with the pH-responsive moieties and the payload release would be triggered by the acid pH found in the scenarios considered in the proposal, namely delayed bone healing and chronic wound healing.

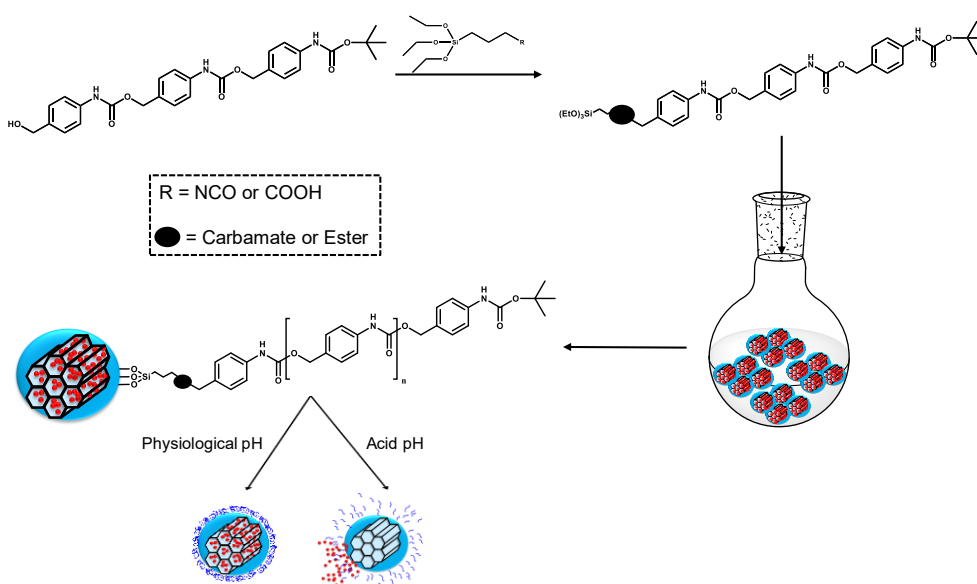
Briefly, bone healing can be postponed for different reasons, including delayed revascularization and appearance of infection. Clinically, a lessened revascularization would prolong the initial phase of acid pH values in the fracture area due to a persisting anaerobic metabolism.<sup>1</sup> In addition, acid pH is also present during the inflammatory phase of bone healing.<sup>2</sup> In this sense, the idea was to use acid pH to trigger the release of pro-angiogenic factors and therapeutic ions from the mesopores of the carriers, which would act synergistically, boosting revascularization and addressing infection, and leading to enhanced bone healing.

On the other hand, while acute wounds usually heal in an efficient manner, chronic wounds persist in a state of chronic inflammation, consequently leading to acid environment, as it happens for bone healing.<sup>3</sup> In this regard, the acid pH would trigger the release of therapeutic and pro-angiogenic ions from the mesopores of the nanocarriers to improve the wound healing process.

The pH-responsive polymeric coating based on self-immolative polymers was produced following the technology developed in Section 2.3.2.3, which was based on a previously reported article.<sup>4</sup> Then, the SIPs were grafted to the different mesoporous nanoparticles, which were provided by the MOZART consortium. A Swedish company, named *Nanolith*, provided SBA-15 nanomatrices.<sup>5</sup> The Friedrich-Alexander-Universität of Erlangen provided mesoporous bioactive glasses. The Politecnico di Torino provided two types of mesoporous bioactive glasses, one synthesized by an ultrasound-assisted method (US)<sup>6</sup> and another one by a spray-drying method (SD).<sup>7</sup> These nanocarriers will be denoted hereafter as Nanolith, FAU and Polito-X (X being US or SD), respectively.

One of the key points of MOZART was the incorporation of therapeutic ions within the silica framework. However, the two-step synthetic protocol described in Section 2.2.2.3 for the synthesis of SIP-coated MSNs might induce a significant loss of ions during the synthesis and subsequent washing steps. In consequence, the methodology had to be changed from a two-step to a one-pot procedure. In this way, the SIP was first attached to an organosilane and then added to the particles, thus minimizing ion leakage. The chloro organosilane employed in Section 2.2 was discarded because the SIP had to be attached at 80°C and, consequently, that temperature might lead to self-condensation of the organosilane prior to the addition, reducing the yield of the grafting. In this sense, 2 alternative organosilanes bearing either isocyanate or carboxylic acid functionalities were explored. In this manner, the coupling should proceed at lower temperature and organosilane self-condensation would be avoided. In addition, the proposal considered the *in vivo* application of the nanoformulations here developed. For that reason, some nanomatrices were labelled with an *in vivo* fluorophore and further functionalized with the SIP coating.

Finally, the effective sealing of the mesopores as well as the pH-responsive behavior of the carriers were evaluated through release experiments, using physiological and acid pH environments to mimic the conditions that would be found in bone and wound healing scenarios. A summary of the work carried out in this chapter is depicted in Scheme 2.10.



**Scheme 2.10.** Schematic representation of the work carried out in Section 2.5. The two-step method used for the synthesis of SIP-coated MSNs was changed to a one-pot protocol to minimize potential premature ion leakage. Different organosilanes bearing either isocyanate or carboxylic acid moieties were explored to graft the SIPs to the particles. Finally, the effectiveness of the pore capping was evaluated performing release experiments at acid and physiological pH.



## 2.4.2. Materials and Methods

The following compounds were purchased from Sigma-Aldrich Inc.: ABA; Phenyl chloroformate; DIPEA; DBTL; Ru; BOC<sub>2</sub>O; APTES; Succinic anhydride; *N,N'*-Dicyclohexylcarbodiimide (DCC); DMAP; THF; DMSO; DMF; DCM; Acetonitrile (AcN). The rest of the chemicals (ethanol, heptane, etc) were of the best quality and were employed as received.

### 2.4.2.1. pH-Responsive Self-Immolative Polymers

The SIPs employed for the functionalization of the MOZART nanomatrices were synthesized using the protocol reported in Section 2.3.2.3. Briefly, ABA was employed as starting material for the synthesis of the monomer (compound **1**) and the trigger (compound **2**). Then, the monomer was polymerized using DBTL as catalyst and, once the polymeric chain preformed, the trigger was added as end-cap, leading to the final pH-responsive polymer (compound **3**). All compounds were characterized by <sup>1</sup>H-NMR.

### 2.4.2.2. SIP-Coated MOZART Nanomatrices

#### ❖ *Synthesis of SIP-Coated MOZART nanomatrices Using an Isocyanate-Based Linker (Protocol A)*

First, to a N<sub>2</sub>-purged flask containing 30 mg of the corresponding batch of particles (SBA-15, FAU, Polito-US or Polito-SD), dry DMF (3 mL) was added and the solution was sonicated to disperse the potential aggregates (solution A). Then, to a N<sub>2</sub>-purged vial containing compound **3** (0.450 g, 0.14 mmol), dry DMF (2.5 mL) and dry DIPEA (47.5 μL, 0.27 mmol) were added and the solution was stirred for 4 hours at 50°C (solution B). After that, 0.8 mL of this mixture (solution B) were added dropwise to the initial dispersion of particles (solution A) and the reaction was stirred at 80°C for 2 hours. Then, another 0.8 mL of solution B were added to Solution A. Finally, after 2 further hours, the rest of solution B was added. Afterward, the whole reaction mixture was magnetically stirred overnight at 80°C. Finally, the product was centrifuged, thoroughly washed with DMF and ethanol and dried under vacuum. The SIP-coated nanomatrices were characterized by means of TGA analysis and FTIR spectroscopy.

#### ❖ *Synthesis of SIP-Coated MOZART Nanomatrices Using a Carboxylic Acid-Based Linker (Protocol B)*

#### ✓ 4-oxo-4-((3-(triethoxysilyl)propyl)amino) butanoic acid (4)

To a N<sub>2</sub>-purged vial containing succinic anhydride (0.1 g, 1 mmol), dry THF (3 mL) and APTES (234 μL, 1 mmol) were added and the reaction stirred overnight at rt. Then,

the solvent was removed under reduced pressure to yield compound **4** as a colorless oil. The compound was characterized through  $^1\text{H-NMR}$ .

✓ SIP-coating on MOZART nanomatrices using a carboxylic acid-based linker

To a  $\text{N}_2$ -purged vial containing compound **4** (0.019 g, 0.06 mmol), DMAP ( $1.9 \cdot 10^{-3}$  g, 0.015 mmol) and DCC (0.013 g, 0.064 mmol), dry DMF (1.2 mL) was added and stirred for 30 minutes. After that, compound **3** (0.2 g, 0.06 mmol) in dry DMF (2 mL) was added dropwise and the reaction was stirred at rt overnight (solution A). Separately, to a  $\text{N}_2$ -purged flask containing the corresponding particles (30 mg), dry DMF (3 mL) was added and the solution was sonicated to disperse the potential aggregates (solution B). Then, 1 mL of solution A was slowly added to the particles and the reaction was heated at  $80^\circ\text{C}$  for 2 hours. Afterward, 1 additional mL of solution A was added to solution B. After 2 further hours, the rest of solution A was injected and reaction mixture was stirred overnight at  $80^\circ\text{C}$ . Finally, the product was centrifuged, thoroughly washed with DMF and ethanol and dried under vacuum. The SIP-coated nanomatrices were characterized by means of TGA and FTIR.

#### **2.4.2.3. SIP-Coated Labelled MOZART Nanomatrices for Future *In vivo* Experiments**

FAU and Polito-US nanomatrices were labelled with a dye appropriate for *in vivo* observation (IRDye® 680RD) in view of a future *in vivo* application of the particles. In addition, Polito-US was also labelled with FITC for the initial grafting tests. The particles (FAU@*in vivo*, Polito@*in vivo*-US and Polito@FITC-US) were labelled by FAU and Polito researchers, respectively, before sending them for the subsequent SIP coating.

FAU@*in vivo* and Polito@FITC-US nanomatrices were functionalized with the polymer using compound **4** as linker and DMF as solvent, as previously described in Section 2.4.2.2 (Protocol B). On the other hand, Polito@*in vivo*-US could not be properly dispersed in DMF. Instead, the particles were dispersed in a mixture of DMF and AcN. Except for that, the protocol was carried out as previously described.

Polito-FITC-US nanomatrices were characterized by means of TGA analysis and FTIR spectroscopy. The samples labelled with the *in vivo* dye were characterized through FTIR spectroscopy (non-destructive characterization technique) to save as much sample as possible for a future *in vivo* experiment.

#### 2.4.2.4. Release Experiments from SIP-Coated MOZART Nanomatrices

##### ❖ *SIP-Coated MOZART nanomatrices loaded with Ru*

First, to a N<sub>2</sub>-purged flask containing the corresponding batch of nanoparticles (30 mg), a solution of Ru (12 mg, 0.015 mmol) in dry DMF (3 mL) was added and the solution was stirred overnight at rt. After that, the functionalization with the SIP was carried out as previously described.

##### ❖ *Release Experiments*

The pH-responsive behavior of the SIP-coated MOZART nanomatrices was evaluated *in vial* following the protocol described in Section 2.2.2.4 for SIP-coated MSNs. Briefly, the particles were dispersed in a solution either at physiological or acid pH and placed in Tranwell® at 37°C with orbital stirring. The media were removed every time point and measured in a fluorimeter to quantify the amount of Ru released. Fresh medium at the corresponding pH was added every time the old media was removed.

### 2.4.3. Results and Discussion

#### 2.4.3.1. Synthesis of pH-Responsive Self-Immolative Polymers

The polymeric coating was synthesized following the optimized protocol described in Section 2.3.2.3, using compounds **1** and **2** as monomer and end-cap, respectively, and DBTL as catalyst. All compounds were accordingly characterized, obtaining analogous results. The average molecular weight of the SIPs was *ca.* 3,300 g/mol. As it will be discussed in the following subsections, the pore size of the nanomatrices greatly affected the efficiency of the SIPS in sealing the mesopores. In this sense, the above-mentioned average molecular weight was the highest that could be obtained. In consequence, the consortium agreed to synthesize an alternative pH-responsive polymer that will be described in Section 2.5.

#### 2.4.3.2. Synthesis of SIP-Coated MOZART Nanomatrices

The synthetic protocol for the functionalization of the MOZART nanomatrices was modified to minimize the potential ion leakage during the reaction and subsequent washing steps. First, the SIPs were reacted with an organosilane and then that mixture was added to the corresponding nanoparticles, as depicted in Scheme 2.10.

Two different organosilanes were used, one bearing an isocyanate and another one bearing a carboxylic acid. The reason for substituting the chloro organosilane previously employed for the synthesis of SIP-coated MSNs (Section 2.2.2.3) relied on the high

temperature that was needed for its coupling with the polymeric chain. Then, in order to avoid any temperature-induced self-condensation events prior to the addition on the nanoparticles, the functionality of the linker was initially changed to an isocyanate (mild reaction temperature) and finally to a carboxylic acid (reaction at rt).

❖ *Synthesis of SIP-Coated MOZART Nanomatrices Using an Isocyanate-Based Linker (Protocol A)*

In a first approach, the isocyanate linker was attached to the self-immolative chain and then this mixture was added to Nanolith and Polito-US nanomatrices. A ratio 1:6 (nanomatrices:SIP) was initially employed. However, the yield was almost negligible and the polymer percentage was increased to 1:15. The SIP-coated Nanolith carriers were characterized by TGA analysis and FTIR spectroscopy to confirm the presence of the polymer (Figure 2.57).

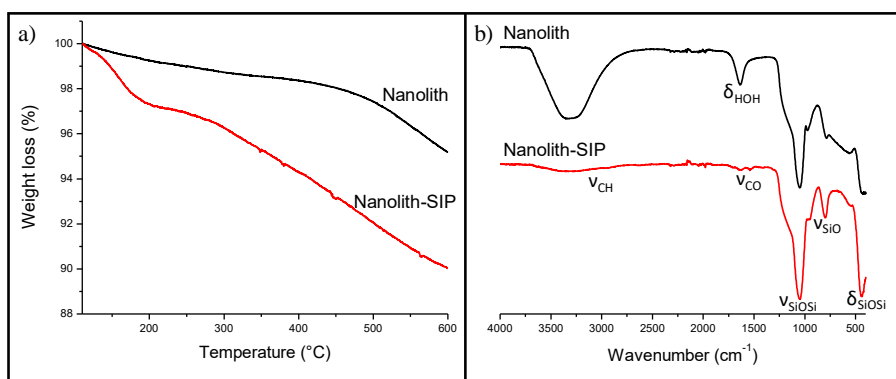


**Figure 2.57.** a) TGA analysis of Nanolith vs Nanolith-SIP. b) FTIR spectroscopy of Nanolith vs Nanolith-SIP. The increase in the weight loss and the appearance of vibration bands associated to the carbamates confirmed the presence of the polymer.

The TGA analysis (Figure 2.57a) showed a weight loss of 4.2% after the SIP coating, which was calculated between 150°C and 450°C. In addition, the FTIR spectroscopy (Figure 2.57b) showed evidences of vibration bands ascribed to the carbamates of the polymer. The combination of both results confirmed the presence of the polymer coating the surface of the particles.

Polito-US samples were also functionalized with the self-immolative polymeric coating using the isocyanate linker and the output of the grafting was characterized through TGA analysis and FTIR spectroscopy (Figure 2.58).

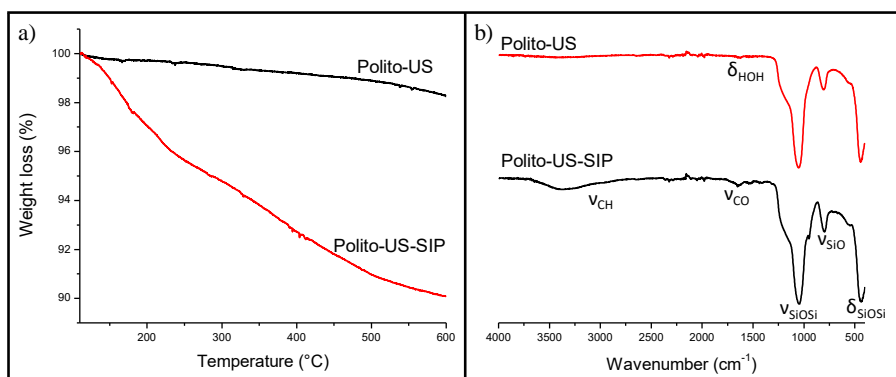


**Figure 2.58.** a) TGA analysis of Polito-US vs Polito-US-SIP. b) FTIR spectroscopy of Polito-US vs Polito-US-SIP. The increase in the weight loss and the appearance of the vibration bands associated to the carbamates confirmed the presence of the polymer.

In this case, the TGA analysis (Figure 2.58a) showed *ca.* 6.5% of additional weight loss after the functionalization. In addition, presence of vibration bands ascribed to the carbamate could be observed in the FTIR spectrum of Polito-US-SIP (Figure 2.58b). In consequence, the maximum amount of organic matter that could be incorporated using a ratio nanomatrices:SIP 1:15 was *ca.* 6.5%, which seemed quite low for such amount of initial polymer. The main reason would be that the addition of the SIP to the isocyanate in DMF was less effective as it is in other solvents, such as dichloromethane. However, the SIP was insoluble in such solvents and a new linker bearing a different functionality was synthesized.

❖ *Synthesis of SIP-Coated MOZART Nanomatrices Using a Carboxylic Acid-Based Linker (Protocol B)*

The linker containing the carboxylic acid functionality was straightforwardly synthesized from APTES and succinic anhydride and its correct synthesis was verified by <sup>1</sup>H-NMR (Figure 2.59).

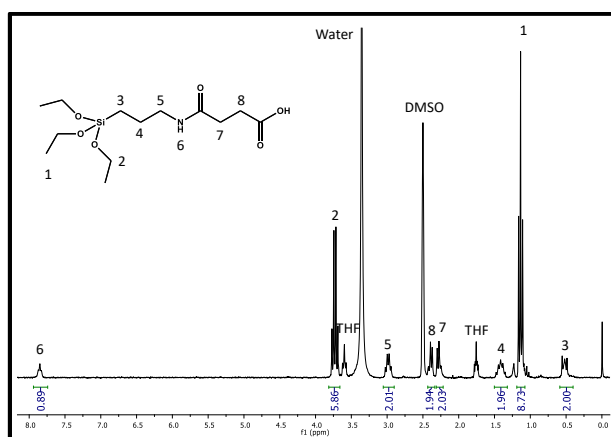


**Figure 2.59.** <sup>1</sup>H-NMR of compound 4. (250 MHz, DMSO) δ 7.86 (t, 1H), 3.74 (q, 6H), 3.86–3.66 (m, 2H), 2.41 (t, 2H), 2.29 (t, 2H), 1.53–1.31 (m, 2H), 1.15 (t, 9H), 0.63–0.45 (m, 2H).

The linker was attached to the SIP *via* carbodiimide chemistry, using catalytic DMAP to create a good leaving group that the alcohol could easily displace under mild conditions.<sup>8</sup> Then, the silylated polymer was added to the particles to yield SIP-coated nanomatrices. In this sense, FAU nanomatrices were employed to evaluate the convenience of using compound **4** to silylate the SIPs. The correct grafting of the polymeric coating was verified through TGA analysis and FTIR spectroscopy (Figure 2.60).

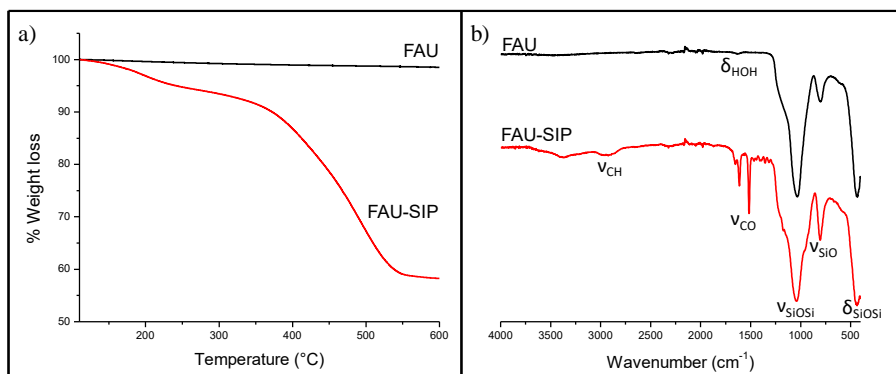


**Figure 2.60.** a) TGA analysis of FAU *vs* FAU-SIP. b) FTIR spectroscopy of FAU *vs* FAU-SIP. The presence of the SIP was confirmed by the great % weight loss and the evident vibration bands associated to the carbamates from the SIP.

The TGA analysis (Figure 2.60a) showed additional *ca.* 40% of weight loss, which was ascribed to the presence of the polymeric coating on the particles. In addition, the functionalization process led to the appearance of vibration bands typical of the SIP in the FTIR spectrum (Figure 2.60b). These results confirmed the presence of a significant amount of polymeric coating in the particles, highlighting the suitability of using compound **4** as silylating agent (Protocol B) rather than the organosilane bearing an isocyanate (Protocol A).

Once a reliable grafting method was developed, the next step was to evaluate if the polymeric coating could close the pore entrances. For such purpose, the MOZART nanomatrices were loaded with the Ru dye prior to the SIP grafting. The presence of the polymer on the Ru-loaded FAU samples was evaluated using TGA analysis and FTIR spectroscopy (Figure 2.61).

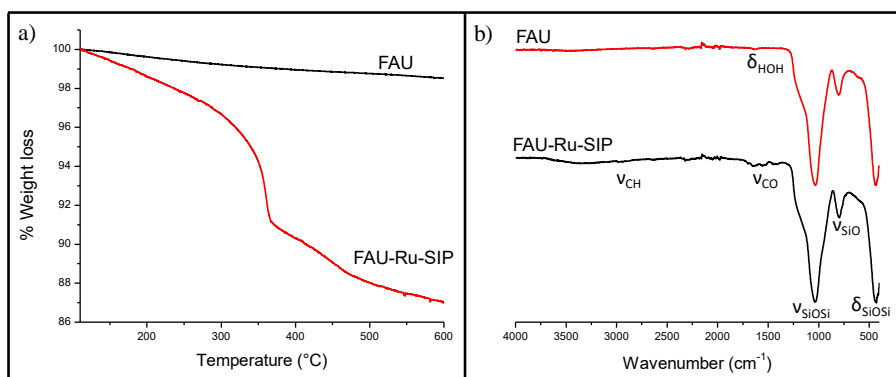


**Figure 2.61.** a) TGA analysis of FAU vs FAU-Ru-SIP. b) FTIR spectroscopy of FAU vs FAU-Ru-SIP. The amount of organic matter incorporated after the functionalization was lower when the Ru dye was present (*ca.* 40% for FAU-SIP vs *ca.* 11% for FAU-Ru-SIP). The FTIR spectra showed vibration bands ascribed to the polymer. The differences might be ascribed to the presence of Ru molecules in the solutions that would interact with the silanol groups of the particles, decreasing the efficiency of the grafting.

As shown in Figure 2.61a, the amount of additional organic matter present in the sample was significantly lower when the grafting was carried out after loading the nanomatrices with the dye (*ca.* 40% for FAU-SIP vs *ca.* 11% for FAU-Ru-SIP). The FTIR spectrum (Figure 2.61b) showed vibration bands associated to the carbamates, confirming the presence of the SIP. From this results, it could be concluded that the presence of Ru molecules influenced the efficiency of the SIP grafting. This might be ascribed to the fact that Ru molecules could also interact with the silanol groups of the particles, decreasing the total amount of reactive points for the silylated SIP, and then, the total amount of organic matter on the sample.

Ru-loaded Polito samples coated with the SIPs were also produced. For that purpose, the particles were initially loaded with the dye and subsequently functionalized with the self-immolative polymeric coating. The success of the SIP coating on Polito-US nanomatrices was evaluated through TGA analysis and FTIR spectroscopy (Figure 2.62).

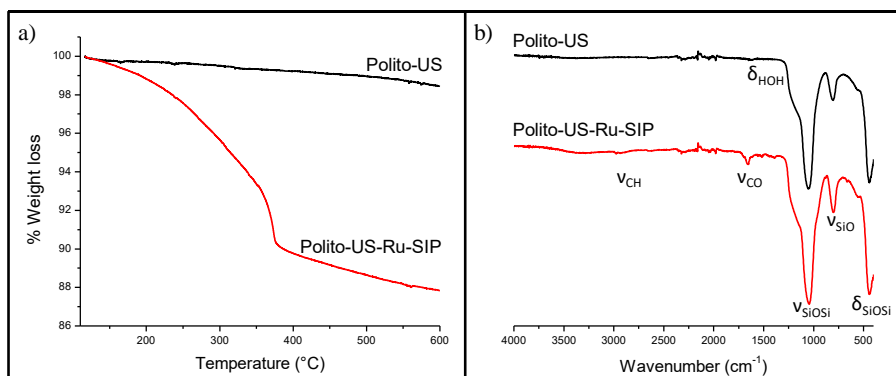


**Figure 2.62.** a) TGA of Polito-US vs Polito-US-Ru-SIP. b) FTIR spectroscopy of Polito-US vs Polito-US-Ru-SIP. The *ca.* 9% of weight loss and the appearance of vibration bands associated with the carbamate confirmed the successful functionalization.

The TGA analysis (Figure 2.62a) showed an increase in the % weight loss of *ca.* 9%, compared to the pristine sample. The FTIR spectroscopy (Figure 2.62b) revealed the presence of vibration bands associated to the SIP carbamates, confirming the presence of the coating in the functionalized samples. The same techniques were applied for the characterization of the SIP-coated Polito-SD nanomatrices (Figure 2.63).

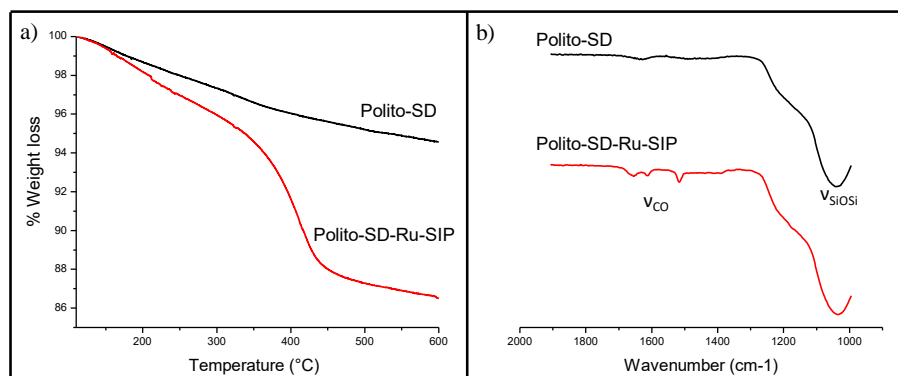


**Figure 2.63.** a) TGA of Polito-SD vs Polito-SD-Ru-SIP. b) FTIR spectroscopy of Polito-SD vs Polito-SD-Ru-SIP. The weight loss and the appearance of the vibration bands associated with the carbamate confirmed the successful functionalization.

In this case, the grafting of the polymer induced *ca.* 7.5% of additional weight loss (Figure 2.63a). Besides, the FTIR spectrum of SIP-coated Polito-SD loaded with Ru demonstrated the presence of vibration bands ascribed to the polymer. Both results confirmed the correct functionalization with the self-immolative polymeric coating.

#### 2.4.3.3. Synthesis of SIP-Coated Labelled MOZART Nanomatrices for Future *In vivo* Experiments

Some nanomatrices (FAU and Polito-US) were labelled with a silylated fluorophore in view of future *in vivo* administration. The labelling was carried out post-synthesis because, otherwise, the calcination process employed to remove the surfactant employed as template during the synthesis of the particles would destroy the organic dye. Calcination was employed for these nanomatrices because the use of solvent extraction would likely remove the calcium from the particles, leading to their degradation.

The first step was to find out if the presence of the fluorophore would affect the SIP coating. The efficiency of the grafting was initially evaluated using Polito-US nanomatrices labelled with a readily available dye, namely FITC. The functionalization was characterized through TGA analysis and FTIR spectroscopy (Figure 2.64).



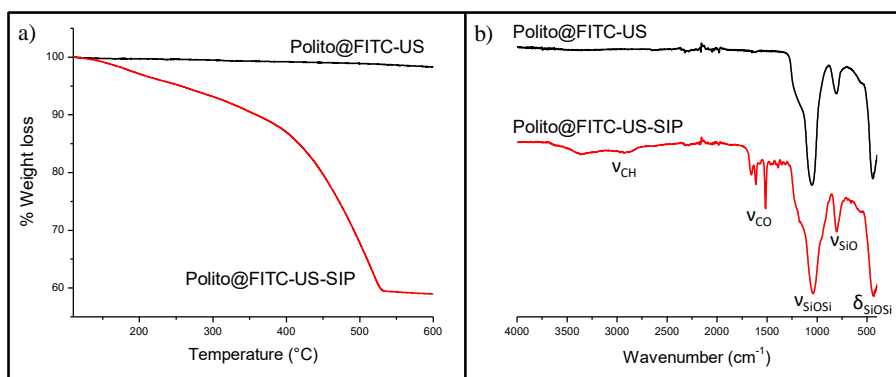


**Figure 2.64.** a) TGA analysis of Polito@FITC-US vs Polito@FITC-US-SIP. b) FTIR spectroscopy of Polito@FITC-US vs Polito@FITC-US-SIP. The great increase in % weight loss and the appearance of vibration bands ascribed to the carbamate confirmed the successful functionalization with the polymer.

As shown in Figure 2.64a, the SIP grafting was unaffected by the presence of the dye, leading to an increase in the weight loss of *ca.* 40%. In addition, the FTIR spectroscopy (Figure 2.64b) revealed the appearance of vibrations bands associated to the carbamates. These 2 results were in agreement with those in Figure 2.60, clearly indicating that (1) the polymer could be grafted to the nanoparticles regardless of the presence of the covalently attached dye and (2) attempting the functionalization without the Ru dye in the medium yielded better results. Once the feasibility of grafting the SIP on the labelled samples was verified, the next step was to functionalize FAU and Polito-US nanocarriers labelled with the *in vivo* dye.

The presence of the *in vivo* dye somehow affected the dispersibility of Polito@*in vivo*-US nanomatrices in DMF and, consequently, the conditions described in Section 2.4.2.2 (Protocol B) could not be applied. A very diluted mixture of DMF and AcN was employed as an alternative. The mixture was adjusted so that (1) the particles could be properly dispersed and (2) the SIP, which was insoluble in AcN, could be added to the particles without precipitating. The output of the reaction was evaluated by FTIR spectroscopy (Figure 2.65).

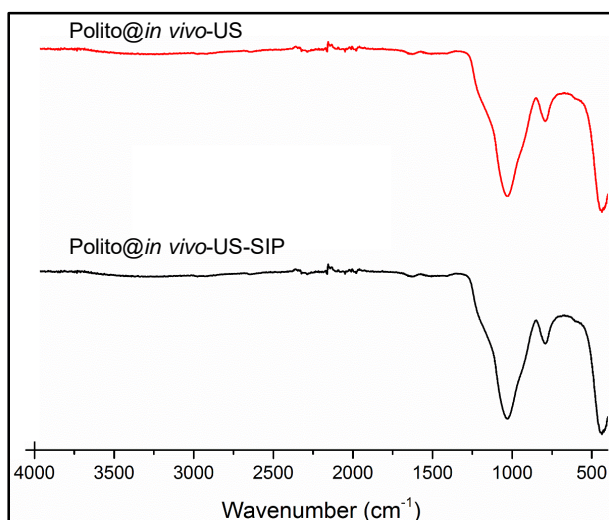


**Figure 2.65.** FTIR spectroscopy of Polito@*in vivo*-US vs Polito@*in vivo*-US-SIP. It could be concluded from comparison between both spectra that the reaction did not proceed.

The vibration bands typical of SIP could not be observed in the FTIR spectrum (Figure 2.65), indicating that the grafting was ineffective, most probably as a consequence of the very diluted conditions employed.

On the other hand, the dispersibility of the FAU nanomatrices after the attachment of the dye remained unaffected. In consequence, the functionalization was carried out following the protocol described in Section 2.4.2.2 (Protocol B, carboxylic acid) and characterized through FTIR spectroscopy (Figure 2.66).

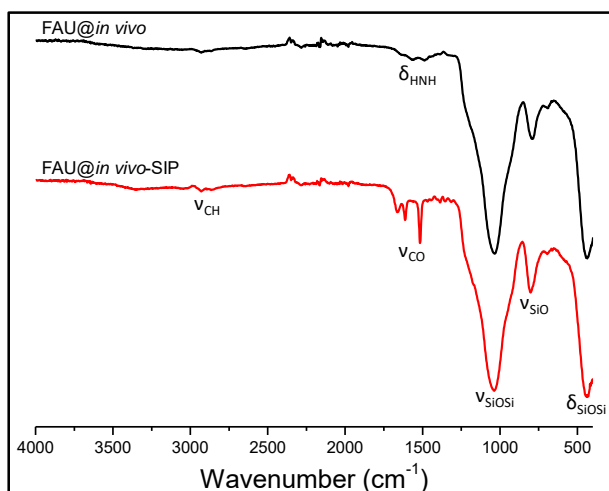


**Figure 2.66.** FTIR spectroscopy of FAU@*in vivo* vs FAU@*in vivo*-SIP. The appearance of the vibration bands associated with the carbamates confirmed the successful functionalization.

The appearance of vibration bands ascribed to the carbamates in Figure 2.66 confirmed the proper SIP grafting. The results were in agreement with those in Figure 2.60 and 2.64, confirming the feasibility of grafting the SIPs on previously labelled nanomatrices.

#### 2.4.3.4. Release experiments

Once verified the presence of the polymer on the nanoparticles, the effective sealing of the pores was evaluated *via* release experiments at physiological and acid pH to mimic the acid environment that was expected to be found in delayed bone healing and chronic wound healing. The release experiment for FAU-SIP is shown in Figure 2.67.

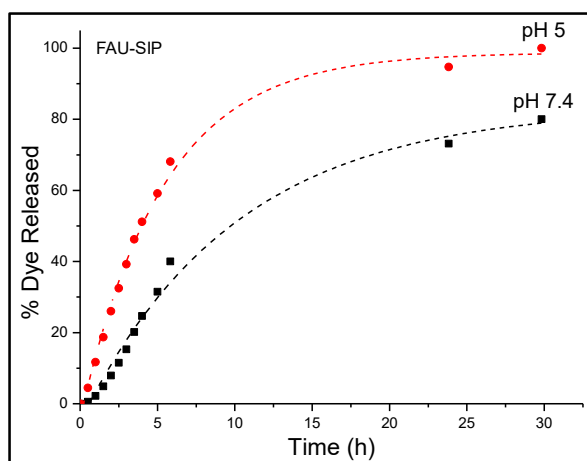


**Figure 2.67.** Release experiment of Ru-loaded FAU-SIP at pH 7.4 and 5. The pore size (*ca.* 4 nm) was too big to close the pore entrances with the SIPs, although the sample at acid pH released more dye, in agreement with the results shown in Sections 2.2 and 2.3.

The release experiment depicted in Figure 2.67 shown that *ca.* 75% of the dye was released at physiological pH, indicating that the SIP coating was ineffective in closing the pore entrances. This was ascribed to the pore size (*ca.* 4 nm), which was too big to be sealed with the here produced polymer chain (3,300 g/mol). Interestingly, the samples at acid pH could still release more amount of dye, in agreement with the pH-responsive behavior previously observed in Sections 2.2 and 2.3. The release experiment for Polito-US-SIP nanomatrices is depicted in Figure 2.68.

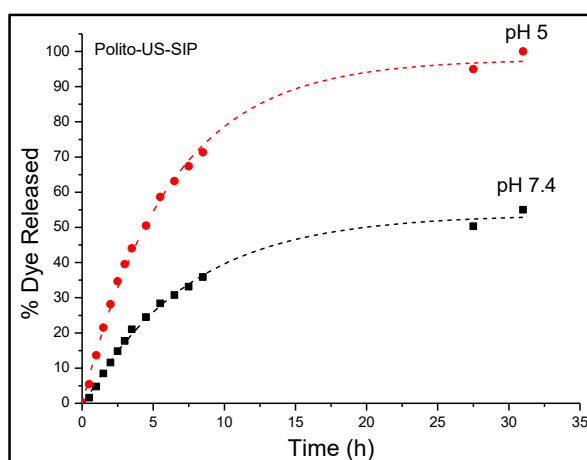


**Figure 2.68.** Release experiment of Polito-US-SIP at pH 7.4 and 5. In this case, the sealing of the mesopores was more efficient, and promising kinetics were obtained.

As shown in Figure 2.68, the SIP coating sealed more efficiently the pore entrances and significantly higher amount of dye was released at acid pH (two times the dye measured at pH 7.4). In addition, this further confirmed the pH-responsive behavior of the SIPs. The more effective capping was ascribed to a smaller pore size, *ca.* 3 nm, closer to MSNs. Finally, the effectiveness of the pore sealing in Polito-SD-SIP was evaluated (Figure 2.69).

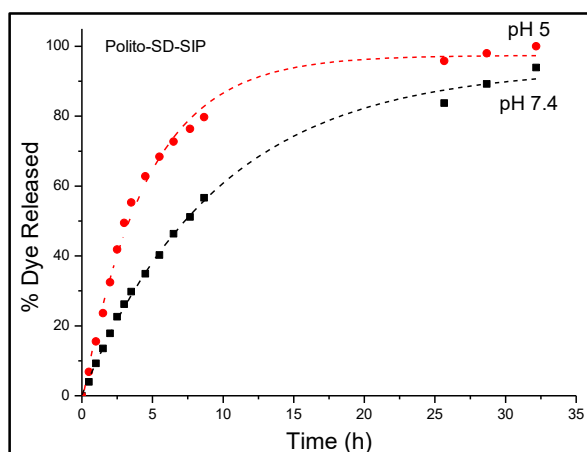


**Figure 2.69.** Release experiment of Polito-SD-SIP at pH 7.4 and 5. In this case, the SIPs coating was ineffective and significant premature release could be observed, probably due to the large pore size (*ca.* 7 nm).

The release experiment of Polito-SD-SIP (Figure 2.69) showed similar kinetics than that of FAU-SIP, showing significant premature release (more than 60% after 12 hours) as a consequence of the ineffective pore capping. This experiment confirmed the hypothesis of the pore size (*ca.* 7 nm in this case), *i.e.*, the higher the pore size, the lower the effectiveness of pore sealing (Figure 2.70).

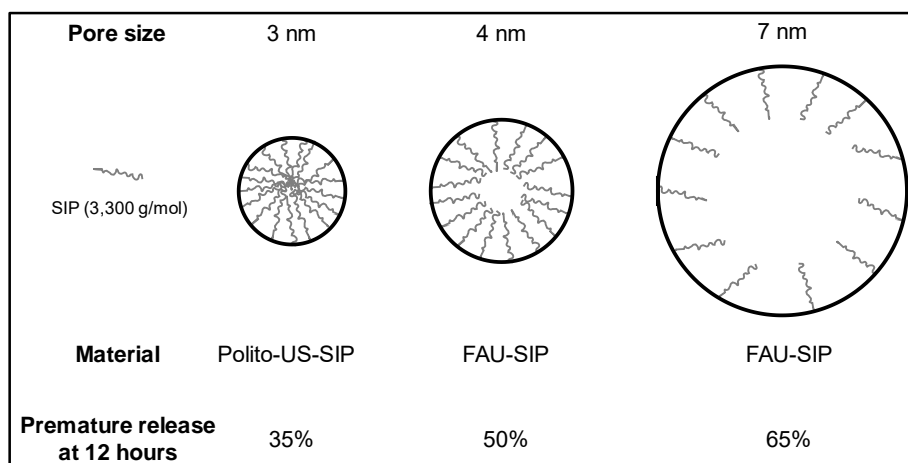


**Figure 2.70.** Premature release at 12 hours. The pore size, polymer length and amount of premature release were interrelated. For the same SIP molecular weight, the lowest premature release was obtained for Polito-US-SIP, which showed the smallest pore size.

As shown in Figure 2.70, the pore size directly influenced the effectiveness of the capping. In this sense, the use of SIPs with higher molecular weights could not be explored because, as it was demonstrated in Table 2.7, there was an upper limit for the molecular weight of the polymers. Therefore, for a fixed molecular weight, the lower the pore size the more effective the sealing of the mesopores and, consequently, the lower premature release. As an alternative, the MOZART consortium agreed to synthesize a new polymer coating that would provide higher molecular weights, which will be addressed in Section 2.5.

#### 2.4.4. Conclusions

The objective of the work here presented was to adapt the self-immolative technology to the different silica-based nanomatrices provided by the MOZART consortium. One of the key points of the proposal was the loading of therapeutic ions within the silica framework to achieve synergistic effects with a variety of co-loaded compounds. In this sense, the two-step grafting protocol described for the synthesis of SIP-coated MSNs was modified to minimize the premature ion leakage as a consequence of the multiple reaction and washing steps. Instead, a one-pot protocol was developed and two alkoxysilanes were explored to effectively attach the SIPs to the nanomatrices, being the carboxylic acid-based (Protocol B) the one that yielded best results.

The experimental evidence showed that the SIP grafting was less efficient when the different nanomatrices were previously soaked in a saturated solution of a model payload. The most probable reason would be that Ru molecules would interact with the silanol groups of the particle, decreasing the reacting points for the silylated SIP and, consequently, the total amount of polymer grafted.

The degree of functionalization was unaffected by the presence of covalently attached fluorescent molecules on the particles. Polito@FITC-US and FAU@*in vivo* nanomatrices provided excellent results in terms of amount of SIP incorporated, although Polito@*in vivo*-US nanomatrices could not be functionalized due to their poor dispersibility, even though much diluted mixture of solvents was employed.

The release experiments carried out for FAU-SIP and Polito-SD-SIP showed significant premature release at physiological pH, clearly indicating the ineffective capping of the pore entrances. This was ascribed to the large pore sizes found in both nanomatrices (*ca.* 4 and 7 nm, respectively), which would be difficult to seal with a

polymer of this molecular weight (*ca.* 3,300 g/mol), which was the maximum molecular weight that could be obtained and, as a contingency plan, the consortium agreed to proceed with a different type of polymer (Section **2.5**). On the contrary, the results obtained for Polito-US-SIP nanomatrices (pore size *ca.* 3 nm) were much promising and significant differences were observed, as a consequence of a more effective sealing. Overall, all samples showed higher release at acid pH, which was in agreement with the pH-responsive behavior of SIPs previously discussed in this thesis.

## References

- (1) Gaber, T.; Häupl, T.; Sandig, G.; Tykwinska, K.; Fangradt, M.; Tschirschmann, M.; Hahne, M.; Dziurla, R.; Erekul, K.; Lautenbach, M.; *et al.* Adaptation of Human CD4+ T Cells to Pathophysiological Hypoxia: A Transcriptome Analysis. *J. Rheumatol.* **2009**, *36*, 2655–2669.
- (2) Hazehara-Kunitomo, Y.; Hara, E. S.; Ono, M.; Aung, K. T.; Komi, K.; Pham, H. T.; Akiyama, K.; Okada, M.; Oohashi, T.; Matsumoto, T.; *et al.* Acidic Pre-Conditioning Enhances the Stem Cell Phenotype of Human Bone Marrow Stem/Progenitor Cells. *Int. J. Mol. Sci.* **2019**, *20*, 1097.
- (3) Schneider, L. A.; Korber, A.; Grabbe, S.; Dissemmond, J. Influence of pH on Wound-Healing: A New Perspective for Wound-Therapy? *Arch. Dermatol. Res.* **2007**, *298*, 413–420.
- (4) Sagi, A.; Weinstain, R.; Karton, N.; Shabat, D. Self-Immolative Polymers. *J. Am. Chem. Soc.* **2008**, *8*, 5434–5435.
- (5) Zhao, D.; Zhao, D.; Feng, J.; Huo, Q.; Melosh, N.; Fredrickson, G. H.; Chmelka, B. F.; Stucky, G. D. Triblock Copolymer Syntheses of Mesoporous Silica with Periodic 50 to 300 Angstrom Pores Triblock Copolymer. *Science* . **1998**, *279*, 548–552.
- (6) Bari, A.; Bloise, N.; Fiorilli, S.; Novajra, G.; Vallet-Regí, M.; Bruni, G.; Torres-Pardo, A.; González-Calbet, J. M.; Visai, L.; Vitale-Brovarone, C. Copper-Containing Mesoporous Bioactive Glass Nanoparticles as Multifunctional Agent for Bone Regeneration. *Acta Biomater.* **2017**, *55*, 493–504.
- (7) Molino, G.; Bari, A.; Baino, F.; Fiorilli, S.; Vitale-Brovarone, C. Electrophoretic Deposition of Spray-Dried Sr-Containing Mesoporous Bioactive Glass Spheres on Glass–Ceramic Scaffolds for Bone Tissue Regeneration. *J. Mater. Sci.* **2017**, *52*, 9103–9114.
- (8) Bernhard, N.; Wolfgang, S. Simple Method for the Esterification of Carboxylic Acids. *Angew. Chemie Int. Ed.* **1978**, *17*, 522–524.

## 2.5. Design of Self-Immolative Polymers Responsive to Alternative pH Values

### 2.5.1. Introduction

Initially, the MOZART proposal devised a scenario where acid pH could be a relevant biomarker for delayed bone healing and chronic wound healing. One of the first tasks of the consortium was the determination of an accurate pH value using *in vivo* models. This value was thought to be close to pH 5 and, in consequence, the acid-responsive self-immolative polymer described in the first the first sections of this thesis was designed as gatekeeper. However, the experimental *in vivo* evidence showed that several pH values, including acid and basic pH, were found in those scenarios.

The pH value in chronic wound healing was studied by members of the MOZART consortium from Sheffield University using a skin tissue model.<sup>1</sup> Skin has an upper protective acid barrier at pH 5.5, value that increases up to 7-8 beneath this boundary. Raman spectroscopy was employed to evaluate the effect that bacterial infection might have on the pH of that skin model. The protonation state of the phosphate groups present throughout the epithelium was analyzed to determine the pH value (Figure 2.71).

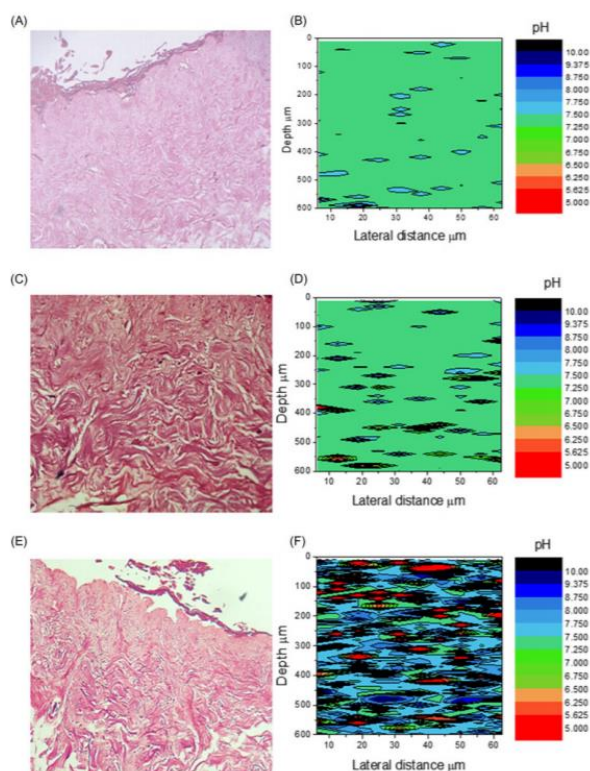


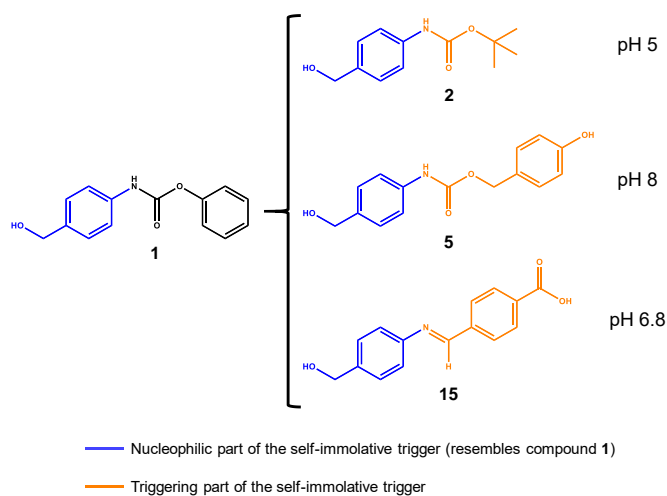
**Figure 2.71.** Measurement of pH in bacterially infected skin. H&E sections (A, C, & E) and pH plots (B, D, E, & F) of control skin (A & B), *S. aureus* infected skin (C & D), and *P. aeruginosa* infected skin (E & F). Reproduced from Ref 1 with permission of Taylor & Francis Online.



It was found that normal skin tissue essentially possessed pH *ca.* 7.5 (Figure 2.71B). However, the analysis of bacterially infected tissue demonstrated the presence of both acid and basic pH values (Figures 2.71D and F). The acid values were ascribed to the presence of biofilm-related microenvironment. The authors speculated that the basic values might be ascribed to the presence of alkaline phosphatase, which functions optimally between pH 8 at 11. The most recurrent value was found to be pH *ca.* 8

The pH value in bone healing processes was evaluated by members of the MOZART consortium from the Julius Wolff Institut, Charité-Universitätsmedizin Berlin (unpublished results). In this work, rat and sheep animal models were employed for the study of pH in bone injury and muscle trauma, respectively. The pH during the first steps of bone healing was recurrently found to be *ca.* 6.8. A profound comparative between healthy and injured tissues concluded that during musculoskeletal lesions the tricarboxyl acid cycle stagnates and the energy is obtained through anaerobic metabolism, thus leading to the slight tissue acidification.

In view of the above-mentioned results, the consortium agreed to explore the synthesis of self-immolative polymers sensitive to pH 8 or 6.8 to trigger the release from the mesoporous matrices in wound and bone healing scenarios, respectively. The polymer backbone was similar to that developed in Sections 2.2 and 2.3, so the main task here was to design acid and basic-responsive self-immolative triggers. These two molecules were designed following an approach similar to that of compound 2, *i.e.*, that of the pH 5-responsive self-immolative trigger (Scheme 2.11).



**Scheme 2.11.** Schematic representation of the design of the self-immolative triggers synthesized in this doctoral thesis. Compound 1 is used as monomer for the polymerization. The triggers are designed so that they show a nucleophilic area that resembles that of compound 1 (in blue). The second part of the trigger (in orange) is tuned so that it can be cleaved by the specific stimulus (pH 5, 8 or 6.8, respectively).

The triggers responsive to pH 8 (Scheme 2.11, compound 5) and 6.8 (Scheme 2.11, compound 15) were designed so that they showed a nucleophilic part with similar reactivity as that of compound 1 (Scheme 2.11, blue). In this way, as it happened with compound 2, these new triggers would be easily introduced as end-cap to the preformed polymeric chain. The second part (Scheme 2.11, orange) would endow the molecules with specific responsiveness to either pH 8 or 6.8, so that the trigger could be cleaved in those particular scenarios.

The starting point for the synthesis of the basic-sensitive trigger was a previous article that showed that 4-hydroxybenzyl alcohol undergoes self-immolation at pH 8.<sup>2</sup> The trigger synthesis was attempted through three different approaches involving synthetic strategies based on (1) the use of isocyanates, (2) the employment of alcohol-amine coupling agents and (3) the use of alcohol protecting groups.

The use of a benzoic imine bond was explored for the design of the acid-responsive trigger, since it is known to be hydrolyzed at pH 6.8.<sup>3</sup> As it will be shown in this section, the incorporation of the trigger into the polymeric chain was unsuccessful and the synthesis of a different polymer with a totally different release mechanism was attempted as a contingency plan.

## 2.5.2. Materials and Methods

The following compounds were purchased from Sigma-Aldrich Inc.: APTES; ABA; DIPEA; 1,1'-Carbonyldiimidazole (CDI); 4-Hydroxybenzyl alcohol (HBA); *tert*-Butyldimethylsilyl chloride (TBDMS-Cl); 4-hydroxybenzaldehyde (HBDA); *p*-Toluenesulfonic acid (TsOH); 3,4-dihydropyran; DBTL; DMAP; Ru; BOC<sub>2</sub>O; 2-Piperidinoethanol; Methacryloyl chloride; Hydroquinone; 4,4'-azobis (4-cyanovaleric acid); DMF; THF; DCM; AcN. The rest of the chemicals (ethanol, heptane, etc) were of the best quality and were employed as received. All compounds were characterized through <sup>1</sup>H-NMR.

### 2.5.2.1. Self-Immolative Polymer Sensitive to pH 8

#### ❖ Protocol A: Amine to isocyanate

The conversion of the amino group of ABA to an isocyanate was carried out following a previously reported method with some modifications.<sup>4</sup> To a vial containing BOC<sub>2</sub>O (0.62 g, 2.84 mmol) in AcN (2 mL), a solution of DMAP (0.024 g, 0.02 mmol) in AcN (0.5 mL) and ABA (0.25 g, 2.03 mmol) in AcN (2 mL) were successively added. Right

after the addition of the amine a white solid precipitated out of the solution, which was filtered and dried under vacuum.

❖ *Protocol B: Coupling agent*

To a N<sub>2</sub>-purged vial containing HBA (0.25 g, 2.01 mmol), dry THF (10 mL) was added. Then, CDI (0.33 g, 2.01 mmol) was added dropwise and the mixture was stirred for 2 hours at rt. After that, ABA (0.496 g, 4.02 mmol) in the minimum amount of dry THF was added and the reaction was stirred overnight. Afterward, the solvent was removed under vacuum.

❖ *Protocol C: Protection of alcohol groups*

✓ phenyl (4-(((*tert*-butyldimethylsilyl)oxy)methyl)phenyl)carbamate (6)

For the synthesis of compound **6**, a previously reported method with slightly modifications was followed.<sup>5</sup> Compound **1** was synthesized as previously described in Section 2.3.2.3. Then, to a vial containing compound **1** (1 g, 4.2 mmol) and imidazole (0.31 g, 4.52 mmol), DCM (20 mL) was added. After that, TBDMS-Cl (0.75 g, 5 mmol) was added dropwise and the mixture was stirred overnight at rt. Afterward, the resulting imidazole salts were removed by filtration and the solvent was evaporated under reduced pressure. Finally, the product was purified on a silica column (DCM) to yield compound **6** as a white solid.

✓ 4-(*tert*-butoxy)benzyl (4-(((*tert*-butyldimethylsilyl)oxy)methyl)phenyl)carbamate (8)

• *tert*-butyl (4-(hydroxymethyl)phenyl) carbonate (7)

To a vial containing HBA (0.5 g, 4.03 mmol) and BOC<sub>2</sub>O (0.88 g, 4.03 mmol), THF (15 mL) and DIPEA (0.70 mL, 4.03 mmol) were added. Then, the mixture was refluxed overnight and subsequently evaporated under vacuum, leading to compound **7** as colorless oil.

• 4-(*tert*-butoxy)benzyl (4-(((*tert*-butyldimethylsilyl)oxy)methyl)phenyl)carbamate (8)

To a vial containing compound **6** (0.5 g, 1.39 mmol) and compound **7** (0.38 g, 1.67 mmol), toluene (10 mL) was added. Then, DBTL (20% mol) was added and the mixture was refluxed for 3 hours. After that, the solvent was removed under vacuum and the product was purified in a silica column (ethyl acetate/heptane, 1:9) to yield compound **8** as a colorless oil.

✓ 4-((*tert*-butyldimethylsilyl)oxy)benzyl (4-(((*tert*-butyldimethylsilyl)oxy)methyl)phenyl)carbamate (11)

- 4-((*tert*-butyldimethylsilyl)oxy)benzaldehyde (9)

To a vial containing HBDA (1 g, 8.2 mmol) and imidazole (0.61 g, 9 mmol), DCM (25 mL) was added. Then, TBDMS-Cl (1.23 g, 8.2 mmol) in DCM (5 mL) was added dropwise and the mixture was stirred overnight at rt. After that, the imidazole salts were filtered off and solvent was removed under reduced pressure. Finally, the product was purified in a silica column (ethyl acetate/heptane, 1:3) to yield compound **9** as a colorless oily product.

- (4-((*tert*-butyldimethylsilyl)oxy)phenyl)methanol (10)

To a vial containing compound **9** (1.2 g, 5.1 mmol), methanol (20 mL) was added. Then, NaBH<sub>4</sub> (0.23 g, 6.12 mmol) was slowly added and the reaction was stirred for 30 minutes. After that, diluted HCl was added and the product was extracted in DCM. The organic layer was washed with a saturated solution of NaCl, dried over sodium sulfate and evaporated under reduced pressure, leading to compound **10** as a yellow oil.

- 4-((*tert*-butyldimethylsilyl)oxy)benzyl (4-(((*tert*-butyldimethylsilyl)oxy)methyl)phenyl)carbamate (11)

To a vial containing compound **6** (1 g, 2.79 mmol) and compound **10** (0.8 g, 3.36 mmol), toluene (45 mL) was added. Then, DBTL (20% mol) was added and the mixture was refluxed for 3 hours. After that the solvent was removed and the product was purified in silica column (ethyl acetate/heptane, 1:10) to yield compound **11** as a colorless oil.

✓ 4-((tetrahydro-2H-pyran-2-yl)oxy)benzyl (4-(((*tert*-butyldimethylsilyl)oxy)methyl)phenyl)carbamate (14)

- 4-((tetrahydro-2H-pyran-2-yl)oxy)benzaldehyde (12)

For the protection of HBDA with the tetrahydropyranyl group, a previously described method was followed.<sup>6</sup> Briefly, to a vial containing HBDA (1 g, 8.2 mmol) and pyridine (0.065 g, 0.82 mmol), DCM was added (25 mL). Then, TsOH (0.14 g, 0.82 mmol) in the minimum amount of DCM was added. After that, 3,4-dihydropyran (1.12 mL, 12.3 mmol) in DCM (5 mL) was added dropwise and the mixture was stirred overnight at rt. After that, the solution was filtered through a short silica column and evaporated. The oily product was dissolved in ether, washed with NaCl and subsequently evaporated to yield an oil that was purified in a silica column (ethyl acetate/heptane, 1:9) leading to compound **12** as a colorless oil.

- (4-((tetrahydro-2H-pyran-2-yl)oxy)phenyl)methanol (13)

To a vial containing compound **12** (0.8 g, 3.87 mmol), dry THF (30 mL) was added. Then, NaBH<sub>4</sub> (0.176 g, 4.64 mmol) in the minimum amount of dry THF was added

dropwise and the mixture was stirred overnight. After that, the solution was extracted in ethyl acetate, washed with NaCl and evaporated to yield compound **13** as an oily product.

- 4-((tetrahydro-2H-pyran-2-yl)oxy)benzyl (4-(((*tert*-butyldimethylsilyl)oxy)methyl)phenyl)carbamate (**14**)

To a vial containing compound **6** (0.72 g, 2 mmol) and compound **13** (0.5 g, 2.4 mmol), toluene (10 mL) was added. Then, DBTL (20% mol) was added and the mixture was refluxed for 3 hours. After that the solvent was removed to yield an oily product that was dissolved in DCM, washed with water, dried over sodium sulfate and finally evaporated. The product degraded when introduced in the chromatography silica column for purification.

#### 2.5.2.2. Self-Immolative Polymer Sensitive to pH 6.8

- ❖ (*E*)-4-(((4-(hydroxymethyl)phenyl)imino)methyl)benzoic acid (**15**)

To a N<sub>2</sub>-purged flask containing ABA (0.25 g, 2.03 mmol) and molecular sieves, anhydrous ethanol (10 mL) was added. Then, 4-carboxybenzaldehyde (0.31 g, 2.03 mmol) in anhydrous ethanol (5 mL) was added dropwise and the reaction was stirred overnight at rt in the dark. Then, the solvent was removed and the product was recrystallized in ethyl acetate and hexane, leading to compound **15** as a yellow solid.

- ❖ Poly(phenyl (4-(hydroxymethyl)phenyl)carbamate) end-capped with compound **15** (**16**)

The synthesis was adapted from a previously reported method.<sup>7</sup> Briefly, to a N<sub>2</sub>-purged flask containing compound **1** (1 g, 4.12 mmol), dry DMSO (2.05 mL) and Et<sub>3</sub>N (0.57 mL, 4.12 mmol) were added and the mixture was heated at 60°C for 6 hours. Then, compound **15** (0.71 g, 2.8 mmol) in dry DMSO (1 mL) was added at rt and the whole reaction mixture was stirred for either 3 or 24 hours. After that, the product was precipitated in an excess of cold methanol, centrifuged and washed with methanol to yield a whitish solid.

#### 2.5.2.3. Polymer Undergoing Conformational Changes at pH 6.8

This polymer was synthesized following a previously reported method with some modifications.<sup>8</sup>

- ❖ 2-(piperidin-1-yl)ethyl methacrylate (**17**)

To a N<sub>2</sub>-purged vial containing hydroquinone (0.12 g, 1.09 mmol), dry inhibitor-free THF (100 mL), 2-piperidinoethanol (15 mL, 112 mmol) and Et<sub>3</sub>N (15.7 mL, 112 mmol) were added. Then, methacryloyl chloride (11 mL, 112 mmol) in dry inhibitor-free THF (10 mL) was added dropwise over 20 minutes at rt. After that, the reaction was refluxed for 2 hours and subsequently filtered to remove the Et<sub>3</sub>N salts. Then, the solvent was

removed under reduced pressure to obtain a yellowish oil that was dissolved in chloroform and washed with water and saturated solutions of NaCl and sodium carbonate. Finally, the solution was dried over sodium sulfate and the solvent was removed under vacuum, leading to a dark green solid. Purification of compound **17** was attempted either through distillation at reduced pressure or through chromatography on a silica column (ethyl acetate/heptane, 1:1).

❖ *Poly(2-(piperidin-1-yl)ethyl methacrylate (18)*

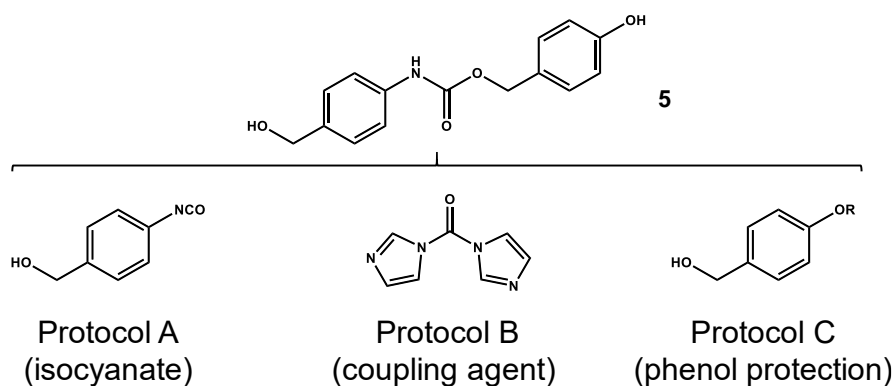
To a N<sub>2</sub>-purged vial containing compound **17** (0.5 g, 2.5 mmol), dry dioxane (1.5 mL) was added and the mixture was deoxygenated. Then, 4,4'-azobis (4-cyanovaleric acid) (1% mol, 0.5% mol, 0.25% mol or 0.125% mol) in deoxygenated dioxane was added and the mixture was introduced in a bath at 80°C and stirred overnight. Afterward, the mixture was precipitated in a (4:3) solution of methanol and 0.2 M NaOH, centrifuged and dried under vacuum to yield compound **18** as a reddish oily product.

## 2.5.3. Results and Discussion

### 2.5.3.1. Synthesis of a Self-Immolative Polymer Sensitive to pH 8

In a first attempt, the general protocol described in Section 2.3 for the synthesis of pH 5-responsive SIPs, *i.e.*, formation of the polymeric chain and subsequent addition of the pH 5 trigger, were adapted for basic-responsive polymers. However, this approximation led to negligible trigger incorporation when using directly HBA instead of compound **2**.

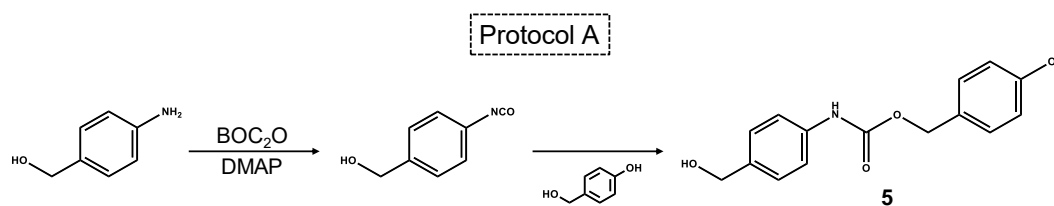
In this sense, the synthesis of a triggering monomer analogous to compound **2** but sensitive to pH 8 (compound **5**) was attempted. Three different strategies were explored (Scheme 2.12).



**Scheme 2.12.** Different approximations for the synthesis of compound **5**. Top: Target molecule. Bottom left corner: Protocol A, which was based on the formation of an isocyanate as intermediate of compound **5**. Bottom center: Protocol B, which was based on the use of coupling agents for alcohols and amines. Bottom right corner: Protocol C, which was based on the protection of alcohol groups.

Once synthesized, compound **5** would be used as end-cap for the preformed polymeric chain produced from compound **1**. It should react with the self-immolative chain through the benzylic alcohol rather than the phenolic one, since it has been reported that a benzylic alcohol reacts preferentially over a phenolic one in the presence of DBTL.<sup>9</sup>

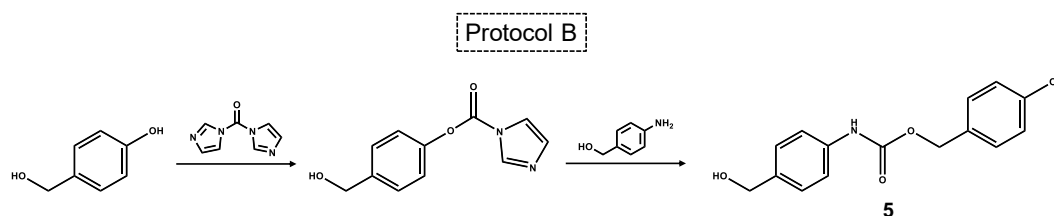
The first approximation for the synthesis of compound **5** consisted in the formation of a carbamate between ABA and HBA. For that purpose, the amino group of ABA was converted to an isocyanate. Then, the benzyl alcohol of HBA would be added to yield compound **5** (Scheme 2.13).



**Scheme 2.13.** Schematic representation of Protocol A. The amino group of ABA would be converted to an isocyanate group, to which HBA would be added to yield compound **5**.

The conversion was observed to be highly efficient. Indeed, (4-isocyanatophenyl) methanol underwent rapid self-polymerization and a white solid, which turned out to be a short SIP chain, precipitated out of the solution and prevented the subsequent addition of HBA.

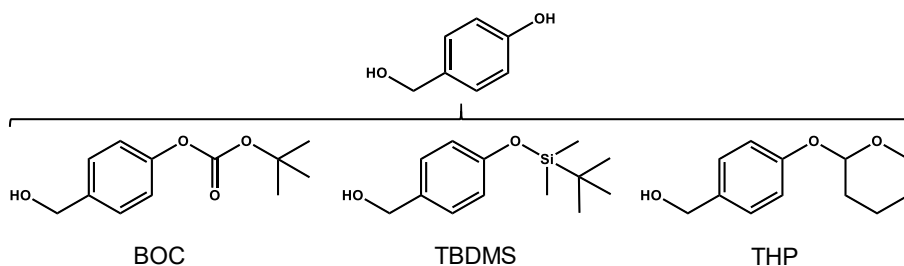
The second approximation consisted in the formation of the carbamate between ABA and HBA through a coupling agent to yield compound **5**. CDI was used to mediate the carbamate formation from the alcohol and the amine.<sup>10,11</sup> The idea was the formation of the CDI intermediate of HBA and the subsequent addition of ABA to create the carbamate (Scheme 2.14).



**Scheme 2.14.** Schematic representation of Protocol B. A coupling agent would be used to initially create an CDI intermediate of HBA to which ABA would then be added, leading to compound **5**.

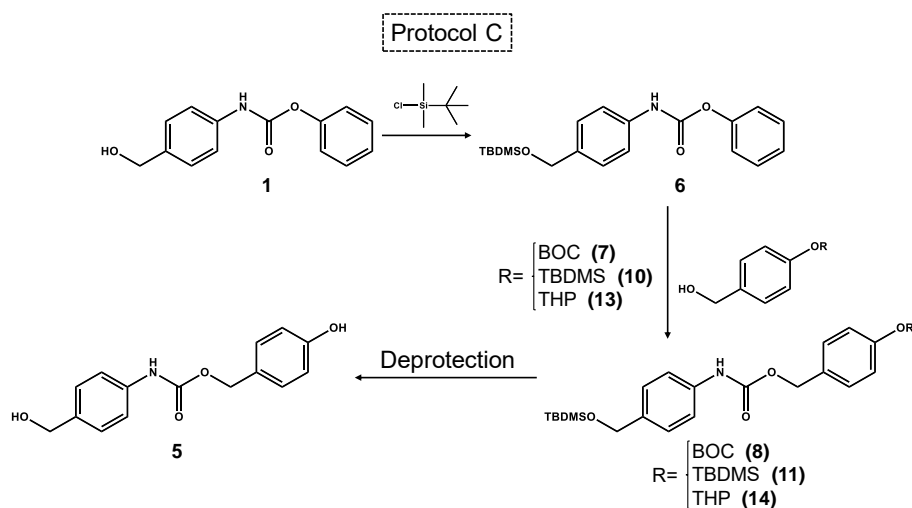
However, due to the similar reactivity of both alcohol groups of HBA, a mixture of benzyl-activated and phenol-activated CDI intermediates together with HBA-HBA carbonates were formed, leading to mixtures whose purification could not be performed. In consequence, this synthetic approximation was discarded.

In view of the unsatisfactory previous results, it was concluded that the similar reactivity of the alcohol groups of HBA constituted the bottleneck of the synthesis. As an alternative, the previous activation of the benzylic alcohol of HBA with a base to enhance its reactivity was explored. However, the more acidic nature of the phenolic alcohol induced its activation over the benzylic one. This observation led to the third synthetic pathway, which consisted in the use of alcohol protecting groups. Three of these groups were explored (Scheme 2.15).



**Scheme 2.15.** Different protecting groups for HBA. Left bottom corner: *tert*-butoxycarbonyl (BOC); Center: *tert*-butyldimethylsilyl ether (TBDMS); Right bottom corner: tetrahydropyranyl (THP).

This third approximation was based on (1) the protection of the benzylic alcohol of compound **1** and (2) the protection of the phenolic alcohol of HBA. Then, these two molecules would be reacted using DBTL to activate the carbamate of compound **6**. In a final step, the alcohol groups would be deprotected to yield compound **5** (Scheme 2.16).



**Scheme 2.16.** Schematic representation of Protocol C. The benzylic alcohol of compound **1** was protected and then phenol-protected HBA was added. The final step would be the deprotection of the alcohol groups to yield compound **5**. R: Protecting group for the phenolic alcohol.

Compound **1** was synthesized using ABA as starting material and subsequently subjected to TBDMS protection to yield compound **6**. This group was chosen for the mild



conditions required for its deprotection (either fluoride or acid treatments at rt).<sup>12,13</sup> The successful synthesis of compound **6** was characterized through <sup>1</sup>H-NMR (Figure 2.71).

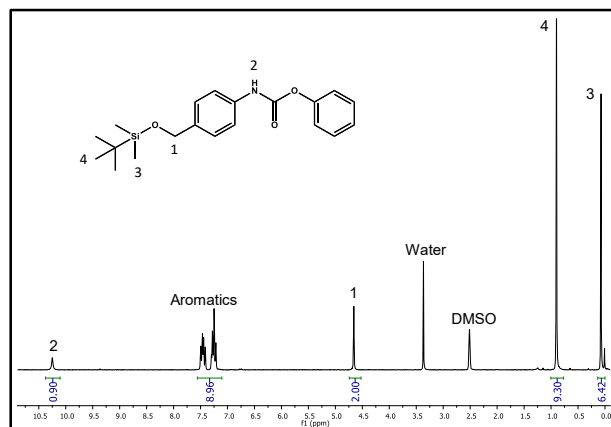


**Figure 2.71.** <sup>1</sup>H-NMR of compound **6**. (250 MHz, DMSO)  $\delta$  10.25 (s, 1H), 7.58–7.12 (m, 9H), 4.66 (s, 2H), 0.90 (s, 9H), 0.07 (d, 6H).

In a first approach, the phenolic alcohol of HBA was activated with a base a subsequently protected with BOC<sub>2</sub>O (Figure 2.72).

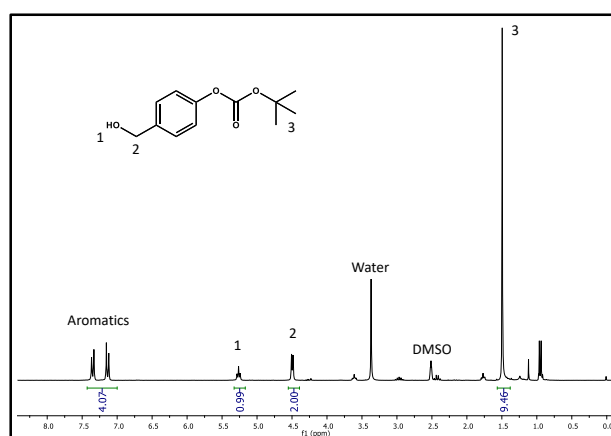


**Figure 2.72.** <sup>1</sup>H-NMR of compound **7**. (250 MHz, DMSO)  $\delta$  7.24 (dd, 4H), 5.26 (t, 1H), 4.50 (d, 2H), 1.49 (s, 9H).

The precursor of compound **5** was synthesized reacting compound **6** and compound **7** in the presence of DBTL (Figure 2.73).

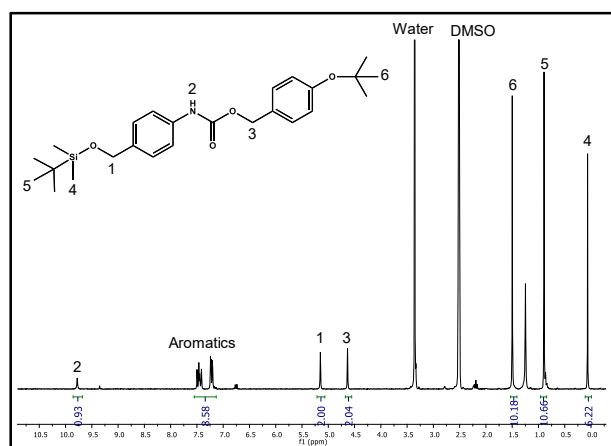


**Figure 2.73.**  $^1\text{H-NMR}$  of compound **8**. (250 MHz, DMSO)  $\delta$  9.78 (s, 1H), 7.58–7.17 (m, 9H), 5.15 (s, 2H), 4.63 (s, 2H), 1.50 (s, 9H), 0.89 (s, 9H), 0.07 (s, 6H).

Once synthesized the precursor of the trigger sensitive to pH 8, the next step was the deprotection of both alcohol groups. TFA in DCM was employed to remove both acid-sensitive protecting groups. First, the cleavage was carried out at rt but the BOC group remained unaffected. The protocol was repeated at DCM reflux, leading to the deprotection of both groups but yielding a molecule where the expected signals could not be observed (Figure 2.74).

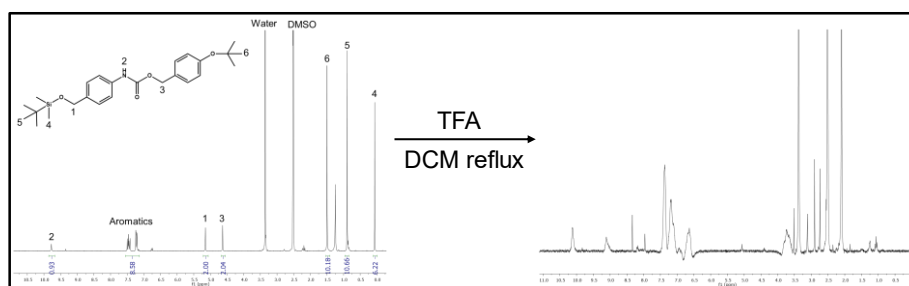


**Figure 2.74.** Deprotection of compound **8**. The application of TFA at DCM reflux led to a compound where the expected signals could not be observed.

In view of these results, the TBDMS protecting group was employed to protect HBA. In a first attempt, the phenolic alcohol of HBA was activated with DIPEA but both alcohols were protected, regardless of the reactivity (Figure 2.75).

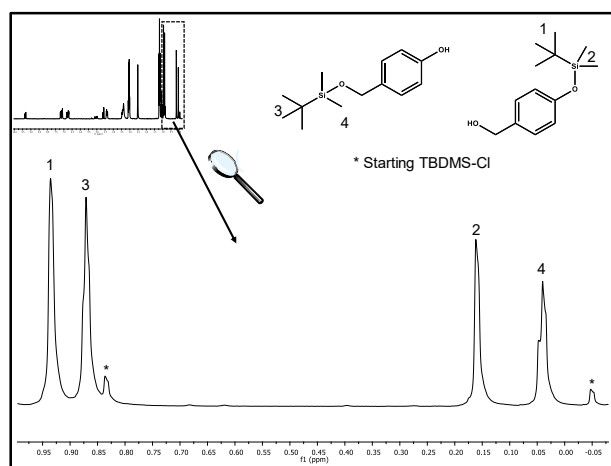


**Figure 2.75.** <sup>1</sup>H-NMR of the protection of HBA with TBDMS. The magnified area represents the TBDMS signals. This protecting group indiscriminately protected both alcohol functionalities of HBA, as demonstrated by signals (1 and 2) and (3 and 4).

In view of Figure 2.75, both alcohols were protected in almost the same proportion. Then, the yield after purification would be *ca.* 50% as much. For that reason, HBDA was chosen as starting material. Its alcohol would be protected and then the aldehyde reduced to yield a benzylic alcohol. The successful protection of HBDA was confirmed through <sup>1</sup>H-NMR (Figure 2.76).

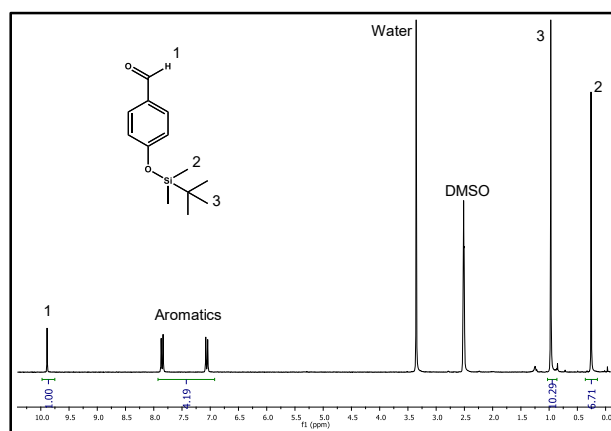


**Figure 2.76.** <sup>1</sup>H-NMR of compound 9. (250 MHz, DMSO)  $\delta$  9.89 (s, 1H), 7.46 (dd, 4H), 0.97 (s, 9H), 0.26 (s, 6H).

Compound 9 was treated with NaBH<sub>4</sub> to reduce the aldehyde, leading to compound 10 (Figure 2.77).

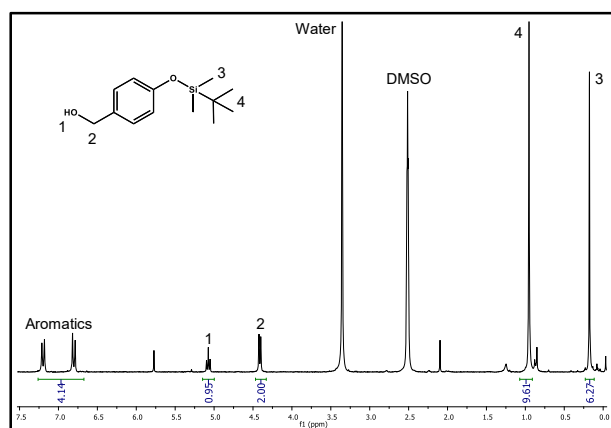


**Figure 2.77.**  $^1\text{H-NMR}$  of compound **10**. (250 MHz, DMSO)  $\delta$  7.00 (dd, 4H), 5.07 (t, 1H), 4.41 (d, 2H), 0.95 (s, 9H), 0.18 (s, 6H).

Finally, the TBDMS-protected analogue of HBA was added to compound **6** in the presence of DBTL to yield compound **11** (Figure 2.78).

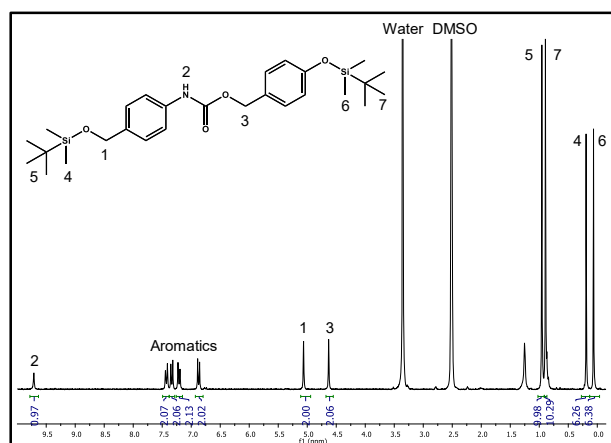


**Figure 2.78.**  $^1\text{H-NMR}$  of compound **11**. (250 MHz, DMSO)  $\delta$  9.71 (s, 1H), 7.56–6.75 (m, 8H), 5.06 (s, 2H), 4.63 (s, 2H), 0.96 (s, 9H), 0.89 (s, 9H), 0.19 (s, 6H), 0.06 (s, 6H).

Once compound **6** was synthesized, the next step was the deprotection of both alcohol groups to yield compound **5**. The different deprotection strategies are summarized in Table 2.10.

**Table 2.10.** Deprotection protocols applied to compound **11**. O.N.: Overnight; (1): Benzylic alcohol; (2): Phenolic alcohol; TBAF: Tetra-*n*-butylammonium fluoride.

Deprotection protocol	Effect
TBAF in THF	Self-immolation $\rightarrow$ molecule degraded
TBAF in THF/Water (4:1), rt, O.N.	0% deprotected
TBAF in THF/Water (4:1), 45°C, O.N.	(1) <i>ca.</i> 40% deprotected; (2) unaffected
TsOH in THF/Water (4:1), 45°C, O.N.	(1) <i>ca.</i> 40% deprotected; (2) unaffected
TsOH/TBAF in THF/Water (4:1), 45°C, O.N.	(1) <i>ca.</i> 70% deprotected; (2) unaffected
TsOH in MeOH/DCM (1:1), 45°C, O.N.	(1) <i>ca.</i> 100% deprotected; (2) unaffected

The standard deprotection protocol for the TBDMS group, *i.e.*, TBAF in THF was initially explored. However, it rapidly induced the self-immolation of compound **11**. A possible explanation for this would be the need of an acidic work-up to transfer a proton to the just deprotected alcohol. In the case of compound **11**, that deprotonated intermediate state would probably start the self-immolation, degrading the molecule.

As an alternative, compound **11** was treated with an aqueous solution of TBAF in THF. In this way, there would be protons in the solution that might be transferred to the alcohol after its deprotection, avoiding self-immolation. However, neither the reaction at rt nor at 45°C deprotected the phenolic alcohol.

Since the TBDMS protecting group is known to be cleaved under acidic conditions, compound **11** was treated with aqueous solutions of TsOH in THF. Nevertheless, none of the explored conditions yielded compound **5**.

Finally, it was found that the TBDMS group of a benzylic alcohol could be readily cleaved using a solution of TsOH in methanol and DCM. However, the phenolic alcohol remained unaffected.

In view of the efficient removal of the TBDMS group of the benzylic alcohol, the next approximation was to use a protecting group able to be cleaved under that condition. In this sense, the THP group, which is known to be efficiently removed by TsOH in methanol,<sup>14,15</sup> was employed.

HBDA was used again as starting material to prevent double alcohol protection. Its protection with the THP protecting group was characterized through <sup>1</sup>H-NMR (Figure 2.79).

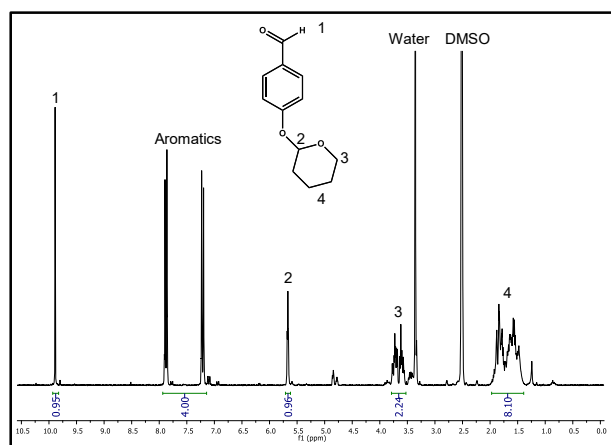


**Figure 2.79.** <sup>1</sup>H-NMR of compound **12**. (250 MHz, DMSO)  $\delta$  9.89 (s, 1H), 7.55 (dd, 4H), 5.67 (t, 1H), 3.81–3.50 (m, 2H), 1.99–1.35 (m, 6H).

Then, compound **12** was treated with NaBH<sub>4</sub> to reduce the aldehyde, leading to compound **13** (Figure 2.80).

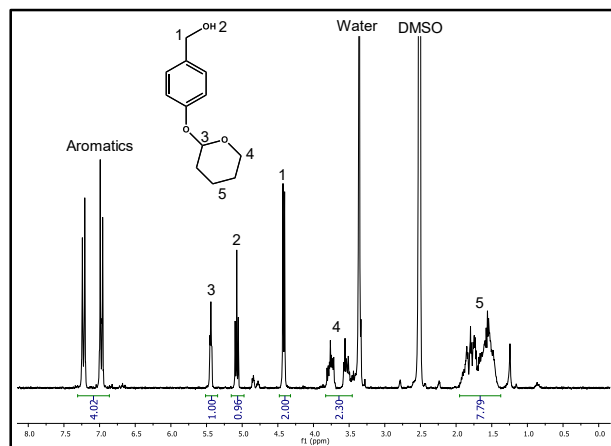


**Figure 2.80.** <sup>1</sup>H-NMR of compound **13**. (250 MHz, DMSO)  $\delta$  7.10 (dd, 4H), 5.44 (t, 1H), 5.08 (t, 1H), 4.42 (d, 2H), 3.90–3.43 (m, 2H), 1.98–1.39 (m, 6H).

Once synthesized the THP-protected HBA, the next step was its addition to compound **6** to produce the precursor of the trigger sensitive to pH 8. However, the compound degraded as it was introduced in the silica column and, consequently, compound **14** could not be effectively synthesized. The most feasible explanation might be that the slightly acidic nature of the silica employed in the column might have cleaved the protecting group, leading to the premature degradation of compound **13**.

In summary, the three approximations here developed (formation of isocyanate, use of coupling agents and use of protecting groups) were ineffective in producing the desired compound **5**. In view of all these results, the consortium agreed to stop the production of a self-immolative polymer sensitive to pH 8.

### 2.5.3.2. Synthesis of a Self-Immolative Polymer Sensitive to pH 6.8

The self-immolative trigger sensitive to pH 6.8 (compound **15**) was synthesized through the reaction of ABA with 4-carboxybenzaldehyde. At pH 6.8, this compound would be hydrolyzed, leading to a free electron pair that would start the self-immolation. The successful synthesis of compound **15** was confirmed through <sup>1</sup>H-NMR (Figure 2.81).

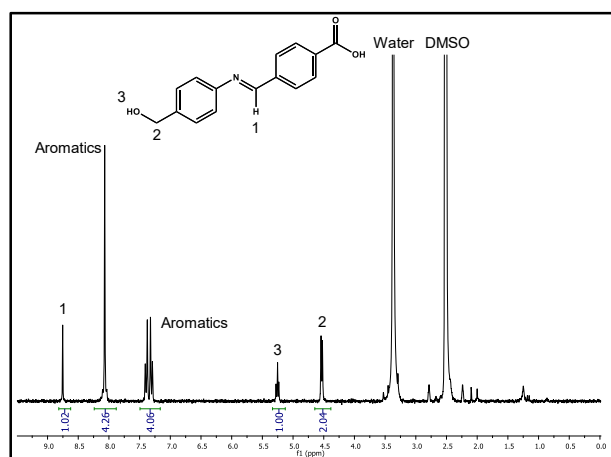


**Figure 2.81.**  $^1\text{H-NMR}$  of compound **15**. (250 MHz, DMSO)  $\delta$  8.75 (s, 1H), 8.17–7.95 (m, 4H), 7.35 (dd, 4H), 5.25 (t, 1H), 4.53 (d, 2H).

Compound **15** was subjected to the SIP synthesis conditions described in Section 2.3.2.3 (85°C, 2 hours) prior to any attempt to end-cap the self-immolative chains. The trigger was analyzed before and after the thermal treatment through  $^1\text{H-NMR}$  (Figure 2.82).

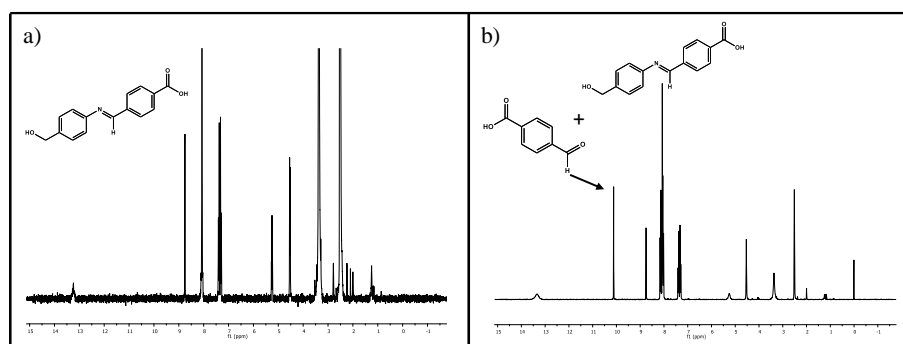


**Figure 2.82.**  $^1\text{H-NMR}$  of compound **15**. a) Before thermal treatment; b) After thermal treatment. The application of the SIP synthesis conditions to compound **15** led to the appearance of the signal ascribed to the aldehyde of the precursor, indicating the degradation of the imine.

The appearance of a signal associated to the aldehyde of 4-carboxybenzaldehyde confirmed the degradation of the imine. In consequence, if compound **15** were added as end-cap for the SIPs, the *in situ* hydrolysis of the imine bond would induce the self-immolation of the polymeric chain, and no SIP would be obtained.

There are some examples in the literature about self-immolative polymers synthesized using monomers similar to compound **1**, at rt and under basic conditions. Those examples include the use of DMAP<sup>16</sup> or Et<sub>3</sub>N and catalytic DMAP<sup>17</sup> in toluene. However, compound **1** was insoluble in toluene so a protocol using Et<sub>3</sub>N in DMSO was followed.<sup>7</sup> The self-immolative chain was synthesized at 60°C. Then, the reaction was cool down to

preserve the integrity of compound **15** and the mixture was reacted for either 3 or 24 hours (Figure 2.83).

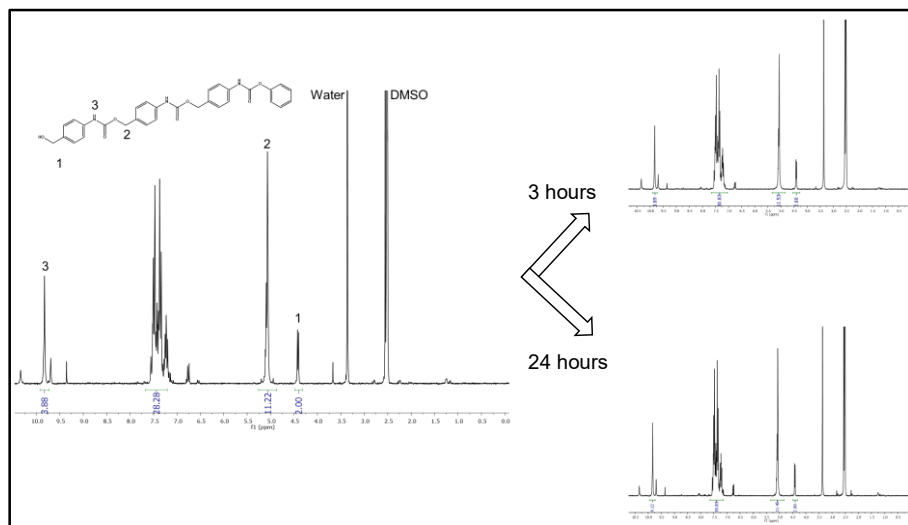


**Figure 2.83.** <sup>1</sup>H-NMR of a base-mediated SIP polymerization. The SIP could be synthesized using Et<sub>3</sub>N as catalyst (left). However, the addition of compound **15** for either 3 or 24 hours (right) did not induce any changes in the spectrum, demonstrating that the trigger could not be introduced employing this methodology.

As shown in Figure 2.83, the polymeric backbone could be formed using a base as catalyst, although the molecular weight was lower than that obtained using DBTL. However, the addition of the trigger for either 3 or 24 hours had no effect and the spectrum remained unchanged.

In view of these results, and in agreement with the MOZART consortium, the synthesis of a self-immulative trigger sensitive to pH 6.8 was discarded and a contingency plan was activated, as it is described in the following section.

### 2.5.3.3. Synthesis of a Polymer Undergoing Conformational Changes at pH 6.8

Even though the proposal devised the use self-immulative polymers, a *safety clause* was included, meaning that if all the approximations for the synthesis of the pH-responsive SIP failed, a totally different approximation might be applied. In this sense, the synthesis of a class of polymer able to undergo conformational changes at pH 6.8 rather than self-immolation was explored.<sup>8</sup> This polymer would be grafted to the particles and would be collapsed on the surface at physiological pH, closing the pore entrances. However, after a slight drop in pH, the polymer chains would adopt an extended conformation, opening the pores and triggering the drug release.



The monomer was synthesized using 2-piperidinoethanol as tertiary amine-source. Compound **17** was characterized through  $^1\text{H-NMR}$  (Figure 2.84).

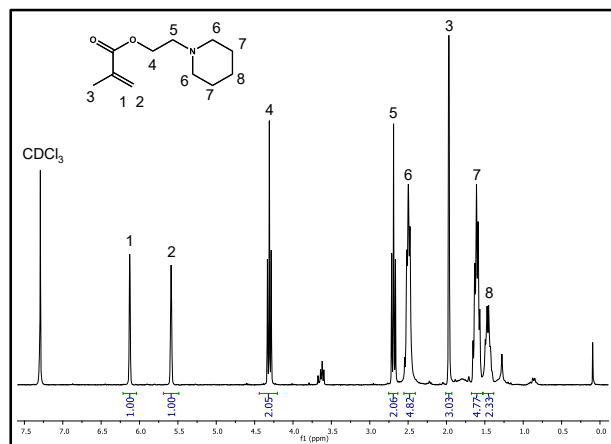


**Figure 2.84.**  $^1\text{H-NMR}$  of compound **17**. (250 MHz,  $\text{CDCl}_3$ )  $\delta$  6.13 (s, 1H), 5.59 (d, 1H), 4.31 (t, 2H), 2.69 (t, 2H), 2.57–2.37 (m, 5H), 1.97 (s, 3H), 1.71–1.53 (m, 5H), 1.53–1.36 (m, 2H).

The polymerization was initially attempted using the Reversible Addition-Fragmentation chain-Transfer (RAFT) polymerization method, using the as-synthesized compound **17** as monomer. The mixture was stirred overnight but no precipitated polymer could be observed when the reaction mixture was poured in a (4:3) methanol:0.2 M NaOH solution. A possible explanation for this might be the presence of amine impurities that induced the aminolysis of the thiocarbonylthio chain transfer agents.<sup>18</sup>

In consequence, two purification methods were explored. In a first approach, a distillation of compound **17** was attempted. Only a small amount of compound **17** could be distilled, even though many conditions were used, including improvements in the distillation set-up. However, this distilled monomer was unable to polymerize, despite several conditions were attempted.

The free radical polymerization, which is unaffected by amine impurities, was used as an alternative. The obtained polymer was characterized through  $^1\text{H-NMR}$  (Figure 2.85).

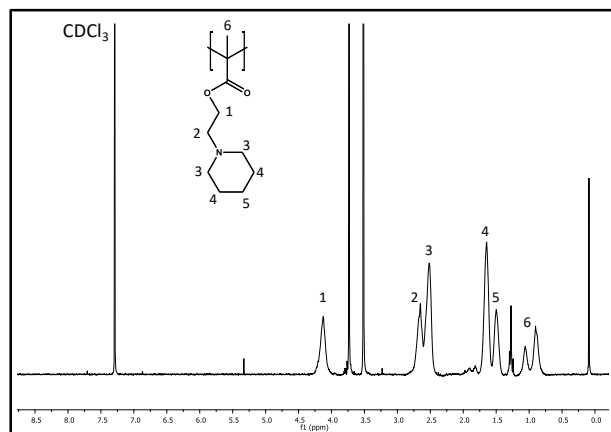


**Figure 2.85.**  $^1\text{H-NMR}$  of compound **18**. The signals obtained in the spectrum were in agreement with those expected for polymer like this. Integrals are not depicted due to the lack of representative signals to normalize the integrals.

According to the literature,<sup>8</sup> polymers with a molecular weight of *ca.* 20,000 g/mol should have been obtained. However, after several attempts, the best result was a polymer with a molecular weight of *ca.* 1,000 g/mol, which was even lower than that of compound **3** (3,300 g/mol) (Figure **2.86**).

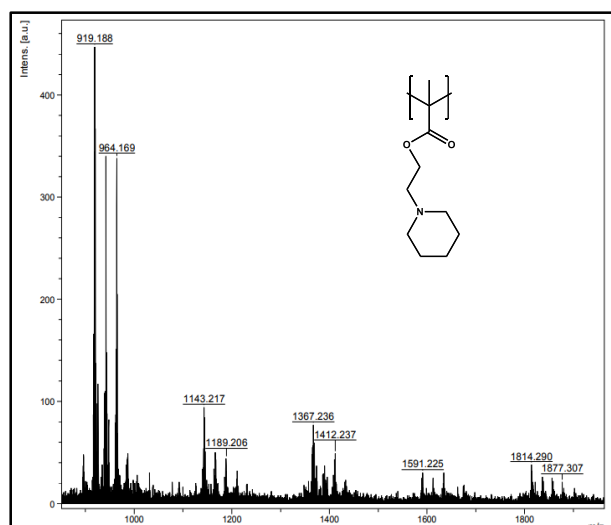


**Figure 2.86.** Mass spectroscopy analysis of compound **18**. The best synthesis led to polymers with a molecular weight of *ca.* 1,000 g/mol, which was even lower than that of compound **3**.

Distilling the monomer yielded poor results, even though some authors suggest this method in the literature. In a final attempt, compound **17** was purified by silica column chromatography. The target compound and the traces could be easily separated in the thin layer chromatography. However, after being eluted through the chromatography column the obtained compound rapidly became a gel that was impossible to dissolve in any solvent (Figure **2.87**).



**Figure 2.87.** Demonstration of the gelification of compound **17** after attempting its purification on a silica chromatography column.

The thin layer chromatography of the crude reaction mixture of synthesis of compound **16** showed several spots. A possible explanation for the gelification might be that the radical inhibitors employed during the synthesis of compound **17** were separated from the target compound, leading to undesired polymerization in the tube.

In consequence, the contingency plan had to be abandoned and idea of developing a polymeric coating sensitive to pH 6.8 was discarded by the MOZART consortium.

#### 2.5.4. Conclusions

In view of the results derived from the *in vivo* measurements of the pH values in bone and wound healing, the efforts in this chapter were headed towards the development of alternative self-immolative polymers sensitive to either pH 6.8 or 8, rather than the SIP sensitive to pH 5 previously described in Sections **2.2** and **2.3**.

First, the direct incorporation of the molecule sensitive to pH 8, HBA, as end-cap for the self-immolative chains was attempted but no incorporation was observed. In consequence, the synthesis of a triggering monomer sensitive to pH 8 was explored. Three different approximations were developed during this work.

In a first approach, the amino group of ABA was converted to an isocyanate, to which HBA would be added to form the trigger. However, ABA underwent self-polymerization as the amine was converted to the isocyanate and the protocol had to be discarded.

Then, the use of coupling agents between alcohol and amines was explored. The similar reactivity of both alcohol groups of HBA induced a mixture of CDI-activated compounds that could not be purified. In consequence, the protocol had to be abandoned.

The use of protecting groups for the phenolic alcohol of HBA was then explored. First, the BOC protecting group was employed. The precursor of the trigger was effectively synthesized, although the deprotection was unsuccessful and compound **5** could not be obtained. Then, the TBDMS group was used to protect HBA, but both alcohols were protected. As an alternative, HBDA was selected as starting material. Initially the phenolic alcohol was protected and then the aldehyde was easily reduced to a benzylic alcohol. Again, the precursor was successfully synthesized and several deprotection approaches were explored. The best result was the complete deprotection of the benzylic alcohol, remaining the phenolic one unaffected. In consequence, this approximation had to be discarded. Finally, Finally, the THP group was employed to protect HBDA. The precursor of the trigger sensitive to pH 8 could be synthesized. However, the attempts to purify the precursor were ineffective and the molecule degraded when subjected to silica column chromatography.

In view of the results and the several synthetic approximations employed, the MOZART consortium agreed to abandon the synthesis of a self-immolative polymeric coating sensitive to pH 8.

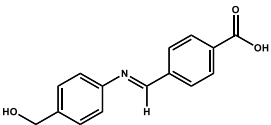
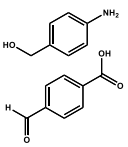
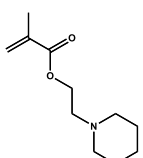
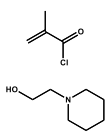
The design of the self-immolative polymer sensitive to pH 6.8 was based on a trigger containing a benzoic imine bond, which is known to be hydrolyzed at pH 6.8. The trigger was successfully synthesized. However, it degraded when subjected to the standard SIP synthesis conditions. Instead, a base-mediated polymerization was attempted. The polymeric chain could be formed but the trigger could not be incorporated, despite various conditions were used.

As an alternative, the MOZART consortium agreed to follow a contingency plan, and a new polymer able to change its conformation upon changes in pH was proposed. The monomer could not be properly purified, even though several purification methods were attempted. Two polymerization methods were employed. The polymer could not be synthesized through the RAFT method, probably due the presence of amine impurities. The free radical method allowed the synthesis of the polymeric chain but low molecular weights were obtained, despite several conditions were explored.

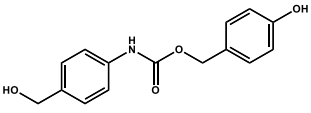
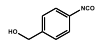
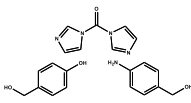
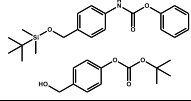
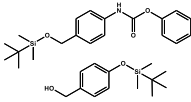
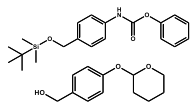
In view of the above-mentioned results, the MOZART consortium agreed to stop the design of a polymeric coating sensitive to pH 6.8.

For the sake of clarity, the conclusions for the synthesis attempts of polymers sensitive to pH 6.8 or 8 are summarized in the Tables 2.11 and 2.12, respectively.

**Table 2.11.** Summary of the synthetic approximations for the synthesis of the trigger sensitive to pH 6.8.

Molecule	Approximation	Description	Success
		Formation of a self-immolative benzoic imine bond between 4-aminobenzyl alcohol and 4-carboxybenzaldehyde	Synthesis: YES Incorporation in the polymer chain: NO (Degraded with temperature and did not end-cap the polymerization mediated by a base)
		Precursor of a poly(methacrylate) that changes its conformation at pH 6.8	Synthesis: NO (Failed purification) Polymer synthesis: NO (Extremely low molecular weights)

**Table 2.12.** Summary of the synthetic approximations for the synthesis of the trigger sensitive to pH 8.

Molecule	Precursors	Description	Success
		Formation of an isocyanate from 4-aminobenzyl alcohol and subsequent addition of 4-hydrobenzyl alcohol	Synthesis: NO (Purification failed) Incorporation in the polymer chain: NO
		Use of a coupling agent to form a carbamate between 4-hydroxybenzyl alcohol and 4-aminobenzyl alcohol	Synthesis: NO (Purification failed) Polymer synthesis: NO
		Protection of (a) benzylic alcohol of compound 1 and (b) phenolic alcohol of 4-hydrobenzyl alcohol	Synthesis: NO (Deprotection of phenolic alcohol failed) Incorporation in the polymer chain: NO
			Synthesis: NO (Degraded during purification) Incorporation in the polymer chain: NO
			

## References

- (1) Bullock, A. J.; Garcia, M.; Shepherd, J.; Rehman, I.; Sheila, M. Bacteria Induced PH Changes in Tissue-Engineered Human Skin Detected Non-Invasively Using Raman Confocal Spectroscopy. *Appl. Spectrosc. Rev.* **2019**, 1–14.
- (2) Juárez, L. A.; Añón, E.; Giménez, C.; Sancenón, F.; Martínez-Mañez, R.; Costero, A. M.; Gaviña, P.; Parra, M.; Bernardos, A. Self-Immolative Linkers as Caps for the Design of Gated Silica Mesoporous Supports. *Chem. Eur. J.* **2016**, *22*, 14126–14130.
- (3) Qu, X.; Yang, Z. Benzoic-Imine-Based Physiological-pH-Responsive Materials for Biomedical Applications. *Chem. Asian J.* **2016**, *11*, 2633–2641.
- (4) Knölker, H.-J.; Braxmeier, T.; Schlechtingen, G. A Novel Method for the Synthesis of Isocyanates Under Mild Conditions. *Angew. Chemie Int. Ed.* **1995**, *34*, 2497–2500.
- (5) Robbins, J. S.; Schmid, K. M.; Phillips, S. T. Effects of Electronics, Aromaticity, and Solvent Polarity on the Rate of Azaquinone-Methide-Mediated Depolymerization of Aromatic Carbamate Oligomers. *J. Org. Chem.* **2013**, *78*, 3159–3169.
- (6) Fu, H.; Zhang, Y.; Wang, X.; Han, Y.; Peng, X.; Efferth, T.; Fu, Y. Synthesis and Anti-Tumor Activity of Novel Aminomethylated Derivatives of Isoliquiritigenin. *Molecules* **2014**, *19*, 17715–17726.
- (7) Peterson, G. I.; Church, D. C.; Yakelis, N. A.; Boydston, A. J. 1,2-Oxazine Linker As a Thermal Trigger for Self-Immolative Polymers. *Polymer* **2014**, *55*, 5980–5985.
- (8) Zhu, L.; Powell, S.; Boyes, S. G. Synthesis of Tertiary Amine-Based pH-Responsive Polymers by RAFT Polymerization. *J. Polym. Sci. Part A Polym. Chem.* **2015**, *53*, 1010–1022.
- (9) Subrayan, R. P.; Zhang, S.; Jones, F. N.; Swarup, V.; Yezrielev, A. I. Reactions of Phenolic Ester Alcohol with Aliphatic Isocyanates—Transcarbamoylation of Phenolic to Aliphatic Urethane: A  $^{13}\text{C}$ -NMR Study. *J. Appl. Polym. Sci.* **2000**, *77*, 2212–2228.
- (10) D'Addona, D.; Bochet, C. G. Preparation of Carbamates from Amines and Alcohols under Mild Conditions. *Tetrahedron Lett.* **2001**, *42*, 5227–5229.
- (11) Rannard, S. P.; Davis, N. J. The Selective Reaction of Primary Amines with Carbonyl Imidazole Containing Compounds: Selective Amide and Carbamate Synthesis. *Org. Lett.* **2000**, *2*, 2117–2120.
- (12) Maiti, G.; Roy, S. C. A Mild and Efficient Method for the Selective Cleavage of Tert-Butyldimethylsilyl Ethers to Alcohols. *Tetrahedron Lett.* **1997**, *38*, 495–498.
- (13) Cunico, R. F.; Bedell, L. The Triisopropylsilyl Group as a Hydroxyl-Protecting Function. *J. Org. Chem.* **1980**, *45*, 4797–4798.
- (14) Sarkar, T. K.; Gosh, S. K.; Subba Rao, P. S. V.; Satapathi, T. K.; Mamdapur, V. R. Cyclopentanoid Allylsilanes in Synthesis of Di- and Triquinanes. A

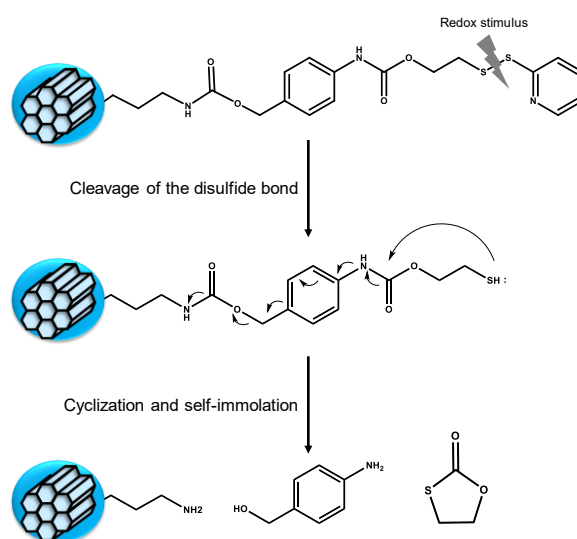
- Stereoselective Synthesis of ( $\pm$ )-Hirsutene. *Tetrahedron* **1992**, *48*, 6897–6908.
- (15) Hama, N.; Matsuda, T.; Sato, T.; Chida, N. Total Synthesis of (-)-Agelastatin A: The Application of a Sequential Sigmatropic Rearrangement. *Org. Lett.* **2009**, *11*, 2687–2690.
- (16) Gnaim, S.; Shabat, D. Self-Immolative Chemiluminescence Polymers: Innate Assimilation of Chemiexcitation in a Domino-like Depolymerization. *J. Am. Chem. Soc.* **2017**, *139*, 10002–10008.
- (17) McBride, R. A.; Gillies, E. R. Kinetics of Self-Immolative Degradation in a Linear Polymeric System: Demonstrating the Effect of Chain Length. *Macromolecules* **2013**, *46*, 5157–5166.
- (18) Janoschka, T.; Teichler, A.; Krieg, A.; Hager, M. D.; Schubert, U. S. Polymerization of Free Secondary Amine Bearing Monomers by RAFT Polymerization and Other Controlled Radical Techniques. *J. Polym. Sci. Part A Polym. Chem.* **2012**, *50*, 1394–1407.

## 2.6. Redox-Responsive Mesoporous Silica Nanoparticles

### 2.6.1. Introduction

Among the available internal triggers mentioned in Section 2.1, and after all the efforts made with pH in previous sections, exploiting the redox environment seemed to be an attractive approximation to tackle cancer treatment using stimuli-responsive drug delivery systems. The rationale behind using this stimulus is the overexpression of glutathione that is found in the cellular cytoplasm as a consequence of increased ROS levels, which is much higher than that found in the extracellular fluid.<sup>1,2</sup> In consequence, that overexpression of glutathione constitutes a reliable trigger as it has been used to trigger the release from many drug delivery systems using several approximations.<sup>3-7</sup>

As it has been extensively mentioned throughout this thesis, the main drawback of mesoporous materials is their open porosity. In this sense, this piece of research consisted in developing a nanocarrier based on MSNs and a stimuli-responsive diffusion barrier that could delay premature release from the mesopores. The design of this diffusion barrier was based on self-immolative chemistry, using similar technology as that developed in Sections 2.2, 2.3 and 2.5. In particular, a small molecule bearing a disulfide bond that could act at the same time as diffusion barrier and as linker for further functionalization was engineered. The structure of this linker was such that the cleavage of the disulfide bond by redox stimuli would lead to a self-immolative event. The hypothesized behavior of the system MSNs + Linker is depicted in Scheme 2.14.



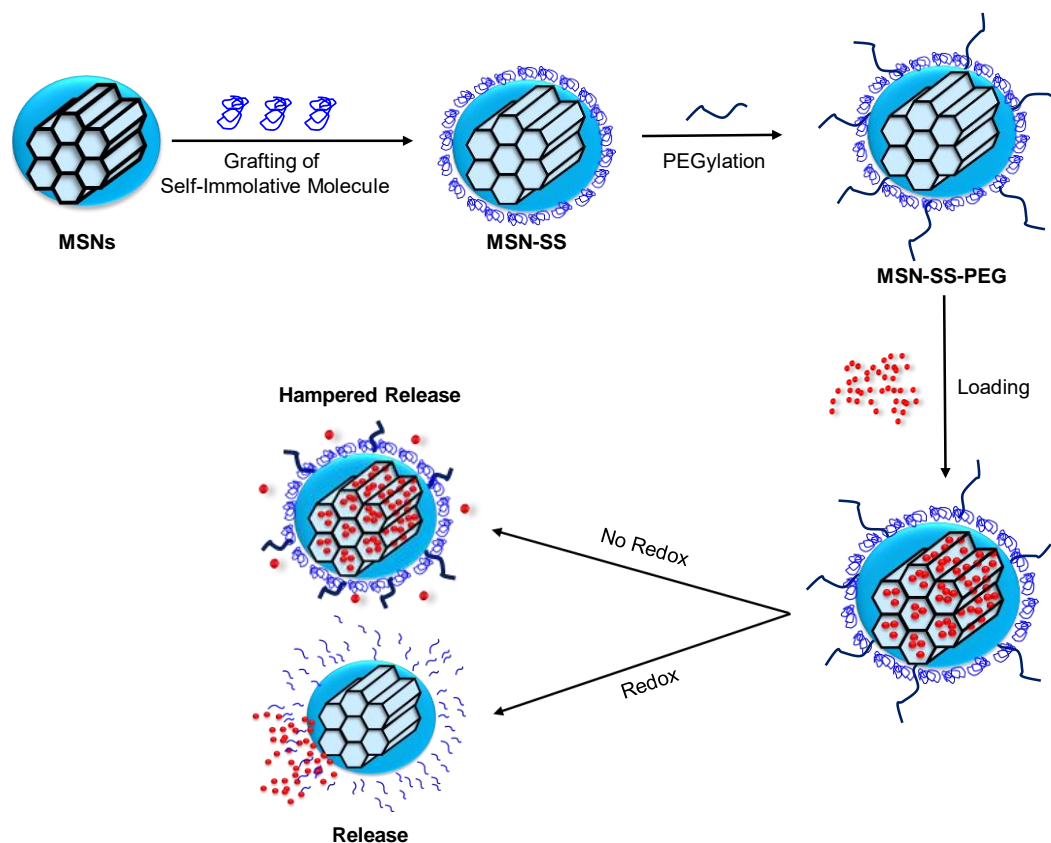
**Scheme 2.14.** Schematic representation of a self-immolative event through cyclization upon application of a redox stimulus to MSNs functionalized with the small molecule bearing a disulfide bond. The cleavage of this bond would lead to the self-immolation of the molecule and the subsequent opening of the mesopores.



The cleavage of the disulfide bond by a redox stimulus would lead to the cyclization and subsequent self-immolation of the grafted Linker, completely opening the pore entrances and triggering the drug release.<sup>8</sup>

The synthesis of the linker as well as its subsequent grafting to MSNs involved a thorough optimization process, as described below. In addition, the hybrid nanoparticles were further functionalized with a PEG chain to endow the carrier with stealth properties and improved colloidal stability. The redox-responsiveness of the PEGylated and non-PEGylated particles was evaluated through different methods using DTT as redox stimulus, which is a molecule widely employed to mimic the reductive environment found in the cytoplasm of cells.<sup>9,10</sup> Finally, the ability of the self-immolative linker to delay the payload release from the mesopores in a preliminary release experiment in the presence or absence of DTT.

A summary of the work carried out in this section is depicted in Scheme 2.15.



**Scheme 2.15.** Schematic representation of the work developed in this section. The self-immolative linker was grafted to MSNs and further functionalized with a PEG chain. Then, the ability of the molecule to close the pore entrances and trigger the release upon application of a redox stimulus was evaluated.

## 2.6.2. Materials and Methods

The following compounds were purchased from Sigma-Aldrich Inc.: TEOS, Ammonium nitrate; CTAB; FITC; APTES; ABA; Phenyl chloroformate; DBTL; 2-Mercaptoethanol; 2,2'-Dipyridyldisulfide; TBDMS-Cl; Ru; 3-(triethoxysilyl)propyl isocyanate; HS-PEG<sub>3500</sub>-NH<sub>2</sub> (PEG-SH); Dithiothreitol (DTT); DMF; THF; DCM, AcN. The rest of the chemicals (ethanol, heptane, etc) were of the best quality and were employed as received.

### 2.6.2.1. Mesoporous Silica Nanoparticles

MSNs were synthesized following the procedure described in Section 2.2.2.1 and characterized using the same techniques. Briefly, the particles were produced following a modification of the Stöber method.<sup>11</sup> In particular, the *sol-gel* method under basic and very diluted conditions was employed, using TEOS as silica source and CTAB as template, which was removed by solvent extraction to obtain empty mesopores.

### 2.6.2.2. Redox-Responsive Linker

All compounds were characterized through <sup>1</sup>H-NMR.

#### ❖ *Phenyl(4-(hydroxymethyl) phenyl)carbamate (1)*

Compound **1** was synthesized as described in Section 2.3.2.3. Briefly, ABA was reacted with phenyl chloroformate to yield pure compound **1** after crystallization in chloroform.

#### ❖ *Phenyl (4-(((tert-butyldimethylsilyl)oxy)methyl)phenyl)carbamate (6)*

Compound **6** was synthesized as described in Section 2.5.2.1. Briefly, compound **1** was reacted with TBDMS-Cl to protect its benzylic alcohol. The crude reaction mixture was purified in a silica column using DCM as mobile phase, leading to compound **6**.

#### ❖ *2-(pyridin-2-yl)disulfaneyl)ethan-1-ol (19)*

Compound **19** was synthesized using a previously reported protocol.<sup>12</sup> Briefly, to a vial containing 2,2'-dipyridyldisulfide (2.42 g, 10.98 mmol), methanol (40 mL) and acetic acid (0.26 mL, 4.55 mmol) were added. Then, 2-mercaptoethanol (0.6 mL, 8.52 mmol) in methanol (10 mL) was added dropwise over 30 minutes and the mixture was stirred for 48 hours at rt. Afterward, the solution was evaporated under reduced pressure to yield a dark yellow oil that was chromatographed in a silica column (ethyl acetate/heptane, 1:1) leading to compound **19** as a light yellow oil.

❖ *2-(pyridin-2-yl)disulfaneyl ethyl (4-(((tert-butyl)dimethylsilyloxy)methyl)phenyl)carbamate (20)*

To a vial containing compound **6** (1.9 g, 5.3 mmol), toluene (25 mL) and compound **19** (1.1 g, 5.9 mmol) in toluene (15 mL) were added. Then, DBTL (20% mol) was added and the mixture was refluxed for 4 hours. After that, the solvent was evaporated to yield a dark orange oil that was chromatographed in a silica column (ethyl acetate/heptane, 1:4) to lead to compound **20** as a pale orange oil.

❖ *2-(pyridin-2-yl)disulfaneyl ethyl (4-(hydroxymethyl)phenyl)carbamate (21)*

Compound **20** (2 g, 4.44 mmol) was dissolved in a 1:1 mixture of methanol and DCM (50 mL). Then, TsOH (10% mol) in a 1:1 mixture of methanol and DCM (15 mL) was added to compound **20** and the whole reaction mixture was refluxed overnight. After that, the solvent was removed under reduce pressure to yield an oil that was subsequently chromatographed in a silica column (ethyl acetate/heptane, 2:1) to yield compound **21** as a colorless oil.

### 2.6.2.3. PEGylated MSNs Functionalized with the Redox-Responsive Linker

❖ *MSN-SS*

To a N<sub>2</sub>-purged vial containing 3-(triethoxysilyl)propyl isocyanate (148.5 μL, 0.60 mmol), dry DCM (0.5 mL) was added (vial 1). A second N<sub>2</sub>-purged vial containing compound **21** (0.24 g, 0.72 mmol) and dry DCM (1.2 mL) was prepared (vial 2). Then, the content of vial 2 was slowly added over vial 1 and the final mixture was refluxed overnight. Afterward, to a vial containing MSNs (50 mg), AcN (5 mL) was added and the particles were sonicated to disperse the particles. Then, the content of the previously reacted mixture was added in three times (two hours between additions) and the mixture was refluxed overnight. Finally, the particles were centrifuged and washed twice with AcN and twice with methanol to yield MSNs functionalized with the redox-responsive linker, which will be denote hereafter as MSN-SS. The particles were characterized by means of TGA, FTIR spectroscopy, DLS and Zeta potential.

❖ *MSN-SS-PEG*

To a flask containing MSN-SS (45 mg), methanol (15 mL) was added and the particles were dispersed with the aid of an ultrasonicator. Then, PEG-SH (15 mg, 0.004 mmol) in methanol (1 mL) was slowly added to the particles and the mixture was stirred at rt overnight. Then, the particles were centrifuged and washed twice with methanol, leading to MSN-SS-PEG. The PEGylated nanoparticles were characterized in terms of TGA, FTIR spectroscopy, TEM, DLS and Zeta Potential.

#### 2.6.2.4. Preliminary Release Experiments from MSN-SS-PEG

❖ *MSN-SS-PEG Loaded with Ru (MSN-SS-PEG-Ru)*

To a vial containing MSN-SS-PEG, a saturated solution of Ru in methanol was added. The mixture was stirred overnight and subsequently centrifuged and washed several times until the Ru dye could not be observed in the media.

❖ *Release Experiment*

The release experiment was carried out following the protocol described in Section 2.2.2.4. To test the redox-responsiveness of the carrier, PBS 1x solutions with and without DTT (10 mM) were used instead of those at pH 7.4 and pH 5 employed in the previous cases. Briefly, the particles were dispersed in the corresponding PBS solution and placed in Transwell® at 37°C with orbital stirring. The media were removed every time point and analyzed in a fluorimeter to quantify the amount of Ru released. Fresh medium was added every time point after the old media were removed.

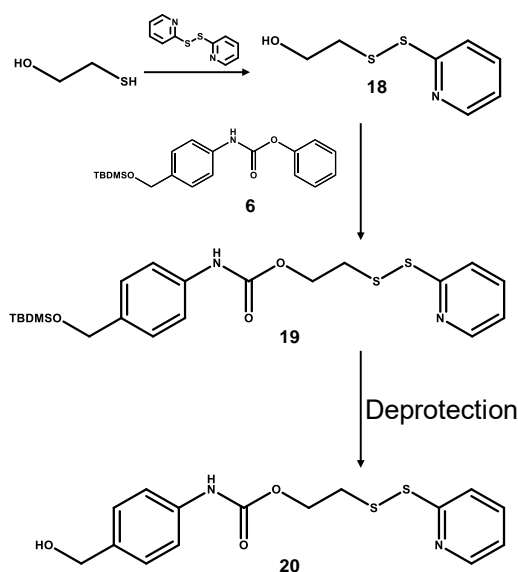
### 2.6.3. Results and Discussion

#### 2.6.3.1. Synthesis of Mesoporous Silica Nanoparticles

The synthesis of MSNs was accomplished following the procedure described in Section 2.2.2.1. Briefly, MSNs were synthesized following a modification of a Stöber method using CTAB as structure directing agent and TEOS as silica precursor, yielding homogenous particles with an array of hexagonally distributed cylindrical mesopores.

#### 2.6.3.2. Synthesis of the Redox-Responsive Linker

The synthesis of the self-immolative molecule sensitive to the overexpression of GSH (compound **21**) was based on the synthetic pathway developed for the synthesis of the different precursors of compound **5** (Scheme 2.14).



**Scheme 2.14.** Schematic pathway for the synthesis of the redox-responsive self-immolative molecule. The disulfide bond that would start the self-immolation was introduced using 2-mercaptoethanol and a thiol coupling agent. Then, compound **19** was added to compound **6** as it was described in Section 2.5. Finally, the TBDMS protecting group was removed to yield compound **21**.

The synthesis of compound **19** was accomplished straightforwardly using 2-mercaptoethanol and 2,2'-dipyridyldisulfide. The correct synthesis was confirmed through the signals observed in the  $^1\text{H-NMR}$  spectrum (Figure 2.88).

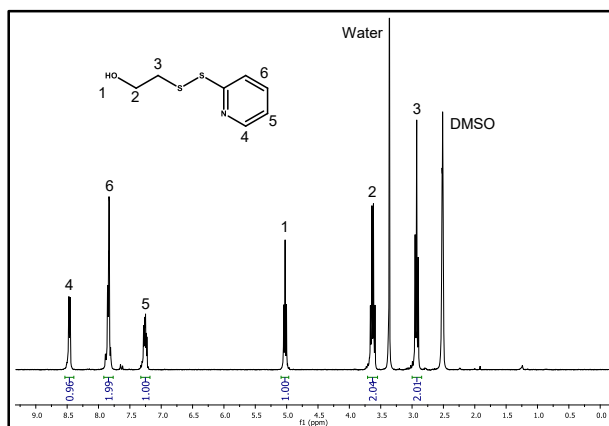


**Figure 2.88.**  $^1\text{H-NMR}$  of compound **19**. (250 MHz, DMSO)  $\delta$  8.46 (d, 1H), 7.91–7.72 (m, 2H), 7.38–7.15 (m, 1H), 5.02 (t, 1H), 3.63 (q, 2H), 2.93 (t, 2H).

Compound **20** was synthesized reacting compound **6** and compound **19**, using DBTL as catalyst. The final product was characterized with  $^1\text{H-NMR}$ , where the expected signals could be observed (Figure 2.89).

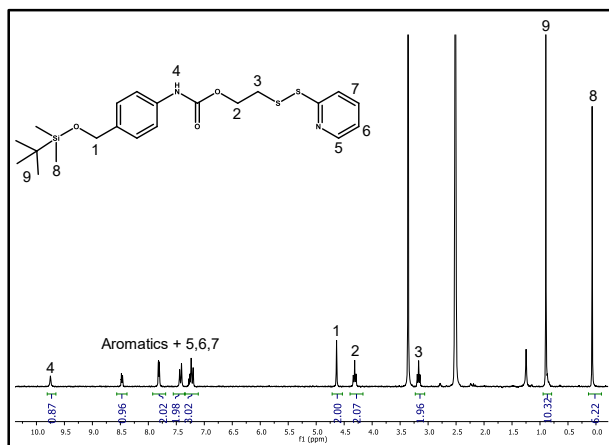


**Figure 2.89.**  $^1\text{H-NMR}$  of compound **20**. (250 MHz, DMSO)  $\delta$  9.75 (s, 1H), 8.47 (dt, 1H), 7.81 (dd, 2H), 7.42 (d, 2H), 7.31–7.15 (m, 4H), 4.64 (s, 2H), 4.31 (t, 2H), 3.17 (t, 2H), 0.90 (s, 9H), 0.07 (s, 6H).

The TBDMS protecting group of compound **20** was efficiently cleaved using TsOH, leading to compound **21** that was characterized with  $^1\text{H-NMR}$ , where the expected signals were found (Figure **2.90**).

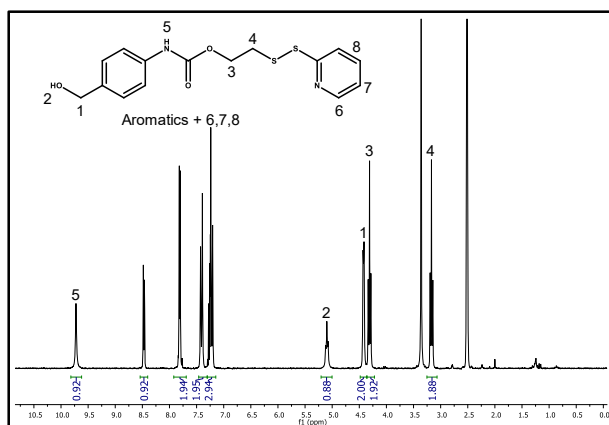


**Figure 2.90.**  $^1\text{H-NMR}$  of compound **21**. (250 MHz, DMSO)  $\delta$  9.73 (s, 1H), 8.47 (dt, 1H), 7.81 (dd, 2H), 7.41 (d, 2H), 7.34–7.15 (m, 4H), 5.10 (t, 1H), 4.42 (d, 2H), 4.31 (t, 2H), 3.17 (t, 2H).

The efficient deprotection was confirmed through the disappearance of the signals 8 and 9 from Figure **2.89** associated to the TBDMS group and the appearance of signal 2 in Figure **2.90** associated to the expected alcohol.

### 2.6.3.3. Synthesis of MSN-SS and MSN-SS-PEG

The first step was to find out a convenient solvent to attempt the coupling between compound **21** and the organosilane. Two solvents, namely THF and DCM, were explored. The efficiency of the silylation of compound **21** was determined through  $^1\text{H-NMR}$  (Figure **2.91**).

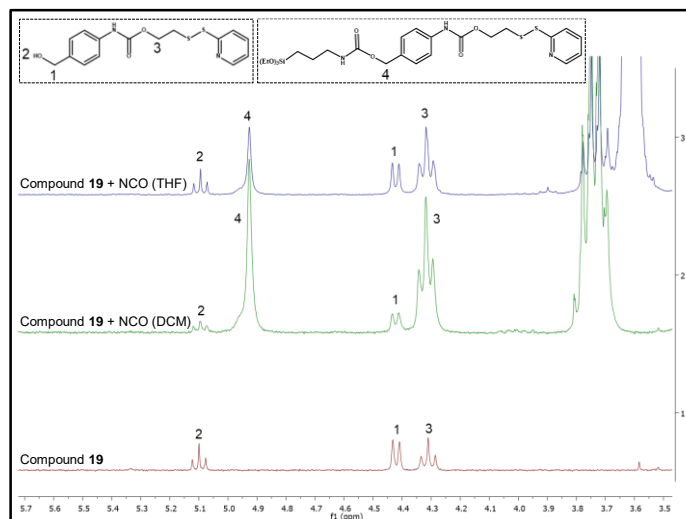


**Figure 2.91.** Determination of the best solvent for the coupling between compound **21** and the alkoxy silane. The appearance of signal 4 and the disappearance of signal 2 were unequivocally ascribed to the addition of the alcohol to the isocyanate. The highest conversion was obtained using DCM.

The efficiency of the coupling between both compounds was determined through comparison of the different signals in Figure 2.91. The appearance of signal 4 and the decrease of signal 1 were unequivocally ascribed to the proper addition of compound **21** to the isocyanate. The comparison of the relative intensities among signals 1, 2 and 3 of each spectrum provided an estimation of the rate of conversion. In this sense, Figure 2.91 clearly showed that the highest conversion into the final molecule was obtained for the reaction carried out in DCM.

A general protocol for grafting alkoxy silanes to MSNs consists in refluxing the mixture in toluene (110°C) under magnetic stirring under inert conditions. However, the redox-responsive linker was insoluble in this solvent. The initial idea was to attempt the grafting of this molecule in DCM. In this sense, the reflux temperature of DCM, *ca.* 40°C, might be insufficient to maximize the degree of functionalization. For that reason, the grafting was performed in a mixture of solvents. The reactions were carried out using a ratio MSNs:Linker 1:1. The silylation of compound **21** was carried out in DCM and then the mixture was added to MSNs dispersed either in DMF or AcN. The efficiency of the grafting was determined through the amount of organic matter incorporated in the MSNs, which was determined by TGA analysis (Figure 2.92).

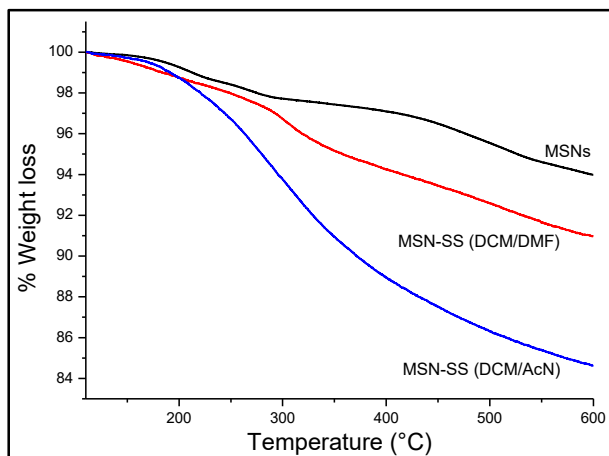


**Figure 2.92.** TGA analysis of the grafting of the linker in different solvents using a ratio MSN:Linker 1:1. The reaction in DMF led to *ca.* 3% of additional % weight loss while that in AcN led to *ca.* 7.5% of incorporated organic matter, confirming its suitability as solvent for the functionalization.

As shown in Figure 2.92, the use of DMF as co-solvent introduced *ca.* 3% of additional organic matter. The best results were obtained using AcN as co-solvent. In this case, the functionalization led to *ca.* 7.5% of additional organic matter, compared to bare MSNs, demonstrating its suitability for the reaction. The reason for that behavior might be that, unlike AcN, DMF presents an unshielded oxygen with high electron density able to form hydrogen bonds with the silanol groups of the particles. Then, these groups are more shielded and the rate of condensation reactions between the organosilane and the surface of the particles is retarded because of the steric hindrance. In consequence, more condensations events would take place when using AcN instead of DMF, for the same reaction time.<sup>13</sup>

The presence of the functional groups of the silylated compound **21** on the functionalized samples was confirmed by FTIR spectroscopy (Figure 2.93).



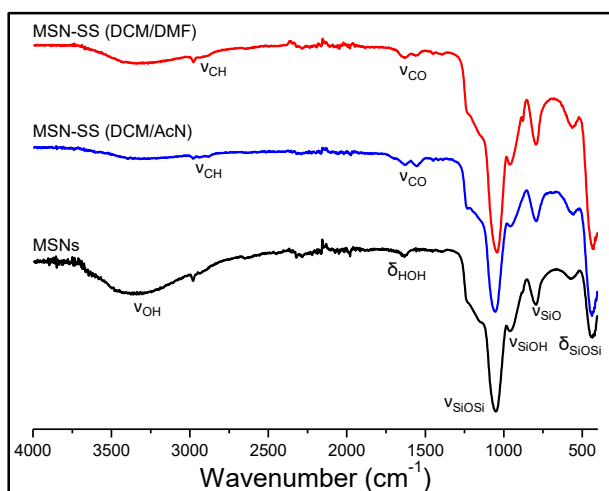


**Figure 2.93.** FTIR spectroscopy of MSNs and MSN-SS synthesized either in DMF or AcN. The addition of the linker led to the appearance of vibration bands ascribed to the carbamate of molecule **20** in both cases, confirming the presence of the compound.

The addition of the silylated compound **21** induced the appearance of vibration bands ascribed to the carbamate of the molecule, regardless of the solvent employed (Figure 2.93), which confirmed the completion of the reaction. The appearance of C-H vibration bands in both spectra also confirmed the presence of the molecule, although the TGA analysis (Figure 2.92) clearly indicated that AcN performed better.

Once the best solvents for the silylation of compound **21** and its subsequent grafting to the surface were determined, the next step in the optimization process was to maximize the amount of organic matter in the sample. Various ratios MSNs:Linker were explored. The output of the different conditions was studied by TGA analysis (Figure 2.94).

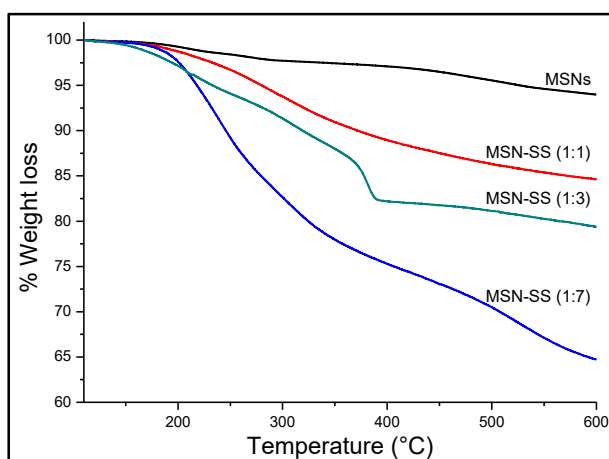


**Figure 2.94.** TGA analysis of the different MSNs:Linker ratios employed for the synthesis of MSN-SS. The best results were obtained for a ratio 1:7, which led to increase of *ca.* 24% of weight loss.

The ratios 1:1 and 1:3 led to an increase of *ca.* 7.5% and *ca.* 10% in the weight loss, respectively. The best results were obtained for the ratio 1:7, which enabled to incorporate *ca.* 24% of additional organic matter in the sample.

Once the MSNs:Linker ratio was optimized (1:7), MSN-SS was partially PEGylated to improve its colloidal stability and endow it with stealth properties. A PEG chain of 3,500 g/mol was employed. MSN-SS-PEG was synthesized introducing a PEG chain *via* thiol exchange with the grafted compound **21**. The overall success of the different functionalization steps was evaluated different characterization techniques. The efficiency of the coupling was initially determined through TGA analysis (Figure 2.95).

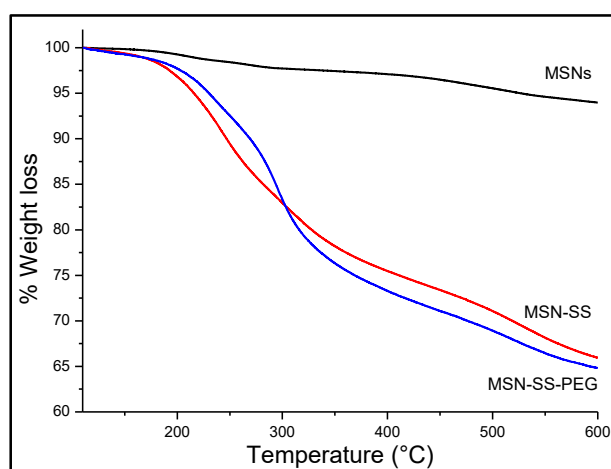


**Figure 2.95.** TGA analysis of the MSNs, MSN-SS and MSN-SS-PEG. The grafting of the linker led to 24% of additional weight loss. The addition of PEG-SH introduced *ca.* 2.5 % of additional weight loss.

As shown in Figure 2.95, the correct PEGylation was confirmed through the increase of *ca.* 2.5% in the weight loss, compared to MSN-SS. It should be mentioned that the effective grafting of each PEG chain entailed the loss of the pyridyl moiety of compound **21** and, consequently, the exact amount of PEG in MSN-SS-PEG was, indeed, higher than the mentioned 2.5%.

The presence of functional groups characteristic of compound **21** in the particles was evaluated using FTIR spectroscopy (2.96).

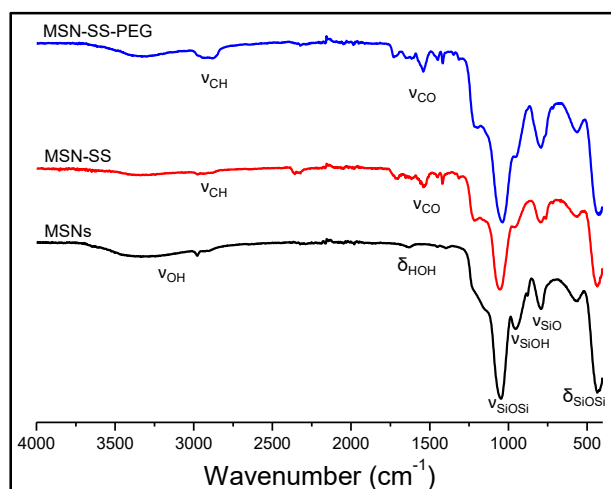


**Figure 2.96.** FTIR spectroscopy of MSN, MSN-SS and MSN-SS-PEG. The vibration bands ascribed to the carbamate of compound **21** further confirmed the correct synthesis of MSN-SS using the ratio 1:7. The higher intensity of the C-H vibration bands confirmed the presence of the PEG chain.

As shown in Figure 2.96, the appearance of vibration bands associated to the carbamate functionality of compound **21** conformed the successful synthesis of MSN-SS. In addition, the spectrum of MSN-SS-PEG showed much deeper C-H vibration bands, which confirmed the correct PEG anchoring.

The effect of the successive functionalization steps on the ordered mesostructure was evaluated through XRD measurements (Figure 2.97).

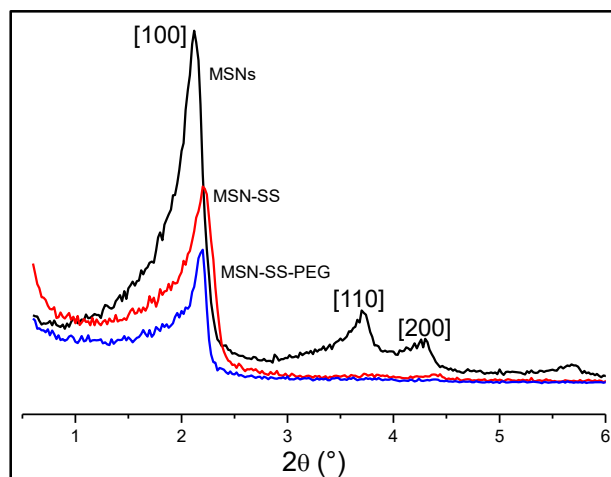


**Figure 2.97.** XRD diffractogram of MSNs, MSN-SS and MSN-SS-PEG. The diffraction pattern of MSNs was preserved after the functionalization steps, indicating that the pore structure was unaffected after both processes.

Overall, the maxima depicted in Figure 2.97 showed the diffraction pattern typical of MCM-41 mesoporous silica materials, confirming that the mesostructure was unaffected by the successive synthetic steps. The lower intensity observed in MSN-SS and MSN-SS-PEG was ascribed to the presence of organic matter around or partially within the

mesopores, leading to slightly lower periodicity, and confirming again the correct grafting.

The effect of the functionalization of MSNs with the redox-responsive self-immolative linker and the PEG chains on the textural properties of the samples was determined with N<sub>2</sub> adsorption (Figure 2.98).

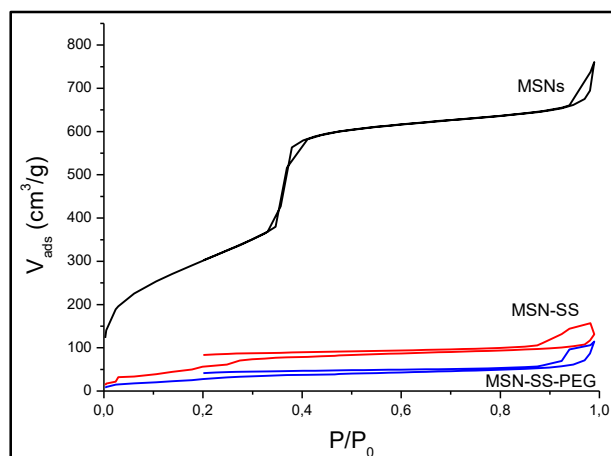


**Figure 2.98.** N<sub>2</sub> adsorption analysis of MSNs, MSN-SS and MSN-SS-PEG. The successive functionalization steps of MSNs induced a marked reduction in the specific surface area, especially after the grafting of the self-immolative linker.

As shown in Figure 2.98, the shape of the type-IV isotherm of MSNs confirmed the presence of cylindrical mesopores.<sup>14,15</sup> The values obtained from the N<sub>2</sub> adsorption analysis are summarized in Table 2.12.

**Table 2.12.** Summary of the values obtained from the N<sub>2</sub> adsorption analysis of MSNs, MSN-SS and MSN-SS-PEG. The significant variations of MSN-SS with respect to MSNs verified the correct functionalization of MSNs with the self-immolative linker.

	MSNs	MSN-SS	MSN-SS-PEG
Surface area (m <sup>2</sup> /g)	1102	259	117
Pore volume (cm <sup>3</sup> /g)	1.02	0.17	0.11
Pore diameter (nm)	3.73	3.27	2.64

The variations in the specific surface area after the successive modifications confirmed the success of the functionalization. The addition of the silylated compound **21** induced a significant reduction of the specific surface area (*ca.* 75%). The changes in the pore volume and pore diameter were ascribed to the presence of molecules within or around the pores, in agreement with the XRD pattern (Figure 2.97).

The morphology of the particles as well as the presence of organic matter on the surface of MSN-SS-PEG was evaluated using TEM microscopy. For that purpose, MSNs and MSN-SS-PEG were stained with phosphotungstic acid prior to observation to observe organic matter (Figure 2.99).

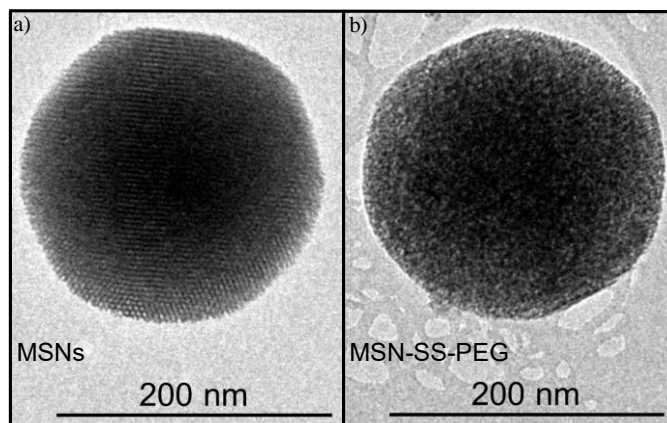


**Figure 2.99.** TEM micrographs of samples stained with phosphotungstic acid. a) MSNs. b) MSN-SS-PEG. The presence of a blurrier surface in MSN-SS-PEG was ascribed to the presence of organic matter in the sample.

The observation of the particles through the TEM microscope confirmed the almost spherical and homogeneous shape of the particles. The blurrier surface observed in MSN-SS-PEG (Figure 2.99b) was ascribed to the presence of organic matter to which phosphotungstic acid bounded.

The colloidal stability and the size distribution of the samples in aqueous solution was analyzed through DLS measurements (Figure 2.100).

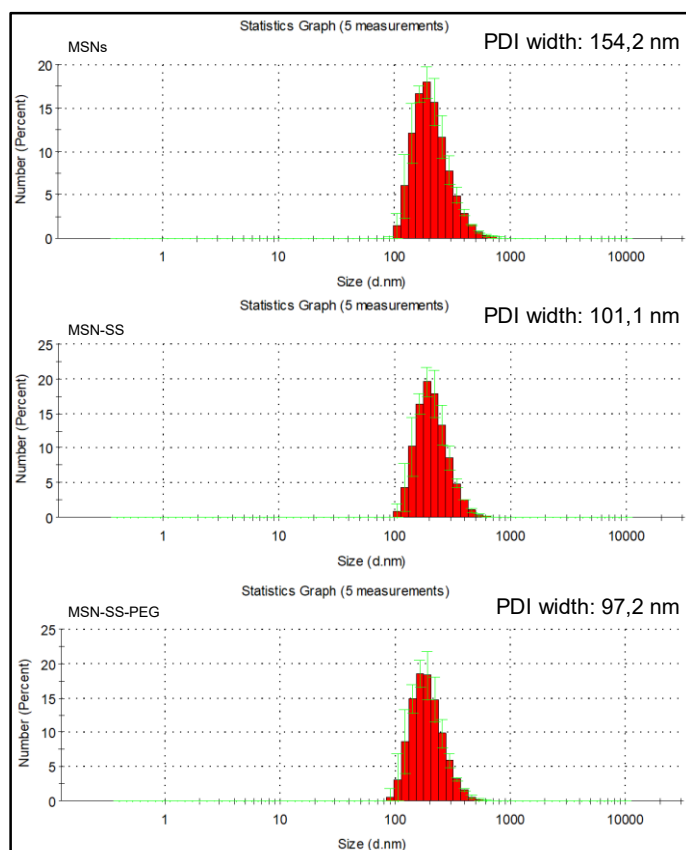


**Figure 2.100.** DLS measurements of MSN, MSN-SS and MSN-SS-PEG (PDI width indicates the width at medium height of the distribution). The size distribution was centered at *ca.* 190-200 nm for all the cases. The successive modifications improved the colloidal stability of the samples, as indicated by the progressively lower value of PDI width.

As observed in Figure 2.100, the distribution was centered at *ca.* 190-200 nm for the three samples synthesized here. The functionalization of MSNs with compound **21** clearly improved the colloidal stability of the samples, as demonstrated by the decrease in the PDI width, which was indicative of better dispersion in the solution. The PEGylation of MSN-SS led to a narrower distribution, which was indicative of improved colloidal stability, confirming its suitability for potential biomedical applications. In addition, the analysis of the changes in the zeta potential further confirmed the correct synthesis of MSN-SS and MSN-SS-PEG (-34.3 mV for MSNs *vs* -30.5 mV for MSN-SS *vs* -24.0 mV for MSN-SS-PEG).

Once all materials were characterized, the next step was to evaluate the redox-responsiveness of here produced materials. For that purpose, the particles were soaked in a solution of DTT (10 mM) in PBS (1x). The sample produced using the ratio 1:3 was initially employed to find out if the self-immolation was actually taking place. The samples were analyzed with elemental analysis (Table 2.14).

**Table 2.14.** Elemental analysis of MSNs, MSN-SS and MSN-SS soaked in DTT. The decrease of all values for MSN-SS (DTT) confirmed the effective cleavage of the disulfide bond.

	C (%)	N (%)	S (%)
MSNs	4.26	0.13	0.03
MSN-SS	11.82	1.73	1.88
MSN-SS (DTT)	6.68	1.32	0.08

The addition of compound **21** increased the amount of organic matter, in agreement with the TGA analysis in Figure 2.95. The presence of sulfur in MSN-SS further confirmed the presence of compound **21**. However, the application of DTT to MSN-SS led to significant changes. The decrease of the amount of carbon and nitrogen meant that, at least, the pyridyl moiety of compound **21** was cleaved. Besides, the sample treated with the redox agent contained negligible amount of sulfur, which would account for the self-immolation process actually taking place through cyclization.

In view of a subsequent release experiment, the sample produced using the ratio 1:7 was also subjected to a redox stimulus. In this case the result was evaluated by FTIR spectroscopy (Figure 2.101).

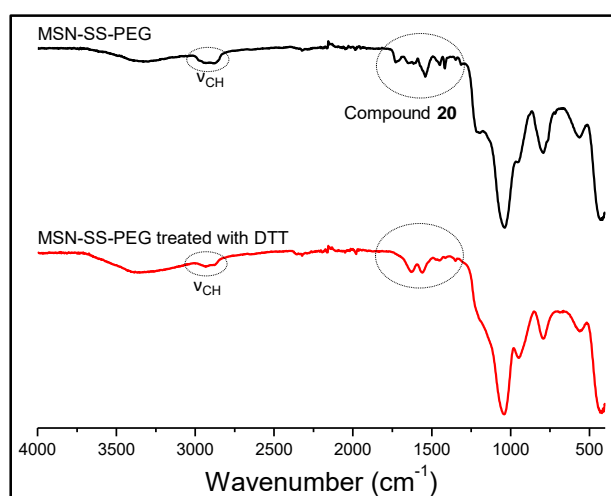


**Figure 2.101.** FTIR spectroscopy of MSN-SS-PEG before and after the exposure to DTT. The application of a redox stimulus led to the disappearance of the vibration bands ascribed to compound **21** and the decrease of the intensity of the C-H vibration bands.

The application of DTT to MSN-SS-PEG led to appreciable changes in the FTIR spectra of the samples (Figure 2.101). The redox-responsiveness of the carrier was confirmed through the disappearance of the vibration bands ascribed to the redox-responsive linker. The decrease of the intensity of C-H vibration bands was ascribed to the cleavage of the PEG chains and the loss of compound 21, in agreement with Table 2.14.

#### 2.6.3.4. Preliminary Release Experiments

The effectiveness of compound 21 to delay the payload release from the mesopores was evaluated loading the PEGylated particles with Ru and performing an *in vial* release experiment using PBS (1x). Two MSNs:Linker ratios were explored, namely 1:3 and 1:7, to evaluate the influence of the amount grafted linker (Figure 2.102).

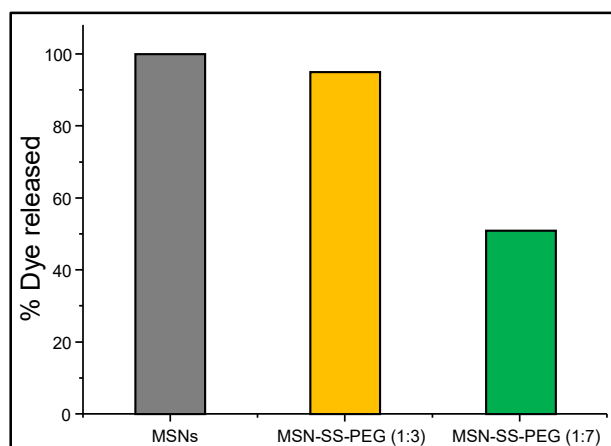


**Figure 2.102.** % Dye released in PBS (1x) at 24 hours for MSNs, MSN-SS-PEG (1:3) and MSN-SS-PEG (1:7). The experiment showed that the ratio 1:7 could hamper the release by *ca.* 50%, compared to the ratio 1:3.

As shown in Figure 2.102, the ratio 1:3 was ineffective in hampering the cargo release and almost 100% of dye was released within 24 hours. The results were much promising when using the ratio 1:7. This condition released *ca.* 50% less amount of dye than the former ratio, indicating a more effective sealing of the mesopores and, consequently, delaying premature drug release.

The next step was to evaluate whether the drug release could be triggered by a redox stimulus. For that purpose, MSN-SS-PEG produced using a ratio 1:7 was loaded with Ru and a release experiment using a 10 mM DTT solution in PBS (1x) was employed as redox stimulus. A control group with just PBS (1x) was also included (Figure 2.103).



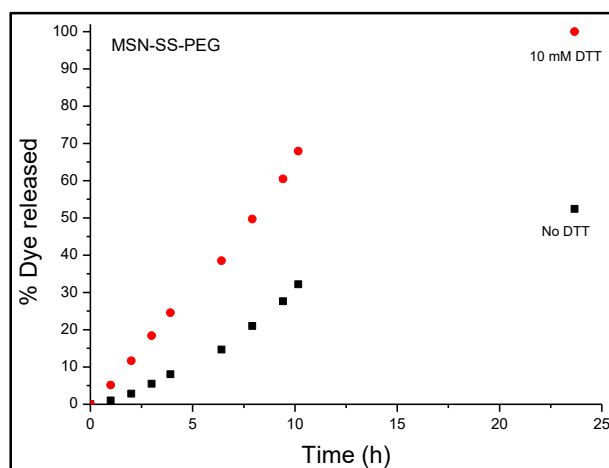


**Figure 2.103.** Release experiment from MSN-SS-PEG using a 10 mM solution of DTT in PBS (1x) (in red) or PBS (1x) as control (in black). The group containing the DTT released more dye, demonstrating that the self-immolative linker could hamper the payload release.

As shown in Figure 2.103, the group receiving the 10 mM DTT solution released *ca.* 50% more dye than the control group after 24 hours, demonstrating that compound **21** could act as a diffusion barrier to delay premature release in absence of a redox stimulus. After 24 hours, the PBS solution of the control group was replaced by the 10 mM DTT solution and the particles were incubated for 6 further hours to provide additional evidence of the redox-responsiveness (Figure 2.104).

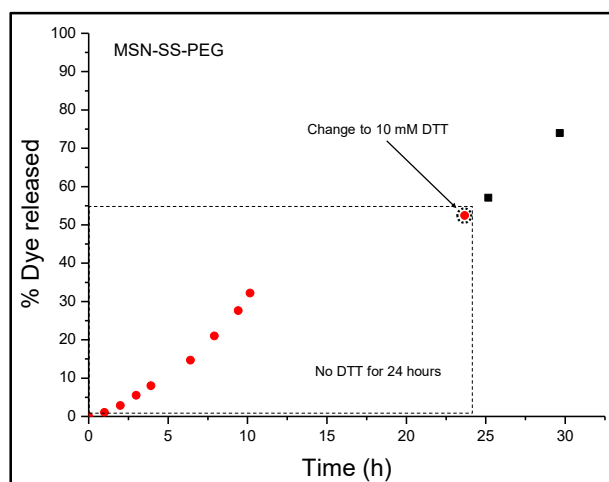


**Figure 2.104.** Release experiment from MSN-SS-PEG initially using a control solution (in red) and changing it to a 10 mM solution of DTT in PBS (1x) after 24 hours (in black). The addition of the redox stimulus led to an increase in the dye release.

As observed in Figure 2.104, the control group only released *ca.* 19% of the dye from 10 to 24 hours of experiment (14 hours). However, the addition of DTT led to the release of *ca.* 21% of the dye in just 6 hours (in black). This enhanced release confirmed that the DTT solution triggered the drug release as a consequence of the cleavage of the disulfide bond of compound **21** and the subsequent self-immolation.

#### 2.6.4. Conclusions

The objective of this work was to develop a stimuli-responsive nanocarrier with potential applicability in cancer therapy. The much higher concentration of glutathione in the cytoplasm, compared to the extracellular fluids, was selected as stimulus to trigger the drug release. In this sense, a carrier based on mesoporous silica nanoparticles and a redox-responsive self-immolative molecule was devised. This molecule would act, at the same time, as diffusion barrier and as linker for further functionalization.

The self-immolative molecule was engineered so that it could undergo cyclization and subsequent self-immolation upon application of a redox stimulus. The functionalization of MSNs with this compound involved 2 different optimizations. First, the silylation of this compound was explored and it was concluded that DCM was provided the best results. Then, the efficiency of the grafting to MSNs was evaluated in different solvents and it was shown that a mixture of DCM and AcN yielded the highest amount of grafted linker. Once the best solvents were determined, the next step was to maximize the amount of grafted linker so that premature release could be hampered. Different MSNs:Linker ratios were explored and it was concluded that a ratio 1:7 led to the greatest degree of functionalization. Finally, the particles were PEGylated and it was observed that their colloidal stability increased as a consequence of the presence of this polymer.

The redox-responsiveness of the particles was evaluated for MSN-SS and MSN-SS-PEG using DTT as redox stimulus. The FTIR spectrum showed that the vibration bands ascribed to the linker disappeared after the application of DTT. In addition, the elemental analysis showed that *ca.* 100% of sulfur disappeared from the sample after applying the stimulus, unequivocally demonstrating that the linker underwent cyclization and subsequent self-immolation.

The PEGylated particles were loaded with a model fluorophore and soaked in PBS (1x) to find out if the self-immolative molecule could hamper premature drug release. Different ratios were explored and it was shown that the ratio 1:7 released 50% less dye than the other conditions. After that, a preliminary release experiment using DTT as redox stimulus was carried out and it was shown that the triggered group released *ca.* 50% after 24 hours. Besides, the medium of the control group was replaced by the DTT solution after 24 hours and significant drug release could be observed in a short period of time, showing further confirmation of the redox-responsiveness of the system.

## References

- (1) Traverso, N.; Ricciarelli, R.; Nitti, M.; Marengo, B.; Furfaro, A. L.; Pronzato, M. A.; Marinari, U. M.; Domenicotti, C. Role of Glutathione in Cancer Progression and Chemoresistance. *Oxid. Med. Cell. Longev.* **2013**, *2013*, 972913.
- (2) Guo, X.; Cheng, Y.; Zhao, X.; Luo, Y.; Chen, J.; Yuan, W. E. Advances in Redox-Responsive Drug Delivery Systems of Tumor Microenvironment. *J. Nanobiotechnology* **2018**, *16*, 74-86.
- (3) Sun, H.; Guo, B.; Cheng, R.; Meng, F.; Liu, H.; Zhong, Z. Biodegradable Micelles with Sheddable Poly(Ethylene Glycol) Shells for Triggered Intracellular Release of Doxorubicin. *Biomaterials* **2009**, *30*, 6358–6366.
- (4) Kataoka, K.; Harada, A.; Nagasaki, Y. Block Copolymer Micelles for Drug Delivery: Design, Characterization and Biological Significance. *Adv. Drug Deliv. Rev.* **2001**, *47*, 113–131.
- (5) Luo, Z.; Ding, X.; Hu, Y.; Wu, S.; Xiang, Y.; Zeng, Y.; Zhang, B.; Yan, H.; Zhang, H.; Zhu, L.; et al. Engineering a Hollow Nanocontainer Platform with Multifunctional Molecular Machines for Tumor-Targeted Therapy *in vitro* and *in vivo*. *ACS Nano* **2013**, *7*, 10271–10284.
- (6) Zhang, J.; Yuan, Z.-F.; Wang, Y.; Chen, W.-H.; Luo, G.-F.; Cheng, S.-X.; Zhuo, R.-X.; Zhang, X.-Z. Multifunctional Envelope-Type Mesoporous Silica Nanoparticles for Tumor-Triggered Targeting Drug Delivery. *J. Am. Chem. Soc.* **2013**, *135*, 5068–5073.
- (7) Luo, Z.; Cai, K.; Hu, Y.; Zhao, L.; Liu, P.; Duan, L.; Yang, W. Mesoporous Silica Nanoparticles End-Capped with Collagen: Redox-Responsive Nanoreservoirs for Targeted Drug Delivery. *Angew. Chemie Int. Ed.* **2011**, *50*, 640–643.
- (8) Alouane, A.; Saux, T. Le; Schmidt, F.; Jullien, L. Self-Immolative Spacers: Kinetic Aspects, Structure–Property Relationships, and Applications. *Angew. Chemie Int. Ed.* **2015**, *54*, 7492–7509.
- (9) Yang, X.; Shi, X.; Ji, J.; Zhai, G. Development of Redox-Responsive Theranostic Nanoparticles for Near-Infrared Fluorescence Imaging-Guided Photodynamic/Chemotherapy of Tumor. *Drug Deliv.* **2018**, *25*, 780–796.
- (10) Remant, R. B.; Chandrashekar, V.; Cheng, B.; Chen, H.; Peña, M. M. O.; Zhang, J.; Montgomery, J.; Xu, P. Redox Potential Ultrasensitive Nanoparticle for the Targeted Delivery of Camptothecin to HER2-Positive Cancer Cells. *Mol. Pharm.* **2014**, *11*, 1897–1905.
- (11) Baeza, A.; Guisasola, E.; Torres-Pardo, A.; González-Calbet, J. M.; Melen, G. J.; Ramírez, M.; Vallet-Regí, M. Hybrid Enzyme-Polymeric Capsules/Mesoporous Silica Nanodevice for *in Situ* Cytotoxic Agent Generation. *Adv. Funct. Mater.* **2014**, *24*, 4625–4633.
- (12) Horikawa, R.; Sunayama, H.; Kitayama, Y.; Takano, E.; Takeuchi, T. A Programmable Signaling Molecular Recognition Nanocavity Prepared by Molecular Imprinting and Post-Imprinting Modifications. *Angew. Chemie Int. Ed.* **2016**, *128*, 13217–13221.

- (13) Artaki, I.; Zerda, T. W.; Jonas, J. Solvent Effects on the Condensation Stage of the Sol-Gel Process. *J. Non. Cryst. Solids* **1986**, *81*, 381–395.
- (14) Kruk, M.; Jaroniec, M.; Sayari, A. Relations between Pore Structure Parameters and Their Implications for Characterization of MCM-41 Using Gas Adsorption and X-Ray Diffraction. *Chem. Mater.* **1999**, *11*, 492–500.
- (15) Kruk, M.; Jaroniec, M.; Kim, J. M.; Ryong Ryoo. Characterization of Highly Ordered MCM-41 Silicas Using X-Ray Diffraction and Nitrogen Adsorption. *Langmuir* **1999**, *15*, 5279–5284.



## Chapter 3

# Overcoming Biological Barriers

*El científico encuentra su recompensa en lo que Henri Poincaré llama el placer de la comprensión, y no en las posibilidades de aplicación que cualquier descubrimiento pueda conllevar.*

*Albert Einstein*



## 3.1. Introduction

### 3.1.1. Aims

One of the major concerns of current chemotherapeutics is their lack of selectivity for cancer tissues. A smart approximation to reduce the nonspecific distribution of the drugs could be the design of stimuli-responsive nanoparticles able to achieve on-demand drug release, as it has been thoroughly discussed in Chapter 2 of this thesis.

Ideally, drug-loaded nanocarriers should preferentially accumulate in the tumor tissues and, once there, their payload should be selectively delivered only to cancer cells. However, nanoparticles may have to face several biological barriers when administered to the bloodstream, including (1) opsonization and subsequent clearance of the particles by the macrophages, (2) nonspecific particle distribution throughout the organism, *i.e.*, lack of selectivity towards cancer tissues, (3) a dense collagen tumoral matrix with high intracellular pressure that hampers nanoparticle penetration into the tumoral mass, (4) lack of selectivity towards cancer cells over normal cells and (5) endo-lysosomal entrapment so that the effective payload release may be compromised.

The implementation of a nanomedicine able to effectively overcome all the above-mentioned biological barriers with a unique nanocarrier remains a chimera. In this sense, the overall objective of this chapter was to engineer a system based on mesoporous silica nanoparticles which were able to address some of these biological barriers, namely (1) the lack of selectivity towards cancer tissues, (2) the lack of selectivity towards cancer cells and (3) the entrapment of the particles within the endo-lysosomal pathway.

In this sense, the **first objective** of this chapter was to engineer a smart solution to tackle the lack of particle selectivity towards cancer cells over normal cells. In this way, the drug-loaded particles here designed would be preferentially internalized by tumoral cells and the cytotoxics would only affect malignant cells.

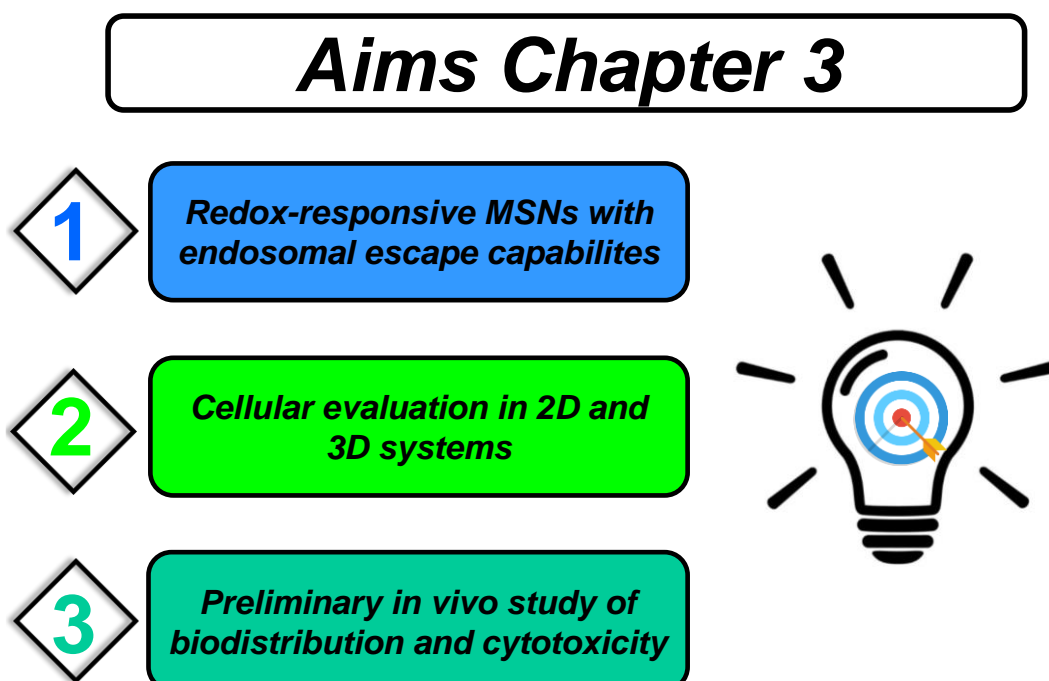
The endo-lysosomal entrapment of the particles constitutes a serious drawback. These subcellular organelles, which are acid in nature, may degrade the cargo or even lead to multidrug resistance. In this sense, the **second objective** of this chapter was to design a solution able to avoid the particle sequestration in the endo-lysosomal pathway. The **first** and **second** objectives were addressed *via* the design of a polyvalent peptidic molecule, whose combination with MSNs was thoroughly studied in different biological scenarios



as a result of a research stay carried out during this PhD in the *Institute for Integrated Cell-Material Sciences (iCeMS)* at Kyoto University, Japan.

The **third objective** of this chapter was to evaluate whether those engineered particles could preferentially accumulate in the tumoral mass rather than being distributed throughout the organism. This last objective was accomplished using a standardized pseudo-*in vivo* model in the *iCeMS*.

In summary, this chapter will provide an introduction to the state-of-the-art on the accumulation of nanoparticles in tumors, their selective uptake by cancer cells and the strategies to bypass endosomal entrapment of these nanomaterials. Then, the methodology and results derived from the use of a targeted stimuli-responsive material against tumoral cells will be thoroughly discussed.



**Scheme 3.1.** Schematic representation of the aims of Chapter 3.

### 3.1.2. Passive and Active Targeting of Solid Tumor Tissues

The encapsulation of cytotoxic compounds in stimuli-responsive nanoparticles constitutes a smart approximation to achieve on-demand drug delivery under certain conditions. Yet achieving preferential cellular internalization in cancer cells is of major importance, the specific accumulation of the particles in the tumoral tissues still needs to be addressed. In other words, before trying to maximize the cellular uptake, it is more important the delivery of as much particles as possible to the tumoral mass. In this sense, passive and active targeting strategies to tumor tissues have been explored, constituting promising tools for the effective delivery of cytotoxics to the tumoral cells.

#### 3.1.2.1. Passive Accumulation in Solid Tumors: The EPR effect.

In 1984, Maeda and coworkers were investigating the biological activity of a polymer-drug conjugate when they discovered in tumor-bearing mice that the conjugate showed much higher accumulation in the tumors than the free drug.<sup>1</sup> Based on that discovery, they labelled proteins of different molecular weights (from 12 to 160 kDa) and observed that only those above 68 kDa were retained in the tumor for longer periods of time (less than 1 hour vs more than 30 hours).<sup>2</sup> Later experiments set the lower limit in 40 kDa.<sup>3</sup> They proposed that this tumor-tropic behavior was a result of the hypervascularity, the enhanced permeability and the poor lymphatic drainage found in many tumors, and called it the *Enhanced Permeability and Retention effect* (EPR effect).

Subsequent research demonstrated that most solid tumors exhibit enhanced vascular permeability to ensure enough supply of nutrients and oxygen for their rapid growth. The rapid growth of these vessels is known as tumor angiogenesis, and is mediated by the secretion of vascular endothelial growth factors by the tumors. Owing to this uncontrolled growth, the newly formed tumor blood vessels present an abnormal architecture, including wide fenestrations (200-2000 nm endothelial cell-cell gaps), irregular vascular alignment or lack of smooth muscle layer, among others. As a result, molecules larger than 40 kDa leak out from them and accumulate in the extravascular tissues. On the contrary, healthy tissues do not show this abnormal development and no accumulation is observed, thus creating a differential selectivity for cancer tissues.<sup>4</sup> In addition, unlike normal tissues where the extracellular fluid is constantly removed, tumors present defective lymphatic drainage and the accumulated macromolecules tend to remain in the tumoral mass for longer periods of time (Figure 3.1).<sup>5</sup>

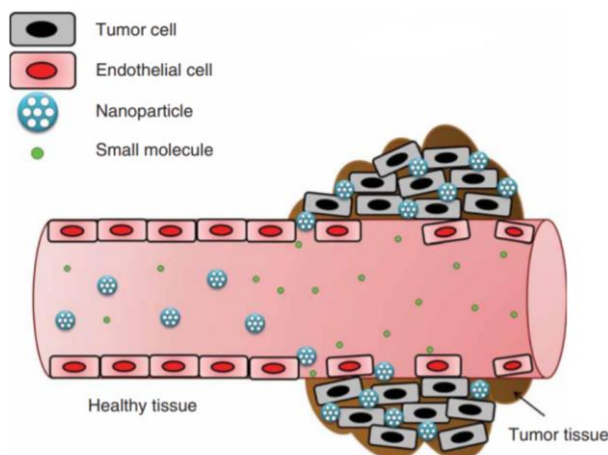


**Figure 3.1.** Schematic representation of the EPR effect. Nanoparticles accumulate in the tumor due to the fenestrations in the blood vessels, and remain there due to the poor lymphatic drainage. Reproduced from Ref 6 with permission of Taylor & Francis Online.

These two phenomena are responsible for the effective accumulation of nanoparticles in tumors and provide a first targeting approximation. This effect is highly marked in several animal models although its magnitude in human patients highly depends on the particularities of the patient and the tumor.<sup>7</sup> However, the EPR effect do constitute a reliable approximation as some commercialized nanomedicines rely on this principle.<sup>8</sup>

### 3.1.2.2. Active Accumulation in Solid Tumors

The non-universality of the EPR effect has fueled the exploration of alternative strategies to enhance the accumulation of nanoparticles in the tumoral mass. Examples of this active vectorization to tumor tissues include the use of tumor-tropic cyclic peptides and tumor-tropic cells, among others.

The use of cyclic peptides has been observed to promote the preferential accumulation of nanoparticles in tumors. In addition, it has been shown that nanoparticles bearing this peptide are able to internalize deeper in the tumoral mass. This phenomenon is based on the existence of an endocytic transcytosis pathway in tumor endothelial cells that can be activated by tumor-penetrating iRGD-like cyclic peptides. In particular, the iRGD peptide consists of the integrin-binding RGD motif and the neuropilin-1 binding motif. First, the RGD motif binds  $\alpha\beta$  integrin present in the membrane of tumor endothelial cells. Then, there is a proteolytic cleavage and the neuropilin-1 motif (previously inactive) is exposed, interacting with the NRP-1 receptor and triggering a trans-tissue transport pathway. The RGD motif can be tuned so that other receptors can be exploited. Interestingly, this preferential pathway exists regardless of whether the peptide is covalently bonded to the surface or co-administered with the particles.<sup>9,10</sup>

On the other hand, there are some types of cells with migratory properties, including different bacteria and mesenchymal stem cells, among others.<sup>11,12</sup> Particle-carrying bacteria are interesting because they can be specifically selected so that they move towards hypoxic areas, as tumors are, enhancing both the extravasation and the penetration through deeper areas of the tumor.<sup>13,14</sup> The main advantage of mesenchymal stems cells over bacteria is their low or non-immune response. These type of cells are interesting because they can carry drug-loaded nanoparticles. In this way, it is possible to transport nanoparticles to the tumor without caring about their undesired interactions with the organism and only triggering the drug release in the tumor.<sup>15-18</sup>

### **3.1.3. Journey Inside the Cells**

Once the nanoparticles have reached the tumoral tissues, whether through active or passive strategies, the next step should be to maximize their cellular uptake and achieve effective intracellular drug release. In this sense, cellular internalization of nanoparticles includes complicated machinery that can be affected by different situations, as described below.

#### **3.1.3.1. Cellular Uptake Mechanisms**

The cell membrane is mostly permeable to small and non-polar molecules, which enter the cells through passive mechanisms. In contrast, polar or charged biomolecules that cannot pass through the hydrophobic membrane are internalized by means of active transport processes, also known as endocytosis. This general process can be classified into phagocytosis and pinocytosis (Figure 3.2). In addition, the latter can be divided into (1) clathrin-mediated endocytosis, (2) caveolae-mediated endocytosis, (3) clathrin- and caveolae-independent endocytosis and (4) macropinocytosis.<sup>19</sup>

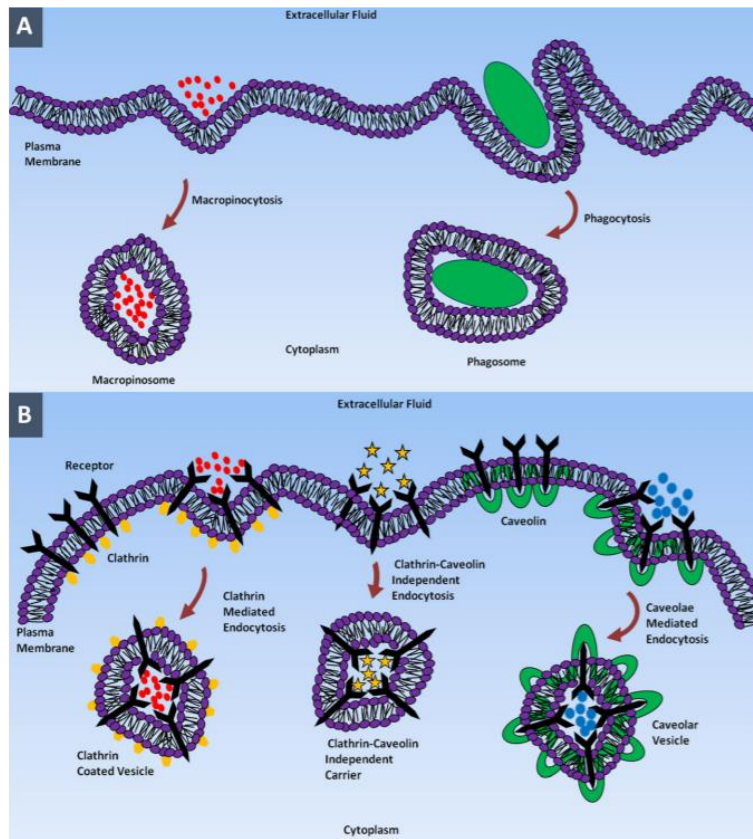


**Figure 3.2.** Different endocytic pathways for nanoparticle uptake. a) Phagocytosis (inherent to macrophages and triggers immune response against foreign materials) and Macropinocytosis (form of endocytosis in which a larger of fluid is internalized in a vesicle) (b) Clathrin-mediated endocytosis and caveolae-mediated endocytosis (internalization mechanism found in cells having clathrin and caveolin proteins in the membrane, respectively); and clathrin and caveolae independent endocytosis (internalization mechanism found in cells lacking in clathrin and caveolin proteins). Reproduced from Ref 19 with permission of Springer.

❖ *Nanoparticle Uptake by Macrophages*

The first biological barrier that nanoparticles have to face when administered *in vivo* is their potential clearance from the bloodstream, which is accomplished by the macrophages.<sup>20</sup> In this way, large materials can be internalized by these cells and removed from the bloodstream. To do so, a membrane-bound vesicle is formed around the materials, forming a phagosome that finally fuses with the lysosomes for cargo degradation.

Nanoparticle clearance is mediated by the phenomenon of opsonization, which consists in the deposition of proteins on the surface of the particles, leading to the formation of a protein corona. The protein corona provides a biological identity to the particles that the immune system can detect, triggering their removal from the bloodstream.<sup>21</sup> Examples of strategies to minimize opsonization include the PEGylation of the nanocarriers or the use of zwitterionic moieties. PEGylation reduces the amount of

proteins adsorbed on the surface by creating a hydration layer around the particles.<sup>22</sup> Zwitterionic surfaces reduce the protein corona creating a neutral surface to which proteins are less prone to attach.<sup>23,24</sup>

❖ *Nanoparticle Uptake by the Rest of Cells*

Cells internalize plasma membrane components and nutrients *via* clathrin-mediated endocytosis. It can take place either *via* receptor-specific uptake (formation of a ligand-receptor complex) or by non-specific adsorptive uptake (non-specific hydrophobic or electrostatic interactions that trigger the uptake). There is a formation of clathrin-coated vesicles that normally end up in the endo-lysosomal pathway and can be exploited for the design of pH-responsive nanocarriers.<sup>19,25</sup> Caveolae-mediated endocytosis is found in epithelial and non-epithelial (adipocytes, smooth muscle, etc) cells. It is characterized by the formation of flask-shaped membrane invaginations composed of caveolin proteins, called caveolae. These vesicles fuse with a cell compartment called caveosome and are able to bypass the endo-lysosomal pathway, preventing degradation. This process can mediate transcytosis processes through the endothelial tumor cells, enhancing nanocarrier penetration in the tumor.<sup>19,25</sup> Clathrin- and caveolae-independent endocytosis occur in cells deprived of clathrin and caveolin proteins. It is the pathway used by growth hormones, extracellular fluid or some proteins, among others.<sup>19</sup> Macropinocytosis, which is found in all cells except brain microvessel endothelial cells, is the mechanism by which cells internalize high amounts of fluids. It is used for the uptake of micron-sized nanoparticles that are not internalized by other mechanisms.<sup>19</sup>

### 3.1.3.2. Factors Affecting the Fate of Nanoparticles

Nanoparticles are engineered to maximize their half-life in the bloodstream, enhance their extravasation in the tumors and achieve as much cellular internalization as possible. It is generally accepted that the size of a nanoparticle must be at least 10 nm in diameter to avoid renal clearance and not bigger than 400 nm, so it can diffuse properly through the tumor interstitium. The best results in terms of cellular uptake are obtained for nanoparticles smaller than 100 nm. However, the appropriate size to balance enhanced circulation time, extravasation and cellular uptake is controversial. In this sense, some authors propose a size of *ca.* 300 nm<sup>26</sup> while others propose a size of *ca.* 100 nm or below.<sup>27</sup>

In addition to size, the shape also affects both the biodistribution and the interaction with cells. It has been shown that rod-like nanoparticles remain longer in the bloodstream

at the same time that are more prone to diverge closer to the blood vessel walls, increasing extravasation, compared to their spherical counterparts.<sup>28,29</sup> However, there is growing controversy regarding whether non-spherical particles show better cellular internalization than their spherical counterparts.<sup>25,30</sup>

Nanoparticles primarily interact with the organism through their surface and, consequently, the surface charge is of major importance. Since the cell membrane is negatively charged, positive nanoparticles show better uptake. However, it has also been shown that positively charged nanoparticles are more prone to undergo opsonization, showing lower circulation time than neutral or negative nanocarriers.<sup>31,32</sup> In addition, there is evidence that cationic nanoparticles tend to accumulate around the tumor mass, while negatively charged particles penetrate deeper in the tumoral mass due to the repulsion between their surface and the negative cell membrane.<sup>33</sup>

### 3.1.3.3. Enhanced Cellular Uptake of Mesoporous Silica Nanoparticles: Active Targeting of Cancer Cells

The size, shape and surface charge affect nanoparticle internalization in cancer cells. In addition, these nanocarriers can be engineered so they selectively recognize cancer cells. In particular, MSNs have been extensively decorated with chemical moieties able to selectively bind receptors that are only overexpressed in cancer cells (Figure 3.3). The targeted nanoparticles interact with the tumoral cells through the formation of ligand-receptor complexes that facilitate their uptake. In consequence, this approximation provides a powerful tool to distinguish between healthy and tumoral cells, improving the efficiency of the delivery.<sup>6,34,35</sup>

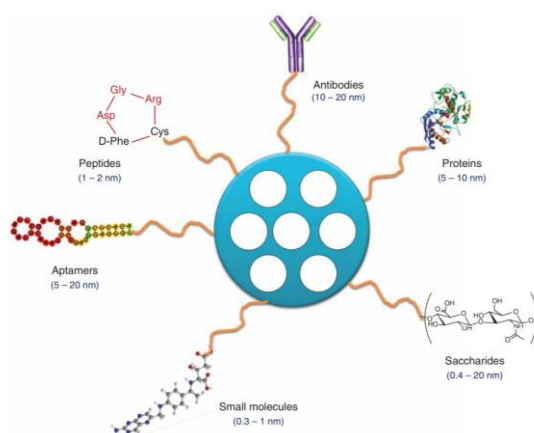


**Figure 3.3.** Most employed targeting agents in combination with MSNs. Clockwise: Antibodies, proteins, saccharides, small molecules, aptamers and peptides. Nanoparticles bearing these agents are able to internalize in cancer cells through the specific interaction with their complementary and overexpressed. Reproduced from Ref 6 with permission of Taylor & Francis Online.

As shown in Figure 3.3, some examples of targeting agents are antibodies, proteins, saccharides, small molecules, aptamers and peptides. Antibodies can target specific antigens present on the membrane of many tumoral cells with high specificity. For instance, the anti-EGFR (EGFR: epidermal growth factor receptor) has been used to target nanoparticles to this receptor, because it is overexpressed in many solid tumors.<sup>36,37</sup> Their high production cost has fueled the research of alternative strategies. In this sense, the use of peptides has attracted much attention because of the ease of their production. In fact, they can be synthesized from well-established standard techniques in small laboratories.<sup>38,39</sup> Some examples are the surface modification with RGD (binds overexpressed  $\alpha\beta$ -integrin in endothelial and many cancer cells),<sup>40–42</sup> NAPamide (binds overexpressed melanocortin-1 receptor in melanoma)<sup>43</sup> or more complex cell-penetrating peptides.<sup>44,45</sup> Aptamers are single-stranded RNA, DNA or unnatural oligonucleotides that can adopt tertiary conformations able to recognize various types of targets with high affinity. Aptamers show comparable specificity compared to antibodies. In addition, they are non-immunogenic and easy to synthesize. Examples are the modification of nanoparticles with the thrombin-binding aptamer<sup>46</sup> or the AS1411,<sup>47</sup> which indeed was the first aptamer to enter clinical trials.

Proteins have also been used as targeting agents. For instance, transferrin mediates iron cellular uptake, and its receptor is highly overexpressed in cancer cells. For such reason, the surface modification of nanoparticles with this protein enhances their cellular internalization in tumoral cells.<sup>48,49</sup> Another example is concanavalin A, which can interact with the overexpressed sialic acid on some tumor cells to enhance the uptake, at the same time that induces cytotoxicity.<sup>50</sup> The use of carbohydrates as targeting agents has also been widely explored owing to their specific recognition by lectin proteins on the cell membrane. Examples are the coating of nanoparticles with lactobionic acid<sup>51</sup> or hyaluronic acid.<sup>52</sup>

The use of small molecules is particularly interesting because many of them are commercially available or can be relatively easily synthesized. For instance, cancer cells require high amounts of vitamins and, as a consequence, present many overexpressed receptors. Widely used examples are folic acid (vitamin B9) or biotin (vitamin H), whose conjugation with nanoparticles enhances their cellular uptake.<sup>53–57</sup> It is also possible to design small synthetic molecules with high affinity for a very specific receptor. For



example, the norepinephrine transporter is highly overexpressed in neuroblastoma cells and can be specifically targeted using benzylguanidine analogues.<sup>58,59</sup>

### 3.1.4. Towards Efficient Cytosolic Delivery: Endosomal Escape

In general, nanoparticles are internalized through the endocytic pathway. In this way, nanocarriers are internalized into an endocytic vesicle that fuses into the early endosomal compartment and matures later into a late endosome, finally leading to the accumulation in the lysosome (Figure 3.4). This process involves the progressive acidification of the different compartments for proteolysis and recycling of unneeded cellular components. In particular, pH drops from 6.5 (early endosomes) to 6 (late endosomes) and finally 4.5-5 (lysosomes).<sup>60-62</sup>

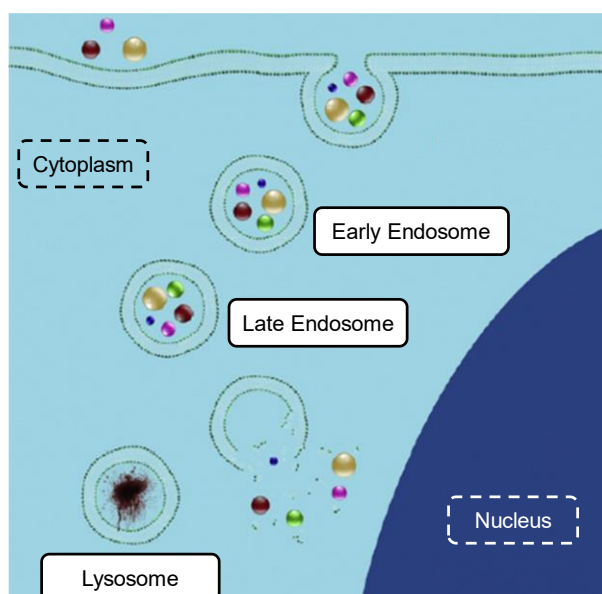


**Figure 3.4.** The endo-lysosomal pathway involves the internalization of the biological in a vesicle that fuse and matures into the early and late endosomes respectively. The content can be delivered in the cytoplasm or degraded in the lysosomes if the endosomal entrapment occurs. Adapted from Ref 63 with permission of Elsevier.

Achieving the endosomal escape before reaching the lysosomes is a major issue since the acid pH may degrade the therapeutics entrapped within this compartment, reducing the efficacy of the treatment.<sup>64</sup> In addition, it has been shown that the accumulation of anticancer drugs which are hydrophobic weak bases in the lysosomes may trigger a mechanism of multidrug resistance, leading to the exocytosis of these drugs.<sup>65</sup> Furthermore, there is growing evidence that endo-lysosomal entrapment may reduce transcytosis events, leading to poor distribution of nanoparticles in the target tissue.<sup>66-68</sup>

The approximations that have been explored so far to overcome endosomal entrapment can be classified into viral and nonviral. The most efficient approximation for the delivery of nucleic acids is the use of virus, although there are concerns about their immunogenicity that limit their use. For such reason, research on nonviral vectors has attracted growing attention. Not all these approximations are based on the same principles and several mechanisms for the endosomal escape have been proposed (Figure 3.5).<sup>60</sup>

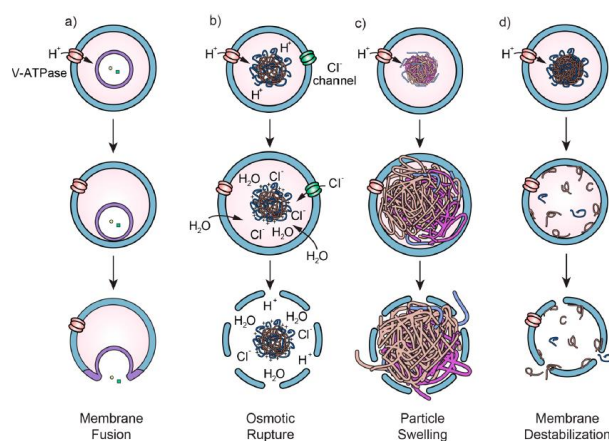


**Figure 3.5.** Endosomal escape mechanisms. a) Membrane fusion between the nanoparticle and the endosomal membrane induces content delivery in the cytosol. b) Entrapment of species with buffering capacity induces an influx of chloride ions, together with fluid that finally disrupt the membrane. c) The swelling of pH-responsive nanogels leads to the destabilization of the membrane due to the increased mechanical strain. d) pH-mediated disassembly of nanoparticles may lead to destabilization of the membrane. Reproduced from Ref 60 with permission of ACS.

Some viruses and liposomal systems induce the endosomal escape through the membrane fusion mechanism, leading to the cytosolic delivery of the content.<sup>69,70</sup> In addition, it is possible to engineer the nanocarriers so that fusion only takes place with the endo-lysosomal membrane, as a consequence of the acid pH, and not with other targets.<sup>71,72</sup> When the entrapped nanoparticles contain protonable functionalities, the endosomal escape can be mediated by the proton sponge effect. The presence of species with buffering capacity induces an influx of protons and chloride counterions and water, increasing the pressure and eventually lysing the membrane.<sup>60,73</sup> It is also possible to design nanoparticles able to swell upon changes in pH and disrupt the membrane. The mechanism is still not completely clear but the disruption is thought to be mediated by the mechanical strain created by the swelling.<sup>74,75</sup> In fact, the contribution of this mechanism along with the proton sponge effect has also been proposed.<sup>76</sup> An additional mechanism of endosomal escape is through membrane destabilization. In this way, polymer nanoparticles are designed so that they undergo disassembling below physiological pH, and that mediates membrane destabilization. Nanoparticles can be

engineered so that the disassembling only takes places at endo-lysosomal pH, avoiding disruption of the cell membrane, which would lead to cytotoxicity.<sup>60</sup>

In conclusion, the *magic bullet*, i.e., a nanomedicine able (1) to significantly accumulate in the tumor tissues, (2) to be preferentially internalized by cancer cells and (3) to effectively deliver its payload within the cells still constitutes a chimera. Nonetheless, there are several promising strategies that should be implemented in every upcoming cutting-edge nanomedicine to overcome those issues and facilitate the clinic translation.

Examples of these strategies are (1) the passive accumulation of nanoparticles *via* EPR effect, which constitutes a reliable approximation in EPR effect-positive patients to selectively address the particles to tumors, (2) the use of readily available small molecules able to specifically recognize cancer cells over normal cells and (3) the implementation of different approximations to bypass the endosomal entrapment of nanoparticles and achieve effective intracellular drug release. In this sense, the main objective of the next section will be to develop a nanocarrier able to merge all these approximations in a single polyvalent nanocarrier with potential applicability in cancer therapy.

## References

- (1) Maeda, H.; Matsumoto, T.; Konno, T.; Iwai, K.; Ueda, M. Tailor-Making of Protein Drugs by Polymer Conjugation for Tumor Targeting: A Brief Review on Smancs. *J. Protein Chem.* **1984**, *3*, 181–193.
- (2) Matsumura, Y.; Maeda, H. A New Concept for Macromolecular Therapeutics in Cancer Chemotherapy: Mechanism of Tumoritropic Accumulation of Proteins and the Antitumor Agent Smancs. *Cancer Res.* **1986**, *46*, 6387–6392.
- (3) Maeda, H.; Wu, J.; Sawa, T.; Matsumura, Y.; Hori, K. Tumor Vascular Permeability and the EPR Effect in Macromolecular Therapeutics: A Review. *J. Control. Release* **2000**, *65*, 271–284.
- (4) Fang, J.; Nakamura, H.; Maeda, H. The EPR Effect: Unique Features of Tumor Blood Vessels for Drug Delivery, Factors Involved, and Limitations and Augmentation of the Effect. *Adv. Drug Deliv. Rev.* **2011**, *63*, 136–151.
- (5) Maeda, H.; Nakamura, H.; Fang, J. The EPR Effect for Macromolecular Drug Delivery to Solid Tumors: Improvement of Tumor Uptake, Lowering of Systemic Toxicity, and Distinct Tumor Imaging *in vivo*. *Adv. Drug Deliv. Rev.* **2013**, *65*, 71–79.
- (6) Baeza, A.; Colilla, M.; Vallet-Regí, M. Advances in Mesoporous Silica Nanoparticles for Targeted Stimuli-Responsive Drug Delivery. *Expert Opin. Drug Deliv.* **2015**, *12*, 319–337.
- (7) Natfji, A. A.; Ravishankar, D.; Osborn, H. M. I.; Greco, F. Parameters Affecting the Enhanced Permeability and Retention Effect: The Need for Patient Selection. *J. Pharm. Sci.* **2017**, *106*, 3179–3187.
- (8) Grodzinski, P.; Kircher, M.; Goldberg, M.; Gabizon, A. Integrating Nanotechnology into Cancer Care. *ACS Nano* **2019**, *13*, 7370–7376.
- (9) Liu, X.; Jiang, J.; Ji, Y.; Lu, J.; Chan, R.; Meng, H. Targeted Drug Delivery Using iRGD Peptide for Solid Cancer Treatment. *Mol. Syst. Des. Eng.* **2017**, *2*, 370–379.
- (10) Ruoslahti, E. Tumor Penetrating Peptides for Improved Drug Delivery. *Adv. Drug Deliv. Rev.* **2017**, *110–111*, 3–12.
- (11) Pawelek, J. M.; Low, K. B.; Bermudes, D. Bacteria as Tumour-Targeting Vectors. *Lancet Oncol.* **2003**, *4*, 548–556.
- (12) Li, Z.; Fan, D.; Xiong, D. Mesenchymal Stem Cells as Delivery Vectors for Anti-Tumor Therapy. *Stem cell Investig.* **2015**, *2*, 6.
- (13) Raj, R.; Dan, S. Prospects of Bacteriotherapy with Nanotechnology in Nanoparticledrug Conjugation Approach for Cancer Therapy. *Current Medicinal Chemistry.* **2016**, *23*, 1477–1494.
- (14) Suh, S. B.; Jo, A.; Traore, M. A.; Zhan, Y.; Coutermarsh-Ott, S. L.; Ringel-Scaia, V. M.; Allen, I. C.; Davis, R. M.; Behkam, B. Nanoscale Bacteria-Enabled Autonomous Drug Delivery System (NanoBEADS) Enhances Intratumoral Transport of Nanomedicine. *Adv. Sci.* **2019**, *6*, 1801309.
- (15) Paris, J. L.; de la Torre, P.; Cabañas, M. V.; Manzano, M.; Grau, M.; Flores, A. I.;

- Vallet-Regí, M. Vectorization of Ultrasound-Responsive Nanoparticles in Placental Mesenchymal Stem Cells for Cancer Therapy. *Nanoscale* **2017**, *9*, 5528–5537.
- (16) Paris, J. L.; Torre, P. de la; Manzano, M.; Cabañas, M. V.; Flores, A. I.; Vallet-Regí, M. Decidua-Derived Mesenchymal Stem Cells as Carriers of Mesoporous Silica Nanoparticles. *In vitro* and *in vivo* Evaluation on Mammary Tumors. *Acta Biomater.* **2016**, *33*, 275–282.
- (17) Wang, X.; Gao, J.; Ouyang, X.; Wang, J.; Sun, X.; Lv, Y. Mesenchymal Stem Cells Loaded with Paclitaxel– Poly(Lactic-Co-Glycolic Acid) Nanoparticles for Glioma-Targeting Therapy. *Int. J. Nanomedicine* **2018**, *13*, 5231–5248.
- (18) Layek, B.; Sadhukha, T.; Panyam, J.; Prabha, S. Nano-Engineered Mesenchymal Stem Cells Increase Therapeutic Efficacy of Anticancer Drug Through True Active Tumor Targeting. *Mol. Cancer Ther.* **2018**, *17*, 1196–1206.
- (19) Foroozandeh, P.; Aziz, A. A. Insight into Cellular Uptake and Intracellular Trafficking of Nanoparticles. *Nanoscale Res. Lett.* **2018**, *13*, 339.
- (20) Swanson, J. A. Shaping Cups into Phagosomes and Macropinosomes. *Nat. Rev. Mol. Cell Biol.* **2008**, *9*, 639–649.
- (21) Barbero, F.; Russo, L.; Vitali, M.; Piella, J.; Salvo, I.; Borrajo, M. L.; Busquets-Fité, M.; Grandori, R.; Bastús, N. G.; Casals, E.; *et al.* Formation of the Protein Corona: The Interface between Nanoparticles and the Immune System. *Semin. Immunol.* **2017**, *34*, 52–60.
- (22) Jokerst, J. V.; Lobovkina, T.; Zare, R. N.; Gambhir, S. S. Nanoparticle PEGylation for Imaging and Therapy. *Nanomedicine* **2011**, *6*, 715–728.
- (23) Izquierdo-Barba, I.; Colilla, M.; Vallet-Regí, M. Zwitterionic Ceramics for Biomedical Applications. *Acta Biomater.* **2016**, *40*, 201–211.
- (24) Estephan, Z. G.; Schlenoff, P. S.; Schlenoff, J. B. Zwitteration as an Alternative to PEGylation. *Langmuir* **2011**, *27*, 6794–6800.
- (25) Behzadi, S.; Serpooshan, V.; Tao, W.; Hamaly, M. A.; Alkawareek, M. Y.; Dreaden, E. C.; Brown, D.; Alkilany, A. M.; Farokhzad, O. C.; Mahmoudi, M. Cellular Uptake of Nanoparticles: Journey inside the Cell. *Chem. Soc. Rev.* **2017**, *46*, 4218–4244.
- (26) Etheridge, M. L.; Campbell, S. A.; Erdman, A. G.; Haynes, C. L.; Wolf, S. M.; McCullough, J. The Big Picture on Nanomedicine: The State of Investigational and Approved Nanomedicine Products. *Nanomedicine. Med.* **2013**, *9*, 1–14.
- (27) Dogra, P.; Adolphi, N. L.; Wang, Z.; Lin, Y.-S.; Butler, K. S.; Durfee, P. N.; Croissant, J. G.; Nouredine, A.; Coker, E. N.; Bearer, E. L.; *et al.* Establishing the Effects of Mesoporous Silica Nanoparticle Properties on *in vivo* Disposition Using Imaging-Based Pharmacokinetics. *Nat. Commun.* **2018**, *9*, 4551.
- (28) Zhao, Y.; Wang, Y.; Ran, F.; Cui, Y.; Liu, C.; Zhao, Q.; Gao, Y.; Wang, D.; Wang, S. A Comparison between Sphere and Rod Nanoparticles Regarding Their *in vivo* Biological Behavior and Pharmacokinetics. *Sci. Rep.* **2017**, *7*, 4131.
- (29) Toy, R.; Peiris, P. M.; Ghaghada, K. B. Shaping Cancer Nanomedicine: The Effect

- of Particle Shape on the *in vivo* Journey of Nanoparticles. *Nanomedicine* **2014**, *9*, 121–134.
- (30) Zhao, J.; Stenzel, M. H. Entry of Nanoparticles into Cells: The Importance of Nanoparticle Properties. *Polym. Chem.* **2018**, *9*, 259–272.
- (31) Gustafson, H. H.; Holt-Casper, D.; Grainger, D. W.; Ghandehari, H. Nanoparticle Uptake: The Phagocyte Problem. *Nano Today* **2015**, *10*, 487–510.
- (32) Arvizo, R. R.; Miranda, O. R.; Moyano, D. F.; Walden, C. A.; Giri, K.; Robertson, J. D.; Rotello, V. M.; Reid, J. M.; Mukherjee, P. Modulating Pharmacokinetics, Tumor Uptake and Biodistribution by Engineered Nanoparticles. *PLoS One* **2011**, *6*, 24374.
- (33) Lu, H.; Stenzel, M. H. Multicellular Tumor Spheroids (MCTS) as a 3D *in vitro* Evaluation Tool of Nanoparticles. *Small* **2018**, *14*, 1702858.
- (34) Yameen, B.; Choi, W. Il; Vilos, C.; Swami, A.; Shi, J.; Farokhzad, O. C. Insight into Nanoparticle Cellular Uptake and Intracellular Targeting. *J. Control. Release* **2014**, *190*, 485–499.
- (35) Baeza, A.; Manzano, M.; Colilla, M.; Vallet-Regí, M. Recent Advances in Mesoporous Silica Nanoparticles for Antitumor Therapy: Our Contribution. *Biomater. Sci.* **2016**, *4*, 803–813.
- (36) Lurje, G.; Lenz, H.-J. EGFR Signaling and Drug Discovery. *Oncology* **2009**, *77*, 400–410.
- (37) Villegas, M. R.; Baeza, A.; Nouredine, A.; Durfee, P. N.; Butler, K. S.; Agola, J. O.; Brinker, C. J.; Vallet-Regí, M. Multifunctional Protocells for Enhanced Penetration in 3D Extracellular Tumoral Matrices. *Chem. Mater.* **2018**, *30*, 112–120.
- (38) Jaradat, D. M. M. Thirteen Decades of Peptide Synthesis: Key Developments in Solid Phase Peptide Synthesis and Amide Bond Formation Utilized in Peptide Ligation. *Amino Acids* **2018**, *50*, 39–68.
- (39) Palomo, J. M. Solid-Phase Peptide Synthesis: An Overview Focused on the Preparation of Biologically Relevant Peptides. *RSC Adv.* **2014**, *4*, 32658–32672.
- (40) Wu, X.; Han, Z.; Schur, R. M.; Lu, Z. Targeted Mesoporous Silica Nanoparticles Delivering Arsenic Trioxide with Environment Sensitive Drug Release for Effective Treatment of Triple Negative Breast Cancer. *ACS Biomater. Sci.* **2016**, *2*, 501–507.
- (41) Xu, H.; Wang, Z.; Li, Y.; Guo, Y.; Zhou, H.; Li, Y.; Wu, F.; Zhang, L.; Yang, X.; Lu, B.; *et al.* Preparation and Characterization of a Dual-Receptor Mesoporous Silica Nanoparticle–Hyaluronic Acid–RGD Peptide Targeting Drug Delivery System. *RSC Adv.* **2016**, *6*, 40427–40435.
- (42) Paris, J. L.; Villaverde, G.; Cabañas, M. V.; Manzano, M.; Vallet-Regí, M. From Proof-of-Concept Material to PEGylated and Modularly Targeted Ultrasound-Responsive Mesoporous Silica Nanoparticles. *J. Mater. Chem. B* **2018**, *6*, 2785–2794.
- (43) Villaverde, G.; Gómez-Graña, S.; Guisasola, E.; García, I.; Hanske, C.; Liz-

- Marzán, L. M.; Baeza, A.; Vallet-Regí, M. Targeted Chemo-Photothermal Therapy: A Nanomedicine Approximation to Selective Melanoma Treatment. *Part. Part. Syst. Charact.* **2018**, *35*, 1800148.
- (44) Cheng, Y. J.; Zhang, A. Q.; Hu, J. J.; He, F.; Zeng, X.; Zhang, X. Z. Multifunctional Peptide-Amphiphile End-Capped Mesoporous Silica Nanoparticles for Tumor Targeting Drug Delivery. *ACS Appl. Mater. Interfaces* **2017**, *9*, 2093–2103.
- (45) Pan, L.; He, Q.; Liu, J.; Chen, Y.; Ma, M.; Zhang, L.; Shi, J. Nuclear-Targeted Drug Delivery of Tat Peptide-Conjugated Monodisperse Mesoporous Silica Nanoparticles. *J. Am. Chem. Soc.* **2012**, *134*, 5722–5725.
- (46) Li, L.-L.; Yin, Q.; Cheng, J.; Lu, Y. Polyvalent Mesoporous Silica Nanoparticle-Aptamer Bioconjugates Target Breast Cancer Cells. *Adv. Healthc. Mater.* **2012**, *1*, 567–572.
- (47) Gao, L.; Cui, Y.; He, Q.; Yang, Y.; Fei, J.; Li, J. Selective Recognition of Co-Assembled Thrombin Aptamer and Docetaxel on Mesoporous Silica Nanoparticles against Tumor Cell Proliferation. *Chem. Eur. J.* **2011**, *17*, 13170–13174.
- (48) Chen, X.; Sun, H.; Hu, J.; Han, X.; Liu, H.; Hu, Y. Transferrin Gated Mesoporous Silica Nanoparticles for Redox-Responsive and Targeted Drug Delivery. *Colloids and Surfaces B: Biointerfaces* **2017**, *152*, 77–84.
- (49) Martínez-Carmona, M.; Baeza, A.; Rodríguez-Milla, M. A.; García-Castro, J.; Vallet-Regí, M. Mesoporous Silica Nanoparticles Grafted with a Light-Responsive Protein Shell for Highly Cytotoxic Antitumoral Therapy. *J. Mater. Chem. B* **2015**, *3*, 5746–5752.
- (50) Martínez-Carmona, M.; Lozano, D.; Colilla, M.; Vallet-Regí, M. Lectin-Conjugated pH-Responsive Mesoporous Silica Nanoparticles for Targeted Bone Cancer Treatment. *Acta Biomater.* **2018**, *65*, 393–404.
- (51) Luo, Z.; Cai, K.; Hu, Y.; Zhao, L.; Liu, P.; Duan, L.; Yang, W. Mesoporous Silica Nanoparticles End-Capped with Collagen: Redox-Responsive Nanoreservoirs for Targeted Drug Delivery. *Angew. Chemie Int. Ed.* **2011**, *50*, 640–643.
- (52) Chen, Z.; Li, Z.; Lin, Y.; Yin, M.; Ren, J.; Qu, X. Bioresponsive Hyaluronic Acid-Capped Mesoporous Silica Nanoparticles for Targeted Drug Delivery. *Chem. Eur. J.* **2013**, *19*, 1778–1783.
- (53) Liong, M.; Zink, J. I.; Lu, J.; Tamanoi, F.; Kovichich, M.; Xia, T.; Nel, A. E.; Ruehm, S. G. Multifunctional Inorganic Nanoparticles for Imaging, Targeting, and Drug Delivery. *ACS Nano* **2008**, *2*, 889–896.
- (54) Porta, F.; Lamers, G. E. M.; Morrhayim, J.; Chatzopoulou, A.; Schaaf, M.; den Dulk, H.; Backendorf, C.; Zink, J. I.; Kros, A. Folic Acid-Modified Mesoporous Silica Nanoparticles for Cellular and Nuclear Targeted Drug Delivery. *Adv. Healthc. Mater.* **2013**, *2*, 281–286.
- (55) Lv, G.; Qiu, L.; Liu, G.; Wang, W.; Li, K.; Zhao, X.; Lin, J. pH Sensitive Chitosan-Mesoporous Silica Nanoparticles for Targeted Delivery of a Ruthenium Complex with Enhanced Anticancer Effects. *Dalt. Trans.* **2016**, *45*, 18147–18155.
- (56) Ren, W. X.; Han, J.; Uhm, S.; Jang, Y. J.; Kang, C.; Kim, J. H.; Kim, J. S. Recent

- Development of Biotin Conjugation in Biological Imaging, Sensing, and Target Delivery. *Chem. Commun.* **2015**, *51*, 10403–10418.
- (57) Russell-jones, G.; Mctavish, K.; Mcewan, J.; Rice, J.; Nowotnik, D. Vitamin-Mediated Targeting as a Potential Mechanism to Increase Drug Uptake by Tumours. *J. Inorg. Biochem.* **2004**, *98*, 1625–1633.
- (58) Villaverde, G.; Baeza, A.; Melen, G. J.; Alfranca, A.; Ramírez, M.; Vallet-Regí, M. A New Targeting Agent for the Selective Drug Delivery of Nanocarriers for Treating Neuroblastoma. *J. Mater. Chem. B* **2015**, *3*, 4831–4842.
- (59) Villaverde, G.; Alfranca, A.; Gonzalez-Murillo, A.; Melen, G. J.; Castillo, R. R.; Ramírez, M.; Baeza, A.; Vallet-Regí, M. Molecular Scaffolds as Double-Targeting Agents For the Diagnosis and Treatment of Neuroblastoma. *Angew. Chemie Int. Ed.* **2019**, *58*, 3067–3072.
- (60) Smith, S. A.; Selby, L. I.; Johnston, A. P. R.; Such, G. K. The Endosomal Escape of Nanoparticles: Toward More Efficient Cellular Delivery. *Bioconjug. Chem.* **2019**, *30*, 263–272.
- (61) Casey, J. R.; Grinstein, S.; Orlowski, J. Sensors and Regulators of Intracellular pH. *Nat. Rev. Mol. Cell Biol.* **2010**, *11*, 50–61.
- (62) Hu, Y. B.; Dammer, E. B.; Ren, R. J.; Wang, G. The Endosomal-Lysosomal System: From Acidification and Cargo Sorting to Neurodegeneration. *Transl. Neurodegener.* **2015**, *4*, 18.
- (63) Varkouhi, A. K.; Scholte, M.; Storm, G.; Haisma, H. J. Endosomal Escape Pathways for Delivery of Biologicals. *J. Control. Release* **2016**, *151*, 220–228.
- (64) Brock, D. J.; Kondow-Mcconaghy, H. M.; Hager, E. C.; Pellois, J. P. Endosomal Escape and Cytosolic Penetration of Macromolecules Mediated by Synthetic Delivery Agents. *Bioconjug. Chem.* **2019**, *30*, 293–304.
- (65) Zhitomirsky, B.; Assaraf, Y. G. Lysosomal Accumulation of Anticancer Drugs Triggers Lysosomal Exocytosis. *Oncotarget* **2017**, *8*, 45117–45132.
- (66) Kim, J. A.; Aberg, C.; Salvati, A.; Dawson, K. A. Role of Cell Cycle on the Cellular Uptake and Dilution of Nanoparticles in a Cell Population. *Nat. Nanotechnol.* **2012**, *7*, 62–68.
- (67) Ye, D.; Raghnaill, M. N.; Bramini, M.; Mahon, E.; Åberg, C.; Salvati, A.; Dawson, K. A. Nanoparticle Accumulation and Transcytosis in Brain Endothelial Cell Layers. *Nanoscale* **2013**, *5*, 11153–11165.
- (68) Cui, Y.; Shan, W.; Zhou, R.; Liu, M.; Wu, L.; Guo, Q.; Zheng, Y.; Wu, J.; Huang, Y. The Combination of Endolysosomal Escape and Basolateral Stimulation to Overcome the Difficulties of “Easy Uptake Hard Transcytosis” of Ligand-Modified Nanoparticles in Oral Drug Delivery. *Nanoscale* **2018**, *10*, 1494–1507.
- (69) Akita, H.; Kudo, A.; Minoura, A.; Yamaguti, M.; Khalil, I. A.; Moriguchi, R.; Masuda, T.; Danev, R.; Nagayama, K.; Kogure, K.; *et al.* Multi-Layered Nanoparticles for Penetrating the Endosome and Nuclear Membrane via a Step-Wise Membrane Fusion Process. *Biomaterials* **2009**, *30*, 2940–2949.
- (70) Dimitrov, D. S. Virus Entry: Molecular Mechanisms and Biomedical Applications.



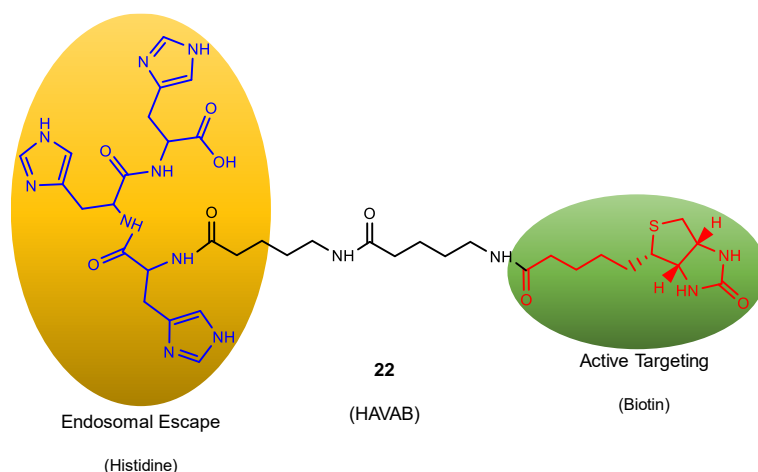
- Nat. Rev. Microbiol.* **2004**, 2, 109–122.
- (71) Sakaguchi, N.; Kojima, C.; Harada, A.; Koiwai, K.; Shimizu, K.; Emi, N.; Kono, K. Enhancement of Transfection Activity of Lipoplexes by Complexation with Transferrin-Bearing Fusogenic Polymer-Modified Liposomes. *Int. J. Pharm.* **2006**, 325, 186–190.
- (72) Kono, K.; Torikoshi, Y.; Mitsutomi, M.; Itoh, T.; Emi, N.; Yanagie, H.; Takagishi, T. Novel Gene Delivery Systems: Complexes of Fusogenic Polymer-Modified Liposomes and Lipoplexes. *Gene Ther.* **2001**, 8, 5–12.
- (73) Argyo, C.; Weiss, V.; Bräuchle, C.; Bein, T. Multifunctional Mesoporous Silica Nanoparticles as a Universal Platform for Drug Delivery. *Chem. Mater.* **2014**, 26, 435–451.
- (74) You, J.-O.; Auguste, D. T. Nanocarrier Cross-Linking Density and pH Sensitivity Regulate Intracellular Gene Transfer. *Nano Lett.* **2009**, 9, 4467–4473.
- (75) Selby, L. I.; Cortez-Jugo, C. M.; Such, G. K.; Johnston, A. P. R. Nanoescapology: Progress toward Understanding the Endosomal Escape of Polymeric Nanoparticles. *Wiley Interdiscip. Rev. Nanomedicine Nanobiotechnology* **2017**, 9, e1452.
- (76) Hu, Y.; Litwin, T.; Nagaraja, A. R.; Kwong, B.; Katz, J.; Watson, N.; Irvine, D. J. Cytosolic Delivery of Membrane-Impermeable Molecules in Dendritic Cells Using pH-Responsive Core–Shell Nanoparticles. *Nano Lett.* **2007**, 7, 3056–3064.

## 3.2. Targeted Mesoporous Silica Nanoparticles with Enhanced Endosomal Escape Capabilities

### 3.2.1. Introduction

The effective translation of nanomedicines to the clinic remains challenging owing to the several biological barriers that nanoparticles encounter when administered *in vivo*, as it was mentioned in Section 3.1. Relevant examples of such biological barriers are (1) the lack of particle selectivity for tumoral cells so that drug-loaded particles may be internalized by normal cells, increasing undesired side effects; (2) the potential sequestration of the particles within the endo-lysosomal pathway, which may lead to cargo degradation or multidrug resistance; and (3) the lack of preferential particle accumulation in the tumoral mass, which may lead to nonspecific particle distribution throughout the organism rather than just to the tumor.<sup>1</sup> In this sense, this last piece of research involved the design of a smart nanocarrier based on MSNs able to overcome these biological barriers.

The idea was to design a molecule that could be grafted to MSNs, leading to a carrier with excellent physical-chemical properties that could address the first and second above-mentioned biological barriers. In this context, a multifunctional peptidic molecule was devised and its synthesis was accomplished using solid phase peptide synthesis. (Scheme 3.2).



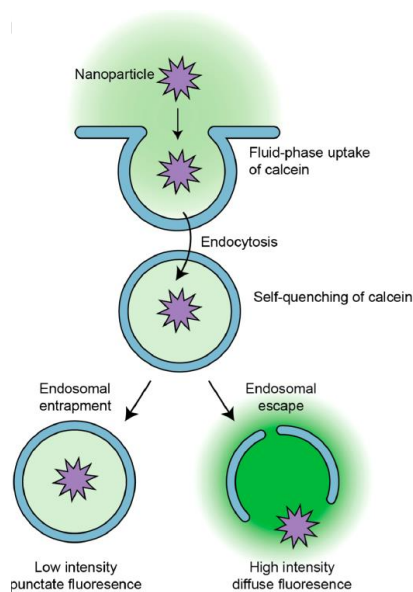
**Scheme 3.2.** Schematic representation of the designed peptidic molecule (compound 22, HAVAB). The biotin molecule allows preferential accumulation in tumor cells overexpressing its receptor. The histidine motif provides buffering capacity to mediate endosomal escape.

As shown in Scheme 3.2, HAVAB was composed of a cell membrane targeting moiety and a fragment with potential endosomal escape capabilities. Biotin was selected as model

targeting agent because its receptor is overexpressed in a wide variety of tumoral cells and can mediate the internalization of drug delivery systems. Examples of cell lines overexpressing this receptor include HeLa, A549 and human ovarian cancer.<sup>2,3</sup> Histidine was included because its imidazole ring presents buffering capacity at the acid pH of endosomes and can induce endosomal escape *via* the proton sponge effect.<sup>4-6</sup> This phenomenon is based on the presence of species with buffering capacity trapped in the endo-lysosomes. These species can capture protons present in these organelles, which is counteracted by influxing protons, chloride counterions and water in the endosomes and lysosomes, increasing the pressure and eventually lysing the membrane.<sup>7,8</sup>

The peptidic fragment was grafted to the redox-responsive system engineered in Section 2.6 and its biological performance was evaluated *in vitro* and *in ovo*. The *in vitro* studies comprised the use of 2D and 3D models. The effect of nanoparticles on 2D cell cultures have been widely studied due to the ease of the experimental methods. This model constitutes a valuable starting point for the study of the cell-material interactions. However, 2D monolayers lack the complex physiology and microenvironment of real tumors and, consequently, the results obtained there, yet provide essential information, are only partially translatable. For that reason, the performance of the biotinylated particles was also evaluated using 3D spheroids, which show several *in vivo* tumor features such as cell-cell interaction, hypoxia and production of extracellular matrix, among others.<sup>9</sup> Spheroids are formed using non-adherent plates where cells self-aggregate rather than attach to the bottom, as it happens with 2D cell cultures.

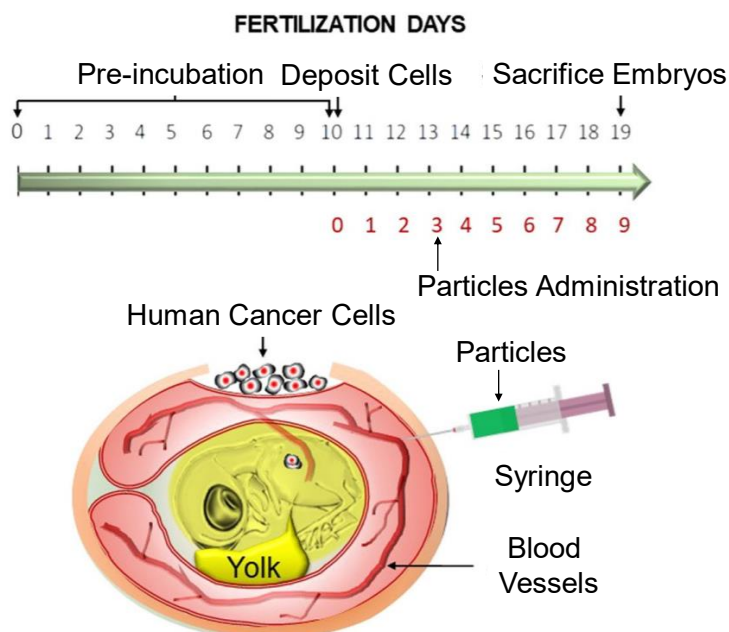
In particular, the biological studies involved the evaluation of the cellular uptake of the targeted carrier, its ability to inhibit cell proliferation and the detection of endosomal escape. The effect of the peptidic fragment on the cellular uptake was quantitatively studied using 2D HeLa cell cultures. The uptake was also qualitatively evaluated using A549 and OVCAR8 2D cell cultures. The accumulation and distribution of the particles were further analyzed in A549 and OVCAR8 spheroids to evaluate the performance of the particles in a more complex scenario. Besides, the particles were loaded with different drugs and their cytotoxic effect was evaluated in 2D and 3D scenarios. Finally, the ability of the carrier to bypass endosomal entrapment was evaluated using calcein in 2D and 3D cell cultures (Scheme 3.3).



**Scheme 3.3.** Schematic representation of the evaluation of endosomal escape using calcein. Its fluorescence self-quenches when entrapped in the endosomes and can barely be detected. However, when calcein leaves the endosomes self-quenching disappears and a strong fluorescence can be detected. Reproduced from Ref 10 with permission of ACS.

Calcein is a membrane impermeable dye which useful for the detection of endosomal escape. If particles remain in the endo-lysosomes, calcein fluorescence self-quenches and it is undetectable. However, if the escape takes place a strong green fluorescence can be observed.

Finally, the biodistribution of the targeted system as well as a preliminary tumor inhibition experiment were evaluated *in ovo* using chicken embryos bearing A549 tumors. The chicken embryo model constitutes a pseudo-*in vivo* tumoral model that provides useful information about the systemic administration of a nanomedicine reducing the number of animals employed (Scheme 3.4).

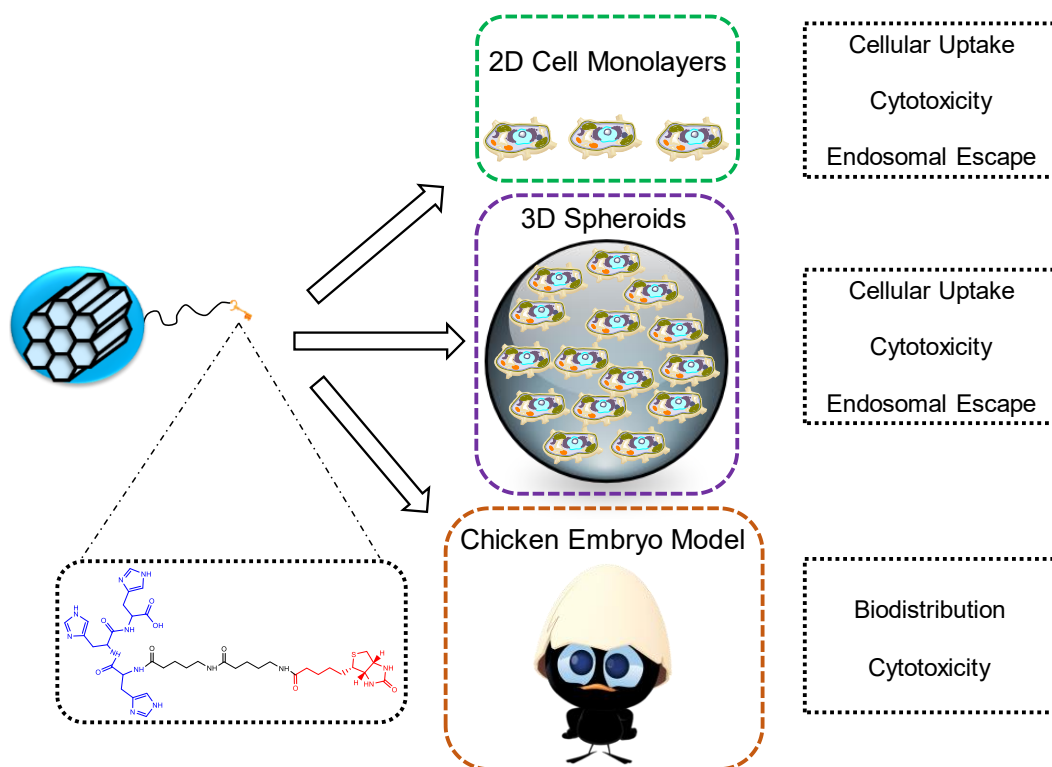


**Scheme 3.4.** Schematic representation of experiments using the chicken embryo model. The freshly fertilized eggs are pre-incubated for 10 days. Then, cancer cells are deposited on the chorioallantoic membrane (CAM) for tumor growth. After that, the particles are administered and the experiments conclude sacrificing the embryos before hatching. Adapted from Ref 11 with permission of Springer Nature Publishing AG.

The freshly fertilized eggs are incubated for 10 days. Then, a small window is opened and tumoral cells are deposited on the chorioallantoic membrane (CAM) for tumor growth. The particles are administered *via* syringe injection in a vein after tumor formation and the embryos are incubated until the experiment finishes, when they are sacrificed. The tumor formed resembles actual cancer patient tumors and contains a highly irrigated extracellular matrix.<sup>11,12</sup>

The main advantages of this model are that (1) the tumor grows within 3-4 days, (2) the results are available 2-3 days after the administration of the particles, (3) the costs are reduced in comparison with animal models and (4) it allows the optimization of nanomedicine so that the *in vivo* experiments can be restricted to the optimized conditions.

A summary of the biological experiments carried out during this work is depicted in Scheme 3.5.



**Scheme 3.5.** Summary of the biological experiments carried out in this work. The engineered nanoparticles were tested in 2D and 3D *in vitro* models to evaluate their cellular uptake, their cytotoxicity when loaded with a drug and their ability to bypass endosomal entrapment. In addition, the biodistribution and cytotoxicity of the particles were tested *in ovo* using the chicken embryo model.

### 3.2.2. Materials and Methods

The following compounds were purchased from Sigma-Aldrich Inc.: TEOS, Ammonium nitrate; CTAB; FITC; APTES; ABA; Phenyl chloroformate; DBTL; 2-Mercaptoethanol; 2,2'-Dipyridildisulfide; TBDMS-Cl; 3-(triethoxysilyl)propyl isocyanate; HS-PEG<sub>3500</sub>-NH<sub>2</sub> (PEG-SH); 2-Chlorotriyl chloride resin; Fmoc-His(Trt)-OH (His); Fmoc-5-Ava-OH (Ava); *N,N,N',N'*-Tetramethyl-*O*-(1*H*-benzotriazol-1-yl)uronium hexafluorophosphate (HBTU), 1-Hydroxybenzotriazole hydrate (HOBt); DIPEA; Biotin N-hydroxysuccinimide Ester (NHS-Biotin); TFA; Triisopropylsilane (TIPS); DCC; Topotecan (TOP); DMF; THF; DCM, AcN. The rest of the chemicals (ethanol, heptane, etc) were of the best quality and were employed as received.

#### 3.2.2.1. Redox-Responsive Mesoporous Silica Nanoparticles (MSN-SS-PEG)

MSNs were synthesized following the procedure described in Section 2.2.2.1. Compound **21** was synthesized following the protocols described in Section 2.6.2.2. The grafting of compound **21** to the MSNs and the subsequent addition of PEG-SH to yield MSN-SS-PEG were carried out following the protocols described in Sections 2.6.2.3 and

**2.6.2.4**, respectively. All materials were characterized using the same techniques, including  $^1\text{H-NMR}$ , TGA analysis, FTIR spectroscopy, DLS and Zeta potential.

### **3.2.2.2. Biotinylated Histidine-Rich Peptide**

The biotinylated peptide (**22**) was synthesized using standard solid phase peptide synthesis techniques and Fmoc-protected amino acids. The amide bond formation was carried out adding a solution of HOBt (107.06 mg, 0.792 mmol), HBTU (300 mg, 0.792 mmol) and the corresponding amino acid (327.54 mg, 0.528 mmol for His, 179.2 mg, 0.528 mmol for Ava) in DMF (3.5 mL) and DIPEA (0.275 mL, 1.58 mmol) to the resin (200 mg, 0.264 mmol). Then, the mixture was shaken in a reactor with a wrist-shaker overnight. Afterward, the resin was thoroughly washed with DMF to remove unbounded amino acids and by-products. Then, a solution of piperidine (20%) in DMF (2 mL) was added to the resin to cleave the Fmoc-protecting group. After that, the resin was extensively washed with DMF and the next amino acid was added following the same procedure. Once the last amino acid was added, NHS-Biotin (270 mg, 0.792 mmol) in DMF (6.5 mL) and DIPEA (0.275 mL, 1.58 mmol) were added to the resin and wrist-shaken overnight in a reactor.

Once the biotinylation of the peptidic chain was accomplished, the resin was thoroughly washed with DMF and DCM. Then, 1.2 mL of a cocktail containing TFA (95%), TIPS (2.5%) and water (2.5%) was added dropwise to the resin, which was gently shaken for 2 hours to accomplish the peptide release from the resin. After that, the solution was filtered and the resin was washed with a small amount of the cleavage cocktail. Both solutions were mixed. The peptide-containing solution was added dropwise to cold ether, leading to a precipitate that was isolated by centrifugation. Finally, the precipitate was purified by molecular exclusion chromatography, using Sephadex® G-25 as stationary phase and water as mobile phase. The collected phases were lyophilized and characterized by  $^1\text{H-NMR}$  and mass spectrometry. This compound will be denoted hereafter either as compound **22** or HAVAB.

### **3.2.2.3. Targeted Mesoporous Silica Nanoparticles**

To a  $\text{N}_2$ -purged flask containing compound **22** (30 mg, 0.04 mmol) in dry DMF (0.6 mL), DCC (21.7 mg, 0.11 mmol) and NHS (12.1 mg, 0.11 mmol) in dry DMF (0.6 mL) were added. The solution was stirred for 1 hours at rt for acid activation. After that, the mixture was added dropwise to  $\text{N}_2$ -purged flask containing MSN-SS-PEG (35 mg) in dry

DMF (3.5 mL) and the whole reaction mixture was stirred at rt for 24 hours. Then, the nanoparticles were thoroughly washed with DMF, ethanol, water and methanol to remove unbounded reagents, dicyclohexylurea by-products, residual DMF and water, respectively. Finally, the particles were dried under vacuum to yield MSN-PEPT. The particles were characterized in terms of TGA analysis, FTIR spectroscopy, DLS and Zeta potential.

#### 3.2.2.4. 2D cellular experiments

##### ❖ 2D Cell Cultures

Cell culture tests were performed using HeLa, A549 and MC3T3-E1 cells. HeLa or A549 cells were plated at a density of 20,000 cells cm<sup>2</sup> in 1 mL DMEM containing 10% of FBS and 1% penicillin–streptomycin at 37°C in a humidified atmosphere of 5% CO<sub>2</sub>. MC3T3-E1 cells were plated using the same conditions but in 1 mL of  $\alpha$ -minimum essential medium. OVCAR8 cells were plated using the same conditions but in 1 mL of Roswell Park Memorial Institute (RPMI) medium. Then, nanoparticles were placed at different concentrations and incubated for different periods of time.

##### ❖ Cell Viability

HeLa or A549 cell proliferation was determined by addition of Alamar Blue solution following the protocol described in Section 2.2.2.5.

##### ❖ Internalization studies

For the fluorescence microscopy studies, cells were seeded following the protocol described in Section 2.2.2.5. The studies were carried out with Rhodamine B-labelled nanoparticles to detect the internalization capability. The endosomal escape was studied using calcein-loaded nanoparticles.

For the flow cytometry studies, HeLa or MC3T3-E1 cells were cultured in each well of a 6-well plate. After 24 hours, the cells were incubated with different concentrations of the fluorescein-labelled nanoparticles. After 2 hours, cells were washed twice with PBS and incubated at 37°C with trypsin–EDTA solution for cell detachment. The reaction was stopped with culture medium after 5 minutes and cells were centrifuged at 1,500 rpm for 10 minutes and re-suspended in fresh medium. Then, the surface fluorescence of the cells was quenched with trypan blue (0.4%) to confirm the presence of an intracellular, and therefore internalized, fluorescent signal. Flow cytometry was performed at an excitation wavelength of 488 nm, green fluorescence was measured at 530 nm. The



trigger was set for the green fluorescence channel. The conditions for the data acquisition and analysis were established using negative and positive controls with the CellQuest Program of Becton–Dickinson and these conditions were maintained during all the experiments. Each experiment was carried out three. For statistical significance, at least 10,000 cells of each sample were analyzed.

For confocal laser scanning microscopy, A549 or OVCAR8 cells were incubated with different concentrations of Rhodamine B-labelled nanoparticles. Each well was thoroughly washed with cold PBS three more times to wash out the non-internalized nanoparticles, and then fixed with ethanol (75%) (kept at  $-20^{\circ}\text{C}$ ) for 10 min. Then, ethanol was removed and the wells were washed with PBS. After that, the nuclei of cells were stained with DAPI for 5 min, respectively, and then washed three times with cold PBS. Cellular uptake of MSNs was recorded by confocal laser scanning microscopy with an excitation wavelength at  $\lambda = 488$  nm. The emission was detected using a 610 nm long pass filter.

### 3.2.2.5. 3D cellular experiments

#### ❖ 3D Cell Cultures

Cells were grown in a 96 U-shaped-well plate for spheroid formation. For that purpose, 10,000 A549 or OVCAR8 cells were inoculated in 200  $\mu\text{L}$  of DMEM or RPMI medium, respectively. Cells were cultured for 7 days at  $37^{\circ}\text{C}$  in a humidified  $\text{CO}_2$  atmosphere. Then, nanoparticles were placed at different concentrations.

#### ❖ Spheroid viability

The viability was evaluated using A549 spheroids. Nanoparticles were added at different concentrations and incubated for 24 hours. Then, the particles were removed and each well was washed three times with PBS 1x and 200  $\mu\text{L}$  of the corresponding medium were added. The spheroids were maintained for 7 days at  $37^{\circ}\text{C}$  in a humidified atmosphere. The spheroids were imaged at different time points. The viability was evaluated in terms of volume variation following the formula:<sup>13</sup>

$$V=0.5 *(\text{short } \phi)^2*\text{long } \phi$$

**Equation 3.1.** Formula for the calculation of the spheroid volume.  $\phi$  denotes the diameter.

#### ❖ Internalization studies

The internalization studies were carried out using A549 and OVCAR8 spheroids. Rhodamine B-labelled Nanoparticles were incubated with the spheroids for 24 hours.

Then, spheroids were thoroughly washed with PBS 1x and placed in an Eppendorf tube. The samples were fixed using a paraformaldehyde solution (4%) at 4°C overnight. Then, spheroids were washed with cold PBS 1x and treated with methanol (99.8%) at -80°C for 30 minutes. After that, the nuclei of the spheroids were stained with Hoechst 33258 solution for 30 minutes for confocal microscopy.

### 3.2.2.6. Chicken eggs experiments

#### ❖ *Tumor Formation*

Freshly fertilized chicken eggs were incubated at 37°C in a humid atmosphere (60%) for 10 days. On day 10, a window was made on the eggshell and a Teflon ring was placed on the CAM membrane. Then 100,000 A549 cells were placed into the ring and the window was sealed for tumor growth.

#### ❖ *Biodistribution Studies*

Once the tumor was formed, normally after 3 days, a small window was opened and Rhodamine B-labelled particles were administered *via* syringe injection in a vein. Afterward, the window was closed and the chicken embryos were incubated for further 2 days. Then, the eggs were imaged in a fluorescence stereomicroscope and subsequently dissected for organ observation.

#### ❖ *Tumor Reduction*

Once the tumor was formed, DOX-loaded Rhodamine B-labelled particles were administered *via* syringe injection in a vein following the above-mentioned protocol. The chicken embryos were incubated for 3 days and subsequently dissected to weight the tumors.

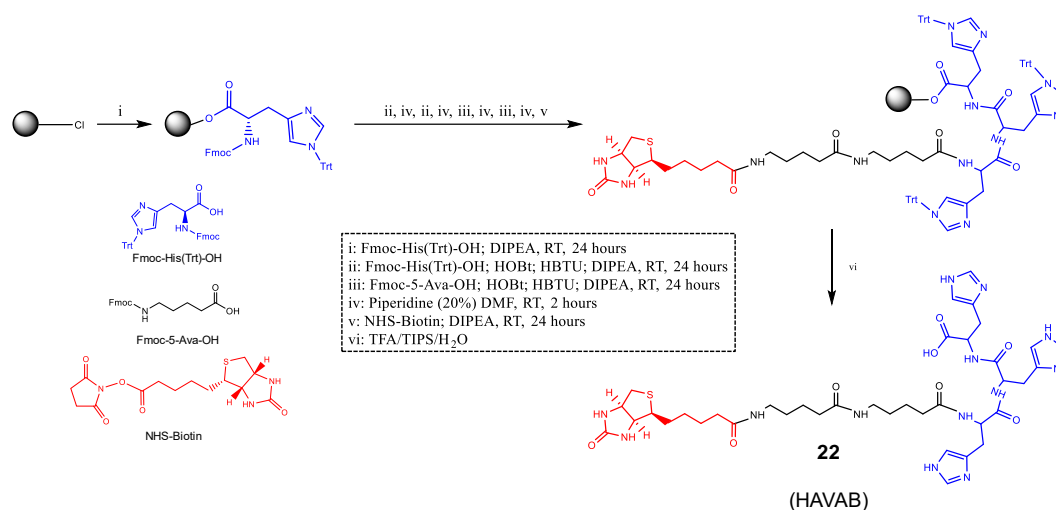
## 3.2.3. Results and Discussion

### 3.2.3.1. Synthesis of Redox-Responsive Mesoporous Silica Nanoparticles

The redox-responsive nanoparticles were synthesized following the methodology described in Section 2.6 and characterized through the same techniques. Briefly, MSNs were synthesized following a modification of a Stöber method, yielding homogenous particles with an array of hexagonally distributed cylindrical mesopores. The carrier was endowed with stimuli-responsiveness through the surface functionalization of the particles with a redox-responsive self-immolative molecule. Its stimuli-responsive behavior was evaluated using DTT as redox agent and their ability to hamper premature release from the particles was analyzed in a preliminary release experiment.

### 3.2.3.2. Synthesis of Biotinylated Histidine-Rich Peptide

The biotinylated peptide was synthesized using standard solid phase peptide synthesis techniques and Fmoc-protected amino acids (Scheme 3.6).



**Scheme 3.6.** Schematic synthesis of HAVAB. The amino acids and the acid activators were sequentially added to the resin. After each amide coupling, the Fmoc group was removed using piperidine (20%) in DMF. Once the last amino acid was added and deprotected, NHS-Biotin was added. After that, the peptide was released from the resin using a cleavage cocktail containing TFA, TIPS and water and purified in a G-25 column.

As shown in Scheme 3.6, the procedure consisted in the formation of an amide bond between the free amino group of the amino acid on the resin and the activated carboxylic acid of the Fmoc-protected amino acid freshly added to the resin. Once the coupling was accomplished, the Fmoc of the latter amino acid was removed and the coupling protocol was carried out again. After the addition of all amino acids, biotin was added, leading to a multifunctional peptide composed of a fragment able to induce endosomal escape and a fragment able to recognize cancer cells over healthy cells. The correct synthesis was evaluated by <sup>1</sup>H-NMR and mass spectrometry.

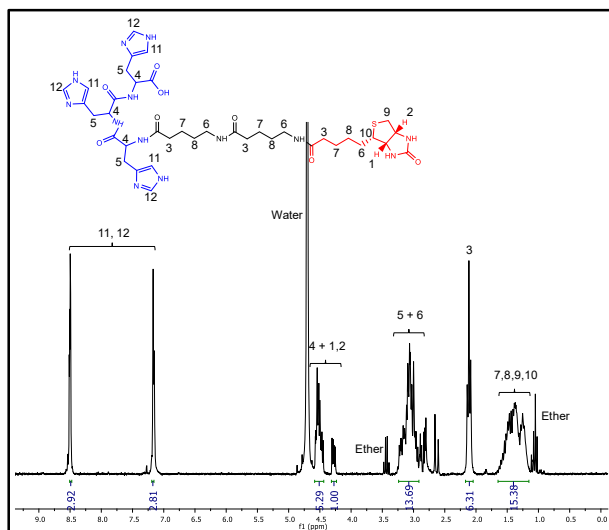


**Figure 3.6.**  $^1\text{H-NMR}$  of HAVAB. (250 MHz,  $\text{D}_2\text{O}$ )  $\delta$  8.50 (t, 3H), 7.16 (s, 3H), 4.59–4.43 (m, 5H), 3.25–2.90 (m, 12H), 2.11 (t, 6H), 1.65–1.15 (m, 15H).

The spectrum shown in Figure 3.6 confirmed the presence of the endosomal escape fragment (signals 4, 5, 11 and 12) and the targeting agent (signals 1, 2, 3, 7, 8, 9 and 10). The peptide was further analyzed by mass spectrometry to confirm the presence of all peptide components (3 His, 2 Ava and 1 biotin) (Figure 3.7).

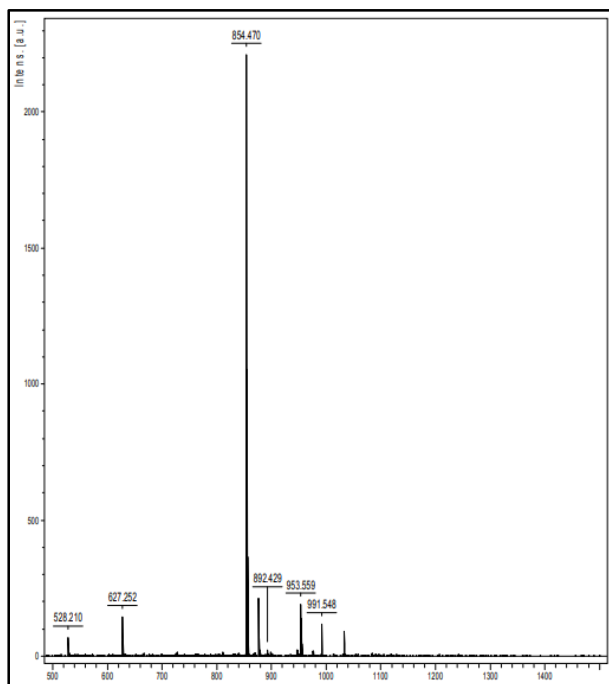


**Figure 3.7.** Mass spectrometry of HAVAB. The concordance between the expected molecular weight and the found molecular weight confirmed the correct synthesis of the peptide.

The calculated molecular weight for the peptidic fragment was 854 g/mol. As shown in Figure 3.7, the analysis of HAVAB by mass spectrometry yielded a value of 854.47 g/mol, in agreement with the expected value. This confirmed the correct synthesis of the

biotinylated peptide and the convenience of using solid phase peptide synthesis to accomplish its synthesis.

### 3.2.3.3. Synthesis of Targeted Mesoporous Silica Nanoparticles

The coupling of the peptidic fragment to the nanoparticles was carried out using carbodiimide chemistry between the amino groups present in the PEG chain and the C-terminal of the peptide. The system containing [MSNs + self-immolative linker + PEG + HAVAB] was denoted as MSN-PEPT. The presence of additional organic matter on the latter material was evaluated using TGA analysis (Figure 3.8).

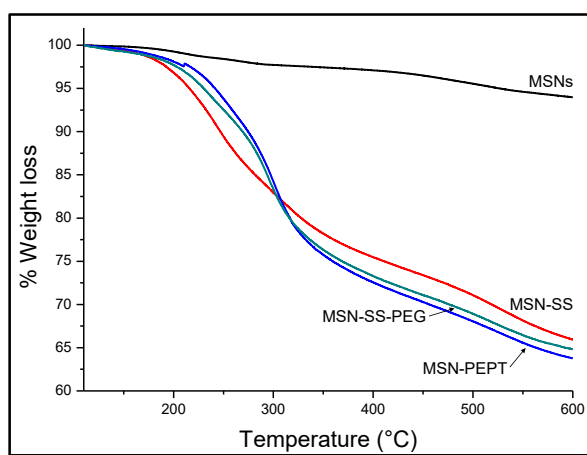


**Figure 3.8.** TGA analysis of all materials synthesized in this chapter. The addition of the peptide induced 1.5% of additional weight loss.

As shown in Figure 3.8, the functionalization of MSN-SS-PEG with HAVAB increased the weight loss *ca.* 1.5%, confirming the correct grafting of the peptide. However, such small additional amount of organic was undetectable in the FTIR spectroscopy (Figure 3.9).

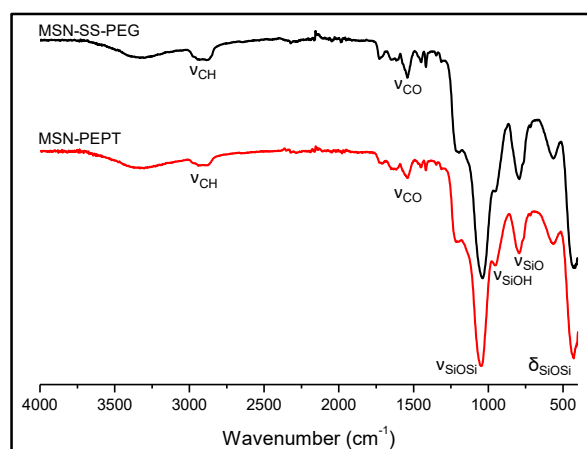


**Figure 3.9.** FTIR spectroscopy of MSN-SS-PEG and MSN-PEPT. No appreciable changes could be observed after the grafting of HAVAB.

The effect of the peptidic fragment on the colloidal stability of MSN-PEPT in aqueous solution was analyzed through DLS measurements (Figure 3.10).

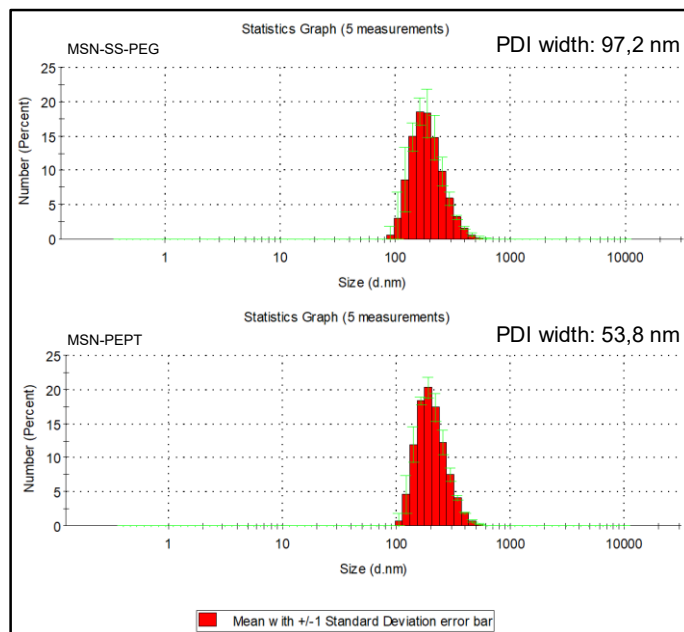


**Figure 3.10.** DLS measurements of MSN-SS-PEG and MSN-PEPT (PDI width indicates the width at medium height of the distribution). The addition of the peptidic fragment improved the colloidal stability, as indicated by the lower value of PDI width.

As observed in Figure 3.10, the colloidal stability of MSN-PEPT improved as a consequence of the introduction of HAVAB, as demonstrated by PDI width values. This result highlights the suitability of MSN-PEPT to be systemically administered as drug delivery system, since this carrier would circulate in the bloodstream without forming aggregates owing to its excellent colloidal stability. Finally, the correct grafting of the peptide was confirmed through the variations in the zeta potential of the samples (-24 mV for MSN-SS-PEG *vs* -37.5 mV for MSN-PEPT). Those values were in agreement with those expected for the peptide presence, which confirmed the success of the synthetic approach here proposed.

#### 3.2.3.4. 2D cellular experiments

##### ❖ 2D cellular internalization studies

Once the complete system was synthesized and characterized, the next step was to find out if the peptidic fragment improved the cellular internalization of the particles. For that purpose, MSN-SS and MSN-PEPT were incubated with HeLa cells. In addition, a group of particles composed of [MSNs + self-immolative linker + PEG + Biotin] was included

as control to further evaluate the effect of HAVAB. This control group was denoted as MSN-PEG-Biotin. The cellular uptake was analyzed by flow cytometry (Figure 3.11).

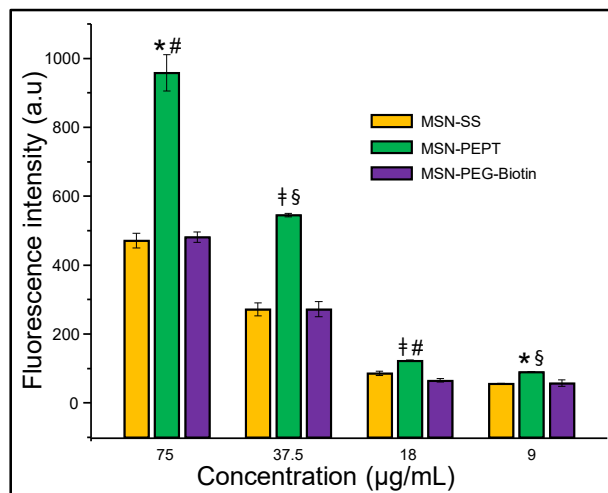


**Figure 3.11.** Flow cytometry of MSN-SS, MSN-PEPT and MSN-PEG-Biotin incubated with HeLa cells. The group containing the complete system (MSN-PEPT) showed better internalization for all the concentrations studied. The graph represents 2 independent experiments: (1) 75 and 37.5 µg/mL and (2) 18 and 9 µg/mL, which confirmed the effect of the peptidic fragment on the cellular uptake. \*  $p < 0.05$  vs MSN-SS; #  $p < 0.05$  vs MSN-PEPT-Biotin; †  $p < 0.01$  vs MSN-SS; §  $p < 0.05$  vs MSN-PEPT-Biotin.

As shown in Figure 3.11, the groups MSN-SS and MSN-PEG-Biotin showed comparable cellular uptake. The unexpectedly high values obtained for MSN-SS might be ascribed to a thiol exchange with some proteins present in the cell membranes of some cellular lines, such as HeLa cells, which has been reported to mediate the internalization of nanoparticles.<sup>14,15</sup>

The best results were obtained for the complete system (MSN-PEPT), which showed higher cellular uptake for all the concentrations studied. Figure 3.11 represents 2 independent experiments, one at concentrations of 75 and 37.5 µg/mL and another one at concentrations of 18 and 9 µg/mL. This fact highlighted the lack of serendipity in the results and confirmed the positive effect of the biotinylated peptidic fragment. The marked differences between the groups MSN-PEPT and MSN-PEG-Biotin might be explained as a consequence of two possible contributions, which might act alone or in combination.

On the one hand, the pKa of histidine is *ca.* 6.5.<sup>16,17</sup> The molecule progressively protonates as pH acidifies, appearing as a combination of its protonated and neutral conformations until pH 4.5, where only the protonated state is observed.<sup>18</sup> Indeed, histidine protonation can be observed at values slightly lower than physiological pH, such as pH 7.2.<sup>19</sup> In addition, cancer cells can slightly acidify culture medium by secretion of

lactic acid.<sup>20</sup> This can be experimentally observed through the subtle color changes of the red phenol indicator included in the medium. In view of these evidences, the higher internalization observed for MSN-PEPT compared to MSN-PEG-Biotin might be explained by the partial protonation of the histidine residues as a consequence of the slight medium acidification. This partial protonation would translate into local positive charge effects that would interact more tightly with the negatively charged cellular membrane. This local charge effect would show a collaborative effect with the active targeting activity of the biotin motif, thus leading to enhanced cellular uptake.

On the other hand, some cell-penetrating peptides internalize through membrane fusion.<sup>21</sup> Besides, it has been shown that proteins or peptides that contain histidine motifs within their structure may lead to membrane fusion upon protonation.<sup>22-25</sup> In consequence, another possible explanation for the results observed in Figure 3.11 might be a collaborative behavior between the biotin active binding and some fusion events that would lead to the observed enhanced internalization. Interestingly, as it was mentioned in Section 2.1.2.1, the pH of the extracellular tumor matrix has been quantified to be within the range 6.5-7, which is a pH lower than the slight deviations than can occur in culture medium. In consequence, the effect observed *in vitro* should be observed *in vivo*, leading to the appearance of local positive charge effects that should enhance the cellular uptake in a more relevant *in vivo* scenario.

Once the effect of HAVAB was validated, the next step was to evaluate whether the complete system could distinguish between healthy and tumoral cells. For that purpose, MSN-PEPT was incubated with HeLa and healthy MC3T3-E1 preosteoblastic cells (Figure 3.12). MSN-SS-PEG was used as control to eliminate the different positive effects observed for MSN-SS (thiol-mediated internalization) and MSN-PEG-Biotin (active targeting through biotin receptors).



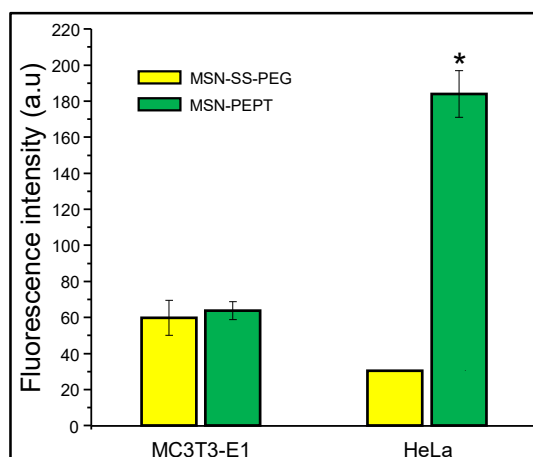


**Figure 3.12.** Flow cytometry of MSN-SS-PEG and MSN-PEPT incubated with MC3T3-E1 and HeLa cells. The group containing the peptide (MSN-PEPT) showed significantly higher cellular uptake in HeLa cells due to the overexpressed biotin receptors. The differences between both groups were imperceptible for the healthy cells. \*  $p < 0.01$  vs MSN-SS-PEPT.

As shown in Figure 3.12, the differences in the cellular uptake between the targeted and non-targeted groups were negligible in the case of healthy cells, as expected for cells lacking overexpressed biotin receptors. The low internalization observed for MSN-SS-PEG was ascribed to the hydration layer created by the PEG chains that hindered the interaction with the cell membrane.<sup>26</sup> On the contrary, only the group containing the peptidic fragment was able to be selectively and greatly internalized by the tumoral cells, as expected for cells overexpressing the biotin receptor. In this sense, a significant difference between the targeted and non-targeted material could be observed, highlighting again the positive effect of the peptidic fragment.

In view of subsequent experiments using A549 and OVCAR8 spheroids, the cellular uptake of MSN-PEPT in these two cell lines was qualitatively evaluated using confocal microscopy (Figure 3.13).

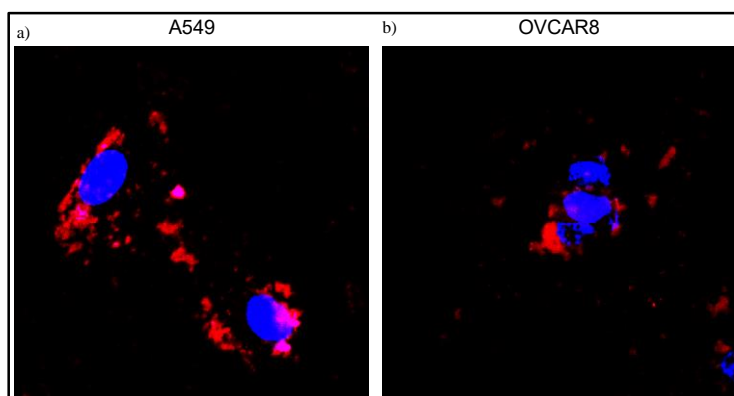


**Figure 3.13.** Evaluation of MSN-PEPT internalization using confocal microscopy. a) A549 cells. b) OVCAR8 cells. The particles (in red) could be internalized by both cells lines, in agreement with the presence of overexpressed biotin receptors.

As shown in Figure 3.13, the biotinylated particles could be effectively internalized in both cell lines, as expected, due to overexpressed biotin receptors in both cells lines. These experiments further confirmed the initial hypothesis of using specific targeting moieties to enhance to efficacy of the particle internalization.

❖ *Endosomal Escape in 2D Cell Cultures*

The endosomal escape capability of MSN-PEPT was first evaluated in 2D cell cultures using A549 cells. For that purpose, the particles were loaded with calcein, which is known to be membrane impermeable. MSNs were also loaded with calcein and used as control. The samples were analyzed using fluorescence microscopy (Figure 3.14).

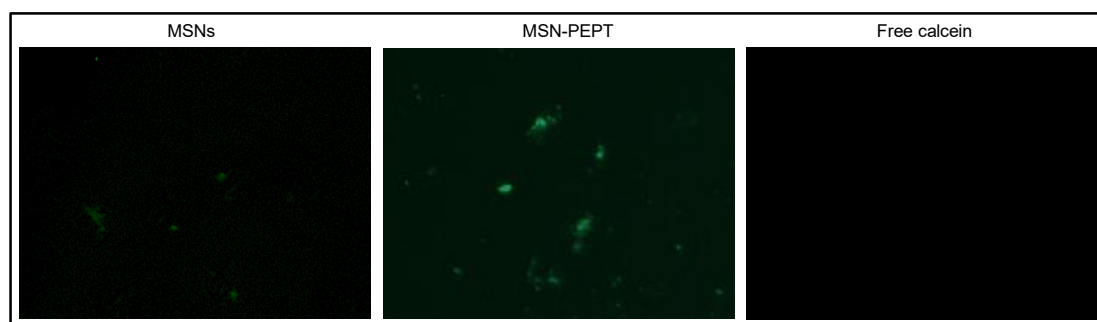


**Figure 3.14.** Evaluation of the endosomal escape in A540 2D cell cultures. Free calcein (right) could not be incorporated in the cells. MSNs (left) remained inside the endo-lysosomes, calcein fluorescence was self-quenched and could barely be observed. MSN-PEPT (center) could escape the endo-lysosomes and calcein fluorescence could be observed more intense and showing slight diffusion.

As shown in Figure 3.14, free calcein could not be internalized by the cells, as it was expected owing to their membrane impermeable nature. Calcein-loaded MSNs showed low green fluorescence. This would be consequence of the endosomal entrapment of the particles, where calcein fluorescence was self-quenched and could barely be detected.<sup>27–29</sup> On the contrary, cells incubated with calcein-loaded MSN-PEPT showed strong green fluorescence with a slight diffusion pattern, which was ascribed to effective endosomal escape.<sup>10</sup> The explanation to this could be based on MSN-PEPT disrupting the endosomes, probably through proton sponge effect.<sup>30</sup> Therefore, calcein would be no longer self-quenched, showing strong green fluorescence and confirming the endosomal escape capabilities of the here designed nanocarrier.

❖ *Evaluation of cytotoxicity in 2D cell cultures*

The cytotoxicity was first evaluated in 2D HeLa cell cultures. For that purpose, MSNs and MSN-PEPT were loaded with TOP and incubated with the cells at a concentration of 25 µg/mL (Figure 3.15).

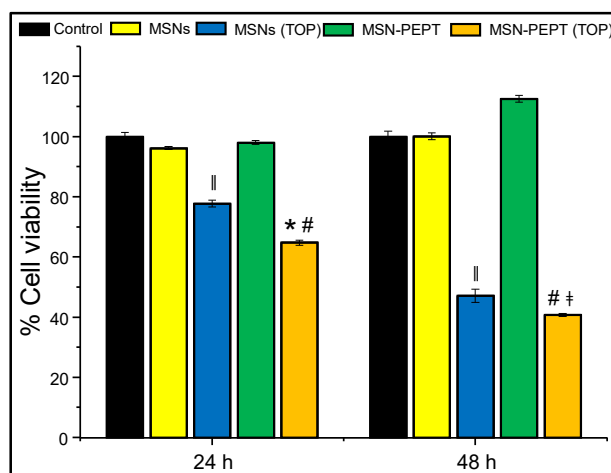


**Figure 3.15.** Evaluation of HeLa cell viability using unloaded and TOP-loaded MSNs and MSN-PEPT. The group MSN-PEPT loaded with the drug was able to induced significant cell death compared to rest of the groups.  $\parallel p < 0.01$  vs MSNs and control;  $* p < 0.01$  vs MSNs (TOP);  $\# p < 0.01$  vs MSN-PEPT and control;  $\ddagger p < 0.05$  vs MSNs (TOP).

As shown in Figure 3.15, the viability of cells incubated with MSNs was unaffected, demonstrating the suitability of using this type of particles as platform for drug delivery. The cytotoxicity of TOP-loaded MSNs was expected to be lower than that observed in Figure 3.15 owing to the lack of targeting agents. However, it should be mentioned that MSNs had no gatekeepers closing the pore entrances and, consequently, the drug could freely diffuse out of the pores. As a result, TOP located outside the cells could passively diffuse inside the cells, leading to higher cytotoxic effect than expected. This observation highlighted the need of a diffusion barrier at the pore entrances.

The viability of the cells incubated with MSN-PEPT remained unaffected during the whole experiment, demonstrating the biocompatibility of the here engineered carrier *per se*. On the other hand, TOP-loaded MSN-PEPT exerted significant toxicity on the cells, highlighting the ability of the system to internalize cytotoxic compounds. Compared to its unloaded counterpart, the drug-loaded group was able to eliminate up to 60% of the cells after 48 hours of experiment. In addition, TOP-loaded MSN-PEPT induced significantly higher cytotoxicity than TOP-loaded MSNs for all the time points studied.

The ability of MSN-PEPT to inhibit cellular proliferation was further evaluated using A549 2D cell cultures. For that purpose, MSNs and MSN-PEPT were loaded with DOX and incubated with the cells at a concentration of 50  $\mu\text{g/mL}$  (Figure 3.16).

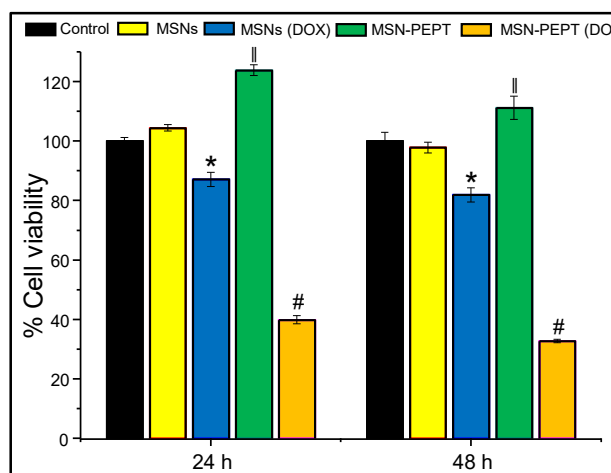


**Figure 3.16.** Evaluation of A549 cell viability using unloaded and DOX-loaded MSNs and MSN-PEPT. The group MSN-PEPT loaded with the drug was able to induced significant cell death compared to rest of the groups. †  $p < 0.01$  vs control \*  $p < 0.01$  vs MSNs and control; #  $p < 0.01$  vs MSN-PEPT, MSNs (DOX) and control.

As shown in Figure 3.16, the viability of the cells incubated with MSNs was unchanged, demonstrating the biocompatibility of mesoporous silica nanoparticles, regardless of the cell line employed. In this case, DOX-loaded MSNs led to reduced cell viability. The experimental evidence is that DOX strongly interacts with the silanol groups of MSNs. In this sense, DOX premature release would be lower than that observed for TOP and, consequently, the amount of free DOX in the medium would be lower, leading to less inhibition of the cell viability. Besides, MSNs lacked of biotin targeting so the total amount of particles in the cells was lower.

MSN-PEPT had a statistically significant positive effect on the viability of A549 cells, indicating again its high biocompatibility, independently of the cell line studied. On the other hand, DOX-loaded MSN-PEPT dramatically reduced the cell viability within the first 24 hours by *ca.* 60% and *ca.* 70% at 48 hours. Interestingly, the cytotoxic effect of DOX-loaded MSN-PEPT was much higher than that of DOX-loaded. This was a direct consequence of the enhanced uptake of the particles bearing the peptidic fragment, confirming the suitability of using active targeting moieties in combination with nanoparticles.

### 3.2.3.5. 3D cellular experiments

#### ❖ Endosomal escape in 3D cell cultures

The endosomal escape capability of MSN-PEPT was further evaluated using A549 3D cell cultures. For that purpose, MSNs and MSN-PEPT were loaded with calcein and

incubated with the spheroids. The outcome of the experiment was evaluated by confocal microscopy (Figure 3.17).

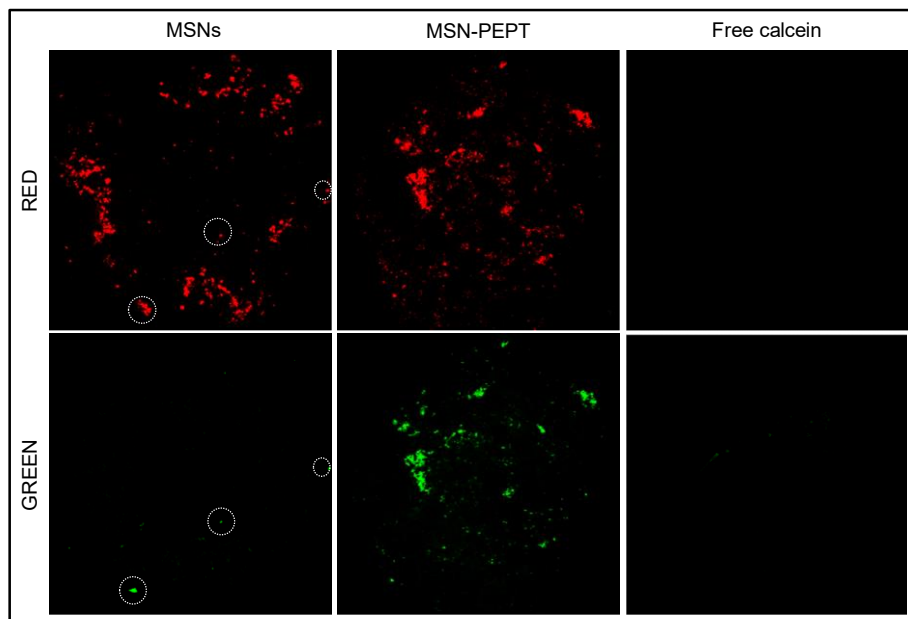


**Figure 3.17.** Evaluation of the endosomal escape of MSNs and MSN-PEPT in A549 spheroids. The MSNs (left) remained trapped within the endo-lysosomes and, consequently, calcein was undetectable. White dots indicate residual areas where endosomal escape took place for MSNs. On the contrary, MSN-PEPT (center) could escape and a strong signal could be detected. Free calcein (right) could not be incorporated owing to its membrane impermeable nature.

As observed in Figure 3.17, free calcein could not be internalized by the cells, in agreement with Figure 3.14. The degree of endosomal escape for MSNs was almost negligible. The particles remained inside the endo-lysosomes and, consequently, calcein fluorescence was self-quenched and its intensity was too low to be detected. Only a residual amount of particles could escape the endosomes and showed strong green fluorescence. On the contrary, strong green fluorescence could be observed in the spheroid treated with MSN-PEPT. This fluorescent signal confirmed that this group of particles was no longer trapped within the endo-lysosomes. In consequence, self-quenching did not take place and calcein could be detected.

The combination of the results shown in Figures 3.14 and 3.17 confirmed the ability of MSN-PEPT to induce endosomal escape. In addition, MSN-PEPT could internalize and release a membrane impermeable cargo. This might be useful to encapsulate membrane impermeable drugs with high biological activity that otherwise would be discarded and would not reach the clinic. Besides, it would be useful to avoid the degradation that some therapeutics compounds might undergo when trapped in the endo-lysosomal pathway, thus increasing the efficacy of the treatment.

❖ *Accumulation of Nanoparticles in 3D Cell Cultures*

The performance of Rhodamine B-labelled MSN-PEPT in 3D cellular spheroids was evaluated using confocal microscopy. MSNs were used as control. First, both groups of particles were incubated with A549 spheroids (Figure 3.18).

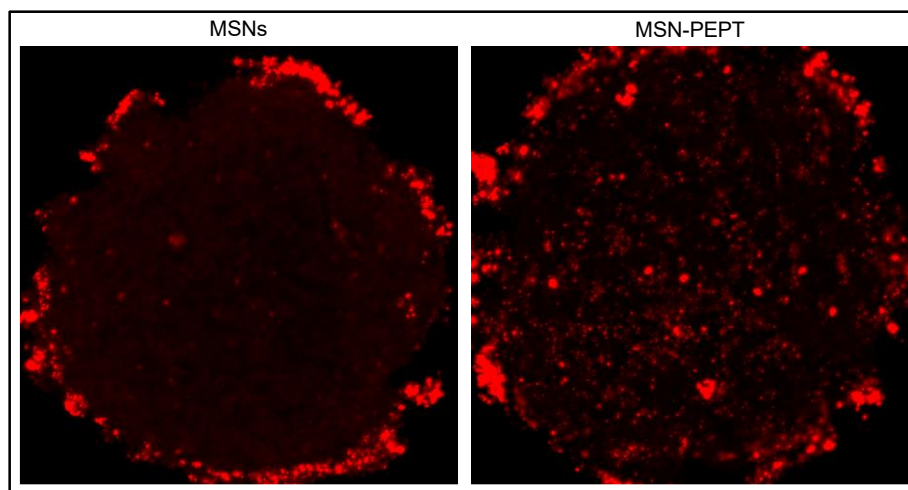


**Figure 3.18.** Confocal microscopy of MSN and MSN-PEPT incubated with A549 3D cellular spheroids. Higher accumulation of particles could be observed for MSN-PEPT, as expected owing to the overexpressed biotin receptors in these cells.

As observed in Figure 3.18, the group MSN-PEPT (right) led to the greater accumulation of nanoparticles, confirming the active targeting of the compound **22**. The depth reached by the particles in the spheroid was analyzed using ImageJ software (Figure 3.19). This software allows the measurement of the red intensity of each layer generated by the confocal microscope, obtaining the distribution of the particles through the spheroids.

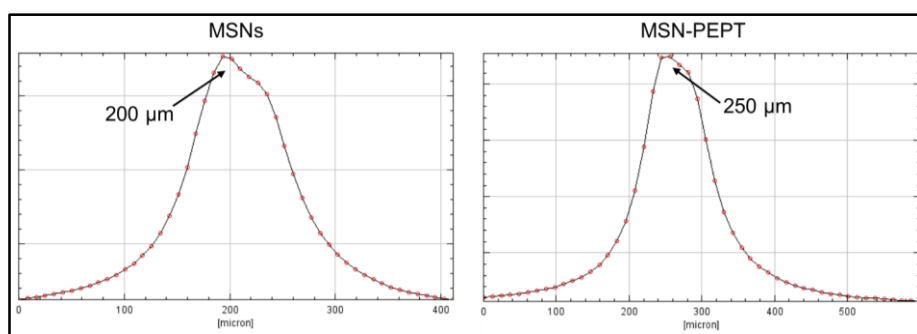


**Figure 3.19.** Depth analysis of MSN and MSN-PEPT using the ImageJ software. The particles containing the biotinylated peptide were able to reach deeper depth (250  $\mu\text{m}$  vs 200  $\mu\text{m}$ ).

The depth analysis (Figure 3.19) demonstrated that the majority of the MSN-PEPT particles (right) could locate deeper in the 3D cellular spheroids (*ca.* 250  $\mu\text{m}$ ) compared to MSNs (left), which could only penetrate *ca.* 200  $\mu\text{m}$ .

Both groups of particles were also incubated with OVCAR8 spheroids and the results were analyzed by confocal microscopy (Figure 3.20).

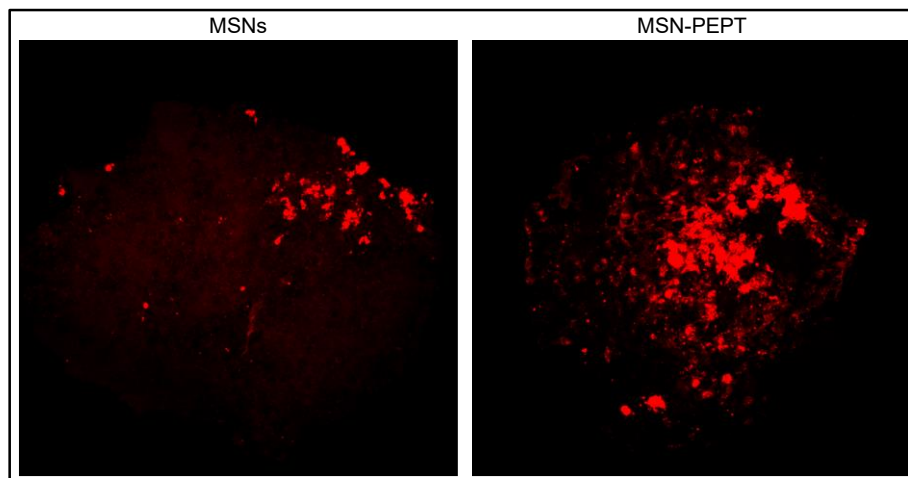


**Figure 3.20.** Confocal microscopy of MSN and MSN-PEPT incubated with OVCAR8 3D cellular spheroids. The group MSN-PEPT yielded a higher accumulation of particles in the spheroids, as expected for cells overexpressing biotin receptors.

Analogous results were obtained when MSN-PEPT were used with OVCAR8 spheroids. As observed in Figure 3.20, the biotinylated particles (right) showed higher accumulation of particles in the spheroid, in agreement with the presence of biotin receptors in these cells. This was a demonstration of the targeting ability of the system here designed and developed, independently of the tumoral cell type evaluated as long as biotin receptors are overexpressed.

The penetration of the particles in the spheroid was analyzed using the ImageJ software (Figure 3.21).

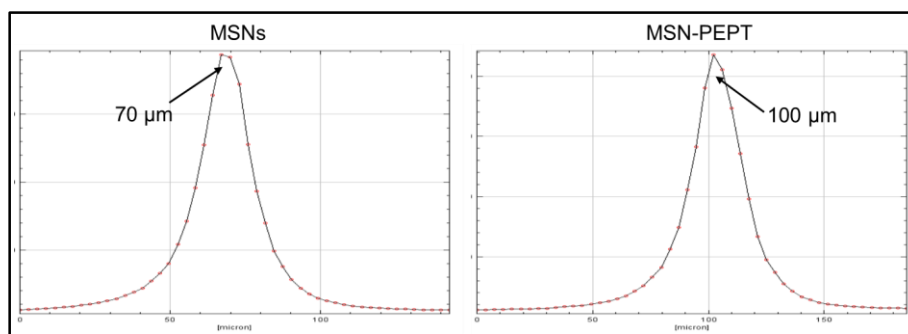


**Figure 3.21.** Depth analysis of MSN and MSN-PEPT using the ImageJ software. MSN-PEPT could reach deeper depth in the OVCAR8 spheroids, compared to pristine MSNs (100 μm vs 70 μm).

The depth analysis of the OVCAR8 spheroids (Figure 3.21) showed analogous results as those observed for A549 spheroids (Figure 3.19). In this case, the majority of the MSN-PEPT particles (right) could penetrate *ca.* 100 μm. On the contrary, bare MSNs (left)

could reach only *ca.* 70  $\mu\text{m}$ . The reason for the lower values obtained in the case of the OVCAR8 spheroids (70 and 100  $\mu\text{m}$  vs 200 and 250  $\mu\text{m}$ ) was the smaller size of these spheroids compared to the A549 ones. The experimental evidence was that A549 cells were objectively bigger than OVCAR8 and, consequently, the former led to bigger spheroids every time both types of spheroids were grown.

Overall, the general trend observed in both types of cellular spheroids was that the particles containing the biotinylated peptide could penetrate deeper than MSNs. The rationale behind these results might rely on the endosomal escape capability demonstrated by MSN-PEPT. In this sense, it has been shown that endo-lysosomal entrapment limits the exocytosis of nanoparticles.<sup>31,32</sup> Besides, it has been demonstrated that the rate of transcytosis decreases when the nanoparticles remain trapped in the lysosomes.<sup>33</sup> Furthermore, it has been reported that nanoparticles that achieve exocytosis lead to higher penetration in spheroids through transcytosis.<sup>34</sup>

In view of the results shown in Figures 3.19 and 3.21 and the just-mentioned reported evidences, the higher penetration observed for MSN-PEPT might be ascribed to transcytosis events. The endosomal escape would lead to the exocytosis of the particles through inner areas of the spheroids and, consequently, these particles would be internalized again by inner cell layers, achieving effective transcellular transport and improving the penetration ability of the system containing the biotinylated peptide.

❖ *Evaluation of cytotoxicity in 3D cellular models*

The cytotoxicity was further studied using A549 3D cellular spheroids. For that purpose, MSNs and MSN-PEPT were loaded with DOX and incubated with the spheroids using 2 different concentrations. A control group without particles was also included. The cytotoxic effect exerted by the particles was evaluated measuring the volume of the spheroids at different time points, according to a previously reported work.<sup>13</sup> Figure 3.22 shows the results obtained at a particle concentration of 35  $\mu\text{g/mL}$ .



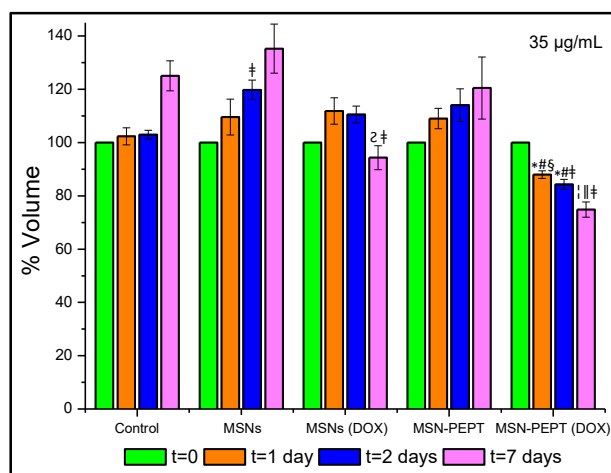


**Figure 3.22.** Evaluation of the spheroid viability in terms of % volume using unloaded and DOX-loaded MSNs and MSN-PEPT at a concentration of 35 µg/mL. The group MSN-PEPT loaded with the drug was able to significantly reduced the volume, compared to rest of the groups. \*  $p < 0.01$  vs MSN-PEPT; †  $p < 0.05$  vs MSN-PEPT; #  $p < 0.01$  vs MSN (DOX); ‡  $p < 0.05$  vs MSN (DOX); §  $p < 0.05$  vs MSN; †  $p < 0.01$  vs Control; §  $p < 0.05$  vs Control.

As shown in Figure 3.22, the volume of the spheroids incubated with MSNs followed the trend observed for the control group without particles, demonstrating the biocompatibility of this type of particles in more complex biological scenarios. Only a slight volume decrease could be observed for DOX-loaded MSNs after 7 days, as it was expected owing to the lack of active targeting.

The growth of the spheroids incubated with unloaded MSN-PEPT was comparable to that of the control group, indicating the biocompatibility of the here designed carrier and confirming the results obtained in Section 3.2.3.6. The best results were obtained for DOX-loaded MSN-PEPT, which was able to reduce the volume by *ca.* 20% after 7 days. Indeed, this group induced significant reduction after only 48 hours compared to all groups. This could be explained taking into account that MSN-PEPT and consequently, DOX, accumulated more and deeper in the spheroids, compared to bare MSNs, leading to higher cytotoxic effects. The results obtained at a concentration of 70 µg/mL are shown in Figure 3.23.

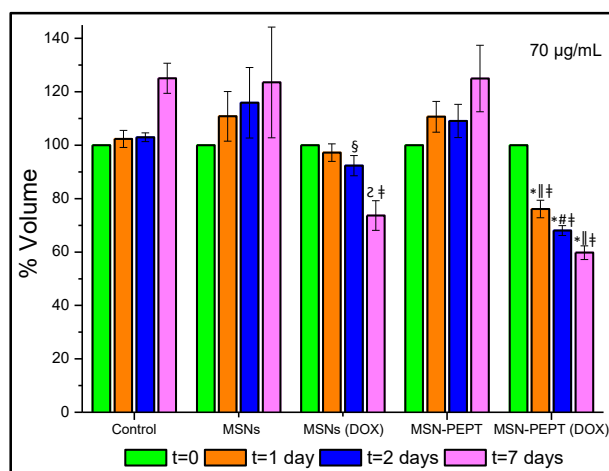


**Figure 3.23.** Evaluation of the spheroid viability in terms of % volume using unloaded and DOX-loaded MSNs and MSN-PEPT at a concentration of 70 µg/mL. The group MSN-PEPT loaded with the drug was able to significantly reduced the volume, compared to rest of the groups. MSN (DOX) was also able to reduce the volume at this concentration. \*  $p < 0.01$  vs MSN-PEPT; †  $p < 0.05$  vs MSN-PEPT; #  $p < 0.01$  vs MSN (DOX); ‡  $p < 0.05$  vs MSN (DOX); §  $p < 0.05$  vs Control; ¶  $p < 0.01$  vs Control.

The incubation of MSNs with spheroids at a higher concentration had no effect on the spheroid volume. In this case, the effect of DOX-loaded MSNs at 7 days was much higher than that observed at a concentration of 35 µg/mL (Figure 3.22), although only a slight reduction could be observed at 48 hours. This might be explained as follows. From the results shown in Figures 3.18 and 3.19, (1) the amount of MSNs in A549 spheroids was lower than that of MSN-PEPT and (2) MSN-PEPT reached deeper areas. For such reason, the amount of DOX in the spheroids incubated with DOX-loaded MSNs would be lower and would penetrate less than that of DOX-loaded MSN-PEPT and, consequently, DOX-loaded MSNs would require longer periods of time to exert appreciable cytotoxicity.

The growth of the spheroids was also unaffected when a higher concentration of unloaded MSN-PEPT (70 µg/mL) was employed, confirming again its highly biocompatible nature and paving the way for future *in vivo* studies of the here engineered carrier. As shown in Figure 3.23, the spheroids incubated with DOX-loaded MSN-PEPT reduced their volume by *ca.* 30% after only 48 hours and *ca.* 40% after 7 days, confirming their ability to penetrate in the spheroid and deliver the drug to the tumoral cells.

### 3.2.3.6. Chicken Embryo Model

Once the behavior of MSN-PEPT was evaluated in 2D and 3D *in vitro* models, the next step was to evaluate its performance in a preliminary *in ovo* model. For that purpose, A549 cells were grown on the CAM membrane of chicken embryos until a tumoral mass could be clearly observed. Then, Rhodamine B-labelled MSN-PEPT was administered

via vein injection and allowed to circulate in the bloodstream for 48 hours. The biodistribution was evaluated through fluorescence microscopy (Figure 3.24).

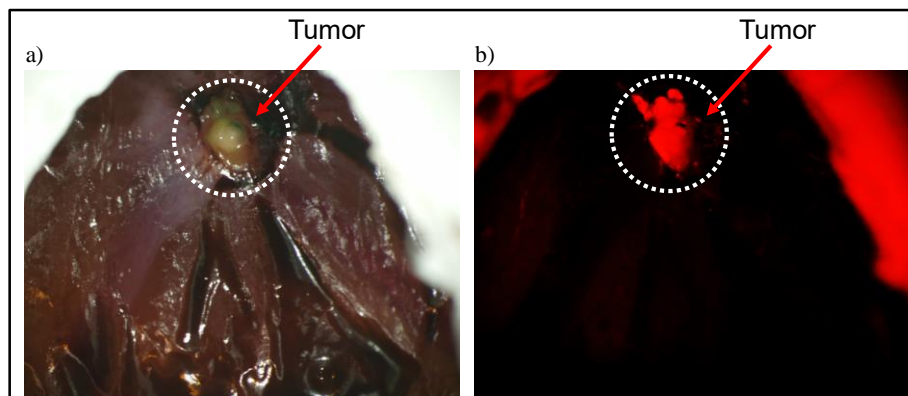


**Figure 3.24.** Analysis of the biodistribution of MSN-PEPT by fluorescence microscopy. a) Bright field. b) Red fluorescence. 48 hours after the injection the red fluorescence of particles could be observed in the tumor, confirming the passive accumulation of the particles.

The red fluorescence of the particles could be detected in the tumor 48 hours after the administration of MSN-PEPT, confirming that the carrier could passively target the tumor *via* EPR effect, as it happens with many commercialized nanomedicines.<sup>35</sup> Then, the animals were dissected and imaged to find out if the particles accumulated preferentially in the tumor (Figure 3.25).

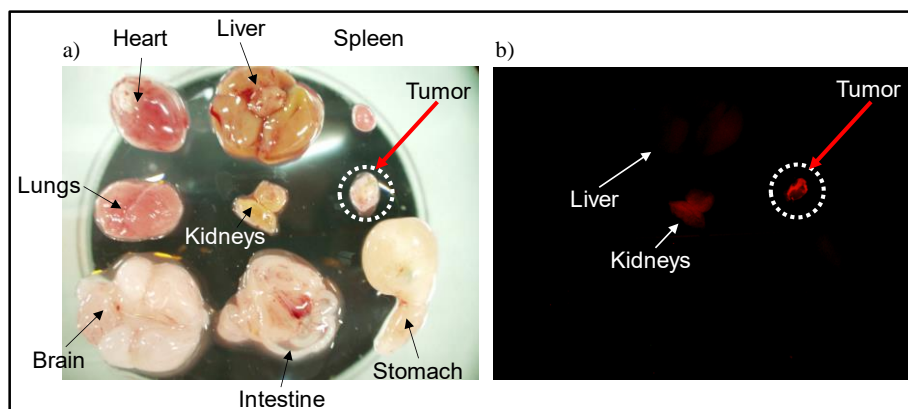


**Figure 3.25.** Imaging of the organs and tumor of dissected chicken embryo. a) Bright field. b) Red fluorescence. The particles preferentially accumulated in the tumor, showing only minor accumulation in the liver and kidneys.

Overall, the particles were undetectable in the organs and only minor accumulation could be observed in the liver and kidneys. On the other hand, the bright red fluorescence in the tumor confirmed the preferential accumulation of MSN-PEPT in the tumor tissue, in agreement with Figure 3.24. These observations confirmed that the here engineered nanocarrier was colloidally stable, since it could circulate for long periods of time in the chicken egg without forming aggregates (otherwise a thrombus would form and the

chicken embryo would dye), leading to its passive accumulation in the tumoral mass *via* the EPR effect. In addition, the preferential accumulation of the particles in the tumor was consequence of their low clearance from the bloodstream, highlighting again the biocompatibility of the here synthesized nanocarrier.

Once the ability of MSN-PEPT to preferentially accumulate in the tumor was confirmed, the next step was to evaluate whether these particles could inhibit tumor growth. For that purpose, a preliminary cytotoxicity study using DOX-loaded MSN-PEPT was carried out. The particles were administered *via* vein injection to tumor-bearing chicken embryos and subsequently imaged after 48 hours (Figure 3.25).

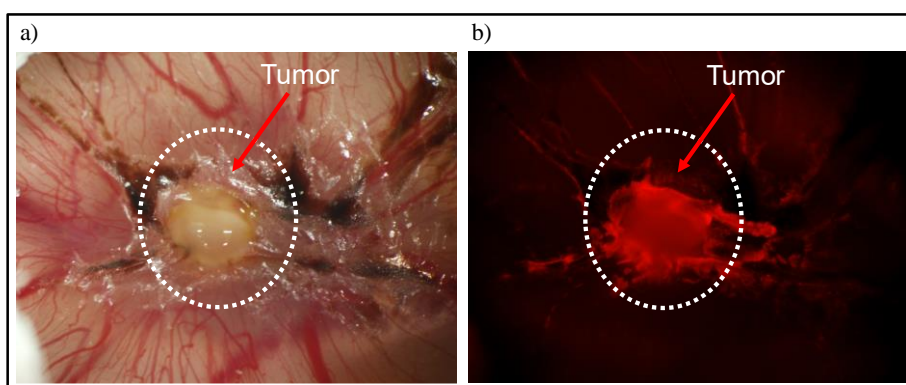


**Figure 3.25.** Analysis of the biodistribution of DOX-loaded MSN-PEPT by fluorescence microscopy. a) Bright field. b) Red fluorescence. The strong red fluorescence confirmed that the encapsulated DOX accumulated in the tumor.

As shown in Figure 3.25, the cytotoxics were accumulated preferentially in the tumor as a consequence of the passive accumulation in the tumor *via* EPR effect of DOX-loaded MSN-PEPT, confirming the suitability of mesoporous carriers to reduce typical side effects originated by the non-specific distributions of the drugs. After 3 days, the chicken embryos were sacrificed and the effect of DOX-loaded MSN-PEPT on the tumor growth was evaluated in terms of tumor weight reduction (Figure 3.26).

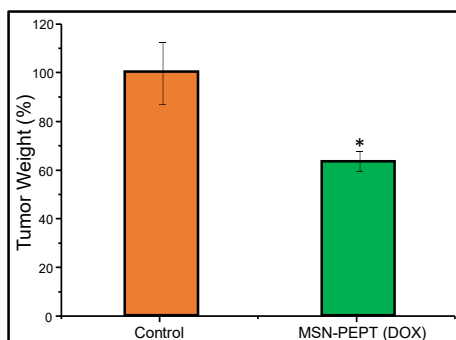


**Figure 3.26.** Inhibition of the tumor growth by DOX-loaded MSN-PEPT. In this preliminary study (n=3 for the control and n=2 for MSN-PEPT (DOX)) the carrier demonstrated its ability to reduce the tumor weight by *ca.* 30% after 3 days.

As shown in Figure 3.26, the DOX-loaded nanocarrier could reduce the tumor weight by *ca.* 30% after only 3 days of treatment, indicating the suitability of MSN-PEPT as drug delivery system with potential applicability to the treatment of solid tumors.

### 3.2.4. Conclusions

The objective of this last work was to develop a system able to overcome some of the biological barriers that nanoparticles have to face when interacting with living organisms. In particular, the accumulation of the particles in the tumoral mass, the preferential targeting of tumoral cells and the avoidance of endo-lysosomal entrapment were studied.

The macromolecule able to target cancer cells and induce endosomal escape was designed using biotin as model binding motif and histidine as buffering agent. That macromolecule was successfully synthesized using standard solid phase peptide synthesis and effectively grafted to the redox-responsive nanoparticles previously developed in this thesis.

The performance of the system with living organisms was thoroughly studied using 2D and 3D cellular models and a preliminary *in ovo* model using chicken embryos. The targeting ability of the peptidic fragment was quantitatively validated using 2D cell cultures. These tests demonstrated the outstanding targeting capacity of the system, probably due to collaborative effects ascribed to the appearance of local positive charges. In addition, the cellular uptake of the system was qualitatively analyzed in alternative cells overexpressing biotin receptors, showing significant particle accumulation within the cells and paving the way for the use of 3D cell cultures.

The endosomal escape was evaluated using calcein as model membrane impermeable dye in 2D and 3D cell cultures. The results here obtained demonstrated that only MSN-PEPT could achieve effective endosomal escape, as demonstrated by the strong green fluorescence observed. However, MSNs remained entrapped in the endo-lysosomes and calcein could barely be detected as a consequence of self-quenching.

The evaluation of particle accumulation in cellular spheroids revealed that MSN-PEPT presented greater and deeper accumulation in the spheroids than pristine MSNs. These results were ascribed to the achievement of effective endosomal escape which, according to the literature, would be related to enhanced transcytosis events.

The biocompatibility of the carrier was evaluated *in vitro*, using 2D and 3D cell cultures, and *in ovo* using the chicken embryo model. To validate the versatility of the carrier, MSN-PEPT was loaded with different drugs and incubated various cell lines. The obtained results demonstrated that only the targeted material could significantly reduce the cell viability. The biocompatibility was further evaluated using spheroids and drug-loaded MSN-PEPT, demonstrating that the highest inhibition of spheroid volume was obtained for the here engineered material.

Finally, the performance of the designed nanocarrier in a more complex system was evaluated using tumor-bearing chicken embryos. The results demonstrated that MSN-PEPT preferentially accumulated in the tumors, probably *via* EPR effect, without aggregating in the bloodstream nor inducing embryo death, demonstrating its colloidal stability and biocompatibility. In addition, a preliminary efficacy study was carried out using drug-loaded MSN-PEPT. The particles showed preferential accumulation in the tumor and could significantly reduce the tumor weight in only 3 days, paving the way for future *in vivo* experiments and for its potential use in cancer treatment.

## References

- (1) Blanco, E.; Shen, H.; Ferrari, M. Principles of Nanoparticle Design for Overcoming Biological Barriers to Drug Delivery. *Nat. Biotechnol.* **2015**, *33*, 941–951.
- (2) Ren, W. X.; Han, J.; Uhm, S.; Jang, Y. J.; Kang, C.; Kim, J. H.; Kim, J. S. Recent Development of Biotin Conjugation in Biological Imaging, Sensing, and Target Delivery. *Chem. Commun.* **2015**, *51*, 10403–10418.
- (3) Russell-Jones, G.; Mctavish, K.; Mcewan, J.; Rice, J.; Nowotnik, D. Vitamin-Mediated Targeting as a Potential Mechanism to Increase Drug Uptake by Tumours. *J. Inorg. Biochem.* **2004**, *98*, 1625–1633.
- (4) Sun, P.; Huang, W.; Kang, L.; Fan, B.; Jin, H.; Wang, Q.-M.; Gao, Z. SiRNA-Loaded Poly(Histidine-Arginine)6-Modified Chitosan Nanoparticle With Enhanced Cell- Penetrating and Endosomal Escape Capacities for Suppressing Breast Tumor Metastasis. *Int. J. Nanomedicine* **2017**, *12*, 3221–3234.
- (5) Midoux, P.; Pichon, C.; Yaouanc, J. J.; Jaffrès, P. A. Chemical Vectors for Gene Delivery: A Current Review on Polymers, Peptides and Lipids Containing Histidine or Imidazole as Nucleic Acids Carriers. *Br. J. Pharmacol.* **2009**, *157*, 166–178.
- (6) Liang, K.; Richardson, J. J.; Ejima, H.; Such, G. K.; Cui, J.; Caruso, F. Peptide-Tunable Drug Cytotoxicity via One-Step Assembled Polymer Nanoparticles. *Adv. Mater.* **2014**, *26*, 2398–2402.
- (7) Smith, S. A.; Selby, L. I.; Johnston, A. P. R.; Such, G. K. The Endosomal Escape of Nanoparticles: Toward More Efficient Cellular Delivery. *Bioconjug. Chem.* **2019**, *30*, 263–272.
- (8) Argyo, C.; Weiss, V.; Bräuchle, C.; Bein, T. Multifunctional Mesoporous Silica Nanoparticles as a Universal Platform for Drug Delivery. *Chem. Mater.* **2014**, *26*, 435–451.
- (9) Zanoni, M.; Piccinini, F.; Arienti, C.; Zamagni, A.; Santi, S.; Polico, R.; Bevilacqua, A.; Tesei, A. 3D Tumor Spheroid Models for *in vitro* Therapeutic Screening: A Systematic Approach to Enhance the Biological Relevance of Data Obtained. *Sci. Rep.* **2016**, *6*, 19103.
- (10) Smith, S. A.; Selby, L. I.; Johnston, A. P. R.; Such, G. K. The Endosomal Escape of Nanoparticles: Toward More Efficient Cellular Delivery. *Bioconjug. Chem.* **2018**, *30*, 263–272.
- (11) Vu, B. T.; Shahin, S. A.; Croissant, J.; Fatieiev, Y.; Matsumoto, K.; Le-Hoang Doan, T.; Yik, T.; Simargi, S.; Conteras, A.; Ratliff, L.; *et al.* Chick Chorioallantoic Membrane Assay as an *in vivo* Model to Study the Effect of Nanoparticle-Based Anticancer Drugs in Ovarian Cancer. *Sci. Rep.* **2018**, *8*, 8524.
- (12) Ribatti, D. The Chick Embryo Chorioallantoic Membrane as a Model for Tumor Biology. *Exp. Cell Res.* **2014**, *328*, 314–324.
- (13) Lee, J. Y.; Chung, S. J.; Cho, H. J.; Kim, D. D. Phenylboronic Acid-Decorated Chondroitin Sulfate A-Based Theranostic Nanoparticles for Enhanced Tumor

- Targeting and Penetration. *Adv. Funct. Mater.* **2015**, *25*, 3705–3717.
- (14) Torres, A. G.; Gait, M. J. Exploiting Cell Surface Thiols to Enhance Cellular Uptake. *Trends Biotechnol.* **2012**, *30*, 185–190.
  - (15) Samanta, S.; Tamura, S.; Dubeau, L.; Mhaweche-Fauceglia, P.; Miyagi, Y.; Kato, H.; Lieberman, R.; Buckanovich, R. J.; Lin, Y. G.; Neamati, N. Expression of Protein Disulfide Isomerase Family Members Correlates with Tumor Progression and Patient Survival in Ovarian Cancer. *Oncotarget* **2017**, *8*, 103543–103556.
  - (16) Putnam, D.; Gentry, C. A.; Pack, D. W.; Langer, R. Polymer-Based Gene Delivery with Low Cytotoxicity by a Unique Balance of Side-Chain Termini. *Proc. Natl. Acad. Sci.* **2012**, *98*, 1200–1205.
  - (17) Bilalis, P.; Tziveleka, L.-A.; Varlas, S.; Iatrou, H. pH-Sensitive Nanogates Based on Poly(L-Histidine) for Controlled Drug Release from Mesoporous Silica Nanoparticles. *Polym. Chem.* **2016**, *7*, 1475–1485.
  - (18) Li, S.; Hong, M. Protonation, Tautomerization, and Rotameric Structure of Histidine: A Comprehensive Study by Magic-Angle-Spinning Solid-State NMR. *J. Am. Chem. Soc.* **2011**, *133*, 1534–1544.
  - (19) Seong, E.; Joon, H.; Na, K.; Han, Y. Poly(L-Histidine)-PEG Block Copolymer Micelles and pH-Induced Destabilization. *J. Control. Release* **2003**, 363–374.
  - (20) Michl, J.; Park, K. C.; Swietach, P. Evidence-Based Guidelines for Controlling pH in Mammalian Live-Cell Culture Systems. *Commun. Biol.* **2019**, *2*.
  - (21) Field, L. D.; Delehanty, J. B.; Chen, Y.; Medintz, I. L. Peptides for Specifically Targeting Nanoparticles to Cellular Organelles: Quo Vadis? *Acc. Chem. Res.* **2015**, *48*, 1380–1390.
  - (22) Hama, S.; Itakura, S.; Nakai, M.; Nakayama, K.; Morimoto, S.; Suzuki, S.; Kogure, K. Overcoming the Polyethylene Glycol Dilemma via Pathological Environment-Sensitive Change of the Surface Property of Nanoparticles for Cellular Entry. *J. Control. Release* **2015**, *206*, 67–74.
  - (23) Washington, W. A. S. Polyhistidine Mediates an Acid-Dependent Fusion of Negatively Charged Liposomes. *Biochemistry* **1984**, *23*, 4409–4416.
  - (24) Buré, C.; Maget, R.; Delmas, A. F.; Pichon, C.; Midoux, P. Histidine-Rich Peptide: Evidence for a Single Zinc-Binding Site on H5WYG Peptide That Promotes Membrane Fusion at Neutral pH. *J. Mass Spectrom.* **2009**, *2008*, 81–89.
  - (25) Krishnan, A.; Verma, S. K.; Mani, P.; Gupta, R.; Kundu, S.; Sarkar, D. P. A Histidine Switch in Hemagglutinin-Neuraminidase Triggers Paramyxovirus-Cell Membrane Fusion. *J. Virol.* **2009**, *83*, 1727–1741.
  - (26) Fang, Y.; Xue, J.; Gao, S.; Lu, A.; Yang, D.; Jiang, H.; He, Y.; Shi, K. Cleavable PEGylation: A Strategy for Overcoming the “PEG Dilemma” in Efficient Drug Delivery. *Drug Deliv.* **2017**, *24*, 22–32.
  - (27) Simões, S.; Slepishkin, V.; Düzgünes, N.; Pedroso de Lima, M. C. On the Mechanisms of Internalization and Intracellular Delivery Mediated by pH-Sensitive Liposomes. *Biochim. Biophys. Acta - Biomembr.* **2001**, *1515*, 23–37.



- (28) Kono, K.; Igawa, T.; Takagishi, T. Cytoplasmic Delivery of Calcein Mediated by Liposomes Modified with a pH-Sensitive Poly(Ethylene Glycol) Derivative. *Biochim. Biophys. Acta - Biomembr.* **1997**, *1325*, 143–154.
- (29) Lattin, J. R.; Javadi, M.; McRae, M.; Pitt, W. G. Cytosolic Delivery via Escape from the Endosome Using Emulsion Droplets and Ultrasound. *J. Drug Target.* **2015**, *23*, 469–479.
- (30) Sun, X.; Luo, Y.; Huang, L.; Yu, B. Y.; Tian, J. A Peptide-Decorated and Curcumin-Loaded Mesoporous Silica Nanomedicine for Effectively Overcoming Multidrug Resistance in Cancer Cells. *RSC Adv.* **2017**, *7*, 16401–16409.
- (31) Ye, D.; Raghnaill, M. N.; Bramini, M.; Mahon, E.; Åberg, C.; Salvati, A.; Dawson, K. A. Nanoparticle Accumulation and Transcytosis in Brain Endothelial Cell Layers. *Nanoscale* **2013**, *5*, 11153–11165.
- (32) Kim, J. A.; Aberg, C.; Salvati, A.; Dawson, K. A. Role of Cell Cycle on the Cellular Uptake and Dilution of Nanoparticles in a Cell Population. *Nat. Nanotechnol.* **2012**, *7*, 62–68.
- (33) Cui, Y.; Shan, W.; Zhou, R.; Liu, M.; Wu, L.; Guo, Q.; Zheng, Y.; Wu, J.; Huang, Y. The Combination of Endolysosomal Escape and Basolateral Stimulation to Overcome the Difficulties of “Easy Uptake Hard Transcytosis” of Ligand-Modified Nanoparticles in Oral Drug Delivery. *Nanoscale* **2018**, *10*, 1494–1507.
- (34) Lu, H.; H. Utama, R.; Kitiyotsawat, U.; Babiuch, K.; Jiang, Y.; Stenzel, M. H. Enhanced Transcellular Penetration and Drug Delivery by Crosslinked Polymeric Micelles into Pancreatic Multicellular Tumor Spheroids. *Biomater. Sci.* **2015**, *3*, 1085–1095.
- (35) Grodzinski, P.; Kircher, M.; Goldberg, M.; Gabizon, A. Integrating Nanotechnology into Cancer Care. *ACS Nano* **2019**, *13*, 7370–7376.





# Chapter 4

## Conclusions / Conclusiones

*Investigar es ver lo que todo el mundo ha visto, y pensar lo que nadie más ha pensado.*

*Albert Szent-Györgyi*



## Conclusions

The overall objective of this doctoral thesis has consisted in the design and evaluation of engineered mesoporous nanoparticles for biomedical applications. In particular, this thesis has comprised the development of smart approximations for the treatment of complex diseases, such as bone and wound healing and cancer. The general conclusions that can be derived from the results here presented and discussed are the following.

- 1) The design of a pH-responsive nanocarrier based on MSNs and self-immolative polymers as gatekeepers was successful. The particles were successfully synthesized using the *sol-gel* method, yielding mesoporous and homogeneous nanoparticles. The synthesis of the polymer involved several optimizations of a previously reported method that provided a polyurethane with adequate molecular weight. Additionally, the pH-responsiveness of the here produced polymer was validated. The grafting protocol was optimized and the pH-responsive behavior of the SIP-coated MSNs was confirmed *in vial*. In addition, a preliminary *in vitro* study was conducted, demonstrating that these particles were biocompatible and could be internalized by tumoral cells.
- 2) The translation of the pH-responsive self-immolative technology to different mesoporous carbon matrices was completely successful. Prior to the functionalization with the pH-responsive polymers, it was shown that both types of carbon particles provided greater loading capacity than MSNs. Then, a grafting protocol was developed and the pH-responsiveness of the carriers was evaluated *in vial*, *in vitro* and *in vivo*, demonstrating that the release could be triggered at acid pH. In addition, it was shown *in vitro* that the presence of the pH-responsive trigger was essential for the self-immolation to occur. The biocompatibility of the SIP-coated carbons was evaluated *in vitro* and *in vivo*, showing excellent results. In addition, the carbons were loaded with a cytotoxic and their ability to inhibit the viability of cancer cells was successfully validated.
- 3) The translation of the pH-responsive self-immolative technology to the different mesoporous silica-based MOZART nanomatrices involved the development of 2 alternative grafting protocols to minimize the potential leakage of therapeutic ions. Using a carboxylic acid linker provided the best results, although the presence of a model fluorophore in the medium highly affected the final output of the functionalization. The SIP-coated MOZART particles were subjected to

release experiments to evaluate whether the self-immolative polymer could seal the mesopores. The results were, in general, not fully satisfactory, although promising results were obtained for one of the samples. The most feasible explanation for the here obtained results could be that the pores were too large to be sealed with this polyurethane. In this sense, the synthesis of bigger polymers was attempted with relatively low success. The functionalization of labelled matrices for future *in vivo* experiments was, in general, successful demonstrating that the polymer could still be grafted, regardless of presence of a covalently attached fluorophore.

- 4) Several *in vitro* and *in vivo* experiments carried out by members of the consortium demonstrated that the pH values found in chronic wound healing and delayed bone healing were 8 and 6.8, respectively. In consequence, the previously self-immolative polymer responsive to pH 5 was modified and the synthesis of alternative self-immolative triggers sensitive to pH 8 and 6.8 was attempted. The synthesis of a trigger sensitive to pH 8 involved the development of 3 protocols. In particular, the one based on using protecting groups involve 3 subprotocols. Unfortunately, all the attempts were unsuccessful and the trigger could not be synthesized. After exposing the results in a project meeting the consortium agreed to discard the synthesis of a trigger responsive to pH 8. With regard to pH 6.8, the trigger was successfully synthesized, although it could not be incorporated as endcap for the self-immolative polyurethane, despite different approaches were employed. In view of these results, the consortium activated a contingency plan and the synthesis of a polymer showing a totally different behavior was attempted. Unfortunately, the polymerization of the monomer was unsuccessful despite different approaches were follow. The consortium finally agreed to discard the synthesis of a polymer responsive to pH 6.8.
- 5) The use of redox species overexpressed in the cytoplasm of cells was explored as alternative stimulus to trigger the release from a carrier with potential application in cancer treatment. A small redox-responsive self-immolative molecule was synthesized and further grafted to MSNs to hamper premature release. This process initially involved the optimization of the silylation of the self-immolative molecule. Then, its grafting to the surface of mesoporous silica was also optimized. The particles were PEGylated to improve their colloidal stability and endow them with stealth properties. The redox-responsive behavior was validated

soaking the particles in a solution containing a redox agent, and it was shown that the self-immolative molecule was no longer grafted to the particles, probably because it suffered cyclization and subsequent self-immolation. Finally, the ability of the molecule to delay premature release was evaluated *in vial*, demonstrating that a higher amount of dye could be released when a redox agent was present in the medium.

- 6) The last part of this thesis involved the development of a system able to overcome relevant biological barriers. For that purpose, the redox-responsive system previously engineered was employed as starting material. A peptidic molecule containing a cancer-specific binding motif and a fragment with endosomal escape capabilities was synthesized and further grafted to the redox-responsive MSNs. The biological performance was evaluated in 2D and 3D cell cultures. The here designed nanocarrier could be preferentially internalized by cancer cells rather than normal cells. Besides, this system shown higher internalization than the rest of the controls, indicating the positive effect of the peptidic fragment. In addition, it was shown that the particles bearing the peptidic molecule could internalize deeper in cellular spheroids, probably thanks to transcytosis events. The targeted redox-responsive nanoparticles were shown to be totally biocompatible in 2D and 3D *in vitro* models. Furthermore, the drug-loaded particles could significantly inhibit cellular growth in cell monolayers and cellular spheroids, indicating its potential applicability as drug delivery systems. The accumulation of the particles in the tumoral mass was validated using tumor-bearing chicken embryos, where it could be observed that the particles preferentially accumulated in the tumoral mass rather than in the rest of the organs, highlighting the excellent biocompatibility of the here designed nanocarrier. Finally, a preliminary tumor elimination experiment was conducted, showing that the drug-loaded particles could significantly inhibit the tumor weight in a short period of time.

In summary, the work carried out during this doctoral thesis reinforces the suitability of using mesoporous nanocarriers as drug delivery systems. In addition, the usefulness of using self-immolative chemistry to endow mesoporous nanocarriers with stimuli-responsiveness has been validated, and might pave the way for future cutting-edge smart gatekeepers. Finally, a simple but effective peptide-like fragment able to overcome relevant biological barriers has been reported, whose main feature is the possibility of



tuning the membrane binding motif so that different types of cancer cells can be targeted on-demand.

## Conclusiones

El objetivo general de esta tesis doctoral ha consistido en el diseño y evaluación de nanopartículas mesoporosas funcionalizadas para aplicaciones biomédicas. En particular, esta tesis ha comprendido el desarrollo de aproximaciones inteligentes para el tratamiento de enfermedades complejas como las de hueso y piel o el cáncer. Las conclusiones generales que pueden derivarse de los resultados aquí presentados y discutidos son las siguientes.

- 1) El diseño de un nanotransportador sensible al pH basado en MSNs y polímeros autoinmolativos como compuertas fue satisfactorio. Las partículas fueron correctamente funcionalizadas utilizando el método *sol-gel*, dando lugar a nanopartículas homogéneas y mesoporosas. La síntesis del polímero implicó varias optimizaciones de un método previamente reportado, el cual finalmente dio lugar a un poliuretano con un peso molecular adecuado. Adicionalmente, la respuesta al pH del polímero fue validada. El protocolo de anclaje fue optimizado y la respuesta al pH de las partículas funcionalizadas con el SIP fue confirmada *in vial*. Además, un estudio preliminar *in vitro* fue llevado a cabo, demostrando que las partículas eran biocompatibles y que podían ser internalizadas por las células tumorales.
- 2) La traslación de la tecnología autoinmolativa sensible al pH a las diferentes matrices mesoporosas de carbono fue exitosa. Antes de proceder a dicha funcionalización, se demostró que ambos tipos de partículas de carbono proporcionaban mayor capacidad de carga que las MSNs. Tras ello, se desarrolló un protocolo de anclaje y la respuesta al pH de las matrices funcionalizadas fue evaluado *in vial*, *in vitro* e *in vivo*, demostrando que la liberación podía ser iniciada a pH ácido. Además, se demostró *in vitro* que la presencia del fragmento iniciador de la autoinmolación sensible al pH era vital para que este proceso ocurriera. La biocompatibilidad de las partículas de carbono funcionalizadas fue evaluada *in vitro* e *in vivo*, mostrando resultados excelentes. Además, las partículas fueron cargadas con un citotóxico y su habilidad para inhibir la viabilidad de células tumores fue demostrada con éxito.
- 3) La traslación de la tecnología autoinmolativa sensible al pH a las diferentes nanomatrices mesoporosas basadas en sílice proporcionadas por el consorcio MOZART implicó el desarrollo de 2 métodos de anclaje alternativos con el fin de

minimizar la potencial pérdida de iones terapéuticos durante los pasos de síntesis y lavado. El uso de un *linker* que contenía un ácido carboxílico proporcionó los mejores resultados, aunque la presencia del fluoróforo en el medio afectó el rendimiento final de la funcionalización. Las partículas funcionalizadas con el polímero fueron sometidas a experimentos de liberación para evaluar si el polímero autoinmolativo podía cerrar los poros. Los resultados fueron, en general, no satisfactorios, aunque se obtuvieron algunos resultados prometedores para una de las muestras. La explicación más probable para estos resultados podría ser que los poros eran demasiado grandes para ser tapados por un polímero como el empleado. En este sentido, se intentó sintetizar polímeros más grandes, aunque con bajo éxito. La funcionalización de las matrices marcadas para futuros experimentos *in vivo* fue, en general, satisfactoria demostrando que el polímero se podía seguir anclando a la superficie independientemente de la presencia de un fluoróforo previamente anclado de forma covalente.

- 4) Varios experimentos *in vitro* e *in vivo* llevados a cabo por miembros del consorcio demostraron que los valores de pH encontrados en ambientes de reparación de heridas en hueso y piel eran, en realidad, 8 y 6.8, respectivamente. En consecuencia, el polímero autoinmolativo sensible a pH 5 anteriormente empleado fue modificado y la síntesis de iniciadores de la autoinmolación alternativos sensibles a pH 8 y 6.8 fue explorada. La síntesis del fragmento sensible a pH 8 involucró el desarrollo de 3 protocolos. En particular, aquel basado en el uso de grupos protectores involucró 3 subprotocolos adicionales. Desafortunadamente, todos los intentos fueron insatisfactorios y la molécula no pudo ser sintetizada. Tras exponer los resultados en una reunión del proyecto, el consorcio acordó descartar la síntesis de la molécula sensible a pH 8. Con respecto al pH 6.8, la molécula iniciadora de la autoinmolación fue sintetizada con éxito, aunque no se pudo incorporar como finalizador del polímero autoinmolativo a pesar de usar diferentes aproximaciones. En vista de estos resultados, el consorcio activó un plan de contingencia y como consecuencia se activó la síntesis de un polímero con un comportamiento diferente, no autoinmolativo. Desafortunadamente la polimerización del monómero fue insatisfactoria a pesar de los diferentes métodos empleados. Finalmente, el consorcio descartó la síntesis del polímero autoinmolativo sensible a pH 6.8.

- 5) El uso de especies redox sobreexpresadas en el citoplasma de las células fue explorado con estímulo alternativo para iniciar la liberación desde el transportador. Una pequeña molécula autoinmolutiva sensible a redox se sintetizó y ancló a las MSNs para retardar la liberación prematura. Este proceso implicó inicialmente la optimización del proceso de sililado la molécula autoinmolutiva. Tras ello, su anclaje a la superficie de la sílice mesoporosa fue también optimizado. Las partículas fueron *PEGiladas* para mejorar su estabilidad coloidal y proporcionar propiedades furtivas. El comportamiento sensible a especies redox fue validado sometiendo a las partículas a una solución que contenía un agente reductor, y se demostró que la molécula autoinmolutiva ya no se encontraba en las partículas tras la aplicación de dicha solución. Finalmente, la habilidad de la molécula para retardar la liberación prematura de la carga fue evaluada *in vial*, demostrando que mayor cantidad de fluoróforo era liberado cuando el agente redox estaba presente en el medio.
- 6) La última parte consistió en el desarrollo de un sistema capaz de superar barreras biológicas relevantes. Para ello, el sistema sensible a redox fue empleado como material de partida. Tras ello, se diseñó una molécula peptídica que contenía una parte capaz de reconocer células tumorales y otra capaz de inducir el escape endosomal. La molécula fue anclada a las partículas y su desempeño biológico fue evaluado en cultivos celulares 2D y 3D. El sistema aquí diseñado pudo ser preferencialmente internalizado por las células tumorales frente a las normales. Además, el sistema mostró mayor internalización que el resto de controles, indicando el efecto positivo del fragmento peptídico. Además, se demostró que las partículas con el fragmento peptídico pudieron internalizar más profundamente en esferoides celulares, probablemente a través de eventos de transcitosis. El sistema aquí diseñado demostró ser totalmente biocompatible en modelos *in vitro* 2D y 3D. Más aún, el sistema cargado con un fármaco pudo inhibir significativamente la viabilidad celular en ambos tipos de modelos celulares, indicando su idoneidad para ser potencialmente aplicado como sistema de transporte de fármacos. La acumulación de las partículas en la masa tumoral fue estudiada usando embriones de pollo en los que se crecieron tumores. Se pudo observar que las partículas se acumularon preferencialmente en la masa tumoral en lugar de en el resto de órganos, indicando la excelente biocompatibilidad del sistema aquí diseñado. Finalmente, un estudio preliminar de eliminación tumoral

fue llevado a cabo, mostrando que las partículas cargadas con un fármaco pudieron reducir significativamente el peso del tumor en un corto periodo de tiempo.

En resumen, el trabajo realizado durante esta tesis doctoral reafirma la idoneidad de usar nanotransportadores mesoporosos como sistemas de transporte de fármacos. Además, la utilidad de usar química autoinmolativa para controlar la liberación prematura de fármacos con sistemas estímulo-respuesta ha sido validada, y podría sentar las bases para futuras compuertas inteligentes. Finalmente, se desarrolló un sistema peptídico muy simple pero efectivo capaz de superar barreras biológicas relevantes, cuya principal característica es la capacidad de modificar fácilmente el fragmento de reconocimiento de células tumorales, de modo que diferentes tipos de estas células pueden ser reconocidas a voluntad.





## Appendix I. Characterization techniques

The objective of this appendix is to provide a brief introduction to the different techniques employed to characterize the performance of the materials produced during this doctoral thesis. The information here presented is a summary of the instructions manuals as well as different online information from the different manufacturers. Table A1.1 summarizes the essential information provided by each technique.

**Table A1.1.** Summary of the techniques employed to characterize the performance of the materials here produced and the information that can be obtained from them.

Characterization technique	Sample Information
Thermogravimetric Analysis (TGA)	Quantification of the amount of organic matter
Fourier Transformed Infrared (FTIR) spectroscopy	Presence or absence of functional groups
X-Ray Diffraction (XRD)	Mesostructure periodicity
Nitrogen porosimetry	Textural properties
Scanning Electron Microscopy (SEM)	Morphology and size
Transmission Electron Microscopy (TEM)	Morphology, porosity and size
Dynamic Light Scattering (DLS)	Colloidal stability and hydrodynamic size
Zeta potential	Surface charge
<sup>1</sup> H-Nuclear Magnetic Resonance ( <sup>1</sup> H-NMR)	Identification of <sup>1</sup> H atoms in an organic compound
X-ray Photoelectron Spectroscopy (XPS)	Functional groups and composition of a surface
MALDI-TOF mass spectrometry	Molecular weight of an organic compound
Elemental analysis	Content of C, H, N, S
Confocal microscopy	Quantitative cellular uptake of the particles
Flow cytometry	Qualitative cellular uptake of the particles

### Thermogravimetric Analysis

This technique provides a quantitative analysis of the sample composition as a function of temperature. It allows to quantify the variations in the sample weight upon application of a heating ramp under a controlled atmosphere. In particular, this technique has been employed during this thesis to evaluate the correct surfactant removal and the amount of organic matter incorporated in the different mesoporous nanomatrices after each functionalization step.

### Fourier Transformed Infrared spectroscopy

This technique allows the determination of the presence or absence of functional groups in a sample upon irradiation with infrared light (4,000-400 cm<sup>-1</sup>). The irradiation of a sample provides a FTIR spectrum, which is composed of vibration bands that are unique for a particular sample. The origin of those bands is the various types of vibrations



that can be detected for the different bonds of the molecule upon infrared irradiation. FTIR spectroscopy finds wide application because it is possible to analyze liquids, gels, fibers, surfaces...In particular, this technique has been employed during this PhD to evaluate the proper surfactant elimination as well as the success of the different grafting steps.

### **X-Ray Diffraction**

This technique provides information about the structural periodicity of a material upon irradiation with x-rays. The x-ray beams are elastically dispersed after interacting with the sample and, consequently, they preserve the initial wavelength. The beams can only be dispersed in certain directions, which are characteristic of a particular periodic system and are determined by the Bragg law (Equation **A1.1**).

$$n\lambda = 2d_{hkl} \sin \Theta$$

**Equation A1.1.** The Bragg law provides the directions in which the x-ray beams are diffracted.  $n$ : diffraction order,  $\lambda$ : wavelength,  $d_{hkl}$ : distance between planes and  $\Theta$ : irradiation angle.

In the case of the mesoporous materials here studied, the small angle XRD allows the determination of the periodicity of the corresponding mesostructure, although they are amorphous at the atomic scale.

### **Nitrogen porosimetry**

This technique provides information about the textural properties of a sample based on the interaction between the nitrogen gas (adsorbate) and the solid to be analyzed (adsorbent). In general, adsorption processes can be classified either as chemisorption (existence of chemical bond between adsorbate and adsorbent) or physisorption (the interaction is labile and take place through Van der Waals interactions). The results of the nitrogen porosimetry, which is based on physisorption processes, are expressed as adsorption-desorption isotherms. These curves provide the volume of gas adsorbed by the surface as a function of the pressure conditions. The raw data obtained by the apparatus is treated using different mathematical models to provide the textural properties. In our case, the textural properties that have been measured are the specific surface area, the pore volume and the pore size:

- Specific surface area: It provides the surface of the solid per unit of mass. The value has been determined using the B.E.T. (Brunauer-Emmett-Teller) mathematical model.
- Pore volume: Nitrogen porosimetry provides the volume occupied by the adsorbate within the adsorbent at a  $p/p_0$  close to 1. In this case, the value is the direct volume filled by the gas molecules and no mathematical models are employed.
- Pore size: This parameter can be elucidated using different mathematical models. The BJH (Barret-Joyner-Halenda) model, which allows to calculate the pore size in the range 2-50 nm, has been employed during this thesis.

This technique has been initially employed during this PhD thesis to determine the textural properties of the different as-produced mesoporous materials. In addition, the variations in the above-mentioned parameters after the different functionalization steps verify the success those synthetic steps.

### **Scanning Electron Microscopy**

This technique provides high resolution images of surface based on the interactions between the electron beam and the surface of the sample. These microscopes present high depth of field so a large area of the sample can be focused at the same time. The samples are required to be conductor for SEM observation. For that purpose, they are usually covered with a carbon or gold layer. The image is formed from the detection of secondary and backscattered electrons by electromagnetic lenses. Finally, the image is formed from the amount and intensity of the electrons detected.

This technique has been employed during this doctoral thesis to evaluate the correct synthesis of the different nanomatrices here produced, in terms of morphology, size or state of aggregation.

### **Transmission Electron Microscopy**

This technique allows the observation of materials, even at the atomic scale (HRTEM), when a high energy electron beam is focused on a thin sample. The beam interacts with the atoms of the sample and consequently, some electrons go directly through the sample while others are scattered. All electrons are then collected and a grayscale image is generated from the different degree of dispersion of the electrons. This technique provides

information about the crystallinity of a material or whether it shows porosity, among others.

This electron microscopy technique has been employed during this thesis to evaluate the presence of porosity in the as-produced mesoporous samples. In addition, the presence of organic matter in the samples can be evaluated if materials are stained with phosphotungstic acid.

### **Dynamic Light Scattering**

This technique allows the determination of the size distribution of particles or emulsions, among others. It is based on the Brownian motion of the particles or molecules present in the solution. As a consequence of this motion, light is dispersed showing different intensities, whose analysis permits the determination of the speed of the Brownian motion. In our case, that speed provides the size of the particles through the Stokes-Einstein equation (Equation A1.2).

$$D = \frac{kT}{3\pi\eta r}$$

**Equation A1.2.** The Stokes-Einstein equations provides the diffusion coefficient  $D$ , which is related to the hydrodynamic size of the particle.  $k$ : Boltzmann constant,  $T$ : Temperature,  $\eta$ : liquid viscosity

In the case of the materials produced during this PhD thesis, this technique has been used to evaluate the correct synthesis of MSNs (indicated by the absence of big aggregates) as well as the colloidal stability of the particles after the different functionalization steps.

### **Zeta potential**

This technique provides information about the surface charge of the particles through the application of an electric field between two electrodes. The magnitude of the zeta potential, which can be positive, negative or neutral, indicates the degree of electrostatic repulsion between adjacent as similarly charge particles in a dispersion. In particular, this technique has been employed during this thesis to evaluate the success of the different functionalization steps as a function of the variations in the surface charge of the particles.

## **<sup>1</sup>H-Nuclear Magnetic Resonance**

This technique is mainly used to elucidate molecular structures of organic compounds, although it can also be applied to thermodynamic and kinetic studies. <sup>1</sup>H has magnetic spin, which moves around a rotation axis as if it were a small magnet. The spins are randomly oriented in absence of magnetic field. However, the field is applied the nuclei can absorb the energy of the spins are promoted to a state of different energy. Nuclei emit signals when they go back to the ground state. That signal depends on the energy gap between the two spin states and can be detected by the apparatus. The magnetic field sensed by each atom and, consequently, the resonance frequency depend on the surrounding environment of each atom. This technique has been thoroughly applied during this doctoral thesis to evaluate the correct synthesis of the different organic molecules grafted to the mesoporous matrices.

## **MALDI-TOF mass spectrometry**

The acronym stands for *Matrix-Assisted Laser Desorption/Ionization - Time-Of-Flight*. This technique allows the analysis of biomolecules (proteins, peptides, lipids, sugars) and other organic molecules (small molecules, polymers, dendrimers...) that tend to be fragile and would be fragmented using other ionization techniques. The sample is initially mixed with a suitable matrix material and applied to a metal plate. Then, a pulsed laser irradiates the sample, leading to the ablation and desorption of the sample and the matrix. Finally, the molecules are ionized and the gaseous state obtained is subsequently accelerated into the mass spectrometer.

This technique has been employed during this PhD thesis to evaluate the molecular weight of particular organic macromolecules, providing additional information to the <sup>1</sup>H-NMR.

## **X-ray Photoelectron Spectroscopy**

This technique provides quantitative information about the elemental composition of the surface of a material. XPS spectra are obtained by irradiating the material with an x-ray beam and, at the same time, measuring the kinetic energy and the amount of electrons that escape from the material under high vacuum conditions.

This characterization technique has been employed during this thesis to evaluate the chemical groups present on the surface of the carbon materials and the subsequent changes upon functionalization with the polymeric coating.

### **Elemental analysis**

This technique provides the amount of carbon, hydrogen, nitrogen and sulfur in a material. Samples are burnt at 1,000°C under an oxygen atmosphere so that organic molecules are converted into simple gases, such as CO<sub>2</sub>, N<sub>2</sub>, H<sub>2</sub>O...that are separated using a chromatography column. The total amount of each one is measured thanks to their thermal conductivity. This technique has been employed during this doctoral thesis to evaluate the success of different functionalization steps as a function of particular atoms. In addition, the analysis of sulfur content was employed to evaluate the redox-responsiveness of one of the materials here produced.

### **Confocal microscopy**

This technique allows the observation of discrete layers of a sample by using a pinhole that discards light that is out of focus. It is possible to generate 3D images from the stacking of individual layers. It is widely employed in biosciences because it allows the detection of light with different wavelengths. In this way, it is possible to stain different parts of the cells and the particles to observe them and to evaluate whether particles and cells are in the same plane, *i.e.*, if particles are inside the cells.

This technique has been employed during this PhD thesis to evaluate the effective internalization of the particles in different cellular models.

### **Flow cytometry**

This technique provides qualitative information about the physical and chemical characteristics of a population of cell. The cells are suspended in a fluid and subsequently injected in the cytometer. Ideally, only one cell flow at a time through the laser beam and the scattered light is characteristic to the particular cell and its components. It allows the detection of fluorescent markers.

This technique has been employed during this thesis to evaluate the amount of particles incorporated in the cells, providing a value of its ability to be internalized by different type of cells.

## Appendix II. Publications

- 1) **Gisbert-Garzarán, M.**; Lozano, D.; Vallet-Regí, M.; Manzano, M. Self-Immolative Polymers as Novel pH-Responsive Gate Keepers for Drug Delivery. *RSC Adv.* **2017**, *7*, 132–136. Cited by: 18; IF: 3.049; Citescore: 3.16.
- 2) **Gisbert-Garzarán, M.**; Manzano, M.; Vallet-Regí, M. pH-Responsive Mesoporous Silica and Carbon Nanoparticles for Drug Delivery. *Bioengineering* **2017**, *4*. Cited by: 13; IF: -; Citescore: 3.14
- 3) **Gisbert-Garzarán, M.**; Manzano, M.; Vallet-Regí, M. Self-Immolative Chemistry in Nanomedicine. *Chem. Eng. J.* **2017**, *340*, 24–31. Cited by: 7; IF: 8.355; Citescore: 8.47.
- 4) **Gisbert-Garzarán, M<sup>1</sup>.**; Berkmann, J-C<sup>1</sup>.; Giasafaki, D.; Lozano, D.; Spyrou, K.; Manzano, M.; Steriotis, Th.; Duda, G-N.; Schmidt-Bleek, K.; Charalambopoulou, G.; Vallet-Regí, M. Engineered pH-Responsive Mesoporous Carbon Nanoparticles for Drug Delivery. *Submitted*.
- 5) **Gisbert-Garzarán, M.**; Matsumoto, K.; Komatsu, A.; Lozano, D.; Manzano, M.; Tamanoi, F.; Vallet-Regí, M. Targeted Redox-Responsive Mesoporous Silica Nanoparticles with Enhanced Endosomal Escape Capabilities. *Under preparation*.
- 6) Boffito, M.; Torchio, A.; Tonda-Turo, C.; Laurano, R.; **Gisbert Garzarán, M.**; Berkmann, J-C.; Cassino, C.; Manzano, M.; Schmidt- Bleek, K.; Vallet-Regí, M.; Duda, G-N.; Ciardelli, G. Hybrid Injectable Sol-Gel Systems Based on Thermo-Sensitive Polyurethane Hydrogel Carrying pH-Sensitive Mesoporous Silica Nanoparticles for the Controlled and Triggered Release of Therapeutic Agents. *Under preparation*.

<sup>1</sup> Both authors contributed equally to the work.



This doctoral thesis is focused on the design, synthesis and physical-chemical and biological evaluation of stimuli-responsive mesoporous nanomatrices with potential applicability for the treatment of bone and wound healing or cancer.

The first part of this doctoral thesis comprises (1) the development of internal stimuli-responsive self-immolative moieties responsive to either pH changes or redox species, (2) the development of synthetic approaches to graft those molecules to the surface of the particles and (3) the evaluation of the pore capping capability of these structures. In addition, the biological performance has been evaluated, showing outstanding biocompatibility and efficiency.

The second part of this doctoral thesis is focused on the development of a simple but unique strategy to bypass some of the biological barriers that nanoparticles have to face when administered in the body. For that purpose, a multifunctional molecule able to (1) selectively recognize cancer cells over normal cells and (2) induce endosomal escape has been synthesized and grafted to mesoporous silica nanoparticles. In addition, (3) a pseudo-*in vivo* model has been employed to validate that these particles are able to preferentially accumulate in the tumoral mass.

Esta tesis doctoral se centra en el diseño, síntesis y caracterización fisicoquímica y biológica de nanomatrices mesoporosas estímulo-respuesta con potencial aplicabilidad en el tratamiento de enfermedades de hueso y piel o cáncer.

La primera parte de la presente tesis doctoral se ha centrado en (1) el desarrollo de estructuras autoinmolativas sensibles a estímulos internos (variaciones de pH y sobreexpresión de especies reductoras), (2) el desarrollo de métodos de anclaje de dichas moléculas a la superficie de las partículas y (3) la evaluación de la eficiencia de estas estructuras para cerrar los poros. Además, se ha evaluado el desempeño biológico de estos sistemas, demostrando su alta biocompatibilidad y eficiencia.

La segunda parte de esta tesis doctoral se ha centrado en el desarrollo de una aproximación capaz de superar algunas barreras biológicas que las nanopartículas tienen que afrontar al ser aplicadas al tratamiento del cáncer. Para ello, se ha desarrollado y anclado a nanopartículas mesoporosas de sílice una molécula capaz, al mismo tiempo, (1) de reconocer selectivamente células tumorales y (2) de inducir el escape endosomal. Además, (3) se ha comprobado en un modelo pseudo-*in vivo* que las partículas son capaces de acumularse preferencialmente en la masa tumoral.

